

# **A Study of Fluid Flow Phenomena around Parallel-Plate Stacks in a Standing Wave Thermoacoustic Device**

A thesis submitted to The University of Manchester for the degree of  
Doctor of Philosophy  
in the Faculty of Engineering and Physical Sciences

2011

XIAOAN MAO

School of Mechanical, Aerospace and Civil Engineering

# Table of Contents

*(Please note that for Chapters 4-7 the sub-sections are those of the original published papers)*

<b>Table of Contents</b> .....	<b>2</b>
<b>List of Figures</b> .....	<b>6</b>
<b>List of Tables</b> .....	<b>10</b>
<b>List of Symbols</b> .....	<b>11</b>
<b>Abstract</b> .....	<b>14</b>
<b>Declaration</b> .....	<b>16</b>
<b>Copyright</b> .....	<b>16</b>
<b>Acknowledgements</b> .....	<b>17</b>
<b>Chapter 1 Introduction</b> .....	<b>18</b>
1.1 Thermoacoustic effect .....	18
1.2 Motivation behind this work .....	19
1.3 Aims and objectives .....	20
1.4 The outline of the thesis .....	22
<b>Chapter 2 Background and literature survey</b> .....	<b>24</b>
2.1 Basic concepts of thermoacoustics .....	24
2.1.1 A short history of thermoacoustics .....	24
2.1.2 Lagrangian point of view of thermoacoustic effect .....	29
2.1.3 Linear theory of general thermoacoustics .....	31
2.2 Fluid mechanical phenomena in oscillatory flows .....	35
2.2.1 General behaviour of oscillatory flow .....	35
2.2.1.1 Transition to turbulence .....	36
2.2.1.2 Pressure drop and friction loss in oscillatory flow .....	40
2.2.1.3 Entrance effects in channels .....	41
2.2.1.4 Patterns of wake flow in oscillatory flow past obstacles (Similarity parameters) .....	42
2.2.1.5 Vortex shedding frequency .....	44
2.2.2 Studies of fluid flow within thermoacoustic devices.....	47
<b>Chapter 3 Overview of the research work, its rationale and summary of papers under “alternative format thesis”</b> .....	<b>60</b>
3.1 Overview of papers submitted in “alternative format” .....	60
3.2 Fulfilling research programme’s aims and objectives .....	62
3.3 Contributions to published works and science and engineering .....	63
<b>Chapter 4 Acoustic coupling between the loudspeaker and the resonator in a standing-wave thermoacoustic device</b> .....	<b>66</b>

(Published in *Applied Acoustics*)

- 1 Introduction
  - 2 Experimental apparatus
  - 3 Theoretical model
    - 3.1 Acoustic equations
    - 3.2 General solutions
    - 3.3 Joining conditions
    - 3.4 Loudspeaker equation
    - 3.5 Solution
  - 4 Experimental results and their comparison to theoretical predictions
    - 4.1 Low amplitude experiments
    - 4.2 High amplitude experiments
    - 4.3 Loudspeaker nonlinearity
    - 4.4 Nonlinear acoustics in the resonator
  - 5 Conclusion
- References

## **Chapter 5 PIV studies of coherent structures generated at the end of a stack of parallel plates in a standing wave acoustic field 67**

(Published in *Experiments in Fluids*)

- 1 Introduction
  - 2 Experimental apparatus and procedure
  - 3 Experimental results
    - 3.1 Overview of the experimental parameters and conditions
    - 3.2 Oscillatory flow around the end of the stack
      - 3.2.1 Ejection stage
        - 3.2.1.1 Formation of a pair of attached symmetric vortices
        - 3.2.1.2 Elongated vortex structure
        - 3.2.1.3 Break-up of elongated vortices into an asymmetric “vortex street”
        - 3.2.1.4 Alternate vortex shedding from the end of the plate
      - 3.2.2 Suction stage
    - 3.3 Comparisons between flows at various peak Reynolds number,  $Re_d$
    - 3.4 Comparisons between flows around Stack I and Stack II
    - 3.5 Frequency of vortex shedding
  - 4 Discussion of results and direction of further studies
    - 4.1 “Mirror” versus “translational” symmetries between adjacent vortex streets
    - 4.2 Reynolds number paradox
    - 4.3 Similarity issues – geometry and flow parameters
  - 5 Conclusion
- Acknowledgements
- References

## **Chapter 6 Application of particle image velocimetry measurement techniques to study turbulence characteristics of oscillatory flows around parallel-plate structures in thermoacoustic devices ..... 68**

(Published in *Measurement Science and Technologies*)

1	Introduction
2	Literature review
3	Experimental apparatus and measurement technique
3.1	Resonator and stacks
3.2	Flow seeding and laser illumination
3.3	Details of PIV measurement
4	Results and discussion
4.1	Validation of velocity measurement
4.2	Ensemble averaging of the velocity field
4.3	Comparison between the instantaneous and averaged flow features
4.4	Turbulence versus “total fluctuation” intensity – spatial distribution
4.5	Separation of fluctuation intensity with regard to length scales: small-scale turbulence intensity
5	Conclusion and future work
	Acknowledgements
	References

**Chapter 7 Oscillatory flow at the end of parallel-plate stacks:  
phenomenological and similarity analysis ..... 69**

(Published in *Fluid Dynamics Research*)

1	Introduction and background
2	Experimental apparatus and method
3	Physics of the oscillatory flow: linear theory versus experimental observations
3.1	Linear theory approximation
3.2	Experimental observation at the end of the stack
4	Non-dimensional parameters controlling oscillatory flows at the stack end
4.1	Normalization
4.2	Illustration of the non-dimensional parameters concept through experimental results
5	Discussion and conclusion
	References

**Chapter 8 Conclusions and suggestions for future work ..... 70**

**Appendix A Additional information about the measurement techniques  
used during the course of the experimental programme.. 73**

A.1	Hot-wire anemometry and experimental measurements ..... 73
A.1.1	Introduction ..... 73
A.1.2	Principles and the hot-wire anemometry system ..... 75
A.1.3	Calibration of a hot wire probe ..... 79
A.1.4	Data acquisition and processing ..... 81
A.2	Particle image velocimetry and experimental measurements ..... 82
A.2.1	Introduction ..... 82
A.2.2	Principle of the particle image velocimetry ..... 83
A.2.3	PIV system and experimental arrangement ..... 87

A.2.4	Image acquisition and post-processing .....	90
A.2.5	Phase locking mechanism .....	92
A.2.6	Determination of vorticity .....	93
<b>Appendix B</b>	<b>Input file for analysis with DeltaEC .....</b>	<b>95</b>
<b>Appendix C</b>	<b>MATLab script for analysis of the coupling of acoustic driver and resonator.....</b>	<b>97</b>
<b>Bibliography</b>	<b>.....</b>	<b>100</b>

**Final word count: 69,858**

# List of Figures

(Please note that for Chapters 4-7 figure numbering of the original published papers is retained)

Figure 1.1	Thermoacoustic device and its main components .....	19
Figure 2.1	Rijke tube and Sondhauss tube .....	25
Figure 2.2	(a) Schematic drawing of a simplified standing wave thermoacoustic engine. (b) Profiles of acoustic pressure and particle velocity along the resonator. (c) Profile of the mean temperature of the fluid within the flow channel and the illustration of the temperature of a gas parcel in one thermodynamic cycle. (d) Illustration of the thermodynamic cycle undertaken by a gas parcel in $p$ - $v$ diagram, with the solid temperature adjacent to the gas parcel in the cycle. ...	29
Figure 2.3	(a) Schematic drawing of a simplified standing wave thermoacoustic refrigerator. (b) Profiles of acoustic pressure and particle velocity along the resonator. (c) Profile of the mean temperature of the fluid within the flow channel and the temperature of the gas parcel in one thermodynamic cycle. (d) Illustration of the thermodynamic cycle undertaken by a gas parcel in $p$ - $v$ diagram, with the solid temperature adjacent to the gas parcel in the cycle. ...	31
Figure 2.4	Stability diagrams: (a) $R_e$ vs. $\lambda$ and (b) $R_\delta$ vs. $\lambda$ . Circle, laminar or distorted laminar flow; Solid circle, weakly turbulent flow; Solid circle with a cross, conditionally turbulent flow. ....	37
Figure 2.5	Boundaries between laminar and turbulent regimes for an oscillating flow in a circular pipe.....	39
Figure 2.6	Three flow regions around a parallel plate stack in a resonator .....	48
Figure 2.7	Smoke visualization of the flow structure at the end of stack plates .....	49
Figure 2.8	Vorticity field around the end of two stacks for three phases .....	50
Figure 2.9	Vorticity fields and contours behind the stack with 0.41 mm spacing and 0.17 mm plate thickness; Top panel: pressure amplitude of 1000 Pa; Bottom panel: pressure amplitude of 4000 Pa .....	52
Figure 2.10	Vorticity fields at the end of stack at high drive ratio .....	53
Figure 2.11	Vorticity plots at the end of the stack with 1 mm thick plate and 4 mm spacing at four different velocity amplitudes .....	54
Figure 2.12	Evolution of the streamfunction distribution for eight phases within acoustic cycle .....	56
Figure 2.13	Numerically obtained vorticity and velocity fields .....	57

## Chapter 4

Figure 1	Sketch of a thermoacoustic refrigerator. The electrodynamic transducer (a loudspeaker) provides an acoustical power $W_{ac}$ to the system. This power is converted into heat flux by the stack of plates due to the thermoacoustic effect. A quantity of heat $Q_c$ can thus be pumped from the cold reservoir to be cooled via the cold heat exchanger, while the excess heat $Q_h$ is released at the hot heat exchanger. The two diagrams in the bottom represent the acoustic pressure and velocity amplitudes, $ p $ and $ u $ , along the resonator for a quarter-wavelength
----------	---

operation. The velocity antinode is at the driver, while the pressure antinode is at the resonator rigid end.

- Figure 2 Left: picture of the whole apparatus; the long Perspex rig (1) and the contracting section (2) are visible. Right: picture of an enlarged view of the contracting section (2) and of the loudspeaker box (3), with one loudspeaker mounted on one of its sides.
- Figure 3 Schematic of the geometry of the loudspeaker and acoustic resonator.
- Figure 4 Drive ratio,  $D_r = |p_c(x_3)|/p_0$ , as a function of the frequency,  $f$ , for a fixed value of the voltage amplitude imposed on the loudspeaker ( $V_e = 0.849$  V): —, theory and  $\Delta$ , experiments.
- Figure 5 Predicted normalized velocity and pressure amplitudes along the resonator for the first mode ( $f = f_1 = 13.1$  Hz) and  $V_e = 0.849$  V: —, pressure and - - -, velocity. The two vertical dotted line indicate the pyramidal contraction limit positions, at  $x = x_1$  and  $x = x_2$ .
- Figure 6 Drive ratio,  $D_r$ , corresponding to the first resonant mode ( $f = f_1 = 13.1$  Hz) plotted versus the loudspeaker driving voltage amplitude,  $V_e$ : —, result given by theory;  $\circ$ , result provided by experiments; - - -, result provided by the numerical code DELTAE, taking into account turbulence; and  $\cdot \cdot \cdot$ , result provided by the numerical code DELTAE, taking into account turbulence and using an impedance to model the minor losses at  $x = x_2$  ( $K = 0.6$ ). The vertical line at  $V_e = 18$  V indicates the limit past which turbulence can be expected.
- Figure 7 Membrane displacement amplitude,  $D_{\text{memb}}$ , corresponding to the first resonant mode ( $f = f_1 = 13.1$  Hz) plotted versus the loudspeaker driving voltage amplitude,  $V_e$ : —, result given by linear theory Eq. (41);  $\circ$ , result provided by experiments and  $\cdot \cdot \cdot$ , result provided by the numerical code DELTAE, taking into account turbulence and using an impedance to model the minor losses at  $x = x_2$  ( $K = 0.6$ ). The horizontal line indicates the linear excursion amplitude  $X_{\text{max}}$  provided by the manufacturer.

## Chapter 5

- Figure 1 Sketch of the experimental apparatus
- Figure 2 Geometry of the stack (only three plates shown)
- Figure 3 Phase-averaged velocity oscillation at point M and corresponding phases at which the PIV measurements are taken.  $dp/dx$  is the axial gradient of acoustic pressure in an oscillation period. (Simple-harmonic oscillation is assumed so that  $dp/dx$  is  $90^\circ$  out of phase of velocity oscillation.)
- Figure 4 Vorticity contour map for the flow around the end of Stack I during one acoustic cycle. a  $\Phi 1$ , b  $\Phi 5$ , c  $\Phi 7$ , d  $\Phi 9$ , e  $\Phi 10$ , f  $\Phi 11$ , g  $\Phi 12$ , h  $\Phi 15$ , i  $\Phi 20$  ( $Re_d = 207$ ,  $D_r = 1.0\%$ ). The unit of vorticity legend is  $s^{-1}$ .
- Figure 5 Transverse profile of axial velocity taken at  $x = 5$  mm. Stack I, drive ratio 1%. a  $\Phi 1$ , b  $\Phi 5$ . ( $Y$  remains the same as the coordinate system used in Fig. 4)
- Figure 6 Vorticity field around the end of one plate in Stack I, shown for five drive ratios and five selected phases within the cycle; a  $D_r = 0.3\%$ ; b  $D_r = 0.6\%$ ; c  $D_r = 1.0\%$ ; d  $D_r = 1.5\%$ ; e  $D_r = 2.0\%$ ; colour scale is the same as for Fig. 4.
- Figure 7 Vorticity field for the flow around the end of Stack II. a  $D_r = 0.3\%$ ; b  $D_r = 0.6\%$ ; c  $D_r = 1.0\%$ ; d  $D_r = 1.5\%$ ; e  $D_r = 2.0\%$ .

- Figure 8 Signal trace of hot-wire sensor output close to the stack end, and the frequency spectrum of the signal trace; a, b Stack I ( $D_r = 1.0\%$ ;  $u_M = 2.7\text{m/s}$ ;  $Re_d = 194$ ); c, d Stack II ( $D_r = 2.0\%$ ;  $u_M = 6.5\text{m/s}$ ;  $Re_d = 2165$ )
- Figure 9 Strouhal number,  $St$ , versus Reynolds number,  $Re_d$ , based on the plate thickness
- Figure 10 Vorticity field (contour) and velocity field (vector) of the flow at the stack end. a, b Stack I ( $D_r = 0.3\%$ ); c, d Stack II ( $D_r = 0.3\%$ ).

## Chapter 6

- Figure 1 Schematic of a simple thermoacoustic cooler arrangement. The acoustically induced compression and expansion of fluid elements causes heat pumping effects along the stack.
- Figure 2 Schematic of experimental apparatus (a); details of the stack and imaging area (b); and block diagram of the triggering mechanism used for phase-locking in PIV measurements (c)
- Figure 3 Phase-averaged velocity oscillation at a point M and corresponding phases at which the PIV measurements are taken.
- Figure 4 Velocity profiles for ten phases in the cycle: solid lines – theoretical predictions; symbols – ensemble averaged measurements. Data shown for Stack II at  $2.4D$  from the channel entry and  $Dr$  of  $0.3\%$ ; arrows indicate the discrepancy between measured and theoretical profiles for  $\Phi_{11}$  and  $\Phi_{13}$ ; error bars for  $\Phi_5$  and  $\Phi_{15}$  show the standard deviation based on averaging of 100 PIV measurements.
- Figure 5 Effect of the number of instantaneous measurements,  $N$ , on the computation of the flow statistics at point P (a) and point Q (b). Note: units of vertical axes are in  $\text{m s}^{-1}$  for all variables. Index  $N$  indicates the number of PIV images taken to calculate a given statistic: either mean velocity or velocity fluctuation.
- Figure 6 Illustration of the variability between vortex structures in three instantaneous images of the vorticity field (a)–(c). The average vorticity field resulting from ensemble averaging of 100 instantaneous images (d). Stack II,  $Dr = 0.6\%$ , phase  $\Phi_6$ .
- Figure 7 Illustration of the variability between vortex structures in three instantaneous images of the vorticity field (a)–(c). The average vorticity field resulting from ensemble averaging of 100 instantaneous images (d). Stack II,  $Dr = 2.0\%$ , phase  $\Phi_8$ .
- Figure 8 Illustration of the variability between vortex structures in three instantaneous images of the vorticity field (a)–(c). The average vorticity field resulting from ensemble averaging of 100 instantaneous images (d). Stack I,  $Dr = 1.0\%$ , phase  $\Phi_{12}$ .
- Figure 9 Distribution of  $x$  and  $y$  components of fluctuation intensity:  $T_x$  and  $T_y$ ; Stack II,  $Dr = 2.0\%$ , phase  $\Phi_8$ .
- Figure 10 Distribution of the total fluctuation intensity,  $T$ ; Stack II,  $Dr = 0.6\%$ .
- Figure 11 Distribution of the total fluctuation intensity,  $T$ ; Stack II,  $Dr = 2.0\%$ .
- Figure 12 Distribution of the total fluctuation intensity,  $T$ ; Stack I,  $Dr = 1.0\%$ .

- Figure 13 Illustration of the integration area for calculating averaged turbulent kinetic energy  $k_A$  over a sample area A (a); plot of  $k_A$  as a function of phase in the cycle for all experimental configurations (b).
- Figure 14 Area and cycle averaged turbulent kinetic energy  $k_{A,T}$  as a function of drive ratio.
- Figure 15 Schematic of the spatial filtering algorithm based on 2D FFT, for separating instantaneous velocity fields according to the length-scales of eddies present in the flow.
- Figure 16 2D amplitude spectrum maps computed from the instantaneous fluctuation  $u'$  (a) and  $v'$  (b) using 2D spatial FFT.  $f_x\Delta x$  and  $f_y\Delta y$  being the spatial-frequency in the respective directions. An arbitrary scale is used for comparisons.
- Figure 17 Velocity and vorticity fields obtained from spatial filtering of data shown in figure 7c, using the cut-off length of 1.9 mm (a and b) and 3.9 mm (c and d). The top row shows large scale vortex structures obtained from instantaneous velocity fluctuation after low-pass filtering, while the bottom row corresponds to high-pass filtering. Stack II,  $Dr = 2.0\%$ , phase  $\Phi_8$ .
- Figure 18 Distribution of the relative large-scale fluctuation; Stack II,  $Dr = 2.0\%$ ,  $\lambda = 3.9\text{mm}$ .
- Figure 19 Distribution of the relative small-scale fluctuation; Stack II,  $Dr = 2.0\%$ ,  $\lambda = 3.9\text{mm}$ .

## Chapter 7

- Figure 1 Illustration of the oscillatory gas motion coupled with heat transfer to/from the solid.
- Figure 2 Schematic illustration of the experimental rig.
- Figure 3 Schematic of velocity profiles in the resonator and inside the stack channels, in the half cycle when the flow direction is from left to right. Only parts of three plates are shown.
- Figure 4 Mean velocity field (black arrows) superimposed on vorticity field (colour contour) in phases  $\Phi_1$  to  $\Phi_8$ , for  $Dr = 0.3\%$ . The streamlines indicate the flow is from left to right. Plate thickness is 1.1mm and plate spacing is 5.0 mm. The positions of the phases corresponding to the acoustic cycle are shown in the bottom right corner.
- Figure 5 Structure of the flow at the end of a stack of sharp-edged plates of finite thickness.
- Figure 6 Distribution of the longitudinal velocity,  $u$ , along the plate centreline for eight phases (a); Illustration of the regions in the wake (b); Data for stack with  $d = 1.1$  mm and  $h = 5.0$  mm, at  $Dr = 0.3\%$ .
- Figure 7 Variation of recirculation region length with consecutive phases in an acoustic cycle, for stack of plates of 1.1 mm thickness.
- Figure 8 Mean velocity field (black arrows) superimposed on the vorticity field (colour contours) for phases from  $\Phi_4$  to  $\Phi_8$  at  $Dr = 1.0\%$ . The streamlines indicate the flow is from left to right. Stack plates are 1.1 mm thick with 5.0 mm gap between plates. Results in the left column are obtained with a higher spatial resolution, while the right column has a lower spatial resolution but a larger investigated area.

Figure 9 Mean velocity field (black arrows) superimposed on the vorticity field (colour contours) for phase  $\Phi_7$  at (a)  $Dr = 0.3\%$  (a close view) and (b)  $Dr = 1.5\%$  (a zoom-out view). Stack plates are 5.0 mm thick with 10.0 mm gap between plates.

Figure 10 Operating conditions of oscillatory flow around stack of plates in non-dimensional parameter groups ( $Re_\omega$  vs.  $Re_d$ ) and ( $Re_\omega$  vs.  $KC$ ).

## Appendix A

Figure A.1 Schematic of a hot-wire anemometer .....	76
Figure A.2 Geometry of hot-wire sensor .....	76
Figure A.3 Time variation of the acoustic velocity, its absolute value and output of the constant temperature anemometer .....	80
Figure A.4 Amplitude of CTA output vs amplitude of reference velocity at different drive ratios, and the fitted polynomial correlation .....	81
Figure A.5 Timing diagram for PIV imaging in frame straddling mode .....	86
Figure A.6 Schematic diagram of the phase locking pulse generator .....	92
Figure A.7 Block diagram of phase-locking mechanism in PIV measurements .....	93

## List of Tables

*(Please note that for Chapters 4-7 table numbering of the original published papers is retained)*

### Chapter 4

Table 1	Geometry of the resonator
Table 2	Linear parameters and cross sectional area of the loudspeaker

### Chapter 5

Table 1	Summary of stack dimensions and experimental conditions
Table 2	Parameters of stack geometry and oscillating flow

## Appendix A

Table A.1 Characteristics of Tungsten wire .....	77
--	----

# List of Symbols

$A$	Cross sectional area Amplitude of travelling wave
$a$	Sound speed Amplitude of oscillation motion
$B$	Magnetic field intensity
$c$	Sound speed Specific heat
$c_p$	Isobaric specific heat
$D$	Channel width between stack plates Pipe diameter Displacement amplitude of loudspeaker membrane
$d$	Stack plate thickness Diameter of cylinder in oscillatory flow Diameter of seeding particle Differential
$E$	Acoustic power Radiation heat transfer rate Electrical voltage on the hot wire sensor
$f$	Frequency Spatial averaged viscous or thermal function Inverse of spatial period
$H$	Stack plate interspacing ( $= h + d$ )
$h$	Stack channel width Damping factor of the suspension of loudspeaker Heat transfer coefficient Viscous or thermal complex function
$I$	Electrical current through the hot wire sensor
$i$	Square root of -1 Index number
$K$	Coefficient of flow resistance
$k$	Wave number Thermal conductivity Turbulence kinetic energy
$L$	Loudspeaker coil inductance
$l$	Length of stack plate; length of loudspeaker coil
$m$	Moving mass of loudspeaker
$N$	Total number of pairs of images capture in each phase
$p$	Pressure
$Q$	Heat input or output
$q$	Heat input or output per unit area, heat flux
$R$	Reflection coefficient Electrical resistance
$r$	Half side length of resonator duct
$r_h$	Hydraulic radius
$S$	Cross sectional area
$s$	Stiffness of the suspension of loudspeaker Entropy
$T$	Temperature Fluctuation intensity

$t$	Time
$U$	Volume flow rate, volumetric velocity Ensemble averaged velocity
$u$	Flow velocity
$V$	Electrical voltage on the loudspeaker coil Ensemble averaged velocity
$v$	Flow velocity Specific volume
$\mathbf{v}$	Velocity vector
$W$	Acoustic power
$w$	Flow velocity
$x$	Distance, position
$y$	Distance, position
$Z$	Impedance
$z$	Distance, position
$Dr$	Drive ratio
$KC$	Keulegan-Carpenter number
$Ma$	Mach number
$Nu$	Nusselt number
$Re, Re_d$	Reynolds number
$Re_\omega$	Kinematic Reynolds number
$St$	Strouhal number
$Wo$	Womersley number

### Greek alphabet

$\alpha$	Temperature coefficient of resistivity of the hot wire sensor
$\beta$	Coefficient of thermal expansion of the hot wire sensor Stokes number
$\gamma$	Ratio of isobaric to isochoric specific heats
$\Delta$	Difference Distance
$\delta$	Viscous or thermal penetration depth
$\varepsilon$	The emissivity of the hot wire sensor Absolute errors of velocity components
$\zeta$	Bulk viscosity of fluids
$\kappa$	Thermal diffusivity
$\lambda$	Wavelength Cut-off length
$\mu$	Dynamic viscosity
$\nu$	Kinematic viscosity
$\xi$	Particle displacement
$\rho$	Density
$\sigma$	Prandtl number Inertial number, $=2^{1/2}D/2\delta_v$ The Stefan-Boltzmann constant, $5.67 \times 10^{-8} \text{ W}/(\text{m}^2 \cdot \text{K}^4)$
$\sigma'$	Nine-component viscous stress tensor
$\tau$	Relaxation time
$\chi$	The electrical resistivity of the hot wire material
$\omega$	Angular frequency Vorticity
$\Phi$	Phase
$\phi$	Porosity of stack

$\theta$  Small scale fluctuation intensity

### Subscripts

0 Variable at rest  
1 Acoustic variable in first order  
2 Acoustic variable in second order  
*A* Amplitude  
Spatial average  
*a* Axial  
*ac* Acoustic  
*c* Cold  
*crit* Critical value  
*e* Electric  
*g* Gas  
*h* Hot  
*l* Large scale  
*m* Mean value  
*mec* Mechanical  
*memb* Membrane  
*p* Particle  
*rms* Root-mean-square value  
*s* Stack  
Small scale  
*u* Velocity  
*w* Hot wire  
*x,y,z* Coordinates  
*v* Viscous  
 $\kappa$  Thermal

### Superscripts

\* Instantaneous value  
Non-dimensional  
Measured value of velocity components  
*prime* Fluctuation component

### Special symbols

$\partial$  Partial derivative  
 $\nabla$  Spatial gradient, the vector differential operator  
Im[] Imaginary part of  
Re[] Real part of  
|| Magnitude of complex number  
 $\mathcal{M}$  Correction factor for radiation in air  
 $\mathcal{R}$  Gas constant  
 $\mathcal{R}$  Higher order terms in the vorticity calculation  
*overdot* Time derivative  
*overbar* Temporal mean  
*tilde* Complex conjugate

# Abstract

Thermoacoustic devices are a group of systems that make use of the thermoacoustic effect to achieve an energy conversion between thermal and acoustic energy. The thermoacoustic effect occurs when a solid boundary is introduced into an acoustic field, and a non-zero net heat transportation takes place while the net mass transfer remains null. Thermoacoustic technologies are gaining an increasing research interest because of their potential applications for building alternative prime movers or heat pumps which do not use working fluids causing environmental damage and require very little maintenance due to their lack of moving part.

However, the operation of this type of system is yet to be fully understood: fluid flow and heat transfer processes within the system components such as thermoacoustic stacks and heat exchangers still require a lot of attention. The performance of the system working with relatively low amplitude acoustic wave can be predicted by the linear thermoacoustic theory, which is already well developed. However, a high amplitude acoustic wave is usually required in order to achieve high power density or high power output. Unfortunately, the performance of such systems can be seriously degraded due to nonlinear effects, such as turbulence, minor loss or high proportion of harmonics. The lack of understanding of these effects impedes the design and construction of high efficiency systems.

The work described in this thesis is focused on the study of flow phenomena taking place around parallel plate stack placed in a standing wave thermoacoustic resonator, by using advanced flow diagnostics techniques such as particle image velocimetry (PIV) and hot wire anemometry (HWA). In order to carry out the experimental study, a standing wave thermoacoustic device working at relatively low frequency of 13.1Hz was designed, commissioned and tested. The frequency response of this device was carefully investigated and compared with the analytical results using linear acoustic equations and a linear model of the loudspeaker. A further comparison with the analytical results obtained with the modelling tool DeltaEC (Design Environment for Low-amplitude Thermoacoustic Energy Conversion) was also presented. The resonator was driven from low to large pressure amplitudes with drive ratios up to 10%. A good agreement is obtained for small amplitudes, but the discrepancies become larger when the driving amplitude is increased. The analysis reveals that the large discrepancy at high amplitude can be attributed to minor losses.

Following the above preliminary work, a more comprehensive study of the flow field around parallel-plate stacks was conducted by means of PIV and HWA. It was shown that the flow around the two studied parallel-plate stacks exhibits rather complicated flow features when the amplitude of the acoustic oscillation varies. Symmetrical and asymmetrical vortex shedding phenomena are observed and two distinct modes of generating “vortex streets” are identified. It is shown that a velocity related parameter such as the Reynolds number, defined on the plate thickness and the velocity amplitude at the entrance to the stack, and a geometrical parameter are not sufficient to define the flow characteristics in this type of flow problem. It is also proposed to introduce an extra frequency related parameter such as the Keulegan-Carpenter number (KC) and to carry out a similarity analysis in order to understand better the physics behind the flow phenomena and their controlling parameters.

Typical ensemble-averaged velocity fields are used in the analysis above. However, the detailed flow features obtained from the ensemble averaged flow fields and the instantaneous flow fields could be different in a substantial way. The flow behaviour, its kinematics, dynamics and scales of turbulence, therefore are further investigated by using the classical Reynolds decomposition to separate the instantaneous velocity fields into ensemble-averaged mean velocity fields and fluctuations in a set of predetermined phases within an oscillation cycle. The mean velocity field and the fluctuation intensity distributions are investigated over the acoustic oscillation cycle. By using fast Fourier transform (FFT) spatial filtering techniques, the velocity fluctuation is further divided into large- and small-scale fluctuations, and their physical significance is discussed.

The physics behind the flow phenomena are further studied by carrying out an analysis of the wake flow during the ejection part of the flow cycle, where either closed re-circulating vortices or alternating vortex shedding can be observed. A similarity analysis of the governing Navier–Stokes equations is then undertaken in order to derive the similarity criteria governing the wake flow behaviour. Similarity numbers including two types of Reynolds number, the KC number and a non-dimensional stack configuration parameter are considered. The influence of these parameters on the flow behaviour is discussed by investigating the experimental data obtained, along with additional data from literature.

# Declaration

No portion of the work referred to in the thesis has been submitted in support of an application for another degree of qualification of this or any other university, or other institution of learning.

## Copyright Statement

- i. The author of this thesis (including any appendices and/or schedules to this thesis) owns certain copyright or related rights in it (the “Copyright”) and s/he has given The University of Manchester certain rights to use such Copyright, including for administrative purposes.
- ii. Copies of this thesis, either in full or in extracts and whether in hard or electronic copy, may be made only in accordance with the Copyright, Designs and Patents Act 1988 (as amended) and regulations issued under it or, where appropriate, in accordance with licensing agreements which the University has from time to time. This page must form part of any such copies made.
- iii. The ownership of certain Copyright, patents, designs, trade marks and other intellectual property (the “Intellectual Property”) and any reproductions of copyright works in the thesis, for example graphs and tables (“Reproductions”), which may be described in this thesis, may not be owned by the author and may be owned by third parties. Such Intellectual Property and Reproductions cannot and must not be made available for use without the prior written permission of the owner(s) of the relevant Intellectual Property and/or Reproductions.
- iv. Further information on the conditions under which disclosure, publication and commercialisation of this thesis, the Copyright and any Intellectual Property and/or Reproductions described in it may take place is available in the University IP Policy (see <http://www.campus.manchester.ac.uk/medialibrary/policies/intellectual-property.pdf>), in any relevant Thesis restriction declarations deposited in the University Library, The University Library’s regulations (see <http://www.manchester.ac.uk/library/aboutus/regulations>) and in The University’s policy on presentation of Theses.

# Acknowledgements

The first and the most grateful thank is given to my supervisor, Dr Atur J. Jaworski for his constant encouragement and valuable advice. I would not have achieved this without his help both on the academic level and in personal life throughout all these years. Special thanks for his understanding and patience, as a mentor and more often as a good friend.

I would also like to thank the Universities UK for providing funding for me to carry out the study under the ORS scheme, and Engineering and Physical Sciences Research Council (EPSRC) for financial support.

I am also grateful to Dr. David Marx who joined the thermoacoustic team in 2004. The invaluable insights based on his PhD experience of PhD study were of benefit to me in so many different ways. I would also like to thank Dr. Zhibin Yu who joined the thermoacoustic group in 2006 for his insightful opinions during our frequent academic discussions.

I would also like to thank all staff and technicians in Goldstein Research Laboratory in Barton and later those supporting my research at the main campus. They were always so kind to offer their generous help whenever I encountered problems in setting up or modifying the experimental apparatus.

Last but not least, I would like to thank my family who gave every support they could.

# Chapter 1 Introduction

## 1.1 Thermoacoustic effect

Thermoacoustic devices are a group of systems that make use of the “thermoacoustic effect” to achieve energy conversion between the thermal energy and the acoustic energy. Depending on the direction of the energy conversion, there are two main applications: One is to maintain and amplify acoustic wave in a resonator by a temperature gradient imposed on a porous medium placed in the resonator. The other is to transport heat from a “cold reservoir”, such as a heat exchanger placed on one side of the porous medium, to a “hot reservoir” on the other side of the porous medium by means of an excited acoustic wave in the resonator. Devices capable of accomplishing the former are usually referred to as thermoacoustic prime movers (thermoacoustic engines) and those with the latter function as thermoacoustic heat pumps (or thermoacoustic refrigerators). The porous medium usually placed between a hot and cold heat exchanger is generally referred to as a *stack* when a standing acoustic wave is used (the acoustic pressure and velocity being approximately 90 degrees out of phase); and as a *regenerator* when a travelling wave is used (the acoustic pressure and velocity being almost in phase).

In a space where no solid boundary is present, the acoustic oscillation is usually an adiabatic process. Viscous and thermal boundary layers, however, are formed when a solid boundary is present in an acoustic field. In the boundary layer region, the velocity and temperature oscillations interact with each other. This produces a non-zero net heat transport between the solid and the acoustic field in a cycle of acoustic oscillation. The phenomenon of non-zero net heat transport occurring in an acoustic field is generally referred to as “the thermoacoustic effect”. Either the acoustic power of the wave is enhanced by means of the heat input, or the acoustic power is used to pump the heat against the temperature gradient.

The simplest form of a thermoacoustic device can be imagined as a straight resonance tube with a stack or regenerator placed inside, as shown in Fig. 1.1. An acoustic wave in the resonance tube causes the gas in the pore of the stack or regenerator to oscillate. Heat exchangers can be further added to the system, and placed at the ends of the stack or regenerator, to input or remove heat to/from the system.

One of the first accounts of the thermoacoustic effect dates back to the 18th century, when Byron Higgins observed that audible sound was emitted from an organ pipe that was open at both ends, when a hydrogen flame was placed at certain positions in the pipe. This is a typical example of heat excited and maintained acoustic wave, as applied in a thermoacoustic prime mover. Lord Reyleigh gave an intuitive explanation of how the sound could be maintained in his well known book, the Theory of Sound (1945).

The discovery of the heat transport induced by an acoustic wave was made much later by Merkli and Thomann (1975a). They accidentally found the cooling effect on the wall of a tube closed at one end and sealed with a moving piston at the other end, when they intended to study the heating effect in a Hartmann-Sprenger tube.

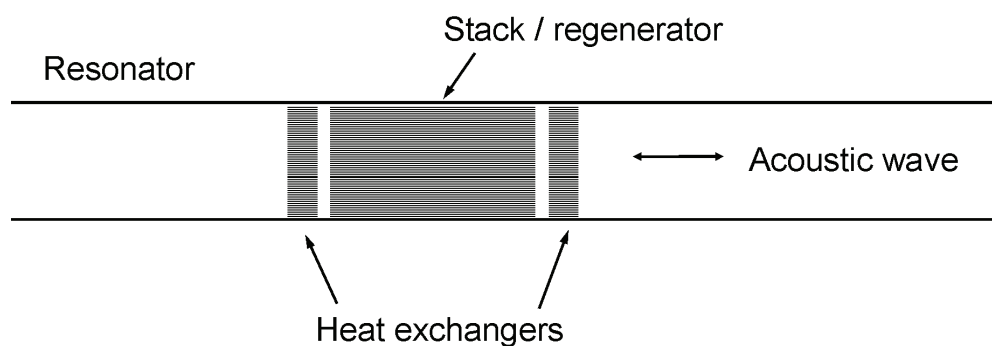


**Figure 1.1 Thermoacoustic device and its main components**

Although thermoacoustic effect was discovered well over two centuries ago, the more advanced and intensive studies of thermoacoustics and its applications started only in 1980s, when a group of scientists in Los Alamos National Laboratory in United States undertook a series of investigations in the context of space missions, due to the unique advantages of thermoacoustic technologies such as simplicity of design and low maintenance.

## **1.2 Motivation behind this work**

Thermoacoustic devices have many potential advantages over the conventional energy-conversion systems, such as internal combustion engines, gas turbine and others. Firstly, they have no mechanical moving parts, except electromagnetic transducers for acoustic excitation or extracting the acoustic power. This makes such systems highly reliable and virtually maintenance-free. Secondly, thermoacoustic devices usually use inert gases as the working media – for example pressurised helium, argon or nitrogen. This makes them

environmentally friendly as there are no chemical compounds involved which could cause global warming or ozone layer depletion. Air can be used as an inexpensive alternative in less demanding applications. Thirdly, they have the potential to be adapted for use of the solar power as the heat source, or utilise low grade waste heat for energy recovery or upgrade. Their simplicity and inherent reliability translate into a low cost, which potentially makes thermoacoustic systems extremely competitive compared to other existing technologies.

For these reasons, thermoacoustic devices are increasingly becoming a focus of many research groups and academic institutions around the world, including the United States, the Netherlands, China, France and Japan. Much work has been dedicated to studying the physics of the thermoacoustic effect and the application of thermoacoustic devices.

Despite the abovementioned potential advantages of thermoacoustic systems, there are still a number of scientific and technological issues, which tend to impede the application of commercially competitive devices in practical situations. These include for example the fluid dynamics of the compressible oscillatory flow associated with the presence of the acoustic field, the nature of resulting heat transfer processes and the overall system efficiency.

From the fluid dynamics point of view, the introduction of the porous medium (e.g. stack) and the heat source/sink (heat exchangers) into the acoustic resonator leads to a rather complicated behaviour of the oscillatory flow around the solid boundary. Typically, the practical use of thermoacoustic devices requires a high power density output, which necessitates the use of high amplitude acoustic waves in the resonator. Under such conditions, there is an increasing influence of nonlinear effects such as turbulence in the flow, higher-order harmonics in the acoustic wave and acoustic streaming. The fundamental nature of some of the problems encountered and their influence on the efficiency of thermoacoustic devices require a more systematic study of the underlying physics. The present study tries to address some of the challenges in understanding the fluid dynamical processes in thermoacoustic systems.

### **1.3 Aims and objectives**

This study was carried out within a standing-wave system, for its flexibility to control the oscillation amplitude while requiring minimum power input. Stacks made of parallel plates

are one of the basic forms widely used in thermoacoustic devices for their relatively simple geometry and ease of construction. Therefore, stacks of this form were chosen as the research object in the present study. The work aimed at gaining the fundamental understanding of the fluid mechanics phenomena that are encountered in a typical thermoacoustic device having a regular geometry thermoacoustic stack placed in the acoustic field.

From the preliminary “scaling” analysis it was apparent that in order to achieve the above, a large-scale thermoacoustic device of a low operating frequency and a low mean pressure would be desirable for the experimental study to be carried out. It was also realised that in order to capture the detailed flow physics, advanced instrumentation would have to be implemented in the challenging environment of a thermoacoustic system.

The objectives of this study were as follows:

1. To design and construct a large scale acoustic resonator working in the standing-wave mode at a low operating frequency and mean pressure in order to obtain a relatively large viscous boundary layer thickness, and thus to enable the measurements to be carried out using standard particle image velocimetry and hotwire anemometry systems;
2. To test the acoustic resonator in order to establish its operating envelope and obtain an understanding of the characteristics of the resonator; To validate the analytical model developed based on linear acoustics with the obtained measurement results;
3. To implement the experimental setups to carry out the experimental studies of the oscillatory flow motion in the vicinity of isothermal parallel-plate stacks of representative dimensions for varied levels of acoustic excitation, by utilizing particle image velocimetry and hot wire anemometry methods;
4. To collect a substantial amount of high quality flow field data and to establish the data post-processing procedures to enable comparative studies of the flow features at various conditions; To collect a substantial amount of flow velocity data with high temporal resolution for the investigation of the vortex shedding process at the end of the stack plates;
5. To carry out comparative studies of the flow features present in the channel between stack plates and at the end of the stack plates, based on the ensemble averaged velocity fields, and to find similarities in the flow features at different conditions; To summarize

- common flow patterns and to investigate the role of conventional Reynolds number as a governing parameter of the oscillatory flows encountered in thermoacoustics;
6. To conduct a similarity analysis based on the theoretical model, and to find main governing similarity numbers which would have a physical link with the common flow patterns/features; Based on the similarity numbers, to classify the typical flow patterns in the appropriate parameter space;
  7. To evaluate the turbulence characteristics of the oscillatory flow around a parallel plate stack and to devise an appropriate approach of defining the fluctuation intensity in this type of application; In particular, to develop a method of separating the velocity component of “turbulent” nature from that caused by the shedding of large-scale coherent structures (vortex shedding process).

#### **1.4 The outline of the thesis**

This thesis is submitted in the “alternative format”, which allows PhD candidates at the University of Manchester to submit their published papers (or papers submitted or prepared for submission) as chapters of their thesis. Therefore the thesis is constructed as follows:

In Chapter 2, a review of the published works relevant to the topic of this study is presented. Some descriptions of the basic concepts of thermoacoustics are given in Section 2.1. A short history of thermoacoustics is given in Section 2.1.1. Section 2.1.2 presents a description of the thermoacoustic effect from the Lagrangian point of view, with a thermoacoustic standing wave engine and a refrigerator as examples. This is followed by an explanation of the linear theory of general thermoacoustics in Section 2.1.3. The following Section 2.2 delivers a review of various fluid flow phenomena studied in oscillatory flows in a general sense, followed by a review of works more closely related to thermoacoustics.

Chapter 3 provides an outline of the actual research work conducted during the PhD programme, and provides an extended introduction to the following chapters (4-7), and explains the rationale of the work undertaken.

Chapter 4 contains the paper published in *Applied Acoustics* which describes the design and construction of the standing wave thermoacoustic resonator, with an analytical model developed and validated against measurement results up to a high acoustic amplitude

(Objectives 1 and 2). Chapter 5 contains the paper published in *Experiments in Fluids* which reports a broad investigation of the flow features around parallel plate stacks (Objectives 3, 4 and 5). Chapter 6 contains the paper published in *Measurement Science and Technology* which outlines the experimental methodology to study turbulence characteristics of the oscillatory flow around parallel plate stacks by using particle image velocimetry (Objective 3, 4 and 7). Chapter 7 contains the paper published in *Fluid Dynamics Research* focused on a similarity analysis and the classification of representative features of oscillatory flow in the non-dimensional parameter space (Objective 6).

Chapter 8 contains the overall conclusions of this thesis, with recommendations for future studies outlined in the end. Finally, Appendix A is a stand-alone section which presents the details of the experimental techniques that were used in the current study in order to allow future research students to carry out similar studies. The input file used for the DeltaEC analysis and the MATLAB script used in the theoretical analysis for the work described in Chapter 4 are included in the Appendix B and C, respectively.

# Chapter 2 Background and literature survey

This research work is focused on the oscillatory flow phenomena that occur in the presence of an acoustic wave in the vicinity of the parallel plate structures placed in a standing wave resonator. It arises from the need to understand the fundamental fluid flow and heat transfer processes in thermoacoustic devices. However, before the details of current research work are presented, relevant literature is reviewed and discussed. At the beginning of this chapter, the basic concepts of the thermoacoustics are introduced and the applications of thermoacoustic effect in engineering for energy conversion are described. In the following part, the studies of the general oscillatory flow phenomena and the fluid flow in thermoacoustic devices are reviewed.

## 2.1 Basic concepts of thermoacoustics

### 2.1.1 A short history of thermoacoustics

The study of thermoacoustics has a rich and interesting history. Sound excitation caused by heat appears to have been first recorded by Byron Higgins, who observed this phenomenon in 1777 (Putnam and Dennis, 1956). When a jet of hydrogen was burned at certain positions in a large organ pipe that was open at both ends, acoustic oscillations were excited and audible sound was emitted from the open ends. This phenomenon is often referred to as a “singing flame” (Richardson, 1922).

In 1859, Petrus L. Rijke discovered that a strong oscillation was generated when heated gauze, instead of a hydrogen flame, was placed in the lower half of a vertical pipe with open ends at the top and bottom (Feldman, 1968a). When the gauze was located in the upper half of the pipe, the oscillation would not occur. Such a device with two open ends is usually called a “Rijke tube”, as shown in Figure 2.1a. Rijke attributed the production of the sound to the successive expansion and contraction of the convection current when it passed the heated screen and the cold pipe wall. Rijke oscillations have been the subject of many studies over the last 150 years, typically for their importance in combustion.

Another early account of thermoacoustic oscillation is that of Sondhauss, published in 1850 (Feldman, 1968b). Centuries ago, glass-blowers noticed that when a hot glass bulb was attached to the end of a cold tubular stem, a sound was sometimes produced. Such a “Sondhauss tube” was open at one end and terminated in a bulb at the other, as shown in

Figure 2.1b. Sondhauss investigated this kind of system quantitatively and found a direct relation between the frequency of the emitted sound and the geometry of the bulb-pipe assembly. He observed that larger bulbs and longer tubes produced lower frequency sounds. He also found that the sound was more intense when the bulb was hotter. The Sondhauss tube can be considered a prototype of the present-day standing wave thermoacoustic heat engine, except that modern thermoacoustic engines are usually constructed as closed systems to harness the acoustic power generated without unnecessary power loss to the surroundings.

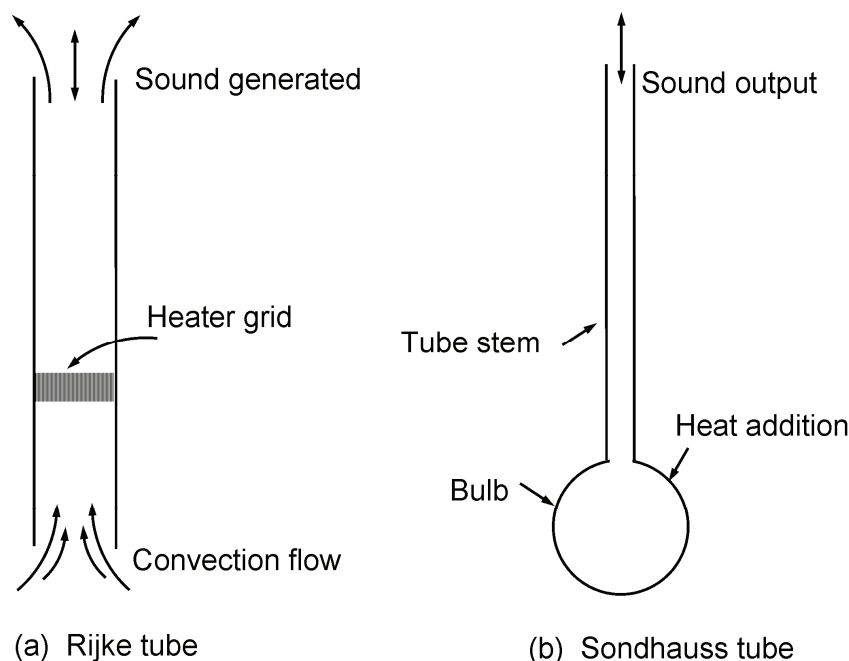


**Figure 2.1 Rijke tube and Sondhauss tube (Feldman, 1986a, 1986b)**

Lord Rayleigh examined and qualitatively explained the three thermoacoustic phenomena described above in famous treatise “The Theory of Sound” (Rayleigh, 1945). He emphasized the importance of the phase relationship of the exchange of heat between the acoustic medium and the heat source/sink to the oscillatory motion in the process.

“... If heat be periodically communicated to, and abstracted from, a mass of air vibrating in a cylinder bounded by a piston, the effect produced will depend upon the phase of the vibration at which the transfer of heat takes place. If heat be given to the air at the moment of greatest condensation, or be taken from it at the moment of greatest rarefaction, the vibration is encouraged. On the other hand, if heat be given at the moment of greatest rarefaction, or abstracted at the moment of greatest condensation, the vibration is discouraged ...”

His observations have been generally accepted as a criterion of the sustaining of thermoacoustic oscillations. However, he did not show how the thermoacoustic oscillations could be initiated.

One of the first major modifications to the basic Sondhauss tube design was the introduction of a bundle of small Pyrex glass tubes to the system by R. L. Carter and his co-workers (Feldmann, 1968b). The assembly of the original Sondhauss tube was replaced by a simple straight tube with one end closed and the other open, the bulb being eliminated. The bundle of small glass tubes, which is now known as the “stack”, was found to be more effective than one large circular glass tube. Tests also showed that the amplitude of oscillation in a tube closed at both ends increased steadily with the system mean pressure. As a continuation of this work, a more extensive study of the Sondhauss oscillation was conducted by Feldman (1968b), who used bundles of glass tubes of various diameters and lengths as inserts in a Sondhauss tube. His most efficient oscillator produced 27 W of acoustic power from 600 W of heat, with a thermal efficiency of 4.5%. Measurements of the oscillatory pressure amplitude and frequency of the sound produced in the Sondhauss tube were made for various pipe lengths, heat power inputs, heat sources and positions of tube-bundle insert, tube diameter and length, and using different operating gases such as air and argon.

Another manifestation of the thermoacoustic effect, a phenomenon commonly encountered in cryogenic storage systems, came to light in 1949, when Taconis and his co-workers noticed that very powerful oscillations (known thereafter as “Taconis oscillation”) could occur in a hollow tube used to stir liquid helium (Taconis et al, 1949). The tube approached the low temperature of the liquid helium at one end and remained at room temperature on the other end. The explanation given was essentially similar to that of Lord Rayleigh for the oscillation in a Sondhauss tube. Experimental studies of thermally driven oscillations in a tube filled with gaseous helium were conducted by Yazaki and his co-workers (Yazaki, Tominana and Narahara, 1979, 1980). For the onset of the oscillation, the significance of the size of the thermal boundary layer compared with the width of the tube was clearly reflected in their measurements.

The process opposite to the generation of sound by heat, the thermoacoustic heat pumping effect, was not observed and investigated until much later. In 1975, Merkli and Thomann discovered a cooling effect on the wall of a gas-filled tube sealed at one end by a piston undergoing a sinusoidal motion and blocked by a solid plate at the other end (Merkli and

Thomann, 1975a). The cooling of the tube wall occurred at the position where velocity was maximal, and usually where viscous dissipation was greatest. A theoretical model of the local time-averaged heat flux penetrating into the tube wall was developed from the second-order energy equation. The analysis showed that there was a net heat transport along the tube wall from a region near the velocity antinode of the standing wave to the velocity node. The experimental results agreed with the theoretical prediction when the amplitude of the oscillating pressure was relatively small and the oscillation frequency is such that a shock does not occur. This phenomenon, called “thermoacoustic streaming” by Rott (1980), is precisely the heat pumping effect responsible for thermoacoustic refrigeration.

Ceperley realized that the gas in a travelling wave would experience a thermodynamic cycle very much similar to that experienced by a gas in a standard Stirling engine (Ceperley, 1979). He pointed out that a travelling wave heat engine could also function as a travelling wave heat pump, because the thermodynamic cycle of the gas would be ideally reversible. However, he was unable to show any cooling effect in the first measurement. Nevertheless, his work may be seen as the beginning of a new era of broad study of thermoacoustics in both travelling wave and standing wave modes.

Wheatley and his group at the Los Alamos National Laboratory began an intensive and very effective programme of research on thermoacoustic effects in the 1980s. Simple “thermoacoustic couples” were first placed in resonators to create a cooling effect and to verify the thermoacoustic theory derived from the work of Rott (Wheatley et al, 1983a, 1983b). A more complete, fully functional thermoacoustic refrigerator was first built by Hofler, who reported the design and analysis of this system in his PhD thesis (Hofler, 1986). His design used a resonance tube of a small diameter between the cold heat exchanger and the buffer volume to reduce the local thermal loss and viscous loss. The highest measured coefficient of performance was 12% relative to Carnot efficiency and the lowest measured ratio of cold to ambient temperature was 0.66. The theoretical analysis did not produce a close agreement with the experimental results. The interference between acoustic flow and the discontinuity of the stack and heat exchanger assembly was thought to be one of the main causes of the discrepancy.

Besides the early experimental studies of thermoacoustic phenomena, there were also a few unsuccessful theoretical efforts to explain them quantitatively. The first calculation of acoustic waves in long tubes which included the attenuation caused by the viscous loss was

made by Helmholtz in 1863 (Rott, 1969). However, the credit for initiating the field of theoretical thermoacoustics is deserved by Kirchhoff, who addressed quantitatively the effect of acoustic wave attenuation in tubes due to heat transfer from the gas to the tube walls, as well as attenuation due to viscous loss in 1868 (Rott, 1980).

Trying to explain the spontaneous oscillation discovered by Taconis et al (1949), Kramers (1949) performed a quantitative calculation of the thermally driven acoustic oscillation by adopting Kirchhoff's theory. His work was recognized as "the first quantitative calculation of thermally driven acoustic oscillations which can be compared to experiments" (Rott, 1969). However, Kramers' theory was unsuccessful in its attempt to achieve an agreement with observations.

Originally directed towards explaining Taconis oscillation, the efforts of Rott developed into a very solid theoretical foundation and one of the most frequently referenced bodies of work in modern thermoacoustics (Rott, 1969, 1973, 1974a, 1974b, 1975, 1976a, 1976b, 1976c). A complete acoustic stability analysis was conducted and shown to be valid for wide and narrow tubes. Rott also focused upon a purely acoustic oscillation, with no other source of inertia except from the fluid, and sharp temperature jumps (discontinuous model). Ultimately, a sound theoretical foundation applicable to basic experiments on both thermoacoustic prime movers and thermoacoustic heat pumps and refrigerators was established. The review article published by Rott in 1980 is recognized as the beginning of a very prolific era in thermoacoustics (Rott, 1980). Many later researches have relied heavily on his work.

In 1988, G. Swift published a review, in which he discussed major aspects of thermoacoustic devices (Swift, 1988) and gave a few examples of prime movers and refrigerators, including detailed theoretical calculations and their interpretations. Taking into account conservation of energy in the wall, Swift extended the theory to stationary problems and proposed a numerical solution for smooth temperature profiles.

Today, interest in thermoacoustics had extended worldwide. Different research groups are interested in various aspects, such as building a competitive but efficient functional device, developing a systematic methodology to design and construct such a device, and more fundamentally, extending Rott's theory beyond the linear limit.

### 2.1.2 Lagrangian point of view of thermoacoustic effect

In principle, a thermoacoustic device could work as an engine (a “prime mover”) or a refrigerator (including a heat pump), depending on whether a temperature gradient is applied in order to generate an acoustic wave or the acoustic wave is utilized to transfer heat from a cold to hot reservoir. The thermoacoustic devices could be also grouped into travelling wave devices and standing wave devices, depending on whether the acoustic pressure and the acoustic velocity are nearly in phase (0 or 180 degree) or 90 degree out of phase. As a consequence, most of the thermoacoustic devices for energy conversion purposes could be classified into four types of devices: standing wave thermoacoustic engine; standing wave thermoacoustic refrigerator; travelling wave thermoacoustic engine; travelling wave thermoacoustic refrigerator.

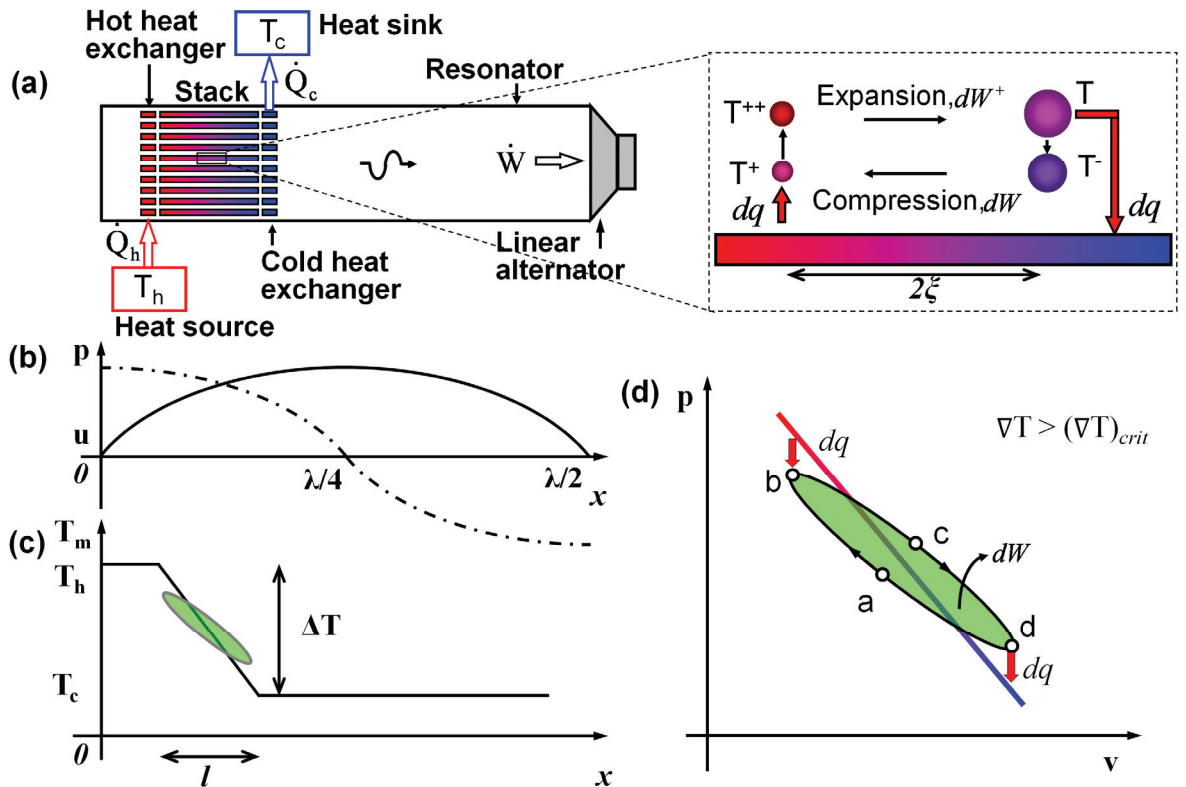


**Figure 2.2 (a) Schematic drawing of a simplified standing wave thermoacoustic engine. (b) Profiles of acoustic pressure and particle velocity along the resonator. (c) Profile of the mean temperature of the fluid within the flow channel and the illustration of the temperature of a gas parcel in one thermodynamic cycle. (d) Illustration of the thermodynamic cycle undertaken by a gas parcel in  $p-v$  diagram, with the solid temperature adjacent to the gas parcel in the cycle.**

A standing wave thermoacoustic engine is schematically shown in Fig. 2.2. A parallel plate stack of length  $l$  is placed between a hot and a cold heat exchanger and the whole structure is placed in the resonator. The gas-filled resonator is connected to a linear alternator at one

end and is blocked at the other end. The length of the resonator corresponds to half of the acoustic wavelength,  $\lambda/2$ . An acoustic oscillation is generated when a large temperature difference  $\Delta T$  is applied across the stack. The acoustic power contained in the resonator could be extracted by the linear alternator in the form of electricity. The gas parcels within the channels between stack plates undergo a thermodynamic cycle as shown on the right. The gas parcel experiences an adiabatic compression and consumes acoustic power  $dW$ , with the temperature increased from  $T^-$  to  $T^+$ , and the volume decreased. Then, the gas parcel experiences an irreversible heat transfer ( $dq$ ) with its adjacent solid at constant pressure (point b in (d)), causing a further increase of the gas temperature up to  $T^{++}$ . The adiabatic expansion of the gas parcel produces an acoustic power of  $dW^+$  and its temperature drops to  $T$ . Then an irreversible heat transfer ( $dq$ ) takes place between the gas parcel and its adjacent solid at constant pressure (point d in (d)). The temperature of the gas parcel further decreases to  $T^-$ , to complete one cycle. A net acoustic power ( $dW^+ - dW$ ) is produced while heat  $dq$  is transferred from temperature  $T^{++}$  to  $T^-$  in every cycle the small gas parcel experiences. The gas parcel has a peak to peak displacement of  $2\xi$ . By the virtue of the *thermoacoustic effect*, the system absorbs heat  $Q_h$  at temperature  $T_h$  and reject heat  $Q_c$  at temperature  $T_c$ , and produces acoustic power  $\dot{W}$ .

A standing wave thermoacoustic refrigerator is schematically shown in Fig. 2.3. The acoustic pressure oscillation is generated by the acoustic driver installed at one end of the gas-filled resonator with its other end closed. The length of the resonator corresponds to half of the acoustic wavelength,  $\lambda/2$ . A parallel plate stack of length  $l$  sitting between a hot and a cold heat exchanger is placed in the resonator. Along the movement driven by the acoustic wave, the gas parcel undergoes a thermodynamic cycle as shown on the right. The gas parcel experiences an adiabatic compression and consumes acoustic power  $dW$ , with an increasing temperature from  $T$  to  $T^{++}$ , and volume decrease. The gas parcel then experiences an irreversible heat transfer ( $dq$ ) from itself to its adjacent solid at constant pressure (point b in (d)), making the gas temperature decreased to  $T^+$ . Afterwards, the adiabatic expansion of the gas parcel produces an acoustic power of  $dW^-$  and its temperature further drops to  $T^-$ . Then an irreversible heat transfer ( $dq$ ) takes place to the gas parcel from its adjacent solid at constant pressure (point d in (d)). The temperature of the gas parcel increases to  $T^-$ , to complete one cycle. A net acoustic power ( $dW - dW^-$ ) is consumed while heat  $dq$  is pumped from temperature  $T^-$  to  $T^{++}$  in every cycle the small gas parcel experiences. The gas parcel has a peak to peak displacement of  $2\xi$ . With this thermodynamic cycle continues in a chain along the stack plate, a substantial temperature difference  $\Delta T$  is created across the stack and maintained by the heat exchangers. Taking

advantage of the *thermoacoustic effect*, the system absorb heat  $Q_c$  at temperature  $T_c$  and reject heat  $Q_h$  at temperature  $T_h$ , with a consumption of acoustic power  $\dot{W}$ .

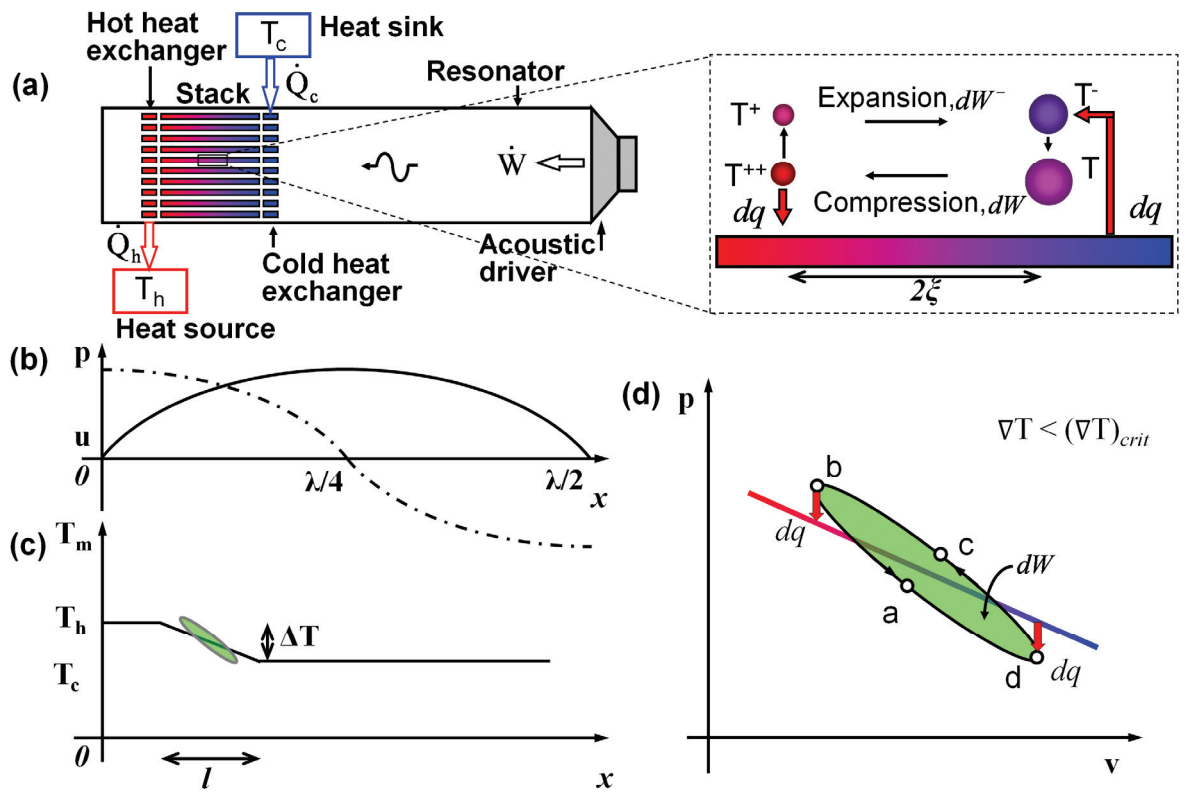


**Figure 2.3** (a) Schematic drawing of a simplified standing wave thermoacoustic refrigerator. (b) Profiles of acoustic pressure and particle velocity along the resonator. (c) Profile of the mean temperature of the fluid within the flow channel and the temperature of the gas parcel in one thermodynamic cycle. (d) Illustration of the thermodynamic cycle undertaken by a gas parcel in  $p$ - $v$  diagram, with the solid temperature adjacent to the gas parcel in the cycle.

### 2.1.3 Linear theory of general thermoacoustics

Over the last few decades, the linear thermoacoustic theory has been well established (Swift, 1988, 2002). The performance of a thermoacoustic system can be correctly predicted under the linear theory if the pressure amplitude of the acoustic oscillation in the system is less than 10% of the mean pressure. The discrepancy between the prediction from the linear theory and the quantities from measurements become substantially larger when the amplitude of the acoustic oscillation increases, possibly due to the nonlinear effects such as the waveform steepening, the pressure loss at the abrupt changes of the cross sectional area for acoustic transmission, the streaming effects or the turbulence in the oscillatory flow. Design Environment for Low-amplitude ThermoAcoustic Energy Conversion (abbr. DELTAEC) (Ward and Swift, 1994), which is built on the linear

thermoacoustic theory with additions to consider the effects such as minor losses, is broadly used to simulate the distribution of the physical quantities such as the acoustic pressure, the velocity and the temperature, or the overall performance for the initial design or the verification of the system behaviour. It shows that thermoacoustic processes can be predicted reasonably well on the grounds of the linear thermoacoustic theory as a first approximation. In this section, essential content of the linear thermoacoustic theory that is most relevant to the current research is described.

Consider a simple straight resonator: An acoustic wave propagates along the axis of the resonator in the direction of  $x$ , at the sound speed  $a$ . The transverse coordinates  $y$  and  $z$  are defined in the cross section of the resonator. An ideal gas is considered, whose bulk viscosity  $\zeta$  is negligible. It is assumed that the transverse dimension of the resonator is much smaller than the acoustic wavelength  $\lambda$ .

Start with the equations of continuity, momentum and heat transfer:

$$\frac{\partial \rho}{\partial t} + \nabla \cdot (\rho \mathbf{v}) = 0 \quad (2.1)$$

$$\rho \left[ \frac{\partial \mathbf{v}}{\partial t} + (\mathbf{v} \cdot \nabla) \mathbf{v} \right] = -\nabla p + \nabla \cdot \boldsymbol{\sigma}' \quad (2.2)$$

$$\rho T \left( \frac{\partial s}{\partial t} + \mathbf{v} \cdot \nabla s \right) = \nabla \cdot k \nabla T + (\boldsymbol{\sigma}' \cdot \nabla) \cdot \mathbf{v} \quad (2.3)$$

Here,  $s$  is the entropy, and  $k$  is the thermal conductivity of the gas.  $\boldsymbol{\sigma}'$  is the nine-component viscous stress tensor. The partial derivative  $\partial/\partial t$  indicates the time derivative at a fixed location through which fluid may move.

Variables such as pressure  $p$ , density  $\rho$ , temperature  $T$  and velocity  $\mathbf{v}$  are considered to be in steady-state sinusoidal oscillation, at frequency  $f$  ( $= a/\lambda$ ) and angular frequency  $\omega = 2\pi f$ . They can be written in the complex notation

$$p = p_m + \text{Re} [p_1(x) e^{i\omega t}] \quad (2.4)$$

$$\rho = \rho_m(x) + \text{Re} [\rho_1(x, y, z) e^{i\omega t}] \quad (2.5)$$

$$T = T_m(x) + \text{Re} [T_1(x, y, z) e^{i\omega t}] \quad (2.6)$$

$$\mathbf{v} = \text{Re}[\mathbf{v}_1(x, y, z)e^{i\omega t}] \quad (2.7)$$

Variables with subscript 1, such as  $p_1$ , are complex numbers. The complex notation makes use of  $i = \sqrt{-1}$  and of the identity  $e^{i\omega t} = \cos(\omega t) + i\sin(\omega t)$ . It is assumed that the time-dependent variables are small, so that  $|p_1| \ll p_m$ ,  $|\rho_1| \ll \rho_m$ ,  $|T_1| \ll T_m$ ,  $|v_1| \ll a$ , etc. The mean velocity is assumed to be zero, with no steady gas motion in the absence of the acoustic oscillation.

Other properties of the gas such as the viscosity and thermal conductivity are assumed to be dependent only on the mean temperature, which is a function of  $x$  only, as follows

$$\mu = \mu(x) \quad (2.8)$$

$$k = k(x) \quad (2.9)$$

With these approximations, the equations of fluid mechanics and heat transfer can be simplified to

$$i\omega\rho_1 + \frac{d\rho_m}{dx}u_1 + \rho_m\nabla \cdot \mathbf{v}_1 = 0 \quad (2.10)$$

$$i\omega\rho_m u_1 = -\frac{dp_1}{dx} + \mu\left(\frac{\partial^2 u_1}{\partial y^2} + \frac{\partial^2 u_1}{\partial z^2}\right) \quad (2.11)$$

$$\rho_m c_p \left(i\omega T_1 + \frac{dT_m}{dx}u_1\right) = i\omega p_1 + k\left(\frac{\partial^2 T_1}{\partial y^2} + \frac{\partial^2 T_1}{\partial z^2}\right) \quad (2.12)$$

Equation (2.11) is a differential equation for  $u_1(y, z)$ . With boundary condition  $u_1 = 0$  at the solid surface, Eq. (2.11) has a solution

$$u_1 = \frac{i}{\omega\rho_m} [1 - h_v(y, z)] \frac{dp_1}{dx} \quad (2.13)$$

The complex function  $h_v(y, z)$  depends on the specific geometry of the flow channel under consideration. An integration of Eq. (2.13) with respect to  $y$  and  $z$  over the cross-sectional area  $A$  of the channel gives the volumetric velocity  $U_1$ :

$$dp_1 = -\frac{i\omega\rho_m}{1-f_v} \frac{dx}{A} U_1 \quad (2.14)$$

$f_v$  is the spatial average of the complex function  $h_v(y, z)$ . Subsequently, after re-organization, Eq. (2.10) and Eq. (2.12) become

$$dU_1 = -\frac{i\omega A dx}{\rho_m} [1 + (\gamma - 1)f_\kappa] p_1 + \frac{(f_\kappa - f_v)}{(1-f_v)(1-\sigma)} \frac{dT_m}{T_m} U_1 \quad (2.15)$$

$$T_1 = \frac{1}{\rho_m c_p} (1-h_\kappa) p_1 - \frac{1}{i\omega A} \frac{(1-h_\kappa) - \sigma(1-h_v)}{(1-f_v)(1-\sigma)} \frac{dT_m}{dx} U_1 \quad (2.16)$$

$h_v(y, z)$  share the same formulae with  $h_\kappa(y, z)$ , and  $f_v$  with  $f_\kappa$ . In particular, when the flow fields in a large pipe and a small channel formed between two parallel plates are considered, the complex functions  $h(y, z)$  and  $f$  are known. For a large pipe for which the viscous effect and thermal conduction due to the solid boundary are limited to a thin boundary layer, and with  $y = 0$  at the solid wall,

$$h = e^{-(1+i)y/\delta} \quad (2.17)$$

$$f = \frac{(1-i)\delta}{2r_h} \quad (2.18)$$

For the small channel between parallel plates, if  $y = 0$  at the centre of the channel of separation  $2y_0 = 2r_h$ ,

$$h = \frac{\cosh[(1+i)y/\delta]}{\cosh[(1+i)y_0/\delta]} \quad (2.19)$$

$$f = \frac{\tanh[(1+i)y_0/\delta]}{(1+i)y_0/\delta} \quad (2.20)$$

In order to find  $h_v(y, z)$  and  $f_v$ , or  $h_\kappa(y, z)$  and  $f_\kappa$ , one only needs to put  $\delta_v$  or  $\delta_\kappa$  in the corresponding places.

Due to the interaction of the sound wave with the walls of the small channel, it leads to a non-zero time-averaged acoustic power. The time-averaged acoustic power produced in a unit length of the channel,  $d\dot{E}_2/dx$  is given by

$$\begin{aligned} \frac{d\dot{E}_2}{dx} = & -\frac{|U_1|^2}{2} \left( \frac{\omega \rho_m \operatorname{Im}[-f_v]}{A |1-f_v|^2} \right) - \frac{|p_1|^2}{2} \left( \frac{\gamma-1}{\gamma} \frac{\omega A \operatorname{Im}[-f_k]}{p_m} \right) \\ & + \frac{1}{2} \operatorname{Re} \left[ \left( \frac{(f_k - f_v)}{(1-f_v)(1-\sigma)} \frac{1}{T_m} \frac{dT_m}{dx} \right) \tilde{p}_1 U_1 \right] \end{aligned} \quad (2.21)$$

## 2.2 Fluid mechanical phenomena in oscillatory flows

It can be seen from the general description given above that *the thermoacoustic effect* is closely related to the fluid flow and heat transfer processes within the channels in the stack, and between the stack and the heat exchangers. The stack and heat exchangers are the core components whereby the thermoacoustic effect and energy conversion take place. It is therefore very important to learn the characteristics of the flow and heat transfer in order to gain a better understanding of the thermoacoustic effects, if one is to design thermoacoustic devices of high efficiency. From the following review, it can be shown that the studies of fluid flow phenomena around thermoacoustic stacks are still in their very early stages, and there is still much to be learned.

### 2.2.1 General behaviour of oscillatory flow

When discussing the underlying physics of the oscillatory flow phenomena, the acoustically induced oscillatory flow in thermoacoustic devices could be considered as one category of oscillatory flows and hence it is useful to review previous works in the general area of oscillatory flows. As a point of interest, sometimes, the oscillatory flow is also referred to as an oscillating flow or a pulsating flow. It is frequently encountered in engineering fields such as coastal engineering, Stirling engines, pulse tube cryocoolers, internal combustion engines, in water hammer processes, and in bioengineering in the context of blood flow in arteries, and many others.

The studies of the oscillatory flow are still an active ongoing research area because of its complexity. Oscillatory flow in circular pipes has been studied extensively (Drake, 1965, Gedeon, 1986, Siegel, 1987, Cooper, Yang and Nee, 1993, Ling and Atabek, 1972, Ramaprian and Tu, 1980, Shemerm, Wygnanski and Kit, 1985, Merkli and Thomann 1975b, Hino, Sawamoto and Takasu, 1976, Ohmi and Iguchi, 1982, Ohmi et al 1982, Ohmi, Iguchi and Urahata, 1982, Kurzweg, Kindgren and Lothrop, 1989). It is known that the velocity profile of an oscillatory flow is quite different from that of a steady flow. In an

experimental study of the flow in the mouth of a Helmholtz resonator, Richardson and Tyler (1929) discovered that the maximum velocity occurs within a close distance to the wall instead of appearing at the centre of the pipe. This is sometimes referred to as the “annular effect” in the literature. This finding was afterwards verified by Womersley (1955a, 1955b) and Uchida (1956) in their analysis of a sinusoidal motion of a fully developed oscillatory flow in a pipe. Similar studies of oscillatory flows were carried out in flow channels of various geometries, such as rectangular channel (Drake, 1965), and channels formed between parallel plates (Gedeon, 1986, Siegel, 1987).

There are also many other interesting and important flow phenomena, such as the transition to turbulence (Sergeev, 1966, Merkli and Thomann, 1975b, Hino, Sawamoto and Takasu, 1976, Ohmi et al, 1982, Seume, 1988, Kurzweg, Lindgren and Lothrop, 1989), the pressure drop in the flow through a pipe or the friction loss in an oscillatory flow (Roach and Bell, 1989, Wu et al, 1990, Zhao and Cheng, 1996a, 1996b), minor loss due to abrupt changes of the cross section of the channel, the entrance effect (Gerrard and Hughes, 1971, Peacock and Stairmand, 1983, Krijger, Hillen and Hoogstraten, 1991, Zhao and Cheng, 1998, Yamanaka et al, 2002, Jaworski et al, 2009) and the flow patterns in the wake of an oscillatory flow past obstacles (Chung and Kang, 2003, Barbi et al, 1986, Tatsuno and Bearman, 1990, Okajima, Matsumoto and Kimura, 1997, Bearman et al, 1985, Anagnostopoulos and Minear, 2004, Iliadia and Anagnostopoulos, 1998, Williamson and Roshko, 1988, Ponta and Aref, 2005, 2006, Nehari, Aarmenio and Ballio, 2004).

#### 2.2.1.1 *Transition to turbulence*

The transition from laminar to turbulent flow is a popular topic in fluid mechanics, because there is a significant effect of the flow characteristics on the flow resistance, drag and lift force on the airfoil and heat and mass transfer. In an experimental study, Sergeev (1966) used a motor and crank mechanism to drive a water column in a vertical pipe. Aluminium powder particles were introduced for flow visualization. The amplitude and frequency of the oscillations were varied during the experiments. It was found that the ratio of the pipe diameter,  $D$  to the boundary layer thickness ( $\delta_v = (2\nu/\omega)^{1/2}$ ,  $\nu$  = kinematic viscosity and  $\omega$  = angular frequency), referred to as the inertial number ( $\sigma = D/\sqrt{2} \delta_v$ ), has a strong effect on the nature of the fluid flow and the transition from laminar to turbulent regime. The critical value of the Reynolds number ( $Re_\delta = \sqrt{2} U_a \delta_v/\nu$ ), defined on  $\delta_v$  and the average velocity amplitude ( $U_a$ ), was found to be approximately 700, for the range of the oscillation

amplitude and frequency tested, with  $D/\delta_v$  between 5.6 and 56. Sergeev (1966) indicated that partial turbulence of the flow was observed in his experiments.

Merkli and Thomann (1975) used a hot-wire anemometer and smoke visualization to investigate transition to turbulence of oscillating flow in a round pipe of variable length. A mechanical sine-wave generator, instead of the crankshaft mechanism, was used to produce oscillations in a gas column, in order to eliminate higher harmonics inherent to a normal crankshaft mechanism. The focus was on the transition to turbulence in the boundary layer (Stokes layer). A major finding of this work was that turbulent bursts were observed around the velocity peaks, and were followed by relaminarization in the same oscillation cycle, when the Reynolds number was at moderate values. The Reynolds number was defined on the Stokes layer thickness and axial velocity amplitude. Turbulence was not observed for a very small Reynolds number. A critical value of Reynolds number ( $Re_\delta = 2^{1/2} u_a \delta_v / \nu$ ,  $u_a$  = axial velocity amplitude) of around 400 was found when transition to turbulence occurred in the oscillating pipe flow. Turbulence was not observed throughout the whole cycle of oscillation in any case.

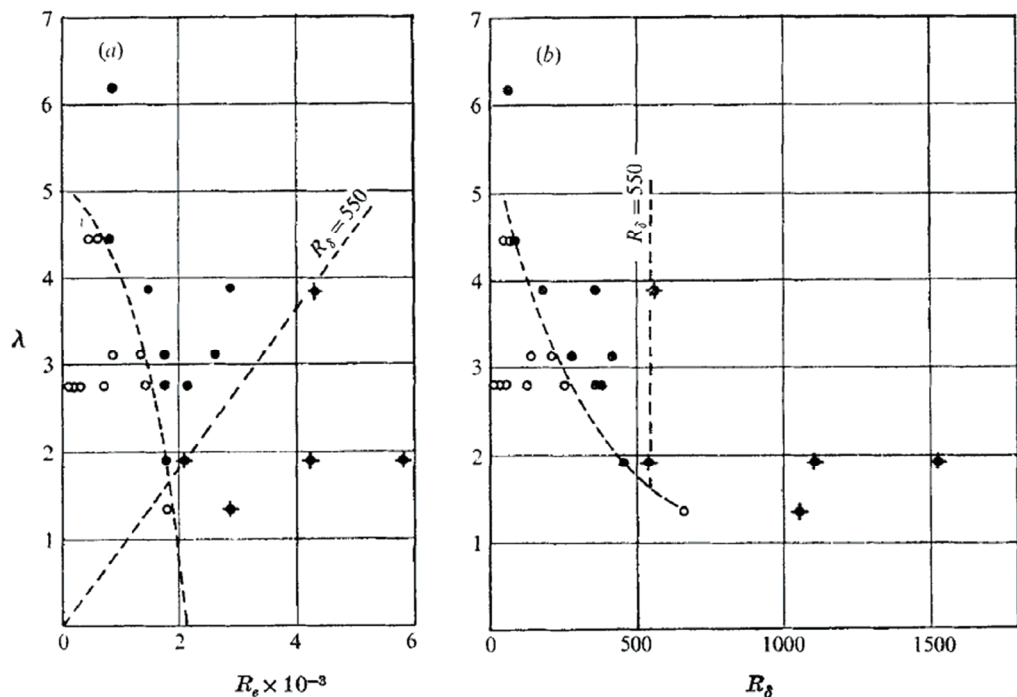


**Figure 2.4 Stability diagrams: (a)  $Re_e$  vs.  $\lambda$  and (b)  $Re_\delta$  vs.  $\lambda$ . Circle, laminar or distorted laminar flow; Solid circle, weakly turbulent flow; Solid circle with a cross, conditionally turbulent flow. (Hino, Sawamoto and Takasu, 1976)**

Hino et al. (1976) carried out a direct measurement of transition in oscillatory pipe flow for the frequency up to 1 Hz, by using a hot-wire anemometer. The ratio of the pipe diameter

to the Stokes layer thickness ( $D/\delta_v$ ) was controlled between 3.8 and 12.4. Two types of turbulent flow regime have been detected: weakly turbulent flow and conditionally turbulent flow. A third flow regime (the fully turbulent flow) was in fact not confirmed in the paper. In the weakly turbulent flow, small amplitude perturbations are superimposed on the distorted laminar flow. The velocity amplitude profiles across the pipe agree well with the theoretical curve of laminar flow, while the phase lag distributions differ considerably from it, particularly in the central part of the pipe. When the Reynolds number increases further, the conditional turbulence is observed. Turbulence is generated suddenly in the decelerating phase and the profile of the velocity distribution changes drastically. In the accelerating phase, the flow recovers to laminar-like flow. Hino et al. remarked that the flow regimes could be defined in the diagrams ( $Re$ , Reynolds number defined on the pipe diameter vs.  $\lambda$ , the ratio of pipe radius to  $\delta_v$ ) or ( $R_\delta (=Re_\delta)$ ,  $\lambda$ ), as shown in Fig. 2.4. The critical value of Reynolds number, when transition from laminar flow to weakly turbulent flow occurs, decreases as the Stokes parameter  $\lambda$  increases. The critical value of  $R_\delta$ , when transition from the weakly turbulent flow to conditionally turbulent flow occurs, is around 550 almost independent of the Stokes parameter.

Ohmi et al. (1982) summarized the previous experimental results on transition to turbulence in an oscillating pipe flow and made further progress through revealing the velocity distributions. They performed experiments in an oscillating pipe flow by using a hot-wire anemometer in the relatively large Reynolds number from 600 to 65000. In addition to the weakly and conditionally turbulent flows, new flow behaviour in which turbulent bursts occur in the accelerating phase as well as in the decelerating phase was observed. However, the limit between previous conditionally turbulent flow and this turbulent flow was still not clear. It was also found that the instantaneous velocity profile in each phase was represented by the well-known  $1/7^{\text{th}}$  power law, but in the laminar-like phase it did not follow the theoretical laminar solutions for a steady oscillating pipe flow. Seume (1988) carried out an experimental investigation of the transition in an oscillatory pipe flow with the parameter range covering the conditions found in the heat exchangers of Stirling engines. Kurzweg, Lindgren and Lothrop (1989) made measurements on the onset of turbulence in oscillating flow of water and found that the oscillatory flows become increasingly stable with decreasing Womersley number (similar to the Stokes parameter).

Cooper, Yang and Nee (1993) carried out an important review on oscillating flows. He postulated that the term “oscillatory” should be used to describe fully oscillatory flows with no mean steady flow superimposed. He also emphasized the differences between an

oscillatory Stokes flow and oscillatory flow. Although the oscillatory flows are macroscopically similar to oscillating Stokes flows, they are driven in a different way. Stokes flows are driven by viscous interactions with uniform far field fluid motion whilst the oscillatory flows are driven by the oscillating pressure gradients. Experimental results (Ling and Atabek, 1972; Ramaprian and Tu, 1980; Shemer, Wygnanski and Kit, 1985) show significant discrepancies from Stokes flow velocity profiles in the shear layers of the oscillatory flows. Laminar oscillatory flows typically correlate well with theoretical research while turbulent flow data shows more uncertainties than steady flows. The review paper summarized experimental data for the transition to turbulence in the oscillatory flows in the previous couple of decades. Turbulence in oscillating flows is typically limited to portions of the oscillation cycles that correspond to the peak velocities. There were no reported cases of turbulence persisting throughout an entire oscillation cycle. In general, research has shown that small amplitude and low frequency of the oscillatory flows tends to stabilize the flow and dampen out disturbances. The favourable pressure gradient in the oscillatory flow during acceleration also helps stabilize the flow and dampen disturbances, while the adverse pressure gradient during the flow deceleration tends to destabilize the flow and sustains flow disturbances (Merkli and Thomann, 1975; Hino, Sawamoto and Takasu, 1976; Ohmi et al, 1982; Kurzweg, Lindgren and Lothrop, 1989). The stabilizing effect of the favourable pressure gradient is responsible for the relaminarization effect noted at the onset of flow acceleration. This paper also showed that with some low Womersley numbers it may be possible to avoid transition entirely. This is because either the fluid tidal displacement is negligibly small or the oscillation frequency is so low that the flow never attains a transitional Reynolds number, or both. Viscous effects in low Womersley number flows are strong enough to dampen out most disturbances or transition induced instabilities.

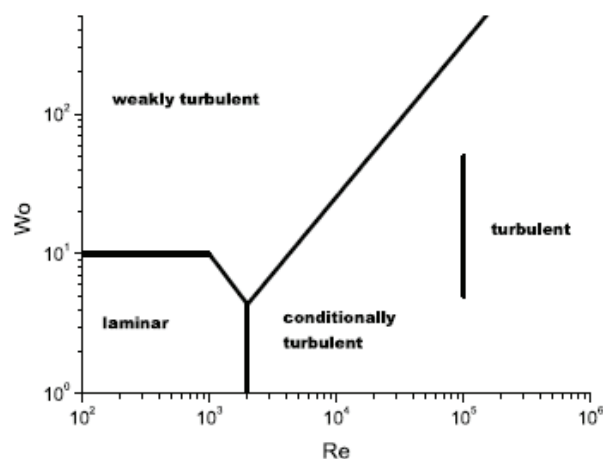


**Figure 2.5 Boundaries between laminar and turbulent regimes for an oscillating flow in a circular pipe**

Approximate boundaries between laminar and turbulent regimes in case of an oscillating flow in a circular pipe as a function of Reynolds and Womersley ( $D/\delta_v$ ) numbers are shown in Fig. 2.5 (Aben and Zeegers, 2006). For low Re and low Wo the flows are in the well understood laminar regime. For sufficiently high Wo the flow becomes weakly turbulent. This means that the turbulence is confined to the centre of the pipe without affecting the boundary layer. In the conditionally turbulent region the flow is turbulent at its peak velocity and becomes laminar again.

#### *2.2.1.2 Pressure drop and friction loss in oscillatory flow*

The frictional losses in the oscillatory flow are an important part in understanding the oscillatory flow. Also, they are of concern in the process of designing the heat exchangers in thermoacoustic and Stirling machines. Roach and Bell (1989) studied the pressure drop in an oscillatory flow experimentally and found that it is independent of the frequency of oscillation. Wu et al. (1990) obtained experimental data for the friction factor in a heat exchanger and acquired the relation between the friction factor and the Reynolds number at given values of the oscillation frequency. Zhao and Cheng (1996b) obtained an analytical expression for the friction coefficient in a fully developed oscillatory laminar pipe flow and found an agreement with their experimental data.

Zhao and Cheng (1996a) also performed experimental studies on the onset of turbulence and frictional losses in an oscillatory turbulent pipe flow. They used a hot-wire anemometer and pressure transducers to measure the velocity oscillations and pressure drops. The mechanisms of the transition to turbulence in a periodically oscillatory flow were investigated. Their findings implied that the instabilities were generated near the wall and the radial momentum transfer caused a lower level of velocity fluctuations near the centreline. This could be due to the “annular effect”. First the fluid flowing near the wall reaches the critical Reynolds number and becomes unstable, and then eddies occur near the wall. These eddies are transferred to the core flow, which causes small fluctuations. They also indicated that the change from a favourable pressure gradient to an adverse pressure gradient is responsible for the onset of turbulence. The physical mechanism leading to the onset of turbulence is a complicated interaction of the inertial force, viscous force and pressure gradient effects. At very large Reynolds number, the interaction of the inertial and viscous force leads to annular velocity profiles in which inflexion points exist near the wall. At the time when the pressure gradient changes from a favourable to an adverse pressure,

the simultaneous existence of large velocity magnitude and the inflexion points in the velocity profiles as well as the adverse pressure gradient leads to the onset of instability. A correlation equation in terms of the kinetic Reynolds number and dimensionless velocity amplitudes for the onset of turbulence was obtained. Finally, a correlation equation for the cycle-averaged friction coefficient of the oscillatory turbulent flow has been obtained and compared with that in the oscillatory laminar flow.

Zhao and Cheng (1998) presented a review of such studies with an emphasis on the onset of turbulence, velocity distribution, and frictional loss of the oscillatory boundary-layer and duct flows, as well as the associated heat transfer characteristics. Through similarity analysis, the kinetic Reynolds number, dimensionless oscillation amplitude, the Prandtl number and the ratio of the pipe length to pipe diameter were chosen as the similarity parameters for incompressible oscillating flow. It is generally agreed from the previous literature that an oscillatory flow becomes unstable with increasing either the kinetic Reynolds number or the dimensionless fluid displacement. They made an analysis and summary of the laminar oscillatory flows, such as the Stokes flow, fully-developed pipe flow including laminar and turbulent oscillatory flow and hydro-dynamically developing pipe flow.

#### *2.2.1.3 Entrance effects in channels*

For the study of laminar developing oscillatory flow, relatively few papers have been reported. Gerrard and Hughes (1971) investigated the development of velocity profiles of an oscillatory flow in the entrance region of a circular pipe using flow visualization techniques. They thought the mechanism of vorticity diffusion in an oscillatory flow is different from the steady flow. In the steady flow the vorticity generated from the wall diffuses to fill the whole cross-section of the pipe, while in the oscillatory flow, the vorticity diffuses in the entrance region only across the oscillating boundary layer thickness. This causes the shorter entrance length than that in the steady flow. Peacock and Stairmand (1983) proposed that the entrance length in a laminar oscillatory flow is shorter than in a steady flow. They speculated that the velocity profiles of an oscillatory flow could not change much in the entrance region because the velocity profiles of an oscillatory flow tend to be flatter than those of a steady flow. Krijger, Hillen and Hoogstraten (1991) suggested the entrance length varied over a cycle and proposed a time dependent entrance length.

Zhao and Cheng (1998) conducted a numerical simulation for developing pipe flow with a finite length. The velocity profiles during a complete cycle at different locations along the pipe length were obtained. The fluid enters the pipe in the first half cycle and the viscous boundary layer grows in thickness downstream. They found that the velocity profiles downstream change from a rectangular shape to a parabola-like shape with velocity overshoots. In the second half of the cycle, the fluid flow reverses its direction. They proposed that the viscous layers in an oscillatory flow may not coalesce at the fully developed region because the velocity in the core is out of phase with the velocity near the wall. Yamanaka et al. (2002) studied the entrance length in a purely oscillatory flow using an ultrasonic velocity profile (UVP) technique. Fast Fourier transform (FFT) was used to make an analysis of the unsteady velocity at the pipe centreline and the “entrance length” was identified as the distance from the entrance where the third harmonic becomes negligible.

Jaworski et al. (2009) investigated the flow structures and entrance length in a thermoacoustic stack in the oscillatory flow conditions using PIV. The velocity profiles at the entrance length were shown. These findings also validate the numerical results of Zhao and Cheng (1998), which is that velocity profiles along the axial direction change from rectangular shapes to a parabolic shape with velocity overshoots. They found that the entrance lengths are varying phase by phase when the fluid enters the stack channel and are in the order of fluid displacement amplitude. Results from numerical simulation were compared with measurement, which improved the understanding of entrance effect in the oscillatory flow.

#### *2.2.1.4 Patterns of wake flow in oscillatory flow past obstacles (Similarity parameters)*

When bluff bodies are introduced in the oscillatory flow, complicated flow patterns would develop before and after the bluff bodies due to the discontinuities of cross section and the nature of oscillatory flow past the bluff bodies. When the oscillatory flow crosses the bluff bodies, such as circular or square cylinder, plates or other geometries, the vortices shed in one half of the cycle impinge on the bluff body when the flow reverses and may interact with vortices shed during the other half of the cycle.

Chung and Kang (2003) carried out a study on the vortex shedding and its lock-on effects behind a square cylinder in an oscillatory incoming flow using a numerical analysis. When a bluff body is located in an oscillatory flow, a resonance between the vortex shedding

behind the bluff body and the oscillatory incoming flow is called lock-on. They found that in the lock-on region, the flow is in a periodic state and there is a strong regularity between the drag and lift forces. When comparing with steady flow, it is found that the time-averaged mean recirculation region is smaller than that for the steady flow. Barbi et al. (1986) carried out a similar study on the vortex shedding and its lock-on effects behind a circular cylinder in an oscillatory flow using numerical simulation.

Tatsuno and Bearman (1990) investigated the structures of the flow induced by a circular cylinder performing sinusoidal oscillations in water at rest by means of a flow visualization. Two similarity parameters, the Keulegan-Carpenter number,  $KC$  (where  $KC = 2\pi a/d$ ,  $a$  is the amplitude of the oscillating motion and  $d$  is the cylinder diameter) and the Stokes number,  $\beta$  (where  $\beta = fd^2/\nu$ ,  $f$  is the frequency of flow oscillation and  $\nu$  the kinematic viscosity of the fluid), were defined to observe the flow regimes. The  $KC$  number was varied from 1.6 to 15, and the Stokes number was in the range of 5-160. In this range of  $KC$  and Stokes number, a number of flow regimes were found. At relatively low values of both  $KC$  and  $\beta$ , the flow structure is described as two-dimensional vortices shed symmetrically per half cycle. As the oscillation amplitude is increased, some asymmetry appears in the flow separation and vortex development behind the cylinder. The process of development and shedding of vortices depends on the values of  $KC$  and  $\beta$ . Most of the resulting flows show a three dimensional instability along the cylinder axis.

Okajima, Matsumoto and Kimura (1997) carried out force measurements and flow visualization for circular and square cylinder in an oscillatory flow. Measurements of both in-line and transverse forces of the square cylinder at various angles of attack were made in a relatively wide range of Keulegan-Carpenter ( $KC$ ) numbers from 1 to 90. The correlations between flow patterns and force coefficients are revealed by flow visualization. A similar study of forces and vortex patterns around a circular cylinder in oscillating flow were carried by Bearman et al. (1985) and Obasaju, Bearman and Graham (1988). Iliadis and Anagnostopoulos (1998) used a finite element method to numerically compute two-dimensional flow around a circular cylinder in oscillating flow at low Keulegan-Carpenter number and Stokes number. They also found that the flow remains symmetrical for low values of  $KC$  number and the trace of the total in-line force is very close to a sine wave. When the  $KC$  number was increasing, the flows appeared asymmetrical and the asymmetry eventually became more pronounced. Then this led to very complicated vortex shedding patterns, which caused generation of higher harmonics in the trace of the in-line force. Anagnostopoulos and Minear (2004) also used a finite element method to study the

blockage effect on the oscillatory flow past a circular cylinder at low Keulegan-Carpenter number. They found the vortex pattern for an increased blockage corresponds to that occurring for a higher KC number in an unblocked condition.

Williamson and Roshko (1988) used a flow visualization technique to observe the vortex formation in the wake of an oscillating cylinder in a steady free stream. Some vortex patterns behind the oscillating cylinder were found, such as the formation of single vortex, vortex pairs or combination of single vortex and vortex pairs and so on. In order to simplify the description of vortex patterns, a method of “symbolic code of letters and numbers” was introduced. They attempted to use a dimensionless oscillating amplitude and frequency parameter to classify various vortex patterns. All vortex patterns found have been summarized on the plane of dimensionless amplitude and frequency parameter.

Ponta and Aref (2005, 2006) also investigated vortex shedding from an oscillating cylinder. They validated both theoretically and numerically the classification of vortex wake patterns of an oscillating cylinder suggested by Williamson and Roshko (1988). Nehari, Armenio and Ballio (2004) made three-dimensional numerical analysis of the oscillatory flow around a circular cylinder at low Keulegan-Carpenter number and Stokes number. They indicated that three-dimensional flow behaviour always appears when the asymmetric vortex pattern has been fully developed.

#### 2.2.1.5 *Vortex shedding frequency*

When the oscillatory flow passes the bluff bodies or the bluff bodies oscillate in still fluid, variations of vortex patterns behind the bluff bodies will lead to variations of vortex shedding frequency. However, the studies on vortex shedding frequency in the oscillatory flow are very limited. The experimental insights into vortex shedding frequency in steady flow will be an important resource when comparing them with oscillatory flow. The vortex shedding frequency was usually expressed in terms of the non-dimensional Strouhal number,  $St = fd/U$ , where  $f$  is the shedding frequency,  $d$  is the characteristic length, and  $U$  is the free-stream velocity.

The studies of shedding frequency in steady flow are extensive (Roshko, 1954, Kovasznay, 1949, Williamson, 1988, Zdravkovich, 1996, Weat and Apelt, 1982, Al-Asmi and Castro, 1992, Ferreira and Vieira, 2004, Guillaume and LaRue, 2001, Leweke, 1993, Okajima, 1982), although they are relatively rare within the scope of oscillatory flows.

Since Strouhal first measured the relation between the shedding frequency and the velocity for Aeolian tones (Roshko, 1954), the study of vortex shedding frequency has been of interest to many investigators. Rayleigh (1945) pointed out that  $fd/U$  (now called the Strouhal number) should be related to the Reynolds number. In order to detect vortex shedding frequency, most investigators chose the hot-wire anemometer with high temporal resolution. Kovasznay (1949) carried out hot-wire investigation of the wake behind cylinders at low Reynolds numbers. He obtained the critical Reynolds number of 40 at which vortices are shed. In the range of Reynolds numbers from 40 to 160, the vortices are not shed directly from the cylinder but appear some distance downstream. This phenomenon can be considered as instability of the laminar wake. The correlation between the Strouhal and Reynolds number from the critical value 40 to around 10,000 was obtained as well. The Strouhal number was based on the observed vortex shedding frequency and the undisturbed mean velocity.

Roshko (1954) investigated wake development behind circular cylinders at Reynolds number from 40 to 10,000 in a low-speed wind tunnel using standard hot-wire techniques. Two distinct Reynolds number ranges according to different periodic wake phenomena behind circular cylinders were observed. In the Reynolds number range from 40 to 150 - called the stable range - the classical stable Karman vortex streets are formed and no turbulence is developed. In the Reynolds number range from 300 to 10,000, the periodic shedding is accompanied by irregular or turbulent velocity fluctuations. The transition range is between 150 and 300. They obtained velocity statistical spectrum and vortex shedding frequencies through measuring the velocity fluctuations behind circular cylinders. In the stable range, the free vortices (which move downstream) decay by viscous diffusion. In the range of irregular velocity fluctuations, the viscous diffusion is turbulent and develops fast, and the wake becomes fully turbulent in the distance of 40 to 50 diameters. In addition to the differences in the nature of the velocity fluctuations, the ranges are characterized by the behaviour of the Strouhal number. In the stable range, the Strouhal number is rising rapidly, in the irregular range it is essentially constant, and in the transition range the Strouhal number is unstable. Thus, they summarized the relation between Strouhal number and the Reynolds number for  $Re$  between 50 and 150, and between 300 and 2000. When the Reynolds number is over 2000, the Strouhal number is constant.

Williamson (1988) carried out a detailed study on the transition regime and confirmed that there exists a complex relation between the Strouhal and Reynolds number. He found that the transition from laminar stable shedding to turbulent regime in the near wake of a circular cylinder involves two distinct discontinuities in the relation of Strouhal vs. Reynolds number. The first discontinuity appears at the Reynolds number of 178. It is related to a change from periodic, laminar vortex shedding to shedding which involved the formation of vortex loops. The second discontinuity appears for the Reynolds number between 230 and 260. It is associated with a change in the three-dimensional structure of the wake from vortex loops to finer-scale stream-wise vortices. Zdravkovich (1996) wrote a review paper on different modes of vortex shedding. He classified the previously observed modes of vortex shedding according to the different mechanics of vortex formation and shedding. He summarized different correlations between the Strouhal and Reynolds number in the low Reynolds number range: Roshko's, Rayleigh's and Berger's. The measurements in the transition range conducted by Williamson were also reviewed.

West and Apelt (1982) investigated the effects of tunnel blockage and Reynolds number on the Strouhal number in the flow past a circular cylinder. The experiments cover a range of blockage from 2% to 16% and the Reynolds number between  $10^4$  and  $10^5$ . For different blockage ratios, there are large differences in the relation between Strouhal and Reynolds number, especially when the Reynolds number is over  $2 \times 10^4$ ; the larger the blockage ratio, the slower the change in the Strouhal number. Al-Asmi and Castro (1992) investigated the geometrical effects of bluff bodies on vortex shedding behaviour in a low-speed wind tunnel. Different geometries of the bluff bodies included flat plate, tee-shape body, triangular body and rectangular body. In addition to the four basic models a further two triangular models with different widths were used to investigate the solid blockage effects. The relation between the Strouhal number and Reynolds number for the blockage ratio of 0.167 was obtained. Above the Reynolds number of  $2 \times 10^4$ , the Strouhal number for the four bodies is independent of the Reynolds number. For the Reynolds number less than  $2 \times 10^4$ , the change in the Strouhal number is apparent for the rectangular body.

Ferreira and Vieira (2004) carried out a study of a steady flow around modified circular cylinders with a longitudinal concave notch. At low Reynolds number, from 100 to around 400, the Strouhal number increases rapidly. Between Reynolds number of 400 and 1000, the Strouhal number remains constant at around 0.2. Similar hot-wire anemometer experiments for a single plate, a plate array, and a ring of circular cross section, designed

to measure the Strouhal number have also been performed by Guillaume and LaRue (2001) and Leweke et al. (1993).

Okajima (1982) investigated in detail the Strouhal number on rectangular cylinders. The Strouhal number variations with four different width-to-height ratios in the range of Reynolds number between 70 and  $2 \times 10^4$  have been observed. He found there is a certain range of Reynolds number for the cylinders with the width-to-height ratios of 2 and 3 where the flow pattern suddenly changes with a sudden discontinuity in Strouhal number. The sudden discontinuity in Strouhal number caused by an abrupt change in flow pattern has been confirmed through measurement of velocity distribution behind the cylinder and flow visualization. The increase of Reynolds number makes the separated flows detach themselves suddenly from the surfaces, which results in a widening of the wake, accompanied by the discontinuous change of Strouhal number. For the rectangular cylinder with the width-to-height ratios of 1 and 4, there are no sudden changes in the Strouhal number when the Reynolds number increases. These investigations into the Strouhal number in steady flow can provide the backdrop against which to assess the Reynolds number or the blockage ratio effects and so on in the case of oscillatory flow.

### **2.2.2 Studies of fluid flow within thermoacoustic devices**

The performance of the thermoacoustic refrigerator heavily relies on the energy conversion efficiency of the thermoacoustic stack and the heat transfer efficiency of the heat exchangers. Thus the information on the flow field around a parallel-plate stack is important for a better understanding of the thermoacoustic effect occurring in the stack. A better understanding of the flow patterns in the area between the stack and the heat exchanger is also crucial to improve the performance of the heat exchangers, as revealed by recent numerical studies (Marx, 2003, Besnoin and Knio, 2004). It is also useful in the design and optimization of heat exchangers, when the heat exchangers take a form of fin and tube combination, which resembles the architecture of a parallel-plate stack.

The analysis of thermoacoustic devices has in large part relied on quasi one dimensional approximation (Swift, 1988). The resulting predictions have been extensively tested against experimental data (Wheatley 1983, Atchley 1990). Generally, good agreement between quasi one dimensional theory and experiments is obtained when the acoustic pressure amplitude is relatively low. When the acoustic pressure amplitude is large,

however, significant deviations between quasi one dimensional prediction and experimental data occur (Atchley 1990). 2D and 3D effects, nonlinear acoustic waves and shocks, transition to turbulence or nonlinear flow-acoustic interactions could be partly responsible for the discrepancies between theoretical predictions and experimental results. To address the connection between the possible causes and their real effect, some experiments and numerical simulation works have been conducted during past years.

According to the main features of the flow phenomena, the flow in the resonator around a stack may be generally divided into three regions as shown in Fig. 2.6. This is intended to help categorize relevant experimental works, because these usually pay attention to selected phenomena which may only happen in certain regions. Region I is the inner region of the stack, where the flow in the channel is not affected by the entrance effects from the discontinuity of the solid boundaries. The flow in a single channel can be well described by the linear theory briefly described in Section 2.1., when the amplitude of the acoustic oscillation is not too large. Region III is sufficiently far away from the heat exchangers in the resonator, so that the plane wave is no longer disturbed by the existence of the heat exchangers and the stack. Similarly, the oscillating flow in this region can be described by the linear theory, when the amplitude of the acoustic oscillation small.

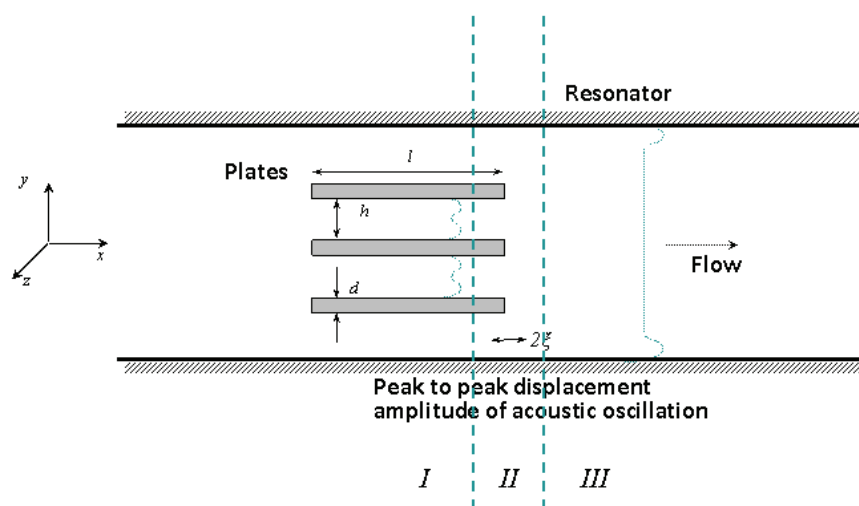


**Figure 2.6 Three flow regions around a parallel plate stack in a resonator**

Region II is the region where the flow is much more complicated because of the presence of the stack ends and heat exchangers, and it is more interesting from the point of view of fluid physics and potentially may affect the thermal performance of the stack and heat exchangers. At a preliminary research stage the combination of stack and heat exchangers is often simplified to a sole stack configuration. For numerical simulation work, the

computational domain is usually divided into longitudinal “slices” that cover all three regions. Thus, the division into the “regions” described above becomes unnecessary.

Herman et al. (1998) used holographic interferometry to visualize the flow near the stack plates of a thermoacoustic refrigerator model. Wetzel and Herman (2000) also used smoke visualization to get an insight into the flow field before any thermal measurements around the stack. Only three images per period of oscillation were captured with a high-speed video camera. The flows around the end of stack plates were investigated when the acoustic pressure amplitudes were about 1000 Pa and 3000 Pa. The presence of a vortex at the edge of a stack plate was observed as shown in Fig. 2.7. The vortex that forms following the shedding of the boundary layer from the plate is outlined by the shape of a black arc in the image and by the sketch. Also shown is the impinging of the vortex on the edge of the plate when the flow reverses. Unfortunately, the results were limited and a precise description of this phenomenon was not achieved.

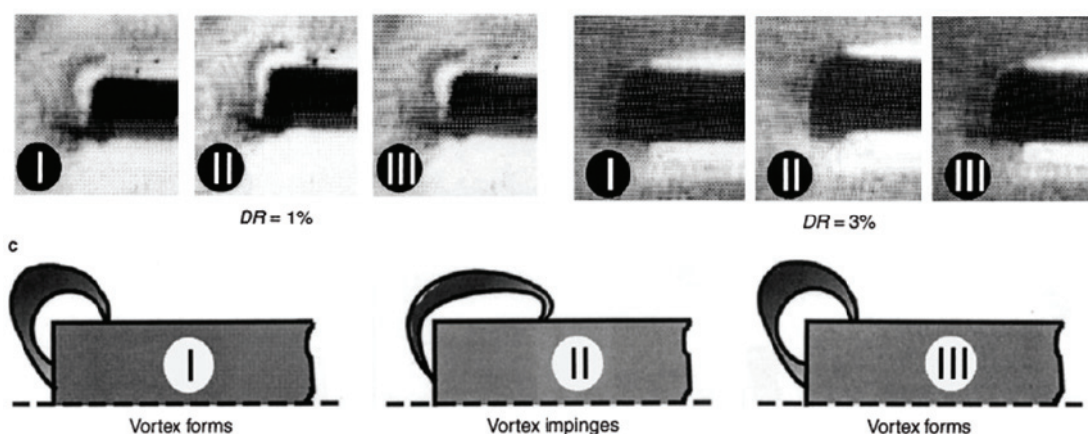


**Figure 2.7 Smoke visualization of the flow structure at the end of stack plates (Wetzel and Herman, 2000)**

Measurements of the flow field with particle image velocimetry were made by Blanc-Benon and co-workers (Duffourd, 2001, Blanc-Benon, Besnoin and Knio, 2003). The flow at the end of the stack plates was measured. In this measurement, a standing wave at the acoustic resonance frequency of 200 Hz was excited in the thermoacoustic resonator. The working gas was air at atmospheric pressure and room temperature. Thus, the viscous penetration depth in the fluid was about 0.15 mm. Two stack configurations were considered. Configuration A, also referred to as a “thick-plate configuration” in the references, has plates of 1.0 mm thickness, 2.0 mm spacing between plates and is 25.8 mm long. Configuration B, a “thin-plate configuration”, has plates of 0.15 mm thickness, 1.0

mm spacing between plates and is 24.0 mm long. For these two stack configurations, the ratio  $h/2\delta_v$  was more than 3. The stacks were located in the resonator about  $\lambda/8$  from the closed end. Measurements of flow field were conducted with configuration A when the amplitude of oscillating pressure at the closed end of the resonator was about 1000 Pa, and with configuration B when the pressure amplitude was about 500 Pa and 1500 Pa. The flows around the ends of the stacks were revealed to be quite different as shown by the vorticity field in Fig. 2.8. Three of sixteen phases in a complete acoustic cycle were shown.

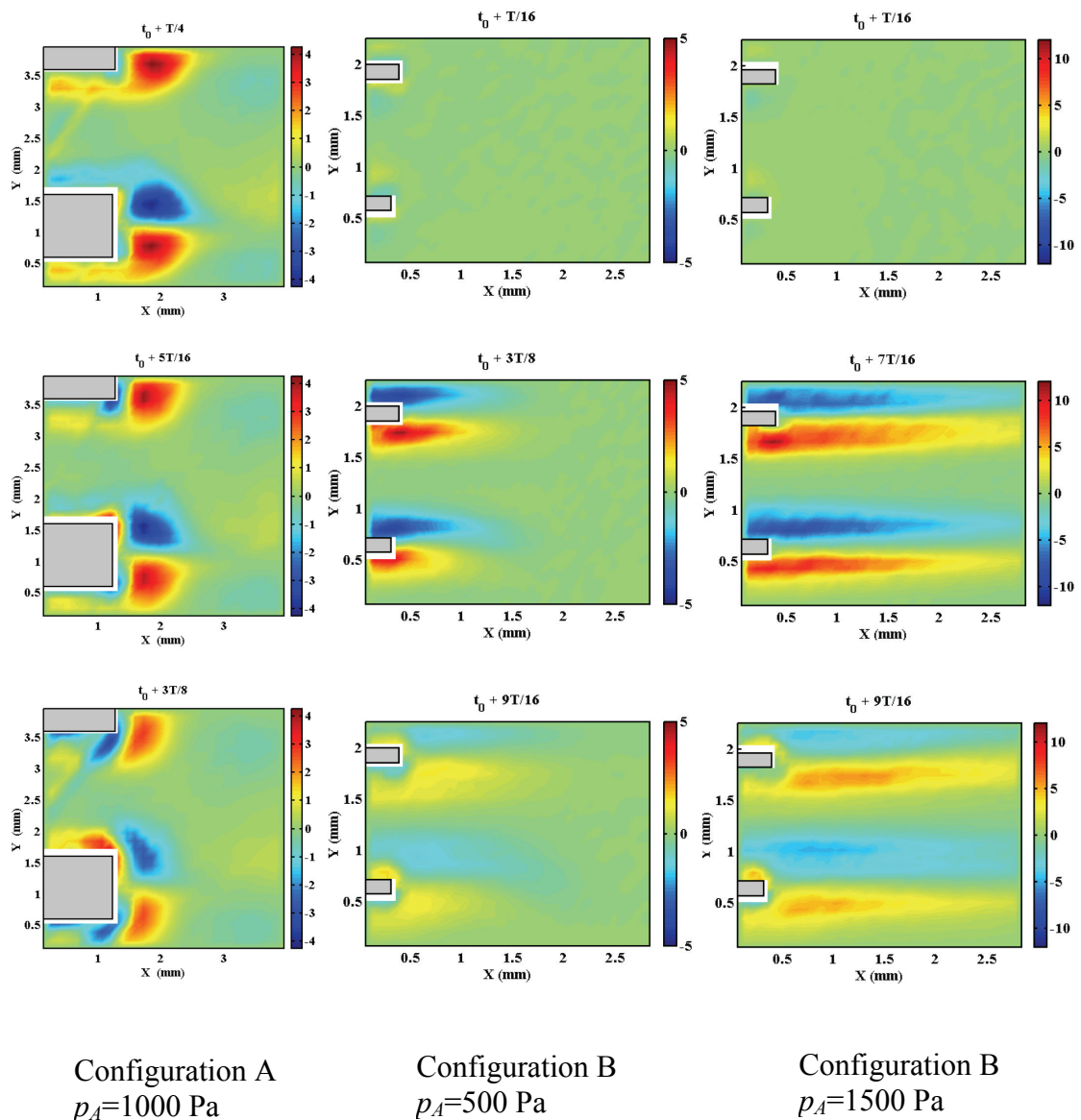


**Figure 2.8 Vorticity field around the end of two stacks for three phases (Duffourd, 2001, Blanc-Benon, Besnoin and Knio, 2003)**

For the stack configuration A, the presence of concentrated vortices is seen near the edge of the plate. Inside the channel, there are also both signs of vorticity present. This is caused by the shear layers (the Stokes layers) present on the plate surface. When the flow is driven back into the channel, the concentrated vortices which previously developed at the edge of the plates are separated and then driven back to impinge onto the plates. Meanwhile, shear layers with opposite signs vorticity build up on the plates. For the stack configuration B, well-defined eddies similar to those that appear for stack configuration A, are not observed, but a pair of elongated vortices generated at the end of plates are present instead. No further discussion of the evolution of the complex structures occurring at the end of the plates and its effect on the flow inside the channel and outside of the stack was presented.

Berson and Blanc-Benon (2007) investigated “nonperiodicity” of the flow within the gap of a thermoacoustic couple at high amplitudes using PIV. They used a smaller resonator with 150mm length, which generated a standing-wave with a frequency around 460 Hz. The acoustic pressure level could reach a drive ratio of up to 5%. Three thermoacoustic stacks were measured separately to observe the oscillation of the flow behind a single stack. The investigation of the flow between two coupled stacks was carried out using two identical stacks placed next to one another. These had 0.17mm thick plates with 0.41mm spacing. An acoustic period was decomposed into 32 equally spaced phases. For each selected phase, velocity fields were averaged over 50 instantaneous velocity fields. For a single stack, measurements show the oscillation of the shear layers flowing out of a single stack, thus forming an asymmetric vortex street of counter-rotating vortex pairs at high acoustic amplitudes as shown in Fig. 2.9. Vorticity layers never extended further than two acoustic displacements away from the stack edge. They considered that shedding occurs when at least two consecutive pairs of counter-rotating vortices detach from the stack. There is no critical Reynolds number value for the onset of oscillation. The paper defined three Strouhal numbers based on the viscous penetration depth, spacing and plate thickness, respectively. At the drive ratio of 5%, development of vortices was also observed within the gap of a thermoacoustic couple. Vortex shedding occurred in the gap and the flow was similar to the flow behind a single stack. They defined a relative standard deviation of velocity measurements to investigate “nonperiodicity”. They obtained the relative standard deviation for three different acoustic pressure levels and various gap widths. The flow was quite repeatable from one acoustic period to another at low acoustic pressure level regardless of the gap width. At high amplitudes of the drive ratio (5%), the relative standard deviation reaches 29%. The flow is no longer periodic. The nonperiodicity of the flow will lead to unsteady heat transfer between the stack and heat exchangers and to the

oscillation of the cooling load. However, the limited number of stack sizes did not allow them to formulate any law of vortex transition and dimensionless numbers.

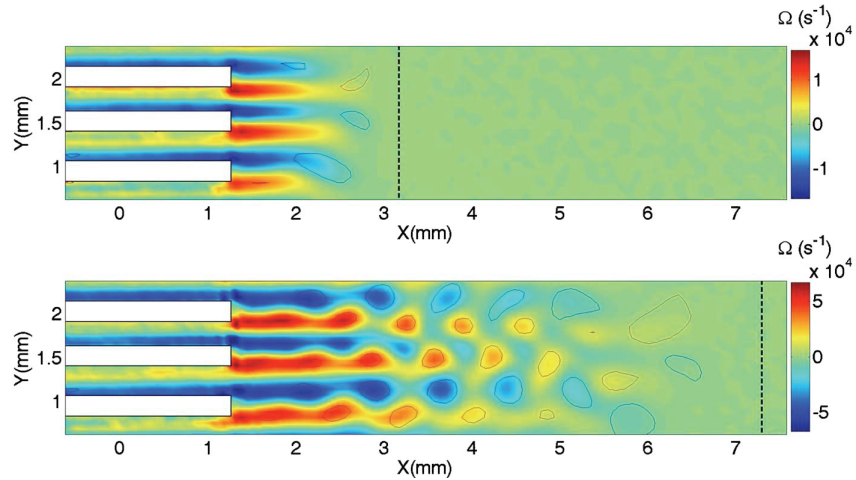


**Figure 2.9 Vorticity fields and contours behind the stack with 0.41 mm spacing and 0.17 mm plate thickness; Top panel: pressure amplitude of 1000 Pa; Bottom panel: pressure amplitude of 4000 Pa (Berson and Blanc-Benon, 2007)**

Berson and Blanc-Benon (2007) obtained a measurement of acoustic velocity in the stack of a thermoacoustic refrigerator using PIV at relatively high amplitudes. The thermoacoustic refrigerator was made of a closed acoustic resonator with a driver at one end and a stack of flat parallel plates inside. The resonator of 0.86m length was filled with air and had a resonance frequency of 214 Hz in half-wavelength mode. The acoustic pressure level inside the resonator reached the drive ratio of 2%. Both thickness of plates and spacing of the stack were 1 mm. A PIV system from LaVision used a 532nm Nd:YAG laser and a camera with  $1280 \times 1024$  pixel resolution. A small mirror was placed inside the resonator to reflect the laser sheet for the measurement plane. The interrogation windows were  $16 \times 16$  pixels with 50% overlap. The flow was seeded with paraffin oil smoke generated by a commercial smoke machine. The diameter of the particles was from 1 to 4 microns. The paper verified the maximum acceptable diameter of 6.38 microns for a particle of paraffin oil smoke in order to follow the flow faithfully at the frequency of 214 Hz. The acoustic cycle was subdivided into 16 equally spaced phases. The measurement method was validated in an acoustic resonator (without stack) by successfully comparing experimental data to a simple plane wave model. Acoustic velocity fields behind the stack plates were characterized. The phase-averaged velocity profiles inside the stack at low and high acoustic pressure were compared with a theoretical linear model. At low acoustic pressure level ( $Dr = 0.5\%$ ), discrepancies between the measurements and the linear model

were within experimental error. At high acoustic pressure level ( $Dr = 2\%$ ), the difference increased due to nonlinear effects.

For the acoustic velocity fields behind the stack plates, vortices appear during the half period of the acoustic cycle when the fluid flows out of the stack. At low acoustic pressure level, counter-rotating vortices are generated at the edges of the plates. They are symmetrical and remain attached to the plates. With increasing acoustic pressure level, structures detach and create an asymmetric street of vortices as shown in Fig. 2.10. For any acoustic pressure level, vortices are not shed further than two acoustic displacements away from the stack edges. The paper also mentioned that when vortices detach the Reynolds number is much lower than the critical Reynolds number. So, the detachment of vortices has nothing to do with the transition to turbulence. However the relationship between the different vortices and controlling parameters was not discussed.

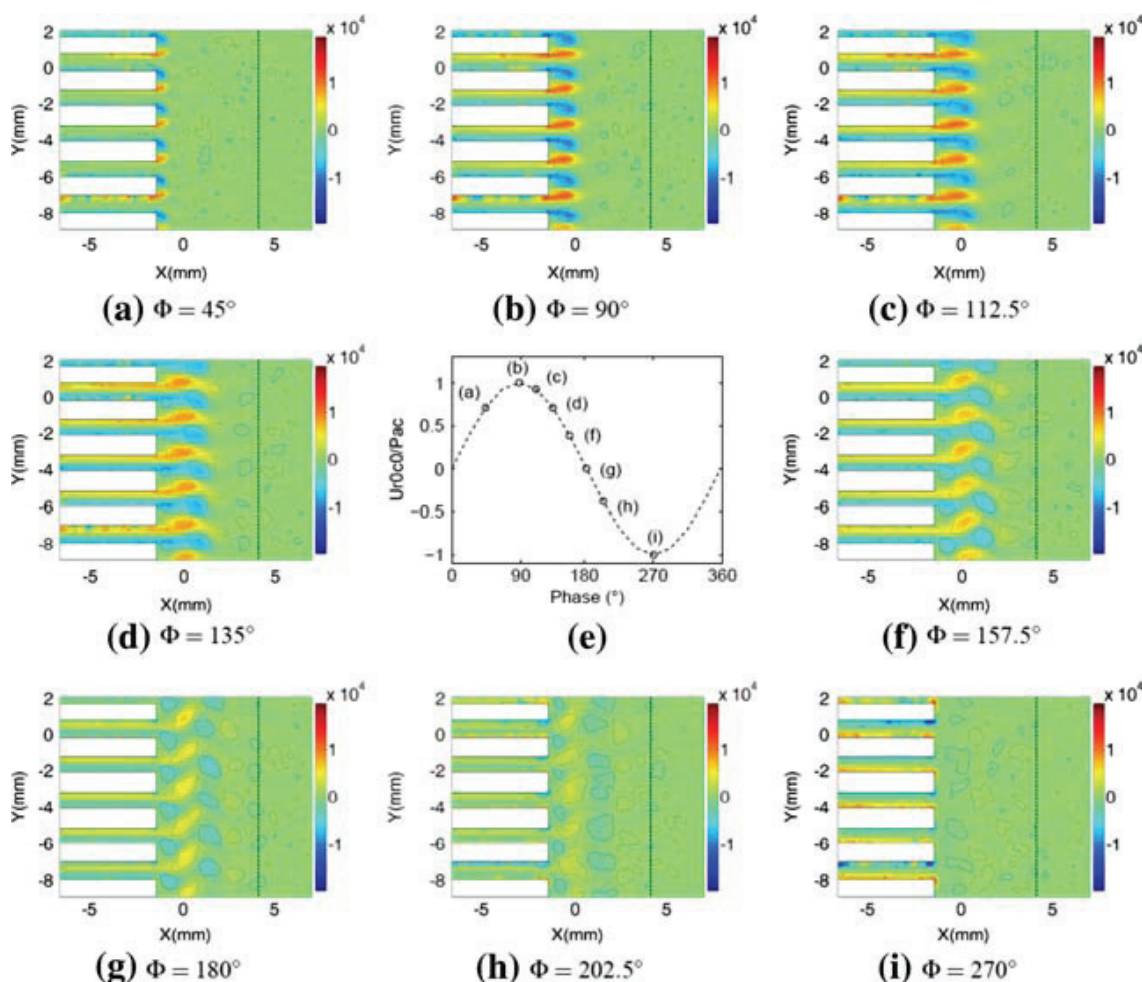


**Figure 2.10 Vorticity fields at the end of stack at high drive ratio (Berson and Blanc-Benon, 2007)**

Aben, Bloemen and Zeegers (2009) carried out a 2-D PIV measurement in stacks of parallel plates in a standing-wave thermoacoustic device. Their paper focused mainly on the measurement of vortex patterns behind the stack and the streaming velocity. The PIV measurements were made in a resonance tube with a length of 1.4m and inner diameter of 25mm. The resonance frequency of 125 Hz determined the viscous penetration depth as 0.2mm. Two configurations of stacks with the same length of 130 mm were used. One stack had a plate thickness of 1 mm and a plate distance of 4 mm. Another had a plate thickness of 0.5 mm and a plate distance of 4.5 mm. Firstly, the paper defined two dimensionless numbers: the Reynolds number and the Strouhal number. The Reynolds number was based on the peak velocity of the main flow just outside the stack and the plate distance. The Strouhal number was the product of the oscillation frequency and the plate distance, divided by the peak velocity.

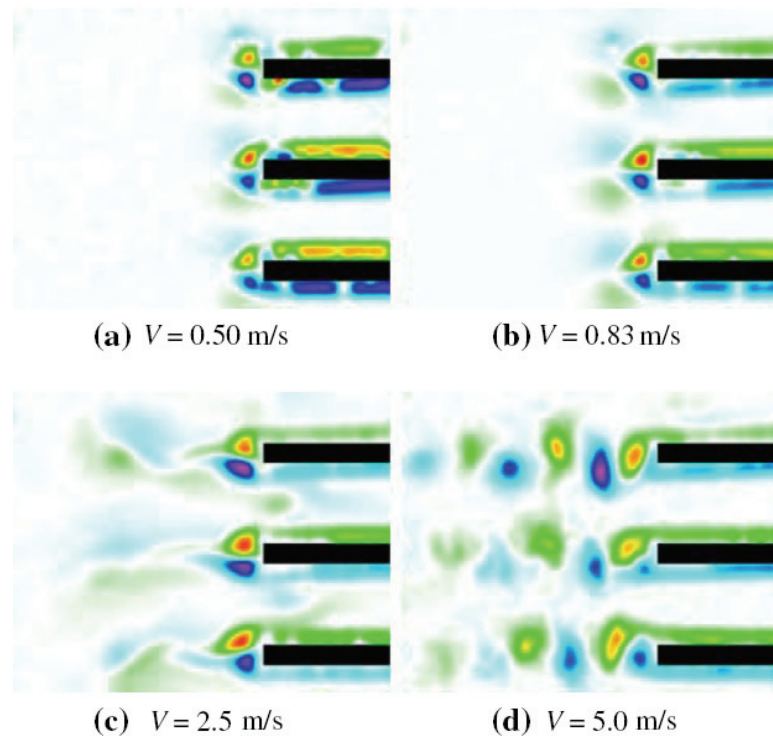


**Figure 2.11 Vorticity plots at the end of the stack with 1 mm thick plate and 4 mm spacing at four different velocity amplitudes (Aben, Bloemen and Zeegers, 2009)**

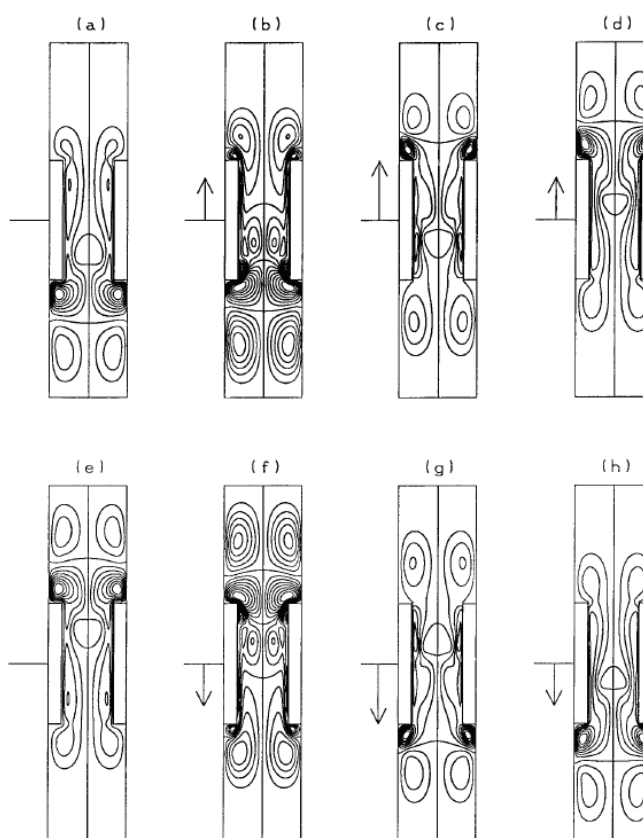
The PIV results showed that the vorticity plots at the stack end can be divided into four categories: two vortices, four vortices, a transition area and a vortex street, as shown in Fig. 2.11. The correlation between the category of vortex formation and the Reynolds number and Strouhal number has been summarized. The effect of plate thickness, spacing, and

plate end shape on the vortex formation has been investigated for rectangular, circular, triangular and sharp triangular shapes. Finally, different methods of measuring streaming by PIV were discussed: the phase method and the average method. The phase method to measure streaming relies on taking the time interval between a PIV image pair equal to exactly one cycle period of the flow. The average method relies on splitting one cycle into a large number of smaller periods. The streaming velocity field is determined by averaging the velocity fields of all different periods during one complete cycle. When making a comparison between experimental results and CFD calculations, the average method gave a better agreement.

Shi, Yu and Jaworski (2010) investigated vortex shedding phenomena at the end of parallel plate stacks in a standing wave thermoacoustic resonator using PIV. The effects of the channel height, plate thickness and the oscillating velocity amplitude on the flow characteristics were investigated based on the obtained velocity and vorticity fields. A range of vortex shedding flow patterns within an acoustic cycle, in particular during the “ejection” stage when the fluid flows out of the stack, were identified, such as symmetric vortices, elongated symmetric vortex structures, alternate shedding vortices, break-up of elongated vortices, chaotic flow state and others. Nine different evolution paths were observed and identified. Furthermore, it was shown that the flow patterns that appear in the flow can be effectively connected to three dimensionless parameters: Reynolds number ( $Re$ ), Keulegan–Carpenter number ( $KC$ ) and Womersley number ( $Wo$ ). In the ( $Re$ ,  $KC$ ) plane ( $Re < 5000$ ,  $KC < 250$ ), four flow pattern regions were defined according to the characteristics of nine types of vortex wake “transitions”.

Shi, Yu and Jaworski (2011) further investigated vortex shedding processes at the end of parallel plate stacks in an oscillating flow, in terms of the shedding frequency. The hot-wire anemometry measurement technique was applied to detect the velocity fluctuations. By varying the stack configuration (the plate thickness and spacing) and the acoustic excitation level, the impact of the stack blockage ratio and the Reynolds number on the Strouhal number has been studied. It was shown that the vortex shedding processes in the oscillatory flow are much more complicated than those in steady flows. In the range of the Reynolds numbers between 200 and 5000, a correlation between the Strouhal number and Reynolds number was obtained. It seems there is some similarity between the oscillatory and steady flows in terms of the relationship between the Strouhal and Reynolds number.

Numerical modelling of thermoacoustic problems in two or three dimensions poses a number of challenges. The length of the resonator is usually in the order of a metre, while the transverse dimension of the resonator, particularly of the stack channel is in the order of a millimetre. The large disparity of the length scales dramatically increases the number of grid points. Moreover, the thermoacoustic effect is a second-order weak nonlinear effect. A large number of oscillations have to be considered for the investigated system to reach a “steady-state” condition. Therefore, the number of time steps is also large, particularly if the thermoacoustic system is working at relatively low frequency so that the period of acoustic oscillation is relatively long.



**Figure 2.12 Evolution of the streamfunction distribution for eight phases within acoustic cycle (Worlikar and Knio, 1996)**

Cao et al (1996) was among the first to simulate thermoacoustic problems numerically in the two dimensional domain over a one dimensional isothermal plate, by solving the full two dimensional Navier-Stokes equations. A simple thermoacoustic couple without heat exchangers was considered. In this work, however, only the analysis of energy flux inside the thermoacoustic core was discussed.

Worlikar and Knio (1996) published their numerical simulation results in a thermoacoustic refrigerator. They used a low Mach-number compressible flow model for simulation of unsteady flow around the thermoacoustic stack. It is based on a quasi-1D idealization of the action of acoustic standing waves and a detailed 2D resolution of flow phenomena occurring around the thermoacoustic stack. They used a series of dimensionless parameters to examine and compare the fundamental features of the flow. Their results focused mainly on the effects of the drive ratio, stack blockage ratio and stack position in the resonator, boundary layer thickness and the plate aspect length, respectively. When investigating any effects of the flow or geometrical parameters, other parameters were kept constant.

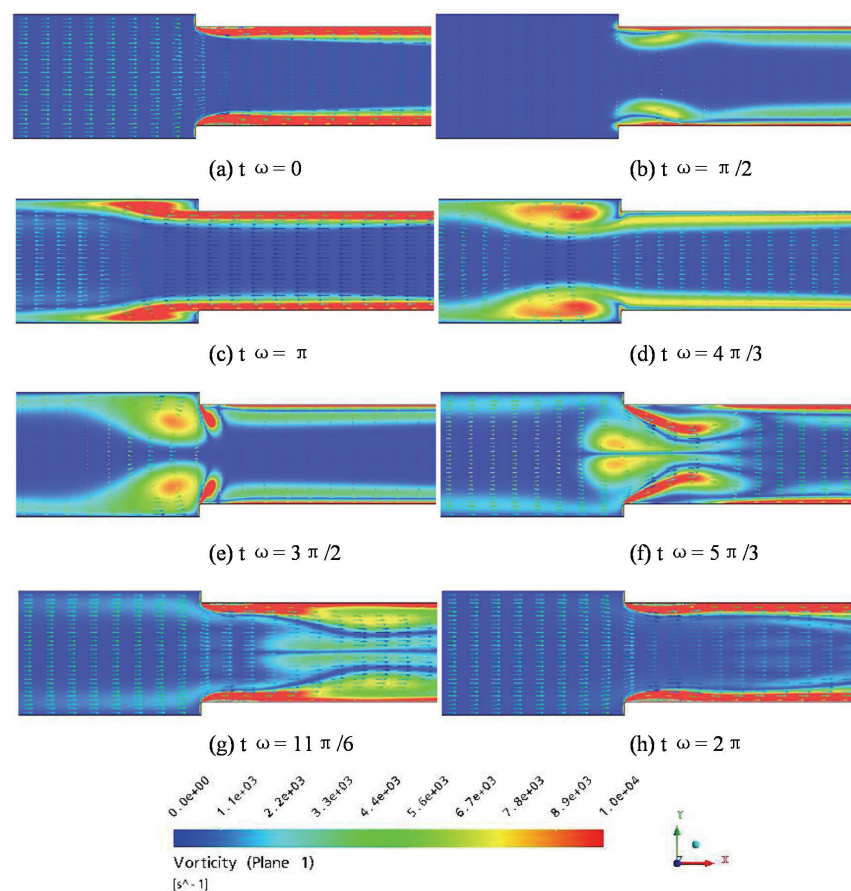


**Figure 2.13 Numerically obtained vorticity and velocity fields (Aben and Zeegers, 2006)**

At the low drive ratio, the stream-function contours show the presence of a pair of concentrated eddies located close to the plates as shown in Fig. 2.12. When the drive ratio is increased, there is a dramatic difference in the impingement of vortical structures on the edges of the stack plates. At high drive ratio, the impingement of the vortices is described by a break-up phenomenon, during which a portion of the eddy is destroyed and another

portion rolls over the plate corners and penetrates the channel. The two vortices migrate towards the channel centreline and stick together to form a vortex bubble. A different position of the stack in the resonator determines a different local gas parcel velocity. This affects the strength of vorticity concentrations. The variation of blockage ratio has a significant impact on the recirculation regions forming near the corners of the plates and the impingement of the vortical structures. When the blockage ratio is decreased, the size of recirculation regions on the plate end increases. The impingement of the vortices leads to a more pronounced flow deformation. The increase in the boundary layer thickness leads to a substantial decrease in velocity gradients. Finally, the effect of plate aspect ratio governs the dynamics of vortex bubbles and recirculation zones in the stack. However, all the flow cases were still realised at relatively low drive ratios; the significant vortex shedding phenomena were not observed.

Aben and Zeegers (2006) used the PIV technique to visualize the flow field in critical parts of a thermoacoustic machine and in the stacks, in particular at high-amplitude oscillatory gas flow. The frequency of this thermoacoustic device is a few tens of Hz in order to obtain larger penetration depths. Numerical simulations were also performed for comparisons with experimental results. The measurement of velocity fields were in good agreement with numerical simulation as illustrated in Fig. 2.13. Finally, although the paper gave three dimensionless numbers: the Reynolds number, the Womersley number and the Keulegan-Carpenter number to predict flow similarities, further analysis was not attempted.

Marx et al. (2008) used PIV to investigate an acoustic flow at an abrupt change in cross-sectional area of an acoustic resonator. The change in section was created by adding a step in the resonator. The radius of curvature of the corner of the step and the particle displacement amplitude could be varied. The ratio of the radius of curvature to the particle displacement amplitude defined a Strouhal number. It was found that when the Strouhal number is lower than a value of the order of 0.5, a vortex is formed in the large channel during the ejection phases. A vortex is also formed in the small channel during the phases of suction at a large radius of curvature of the step. The evolutions of the vortices and their reproducibility have been studied based on the detection of their centres. It was found that the ejection vortex has usually a longer time of existence and a larger spatial extent than the suction vortex. The ejection vortices tend to move over larger distances from the edge when the radius of curvature is decreased. The reproducibility decreases when the radius is reduced or as the particle displacement amplitude is increased. Finally, Proper Orthogonal

Decomposition (POD) was used to separate the global movement from the localized nonlinear acoustic movements.

Besnoin and Kino (2004) performed a numerical simulation of the unsteady flow above one stack plate in a thermoacoustic refrigerator. Two regions were distinguished. At the plate extremities, time averaged vortical motion was observed, due to the abrupt change from slip to non-slip conditions at the plate edges. Above the plate centre, time-averaged motion corresponding to classical acoustic streaming patterns was found. When the plate's separation was reduced to about ten boundary layer thicknesses, the outer vortices predicted by Rayleigh's theory disappeared. Only two inner vortices were present. They also disappeared when the plate's separation became less than about one viscous boundary layer thickness. It was also noticed that the thermal condition at the plate (isothermal/adiabatic) has a slight but not negligible effect on the acoustic streaming phenomena. Marx and Blanc-Benon (2004) carried out a numerical investigation on the second-order mean velocity field above a stack plate in a thermoacoustic refrigerator. They distinguished two regions with different flow characteristics. The first region was at the plate end; time-averaged vortical motions were observed due to the abrupt change from slip to non-slip conditions at the plate edges. The second region was above the plate centre; time-averaged motions corresponding to classical acoustic streaming patterns were found.

Although these PIV measurements and numerical simulations provide important information for a better understanding of the fluid flow in thermoacoustic stacks and heat exchangers, in general the studies of the fluid flow around stacks are still very limited. Also, it is found that the flow cases in each paper only cover limited flow parameter ranges. Thus, no scaling laws for controlling the characteristics of the vortex patterns and their corresponding transition paths have been formed so far. More work is therefore required to both investigate the complex flow behaviour in thermoacoustic stacks and obtain the relationship between the vortex patterns and their transitions around the stack and appropriate similarity parameters.

# Chapter 3 Overview of the research work, its rationale and summary of papers under “alternative format thesis”

This chapter summarizes four published journal papers, which are included within this thesis under the “alternative format” regulations as Chapters 4 – 7. They are presented from three different viewpoints. Firstly, section 3.1 simply lists the titles, authorship and abstracts to give the Reader a general idea of the problems tackled by the candidate. Section 3.2 relates the contents of the papers to the aims and objectives of the PhD programme indicated in section 1.3. Section 3.3 discusses the contribution of the candidate to the individual papers as well as his contribution to general science and engineering achieved through the works presented in this thesis.

## 3.1 Overview of papers submitted in “alternative format”

### Paper 1 (Chapter 4):

#### **Acoustic coupling between the loudspeaker and the resonator in a standing-wave thermoacoustic device**

by D. Marx, **X. Mao** and A. J. Jaworski

Published in: *Applied Acoustics*

**Abstract:** Thermoacoustic refrigerators work with high amplitude sound waves, which are often created using an acoustic source coupled to a resonator. This coupling can be calculated analytically using linear acoustic equations and a linear model of the loudspeaker. This paper makes a comparison between such a coupling and measurements obtained in a large-scale thermoacoustic resonator constructed at the University of Manchester. The resonator was driven from low to large pressure amplitudes, with drive ratios up to 10%. It is shown that a good agreement is obtained for small amplitudes and this progressively worsens as the amplitude is increased. In the absence of wave harmonics and loudspeaker nonlinearities, the increasing discrepancy is attributed to the presence of minor losses.

**Paper 2 (Chapter 5):**

**PIV studies of coherent structures generated at the end of a stack of parallel plates in a standing wave acoustic field**

by X. Mao, Z. Yu, A. J. Jaworski and D. Marx

Published in: *Experiments in Fluids*

**Abstract:** Oscillating flow near the end of a stack of parallel plates placed in a standing wave resonator is investigated using Particle Image Velocimetry (PIV). The Reynolds number,  $Re_d$ , based on the plate thickness and the velocity amplitude at the entrance to the stack, is controlled by varying the acoustic excitation (so-called drive ratio) and by using two configurations of the stacks. As the Reynolds number changes, a range of distinct flow patterns is reported for the fluid being ejected from the stack. Symmetrical and asymmetrical vortex shedding phenomena are shown and two distinct modes of generating “vortex streets” are identified.

**Paper 3 (Chapter 6):**

**Application of PIV measurement techniques to study turbulence characteristics of oscillatory flows around parallel-plate structures in thermoacoustic devices**

by X. Mao and A. J. Jaworski

Published in: *Measurement Science and Technology*

**Abstract:** This paper describes the development of the experimental setup and measurement methodologies to study the physics of oscillatory flows in the vicinity of parallel plate stacks by using the particle image velocimetry (PIV) techniques. Parallel-plate configurations often appear as internal structures in thermoacoustic devices and are responsible for the hydrodynamic energy transfer processes. The flow around selected stack configurations is induced by a standing acoustic wave, whose amplitude can be varied. Depending on the direction of the flow within the acoustic cycle, relative to the stack, it can be treated as an entrance flow or a wake flow. The insight into the flow behaviour, its kinematics, dynamics and scales of turbulence, is obtained using the classical Reynolds decomposition to separate the instantaneous velocity fields into ensemble-averaged mean velocity fields and fluctuations in a set of predetermined phases within an oscillation cycle. The mean velocity field and the fluctuation intensity distributions are investigated over the acoustic oscillation cycle. The velocity fluctuation is further divided into large- and small-scale fluctuation by using Fast Fourier Transform (FFT) spatial filtering techniques.

#### **Paper 4 (Chapter 7):**

#### **Oscillatory flow at the end of parallel plate stacks – phenomenological and similarity analysis**

by X. Mao and A. J. Jaworski

Published in: *Fluids Dynamics Research*

**Abstract:** This paper addresses the physics of the oscillatory flow in the vicinity of a series of parallel plates forming geometrically identical channels. This type of flow is particularly relevant to thermoacoustic engines and refrigerators, where a reciprocating flow is responsible for the desirable energy transfer, but it is also of interest to general fluid mechanics of oscillatory flows past bluff bodies. In this paper the physics of an acoustically induced flow past a series of plates in an isothermal condition is studied in detail using the data provided by PIV imaging. Particular attention is given to the analysis of the wake flow during the ejection part of the flow cycle, where either closed re-circulating vortices or alternating vortex shedding can be observed. This is followed by a similarity analysis of the governing Navier-Stokes equations in order to derive the similarity criteria governing the wake flow behaviour. To this end, similarity numbers including two types of Reynolds number, Keulegan-Carpenter number and a non-dimensional stack configuration parameter,  $d/h$  are considered and their influence on the phenomena discussed.

### **3.2 Fulfilling research programme's aims and objectives**

The research work contained in these papers is a reflection of the aims and objectives listed in Section 1.3. In particular, Paper 1 describes in detail the design and construction of the large scale standing wave thermoacoustic rig. The analytical model of the acoustic field (pressure and velocity) is established by employing the linear acoustics and a linear model of the loudspeaker. The analytical results show a very good agreement with the data obtained from the DeltaEC simulation and are verified by the experimental results obtained at low driving amplitudes, as well as at high driving amplitudes when various sources of minor loss are considered.

Paper 2 then investigates experimentally the features of the oscillatory flow induced around two geometrically different stacks of parallel-plates in the thermoacoustic rig by using particle image velocimetry and hot wire anemometry. The experimental results show that the flow around the two stacks has markedly different and rather complex features when the amplitude of the acoustic oscillation varies. Symmetrical and asymmetrical

vortex shedding phenomena are observed and two distinct modes of generating “vortex streets” are identified. A combination of a velocity related parameter (such as the Reynolds number, defined on the plate thickness and the velocity amplitude at the entrance to the stack), and a geometrical parameter seems insufficient to define the flow characteristics. Typical ensemble-averaged velocity fields are used in the analysis.

However, the detailed flow features obtained from the ensemble averaged flow fields and the instantaneous flow fields could be substantially different. Therefore, in Paper 3, the flow behaviour, its kinematics, dynamics and scales of turbulence are further investigated by using the classical Reynolds decomposition to separate the instantaneous velocity fields into ensemble-averaged mean velocity fields and fluctuations in a set of predetermined phases within an oscillation cycle. By using fast Fourier transform spatial filtering techniques, the velocity fluctuation is further divided into large- and small-scale fluctuations. The mean velocity field and the fluctuation intensity distributions are investigated over the acoustic oscillation cycle.

Paper 4 is a continuation of the work presented in Paper 2 in order to carry out the similarity analysis of the governing Navier–Stokes equations in order to derive the similarity criteria governing the wake flow behaviour. Similarity numbers including two types of Reynolds number, the KC number and a non-dimensional stack configuration parameter are proposed. The physics behind the flow phenomena are further understood by carrying out an analysis of the wake flow during the ejection part of the flow cycle, where either closed re-circulating vortices or alternating vortex shedding can be observed. The influence of these parameters on the flow behaviour is then discussed by investigating the experimental data obtained.

### **3.3 Contributions to published works and science and engineering**

The University regulations on the “alternative format theses” require an explanation and justification of the candidate’s own contribution, as well as the co-authors’, to the papers presented as thesis chapters. This is explained below:

As is clear from the names on the papers there have been three co-authors involved apart from the candidate: Dr Marx, Dr Yu and Dr Jaworski. Dr Jaworski has been the main supervisor of the candidate’s PhD programme and is typically included at the end of the author list to reflect his general research guidance. He has also been the corresponding author on all papers. Drs Marx and Yu were post-doctoral researchers, working in Dr

Jaworski's group, who had the responsibility for a day-to-day advisory role towards the candidate. Dr Marx was in post between 2004 and 2006, while Dr Yu has been in post since 2006.

The changes in the order of the author names and number of co-authors are also a reflection of the research development of the candidate during his PhD programme. As initially the candidate was relatively inexperienced the write up of Paper 1 was in effect "driven" by Dr Marx (this is not to say that Dr Marx did the majority of the actual research work). As the candidate became more confident, he took the responsibility of being the lead author on Paper 2, where the other names reflected their supporting role (by then Dr Marx had left and his name – last in the order of appearance – was simply to recognise some preliminary guidance given to the candidate). Finally, by the time of writing Papers 3 and 4 the candidate became an independent researcher responsible for planning and carrying out his research and writing up his findings. It was only necessary to include the supervisor's name to credit the overall research guidance and advice.

Given the above, if one was to put numerical values on the percentage contributions of the candidate to the individual papers, it would seem appropriate to credit the candidate at 50% level for Paper 1. The candidate was clearly responsible for the design of the experimental apparatus, and carried out all experimental measurements reported and the data processing. Paper 2 should be credited to the candidate at the level of 75-80%, while Papers 3 and 4 at the level of 90% each. A clear majority of the work presented in Papers 2 – 4 was conducted under the candidate's PhD programme and by the candidate. He was responsible for the experimental setup, the development of the measurement methodology, the actual measurements, data processing and analysis as well as theoretical developments.

Finally, as part of the requirements for the presentation of the thesis the candidate needs to provide a statement clarifying his contribution to science and engineering. This in some way has already been done in sections 3.1 and 3.2 so some repetition is inevitable, however here the candidate would like to list a few "overarching themes" in his work that demonstrate "addition to knowledge" achieved by candidate's research.

The candidate sees his contribution in the following areas:

The first area is related to the development of experimental facilities and measurement methodologies in a challenging area of acoustically induced oscillatory flows. This is exemplified by the construction and commissioning of the standing wave resonator capable of 10% drive ratio and with appropriate internal structures; implementation of the PIV measurement methodology, including seeding mechanism, illumination aspects, phase-

locking circuitry, data acquisition mechanisms or setting out the standards for ensemble averaging techniques in the class of problems investigated; and adapting the hot-wire anemometry technique for this research area.

The second type of contribution includes obtaining the body of data related to the fundamental behaviour of fluids under oscillatory conditions present in the thermoacoustic context. This has been demonstrated on several levels: In Paper 1 some investigations of the minor loss occurring at the discontinuity formed by the contraction sections in the oscillatory flows have been performed and these suggested its dependence on the amplitude of the oscillation. In Paper 2, two types of vortex shedding mechanisms in oscillatory flows past parallel plates were unravelled and their behaviour compared through the resulting Strouhal numbers. Paper 3 documented the cycle-to-cycle variability of the flow field and focused on determining scales of turbulence, but also looked at three-dimensionality of the flows around stacks. Paper 4 extended the work in Paper 2 related to classification of shedding patterns.

The third type of contribution relates to the theoretical treatment of the flows under investigation. This effort starts in Paper 1 with building an analytical model of the acoustic coupling in the resonator designed for investigating oscillatory flows in the thermoacoustic context. In Paper 3 a novel analysis of turbulence length scales has been proposed, while Paper 4 focused on the non-dimensional analysis of the vortex shedding processes using two-dimensional Navier-Stokes equations as a starting point.

Finally, it is also worth mentioning the data processing techniques developed during the course of the current investigations. This can be exemplified by Paper 2, where the post processing of the time-dependent hot wire data from vortex shedding using FFT techniques led to obtaining spectral information for calculating the Strouhal numbers. Similarly, in Paper 3, a new technique of decomposition of the velocity fluctuation into large- and small- scale fluctuations is demonstrated by using fast Fourier transform spatial filtering techniques. However, more traditional techniques are also shown in Paper 3: the unsteadiness of the flow in the ejection stage is characterised by the total fluctuation intensity and the turbulence kinetic energy in the flow. Finally Paper 4 demonstrates the use non-dimensional analysis for studying and representing/grouping the flow patterns based on non-dimensional parameters such as Reynolds and KC number and some important geometrical ratios of the thermoacoustic stacks.

## Chapter 4

# Acoustic coupling between the loudspeaker and the resonator in a standing-wave thermoacoustic device

by D. Marx, X. Mao and A. J. Jaworski

Published in *Applied Acoustics*



ELSEVIER

Available online at [www.sciencedirect.com](http://www.sciencedirect.com)

SCIENCE @ DIRECT®

Applied Acoustics 67 (2006) 402–419

**applied  
acoustics**

[www.elsevier.com/locate/apacoust](http://www.elsevier.com/locate/apacoust)

# Acoustic coupling between the loudspeaker and the resonator in a standing-wave thermoacoustic device

David Marx<sup>1</sup>, Xiaohan Mao, Artur J. Jaworski<sup>\*</sup>

*School of Mechanical, Aerospace and Civil Engineering (George Begg Building), University of Manchester, Sackville Street, PO Box 88, Manchester M60 1QD, UK*

Received 26 January 2005; received in revised form 21 July 2005; accepted 1 August 2005

Available online 19 September 2005

---

## Abstract

Thermoacoustic refrigerators work with high amplitude sound waves, which are often created using an acoustic source coupled to a resonator. This coupling can be calculated analytically using linear acoustic equations and a linear model of the loudspeaker. This paper makes a comparison between such a coupling and measurements obtained in a large-scale thermoacoustic resonator constructed at the University of Manchester. The resonator was driven from low to large pressure amplitudes, with drive ratios up to 10%. It is shown that a good agreement is obtained for small amplitudes and this progressively worsens as the amplitude is increased. In the absence of wave harmonics and loudspeaker nonlinearities, the increasing discrepancy is attributed to the presence of minor losses.

© 2005 Elsevier Ltd. All rights reserved.

*PACS:* 43.20.Ks; 43.38.Ja; 43.35.Ud

*Keywords:* Resonator; Loudspeaker; Thermoacoustics; Minor losses

---

<sup>\*</sup> Corresponding author. Tel.: +44 (0) 161 275 4352; fax: +44 (0) 870 130 7474.

*E-mail addresses:* [david.marx@manchester.ac.uk](mailto:david.marx@manchester.ac.uk) (D. Marx), [x.mao@student.manchester.ac.uk](mailto:x.mao@student.manchester.ac.uk) (X. Mao), [artur.jaworski@manchester.ac.uk](mailto:artur.jaworski@manchester.ac.uk) (A.J. Jaworski).

<sup>1</sup> Present address: The University of Manchester, Goldstein Laboratory, Barton Airport, Eccles, Manchester M30 7RU, UK. Tel.: +44 (0)161 789 2328; fax: +44 (0)161 787 8749.

## 1. Introduction

In thermoacoustic refrigeration, the transport of energy from a cold to a hot reservoir is established by imposing an acoustic field in the vicinity of a solid boundary, which often takes the form of a stack of parallel plates for a standing wave device. For mainly practical reasons, the stack is sometimes made of a porous material instead of parallel plates. Expansion and compression of gas elements coupled with their oscillatory movement – due to the acoustic field imposed – enable hydrodynamic energy transport up a temperature gradient, which constitutes the essence of the thermoacoustic effect [1]. Thermoacoustic effect is a second-order phenomenon, and so intense sound waves are needed to obtain sufficient cooling powers. The necessary excitation is usually created using an acoustic source coupled to an acoustic resonator. Fig. 1 shows schematically a thermoacoustic refrigerator, with associated energy fluxes.

The wave within the resonator depends both on the characteristics of the resonator and on those of the source. Recently, a combination of linear acoustic equations and linear equations for the loudspeaker was used by Bailliet et al. [2] to predict the acoustic level in a resonator, and some measurements were done in the case of a straight resonator. The agreement was within 30%, but the measurements were limited to low amplitudes. Using the same kind of analysis, Tijani et al. [3] suggested the use of an adjustable piston on the back cavity of the loudspeaker in order to adjust the resonance frequency and the electro-acoustic efficiency in the coupled system comprising the loudspeaker and the resonator. An important parameter in thermoacoustics is the drive ratio,  $D_r$ , defined as the ratio of the maximum acoustic pressure amplitude in the resonator (i. e. the amplitude at the pressure antinode) to the mean pressure in the resonator. In the work of Bailliet et al. [2], the drive ratio did not

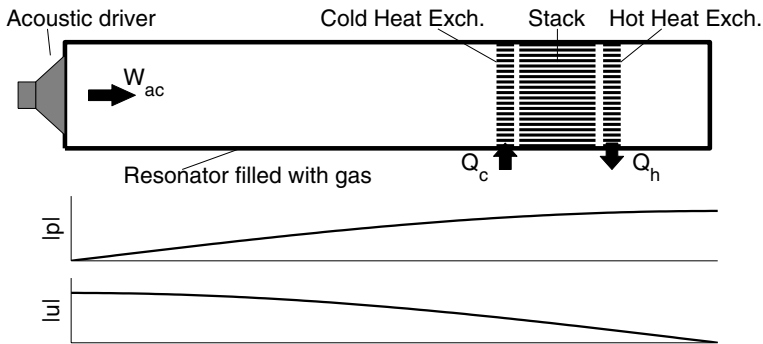


Fig. 1. Sketch of a thermoacoustic refrigerator. The electrodynamic transducer (a loudspeaker) provides an acoustical power  $W_{ac}$  to the system. This power is converted into heat flux by the stack of plates due to the thermoacoustic effect. A quantity of heat  $Q_c$  can thus be pumped from the cold reservoir to be cooled via the cold heat exchanger, while the excess heat  $Q_h$  is released at the hot heat exchanger. The two diagrams in the bottom represent the acoustic pressure and velocity amplitudes,  $|p|$  and  $|u|$ , along the resonator for a quarter-wavelength operation. The velocity antinode is at the driver, while the pressure antinode is at the resonator rigid end.

exceed 0.6%. Tijani et al. [3] did not specify their drive ratio, but their comparison between measurements and theoretical results show significant quantitative differences. In most thermoacoustic devices, the drive ratio needs to be relatively large, typically between 5% and 10%. The present paper investigates this range.

The study presented in this paper is an initial stage of a wider research programme carried out at the University of Manchester aiming at understanding the heat transfer and fluid flow processes within a stack and heat exchangers of a standing wave thermoacoustic device. To this end, a large-scale, high-amplitude and low-frequency flow rig is being built to enable PIV, LDA and hot wire measurements within relatively thick thermo-viscous boundary layers. Similarly, the flow rig will operate at an appreciable temperature gradient (200 K temperature difference) and so it will be made of steel and glass components. However, to enable initial trials and theoretical modelling for the (costly) final design, a Perspex-based resonator has been initially built and tested, which is the background for the current paper.

In this paper, measurements performed on a large resonator including a “loudspeaker box” section connected to a straight section by a pyramidal contraction are compared to theoretical results. Moderate to large drive ratios are investigated, from 0.15% to 10%. The details of the experimental apparatus are given in Section 2, while the theoretical model of the acoustic coupling is given in Section 3. Comparisons between theoretical and experimental results are reported in Section 4. It is observed that a good agreement between experimental results and theory is reached at low drive ratios, but this becomes progressively worse when the drive ratio is increased. It is shown that minor losses in the pyramidal contraction could mostly account for the observed discrepancies.

## 2. Experimental apparatus

Photograph in Fig. 2 shows the general view of the experimental apparatus constructed during this work. It consists of a cube-shaped loudspeaker box with

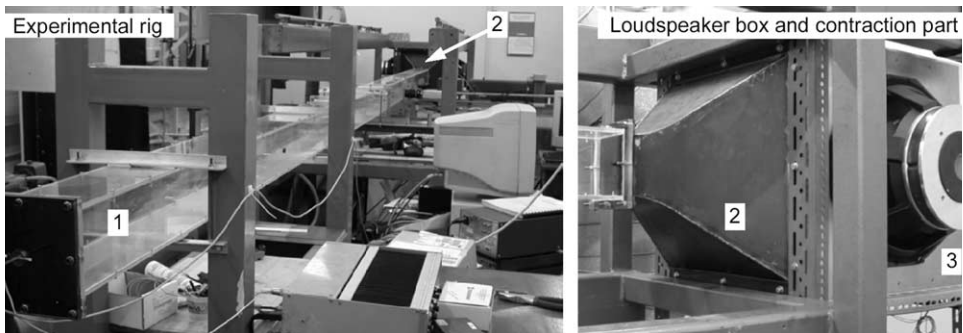


Fig. 2. Left: picture of the whole apparatus; the long Perspex rig (1) and the contracting section (2) are visible. Right: picture of an enlarged view of the contracting section (2) and of the loudspeaker box (3), with one loudspeaker mounted on one of its sides.

dimensions 600 mm × 600 mm × 600 mm. Five walls of the loudspeaker box have circular openings which mate with the loudspeakers attached to the box, and it is possible to use up to 5 loudspeakers in phase to generate high amplitude excitation while keeping the driving voltage low. In the current study, the arrangement includes a single loudspeaker which is mounted on the side the box opposite the resonator (this arrangement is different from the one photographed when producing Fig. 2). The unused openings are blocked by wooden lids. The loudspeaker box is coupled to the resonator using a contraction, which essentially reduces the internal square cross-section from 500 mm × 500 mm on the box end to 136 mm × 136 mm on its resonator end. The contraction, welded from four sheets of metal and equipped with appropriate mating flanges is made in such a way that it includes a pyramidal section (cone of square cross-section with a top of the pyramid sliced off) and a curved section on top, which ensures a smooth connection with the resonator. The total length of the contraction is 300 mm (later in the text, this contraction will be split into a pyramidal part of length 220 mm and a square tube of length 80 mm). Finally, the resonator section is connected to the contraction using suitable flanges. The resonator is a square cross-section Perspex channel with internal dimensions 136 mm × 136 mm and the wall thickness 8 mm. For convenience of handling, the resonator is made out of four sections. All parts of the apparatus are supported by suitable frames as seen in Fig. 2. In the work presented here there was no thermoacoustic stack present in the resonator.

During the experiments the acoustic excitation was provided by a large woofer-type loudspeaker, model PD 1850, manufactured by Precision Devices, with the membrane diameter 357 mm. The loudspeaker was excited by an amplifier fed with a sinusoidal excitation, provided by a signal generator, TTi TG1010. The RMS voltage fed to the loudspeaker was measured with a voltmeter. The resonator is equipped with a series of pressure ports along the side wall as well as one at the end cap of the resonator. The pressure measurements were made by means of a piezoresistive pressure transducer Endevco 8510-B2, which was calibrated using a Betz manometer, with precision of 0.1 mm H<sub>2</sub>O (approximately 1 Pa). The signal obtained from the transducer was collected on a laboratory PC using a data acquisition card. This allowed calculating the drive ratio. For some measurements and in order to assess loudspeaker linearity, a laser positioning system KEYENCE LK-503 (sensitivity up to 100 mV/mm) is placed in the loudspeaker box, and allows the displacement of the membrane to be monitored. The first resonance frequency of the resonator described here, corresponding roughly to the quarter-wavelength mode of operation, is 13.1 Hz.

### 3. Theoretical model

For the purpose of the analysis, the somewhat complex shape of the contracting section of length 300 mm is approximated by a pyramidal contraction of length 220 mm and a pipe section of length 80 mm, which is very close to reality indeed. The schematic of the geometry of the acoustic resonator and loudspeaker assembly

is represented in Fig. 3. Part A is located between  $x_0 \leq x \leq x_1$ . It consists of a square tube of half-side length  $r_A$ . Part A is the loudspeaker box referred to above. Part B is the pyramidal contraction, located between  $x_1 \leq x \leq x_2$ . The half-side length of the large end of this part is  $r_B$ ; for the small end it is  $r_C$ . The pyramidal nozzle apex axial position is  $x_a$ . Final part C is a long square tube located between  $x_2 \leq x \leq x_3$ , terminated by a rigid cap at  $x = x_3$ . Its half-side length is  $r_C$ . The values of geometrical properties are given in Table 1.

3.1. Acoustic equations

To calculate the acoustic field in the resonator, the equations for sound propagation in each part of the system are required. Complex notation is used: any real variable  $\tilde{\psi}$  will be written  $\tilde{\psi} = \psi_0 + \text{Re}[\psi e^{i\omega t}]$ , where  $\psi_0$  is the value of the variable at rest,  $\psi$  is the complex amplitude of the acoustical part of the variable, and  $\omega$  is the angular frequency. For part A and C, the linear acoustic equation for the complex acoustic pressure  $p$  in a square channel tube including thermo-viscous effects is [1]:

$$[1 + (\gamma - 1)f_\kappa]p + \frac{c_0^2}{\omega^2} (1 - f_v) \frac{d^2 p}{dx^2} = 0. \tag{1}$$

The functions  $f_v$  and  $f_\kappa$  are viscous and thermal functions [1] and depend on the geometry of the channel [4]. Their expressions in the boundary layer approximation for a square pipe of half-side length  $r$  are simply

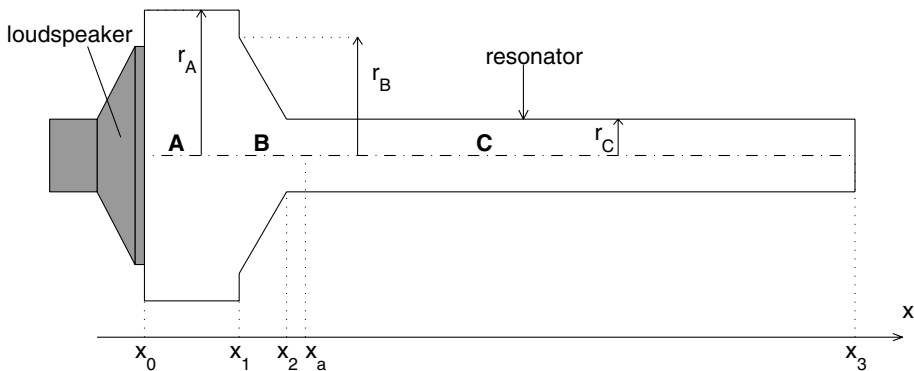


Fig. 3. Schematic of the geometry of the loudspeaker and acoustic resonator.

Table 1  
Geometry of the resonator

$x_0 = 0$	$r_A = 0.3 \text{ m}$	$S_A = 0.36 \text{ m}^2$
$x_1 = 0.6 \text{ m}$	$r_B = 0.25 \text{ m}$	$S_B(x_1) = 0.25 \text{ m}^2$
$x_2 = 0.82 \text{ m}$	$r_C = 0.068 \text{ m}$	$S_B(x_2) = S_C = 0.0185 \text{ m}^2$
$x_a = 0.90 \text{ m}$		
$x_3 = 8.3 \text{ m}$		

$$f_v = (1 - i) \frac{\delta_v}{r} \quad \text{and} \quad f_\kappa = (1 - i) \frac{\delta_\kappa}{r}, \tag{2}$$

where the viscous and thermal penetration depths are, respectively, defined by

$$\delta_v = \sqrt{\frac{2\nu}{\omega}} \quad \text{and} \quad \delta_\kappa = \sqrt{\frac{2\kappa}{\omega}}. \tag{3}$$

The boundary layer approximation holds as long as  $r \gg \delta_v, \delta_\kappa$ , which is true in the experiments presented here. In these expressions,  $\nu$  is the kinematic viscosity,  $\kappa$  is the thermal diffusivity defined by  $\kappa = K/\rho_0 c_p$ ,  $K$  is the fluid thermal conductivity,  $\rho_0$  is its ambient density,  $c_p$  is its isobaric specific heat,  $\gamma$  is the ratio of specific heats, and  $c_0$  is the speed of sound. The fluid is air, considered to be a perfect gas of perfect gas constant  $\mathcal{R}$ . Thus  $c_p = \gamma\mathcal{R}/(\gamma - 1)$ . The following values are taken:  $\mathcal{R} = 287 \text{ J K}^{-1} \text{ kg}^{-1}$ ,  $\nu = 1.5 \times 10^{-5} \text{ m}^2 \text{ s}^{-1}$ ,  $\gamma = 1.4$ . Ambient temperature, pressure, and speed of sound are  $T_0 = 298 \text{ K}$ ,  $p_0 = 10^5 \text{ Pa}$ , and  $c_0 = \sqrt{\gamma\mathcal{R}T_0}$ . The section-averaged complex acoustic velocity,  $u$ , is given by [1]:

$$u = -\frac{(1 - f_v) dp}{i\omega\rho_0 dx}. \tag{4}$$

For part B, thermoviscous effects are not taken into account to obtain simplified analytical results. The pyramidal section is short enough, and shallow enough, so that this does not affect the result significantly. Thus equation for pressure in part B is

$$\frac{\partial^2 p}{\partial t^2} - \frac{c_0^2}{x'^2} \frac{\partial}{\partial x'} \left( x'^2 \frac{\partial p}{\partial x'} \right) = 0. \tag{5}$$

This equation is simply the propagation equation written in spherical coordinates, where radial coordinate is  $x' = x - x_a$ . The velocity is given by the spherical momentum equation

$$\rho_0 \frac{\partial u}{\partial t} = -\frac{\partial p}{\partial x'}. \tag{6}$$

### 3.2. General solutions

The general solution to Eqs. (1), (4), (5), and (6) are now written for each part of the resonator:

*Part A* ( $x_0 \leq x \leq x_1$ ):

$$p_A = A(e^{-ik_A x} + R_A e^{ik_A x}), \tag{7}$$

$$u_A = \frac{k_A(1 - f_{v,A})}{\omega\rho_0} A(e^{-ik_A x} - R_A e^{ik_A x}), \tag{8}$$

$$k_A = \frac{\omega}{c_0} \sqrt{\frac{1 + (\gamma - 1)f_{\kappa,A}}{1 - f_{v,A}}}, \tag{9}$$

$$f_{v,A} = (1 - i) \frac{\delta_v}{r_A}, \quad f_{\kappa,A} = (1 - i) \frac{\delta_\kappa}{r_A}. \tag{10}$$

*Part B* ( $x_1 \leq x \leq x_2$  and  $x' = x - x_a$ ):

$$p_B = \frac{B}{x'} (e^{-ik_B x'} + R_B e^{ik_B x'}), \tag{11}$$

$$u_B = \frac{1}{\rho_0 c_0} \frac{B}{x'} \left( \left( 1 - \frac{i}{k_B x'} \right) e^{-ik_B x'} - R_B \left( 1 + \frac{i}{k_B x'} \right) e^{ik_B x'} \right), \tag{12}$$

$$k_B = \frac{\omega}{c_0}. \tag{13}$$

*Part C* ( $x_2 \leq x \leq x_3$ ):

$$p_C = C (e^{-ik_C x} + R_C e^{ik_C x}), \tag{14}$$

$$u_C = \frac{k_C (1 - f_{v,C})}{\omega \rho_0} C (e^{-ik_C x} - R_C e^{ik_C x}), \tag{15}$$

$$k_C = \frac{\omega}{c_0} \sqrt{\frac{1 + (\gamma - 1) f_{\kappa,C}}{1 - f_{v,C}}}, \tag{16}$$

$$f_{v,C} = (1 - i) \frac{\delta_v}{r_C}, \quad f_{\kappa,C} = (1 - i) \frac{\delta_\kappa}{r_C}. \tag{17}$$

The amplitudes of the right-travelling waves are *A*, *B*, and *C* in parts A, B, and C, respectively. The reflection coefficients are  $R_A$ ,  $R_B$ , and  $R_C$ .

### 3.3. Joining conditions

To find the solution to the problem, the joining conditions must be written. They are the pressure and volume flow rate continuity:

$$x = x_0 : S_A u_A(x_0) = U_0, \tag{18}$$

$$x = x_1 : p_A(x_1) = p_B(x_1), \tag{19}$$

$$S_A u_A(x_1) = S_B(x_1) u_B(x_1), \tag{20}$$

$$x = x_2 : p_B(x_2) = p_C(x_2), \tag{21}$$

$$S_B(x_2) u_B(x_2) = S_C u_C(x_2), \tag{22}$$

$$x = x_3 : u_C(x_3) = 0, \tag{23}$$

where  $S_A$  is the cross-section area of part A,  $S_B(x)$  is the cross-section area of part B at abscissa  $x$ , and  $S_C$  is the cross-section area of part C. In Eq. (18),  $U_0$  is the volume flow rate at the loudspeaker membrane. To calculate this, one needs to consider the equation of the loudspeaker given in the next section.

### 3.4. Loudspeaker equation

The loudspeaker is a mechanical oscillator driven by electromagnetic forces, mechanical forces (spring and damping) and by acoustic force on its membrane. A linear model of the loudspeaker is used in this paper [5]. In this description, the most important parameters for the loudspeaker are: the electrical resistance  $R_e$  and

impedance  $L_e$  of the coil; the force factor  $Bl$ ; and the mechanical parameters: the damping  $h$ , the stiffness  $s$ , and the moving mass  $m$ . In the frequency range considered here (<100 Hz), the effect of the inductance is negligible.

The volume velocity at the membrane  $U_0$  when the loudspeaker is driven by the voltage amplitude  $V_e$  is

$$U_0 = S \frac{Bl}{Z_e(Z_{\text{mec}} + S^2 Z_{\text{ac}}) + (Bl)^2} V_e. \quad (24)$$

The driving voltage is taken to be the reference of phase. Hence the voltage amplitude  $V_e$  is considered to be a real quantity.  $S$  is the loudspeaker membrane cross-section.  $Z_e = R_e + iL_e\omega$  is the electrical impedance of the loudspeaker coil, and  $L_e$  will be neglected in the following.  $Z_{\text{mec}}$  is the mechanical impedance of the loudspeaker, given by

$$Z_{\text{mec}} = h + i\left(m\omega - \frac{s}{\omega}\right). \quad (25)$$

Finally  $Z_{\text{ac}}$  is the acoustical impedance of the resonator and thus represents the effect of acoustic forces on the loudspeaker membrane. It is given by

$$Z_{\text{ac}} = \frac{p_A(x_0)}{S_A u_A(x_0)}. \quad (26)$$

Having neglected the inductance, five linear parameters are required to describe the loudspeaker, namely  $R_e$ ,  $Bl$ ,  $h$ ,  $s$ , and  $m$ .  $R_e$  is directly measured at the terminals of the coil.  $Bl$  can be calculated by applying a known force on the membrane and measuring the steady current necessary to get the membrane back to its equilibrium position. Finally, the electrical impedance of the loudspeaker suspended in air is measured in the frequency range 5–80 Hz, and its least-square fitting to the theoretical electrical impedance given by

$$Z_{e,\text{tot}} = R_e + \frac{Bl^2}{Z_{\text{mec}}} = R_e + \frac{Bl^2}{h + i((m + \mathcal{M})\omega - s/\omega)} \quad (27)$$

provides the remaining three parameters,  $h$ ,  $s$ , and  $m$ . The quantity  $\mathcal{M}$  is a correction to account for radiation in air, and is given by  $\mathcal{M} = 2 * 0.67\rho_0(\sqrt{S/\pi})^3$ . Measured values of the important characteristics of the loudspeaker are summarized in Table 2. Some limitations of the linear model presented here will be given below.

Table 2  
Linear parameters and cross-sectional area of the loudspeaker

Moving mass, $m$	193 g
Product, $Bl$	31.6 Tm
Electrical resistance of the coil, $R_e$	5.5 $\Omega$
Stiffness, $s$	10,970 N m <sup>-1</sup>
Damping, $h$	8 N s m <sup>-1</sup>
Cross-sectional area, $S$	0.10 m <sup>2</sup>

### 3.5. Solution

The acoustic field in the system is given by the solution of acoustic equations (7)–(17), related through the joining conditions (18)–(23), and the electromechanical equation of the loudspeaker (24). The solution consists of finding  $R_C$ ,  $R_B$ ,  $R_A$ ,  $Z_{ac}$ ,  $U_0$ ,  $A$ ,  $B$ , and  $C$  in that order, each coefficient depending on the previous one. Starting with condition (23) at the end cap,  $R_C$  is found, and then  $R_B$  and  $R_A$  using the other conditions. This gives

$$R_C = e^{-2ik_Cx_3}, \tag{28}$$

$$R_B = \frac{\frac{Z_2}{Z_{s,B,2}} \left(1 - \frac{i}{k_Bx'_2}\right) - 1}{1 + \frac{Z_2}{Z_{s,B,2}} \left(1 + \frac{i}{k_Bx'_2}\right)} e^{-2ik_Bx'_2}, \tag{29}$$

where

$$Z_2 = Z_{s,C} \frac{e^{-ik_Cx_2} + R_C e^{ik_Cx_2}}{e^{-ik_Cx_2} - R_C e^{ik_Cx_2}}, \tag{30}$$

$$Z_{s,C} = \frac{\omega\rho_0}{S_C k_C (1 - f_{v,C})}, \tag{31}$$

$$Z_{s,B,2} = \frac{\rho_0 c_0}{S_B(x_2)}, \tag{32}$$

$$R_A = \frac{\frac{Z_1}{Z_{s,A}} - 1}{1 + \frac{Z_1}{Z_{s,A}}} e^{-2ik_Ax_1}, \tag{33}$$

where

$$Z_1 = Z_{s,B,1} \frac{e^{-ik_Bx'_1} + R_B e^{ik_Bx'_1}}{\left(1 - \frac{i}{k_Bx'_1}\right) e^{-ik_Bx'_1} - R_B \left(1 + \frac{i}{k_Bx'_1}\right) e^{ik_Bx'_1}}, \tag{34}$$

$$Z_{s,B,1} = \frac{\rho_0 c_0}{S_B(x_1)}, \tag{35}$$

$$Z_{s,A} = \frac{\omega\rho_0}{S_A k_A (1 - f_{v,A})}. \tag{36}$$

Knowing the reflection coefficient  $R_A$  in part A it is possible to calculate the acoustic impedance  $Z_{ac}$  (Eq. (26)) seen by the loudspeaker

$$Z_{ac} = Z_{s,A} \frac{e^{-ik_Ax_0} + R_A e^{ik_Ax_0}}{e^{-ik_Ax_0} - R_A e^{ik_Ax_0}}. \tag{37}$$

Then the volume flow rate at the loudspeaker membrane  $U_0$  is calculated using Eq. (24) for the loudspeaker. Finally,  $U_0$  being known, the direct coefficients are found:

$$A = Z_{s,A} U_0 \frac{1}{e^{-ik_A x_0} - R_A e^{ik_A x_0}}, \tag{38}$$

$$B = Ax'_1 \frac{e^{-ik_B x'_1} + R_B e^{ik_B x'_1}}{e^{-ik_B x'_1} + R_B e^{ik_B x'_1}}, \tag{39}$$

$$C = \frac{B}{x'_2} \frac{e^{-ik_B x'_2} + R_B e^{ik_B x'_2}}{e^{-ik_C x_2} + R_C e^{ik_C x_2}}. \tag{40}$$

These formula can easily be calculated by a mathematical programme. Knowing all the coefficients, it is possible to obtain results of the type  $D_r = f(V_e, \omega)$ , where  $D_r = |p_c(x_3)|/p_0$  is obtained using Eq. (14), the coefficients in it resulting of Eqs. (28) and (40). The voltage amplitude and frequency are indeed the only constraints imposed during the experiments.

#### 4. Experimental results and their comparison to theoretical predictions

As explained in Sections 2 and 3.5 the quantities controlled during the experiments presented here were the excitation voltage provided to the loudspeaker and its frequency. The main measured quantity was the pressure amplitude at the end cap of the resonator which, when normalized by the ambient pressure, resulted in obtaining the drive ratio  $D_r$ . In some cases, the displacement of the loudspeaker membrane was monitored.

##### 4.1. Low amplitude experiments

The initial set of experiments involved a relatively low value of the voltage amplitude, namely  $V_e = 0.849$  V. The frequency response of the apparatus is shown in Fig. 4. The first three modes of the resonator are included, and the general agreement between the measurements and the theoretical predictions is good. The first three

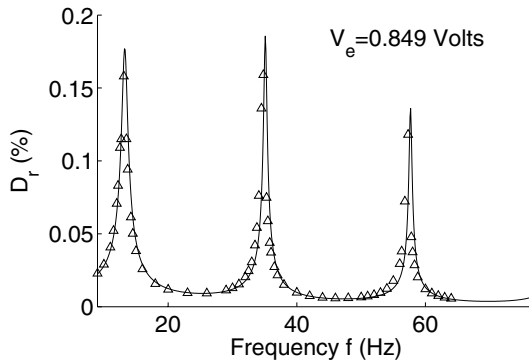


Fig. 4. Drive ratio,  $D_r = |p_c(x_3)|/p_0$ , as a function of the frequency,  $f$ , for a fixed value of the voltage amplitude imposed on the loudspeaker ( $V_e = 0.849$  V): —, theory and  $\Delta$ , experiments.

measured resonance frequencies:  $f_1 = 13.1$  Hz,  $f_2 = 34.8$  Hz, and  $f_3 = 57.3$  Hz correspond to a one quarter, a three quarter, and a five quarter-wavelength mode, respectively. They compare well with the predicted values: 13.1, 35.1, and 57.7 Hz, respectively. Fig. 5 shows the predicted variation of pressure and velocity amplitudes as a function of  $x$ -coordinate for the first mode ( $f = f_1$ ). This is the quarter wavelength mode (similar to the one represented in the bottom of Fig. 1) with a velocity antinode close to the pyramidal contraction ( $x \sim x_2$ ), and a pressure antinode at the end of the resonator ( $x = x_3$ ). As can be seen from Fig. 4, the drive ratio of this first mode is within 10% of its predicted value. A better agreement was obtained by decreasing the voltage, but the best error the authors reached was 8.5% at 0.14 V. Such an error is similar to that found in other works [2]. Agreement between the measured and predicted drive ratio gets progressively worse when the frequency increases; the error is 14% for the second mode, and 15% for the third mode. An increasing disagreement between theory and measurements with increasing the mode number was also observed by Bailliet et al. [2] at low amplitudes. In addition, when the voltage amplitude was increased past 0.849 V, the error increased for all the modes but grew faster for the lower frequencies. In particular, it is faster for the first mode. For example, when a very high voltage  $V_e = 70.2$  V is used, the error is 28.5% for the first mode, 24.5% for the second mode, and 19.2% for the third mode, meaning that the error is approximately the same for the first two modes, while the error on the third mode has not changed much compared to very low voltages.

4.2. High amplitude experiments

Having established a good agreement between experimental and theoretical results for low excitation voltage, the second set of experiments involved variation of the excitation voltage for the first resonant mode at  $f = f_1 = 13.1$  Hz. The

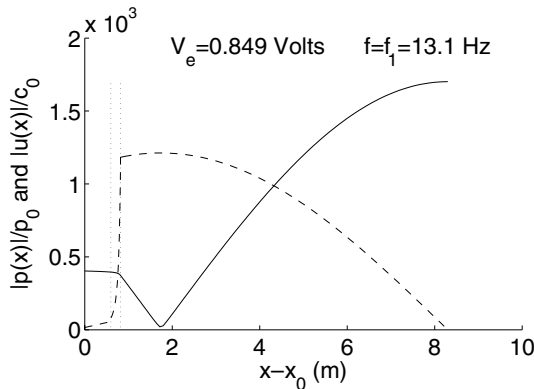


Fig. 5. Predicted normalized velocity and pressure amplitudes along the resonator for the first mode ( $f = f_1 = 13.1$  Hz) and  $V_e = 0.849$  V: —, pressure and - - -, velocity. The two vertical dotted line indicate the pyramidal contraction limit positions, at  $x = x_1$  and  $x = x_2$ .

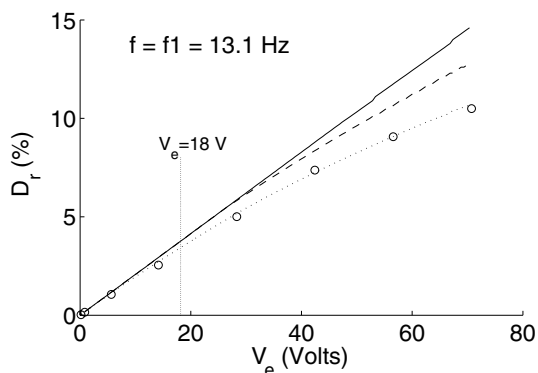


Fig. 6. Drive ratio,  $D_r$ , corresponding to the first resonant mode ( $f = f_1 = 13.1$  Hz) plotted vs. the loudspeaker driving voltage amplitude,  $V_e$ : —, result given by theory;  $\circ$ , result provided by experiments; - - -, result provided by the numerical code DELTAE, taking into account turbulence; and  $\cdots$ , result provided by the numerical code DELTAE, taking into account turbulence and using an impedance to model the minor losses at  $x = x_2$  ( $K = 0.6$ ). The vertical line at  $V_e = 18$  V indicates the limit past which turbulence is expected [10].

variation of the voltage amplitude  $V_e$  is equivalent to varying the drive ratio, as far as the physics remains globally linear. Fig. 6 shows the drive ratio corresponding to the first resonant mode plotted against the driving voltage amplitude. It is observed that the agreement between the experiments and the theory worsens as the driving voltage amplitude increases. At the highest voltage, the experimental  $D_r$  is nearly 30% lower than predicted. The difference between experiments and theory grows as the square of the voltage<sup>1</sup> (the square of the drive ratio) meaning that some nonlinear effects are taking place. In the coupled system, there are two possible causes of nonlinearities: the loudspeaker behavior, or the acoustic wave in the resonator.

#### 4.3. Loudspeaker nonlinearity

The model for the loudspeaker presented in Section 3.4 is a linear model. In this model, the parameters  $R_e$ ,  $Bl$ ,  $m$ ,  $s$ , and  $h$  do not depend on the operating conditions. This is an approximation, and in practice the parameters depend on the amplitude of the membrane excursion [6], on the current, and on the frequency. In the low frequency range concerned here, this last dependence is negligible (although there could be creeping effects [7] at low frequency). One effect of high currents is that they increase  $R_e$  due to temperature rise resulting from heat dissipation. In the present measurements, at high voltage amplitudes, the measured membrane displacement, pressure, and intensity tend to decrease with time due to this heating. This is especially true for the first resonant frequency (the reason for this comes from orders

<sup>1</sup> In Fig. 6, the theoretical curve is given by  $D_r = 0.207V_e$ , while the measured curve is well fitted by  $D_r = 0.207 * V_e - 0.00081 * V_e^2$ , where  $V_e$  has to be expressed in Volts and  $D_r$  in %.

of magnitudes in Eq. (24)). To avoid including this drift in the measurements (as well as burning the coil), the measurements are taken immediately after switching on the loudspeaker for each measurement. Hence, the only important nonlinearity source in the present study is the amplitude dependence of the parameters. The membrane displacement amplitude  $D_{\text{memb}}$  is given by  $D_{\text{memb}} = (U_0/S)/\omega$  and can thus be obtained directly from Eq. (24). It depends on  $V_e$ , and it is possible to emphasize the voltage dependence of the parameters by writing  $Bl(V_e)$ ,  $s(V_e)$ ,  $h(V_e)$ , and expressing the membrane displacement amplitude as

$$D_{\text{memb}} = \frac{1}{\omega} \left[ \frac{Bl(V_e)}{Z_e(h(V_e) + i(m\omega - s(V_e)/\omega) + S^2Z_{ac}) + (Bl(V_e))^2} \right] V_e. \quad (41)$$

The possible  $Bl$  dependence on  $V_e$  is especially important due to order of magnitudes in Eq. (41).

To assess the nonlinear dependence of the parameters, there are ideally two possible options. The first is to measure the parameters directly in situ [8] and observe whether they depend on  $V_e$ . The second is to measure the displacement of the membrane in situ, and then to measure the parameters on the loudspeaker only, imposing the same displacement amplitudes as in the in situ measurement. The approach taken here is more pragmatic. Consider Eq. (41) for the displacement amplitude. If the loudspeaker exhibits some nonlinearity, the quantity in brackets does depend on  $V_e$ , and  $D_{\text{memb}}$  has a nonlinear variation with  $V_e$ . If not, then the parameters do not depend on  $V_e$  and neither does the quantity in brackets, so that the displacement  $D_{\text{memb}}$  is linear in  $V_e$ . Indeed we expect such a linear behavior because the magnitude of the displacement (about 10 mm) at higher voltages is moderate considering the nominal size of the loudspeaker. For reference the linear excursion  $X_{\text{max}}$  given by the manufacturer is 11.25 mm (the displacement limit being 32 mm). The displacement amplitude of the membrane is given in Fig. 7 as a function of the excitation voltage, for the first resonant mode. The theoretical line results from Eq. (41) with the parameters constant and equal to their linear values given in Table 2. The experimental results have been obtained using the laser positioning system. All but the last point (at  $V_e = 70.2$  V) fall on a straight line, indicating that the loudspeaker behavior remains linear for  $V_e < 60$  V. For the second and third mode, the results also fall on a straight line, for all voltages. Also, no distortion is visible in the displacement signal, even at the highest voltage amplitudes. These observations tend to confirm that the loudspeaker has a linear behavior, and that the nonlinear phenomena happen in the resonator, and are mostly due to nonlinear acoustics.

#### 4.4. Nonlinear acoustics in the resonator

The next candidate for explaining the nonlinear acoustics is acoustic propagation in the resonator, that would result in wave steepening if it occurred. This can be avoided using the right shape of the resonator [9]. In the present case, the shape of the resonator and the coupling with the loudspeaker were chosen so that the quantity of created harmonics is negligible even at higher drive ratios, so no distortion

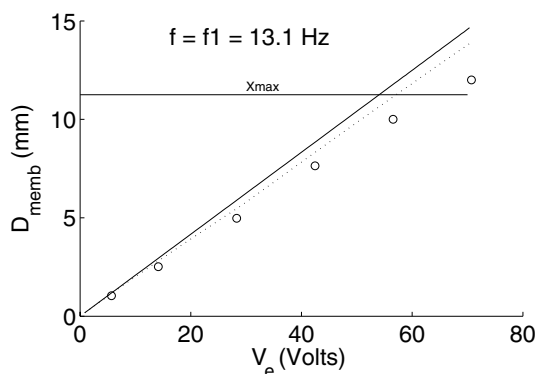


Fig. 7. Membrane displacement amplitude,  $D_{\text{memb}}$ , corresponding to the first resonant mode ( $f=f_1=13.1$  Hz) plotted vs. the loudspeaker driving voltage amplitude,  $V_e$ : —, result given by linear theory Eq. (41);  $\circ$ , result provided by experiments and  $\cdots$ , result provided by the numerical code DELTAE, taking into account turbulence and using an impedance to model the minor losses at  $x=x_2$  ( $K=0.6$ ). The horizontal line indicates the linear excursion amplitude  $X_{\text{max}}$  provided by the manufacturer.

occurs. It is worth noting in particular that  $f_2$  and  $f_3$  are not multiples of the fundamental frequency  $f_1$ . Hence the problem remains harmonic and the linear analysis presented in Section 3 remains valid from the acoustical propagation point of view. Thus the difference observed in Fig. 6 is likely due to a combination of turbulent losses and minor losses, which are now explained.

Turbulence in oscillating pipe flows appears when the Reynolds number exceeds a critical value [10]. In oscillating flows, a possible definition of the Reynolds number is  $A = 2u_a/\sqrt{\nu\omega}$ , where  $u_a$  is the velocity amplitude. In the resonator described here, the critical value  $A_c \sim 400$  [10] is reached at the velocity antinode (end of the pyramidal part at  $x \sim x_2$ , as in Fig. 5) when  $V_e \sim 18$  V. The vertical segment in Fig. 6 represents this voltage which may signify the onset of turbulence. In order to estimate the turbulent losses, the numerical code DELTAE has been used [11]. This code can simulate linear acoustic and thermoacoustic networks, and has an appended turbulence algorithm based on steady flow correlations. Of course application of steady flow correlations to oscillatory flows is an approximation but it has given useful results during thermoacoustic devices designs [12]. When using DELTAE for the loudspeaker-resonator assembly without the turbulence algorithm, results similar to the analysis of Section 3 are obtained. Negligible differences are due the losses in the pyramidal part that are included in DELTAE, but not in the analysis. Including the turbulence algorithm (with a relative roughness equal to  $2 \times 10^{-4}$ , corresponding to a dimensional roughness of about 25  $\mu\text{m}$ ) provides the result given by the dashed line in Fig. 6. It appears that turbulence reduces the expected drive ratio towards experimental results, but seems insufficient to explain alone the difference observed above, especially because the value used for the roughness is a maximum one for perspex walls. In what follows, the same value of the roughness is kept, the turbulence having virtually no effect anyway, because the other nonlinear effect

involved (minor losses) reduces the amplitude enough for the turbulence to become negligible.

In the resonator discussed here, as in most of the existing thermoacoustic devices, there is a convergent part (pyramidal part B) that may be the cause of minor losses. In steady flows, “minor” or “local” losses are responsible for pressure drop at geometric discontinuities [13]. The pressure drop  $\Delta P$  is given by the minor losses equation (equivalent to the Darcy–Weisbach equation for friction losses)

$$\Delta P = K \frac{\rho U^2}{2}, \quad (42)$$

where  $\rho$  is the density,  $U$  is the steady velocity, and  $K$  is a coefficient of fluid resistance, often provided by experimental data. Minor losses in oscillating flows are much less understood, although some studies have addressed the problem recently. Studies have mostly focused on the minor losses at the end of very thin channels (a few viscous penetration depths high), representing the exit of a stack of plates or of a heat exchanger in a thermoacoustic device. Morris et al. [14] have shown that the coefficient  $K$  used in the correlation tends to be higher than its steady flow counterpart. Wakeland et al. [15] have studied the effect of flow cross-sectional non-uniformity on the coefficient  $K$ , and shown that this non-uniformity increases the value of  $K$  as well. Smith and Swift [16] have studied the effect of the channel curvature effect on the minor losses. Petculescu and Wilen [17] have studied the value of  $K$  for jet pumps with different taper angles and curvature radius. More recently Doller [18] has studied the energy losses through a change in a resonator cross-section. Contrary to the other mentioned studies this investigation is not restricted to the thin channel case. Abrupt or conical cross-section changes were tested. For the abrupt change, the coefficient  $K$  was higher than the steady flow correlations suggest, and for a conical section, it was nearly the same.

For oscillating flows, it has been proposed to simply apply the above relation to the instantaneous acoustic pressure  $\tilde{p}$  and section-averaged velocity  $\tilde{u}$  [12,19], using

$$\Delta \tilde{p}(t) = -K \frac{\rho_0 |\tilde{u}(t)| \tilde{u}(t)}{2}, \quad (43)$$

where the negative sign provides the correct sign between the direction of the fluid flow and the direction of the pressure drop. In complex notation, and keeping only the Fourier component corresponding to the fundamental acoustic frequency, this gives [19]

$$\Delta p = -\frac{4}{3\pi} K \rho_0 |u| u. \quad (44)$$

Moreover,  $K$  is usually written as the average of a blowing coefficient  $K_B$  when the flow is in one direction during the first half of the acoustic cycle, and a suction coefficient  $K_S$  when the flow is in the opposite direction during the second half of the acoustic cycle. Thus  $K = (K_B + K_S)/2$ . In the present case, when the flow is directed towards  $x < 0$  the change in section between  $x_1$  and  $x_2$  may be considered as a pyramidal diffuser, with a value  $K_B = 1$  [13]. When the flow is directed towards  $x > 0$ , the

losses are essentially due to a vena contracta effect in the small pipe, and this is assumed to be taken into account by a converging bellmouth geometry [13], with  $K_S \sim 0.2$  as a maximal value. Thus  $K = (K_B + K_S)/2 = 0.6$ . This value should probably be increased by some factor to take into account the partial laminarity of the oscillating flow. This calculation of  $K$  is approximated in several ways. First, in steady flow, the two discontinuities at  $x = x_1$  and  $x = x_2$  are taken into account in a lump. The same would be justified in the experiments reported here if the acoustic particle displacement amplitude  $|u/\omega|$  were large compared to the length  $x_2 - x_1 = 0.22$  m of the convergent part. Indeed the particle displacement amplitude equals the length of the pyramidal part only at the highest value of the voltage amplitude (at  $V_e = 65$  V,  $|u/\omega|_{x=x_2} = 0.22$  m). Second, due to the important area contraction ratio of the convergent part (about 14), the velocity at  $x = x_2$  is much more important than the velocity at  $x = x_1$ . As a result, minor losses, which depend on the square of the velocity, occur mostly at  $x = x_2$ . The pressure drop, Eq. (44), can then be taken into account using the DELTAE code, which, in addition to turbulence, can also account for impedances  $Z$  such that  $\Delta p = Zu$ . The impedance corresponding to minor losses is  $Z = -\frac{4}{3\pi} K \rho_0 |u|$ , and it is added to the model for the loudspeaker-resonator assembly at position  $x = x_2$ . In this case, results obtained from DELTAE fit well the experimental results, as is shown in Fig. 6. As was mentioned, this fit is virtually independent of the roughness coefficient, because the minor losses decrease the velocity in the resonator enough for the turbulence to have a minor effect. For the second mode, it appears that the  $D_r$  vs.  $V_e$  relation exhibits a nonlinear dependence similar to the first mode, but that a value  $K = 0.3$  is sufficient to fit the experimental curve. Finally, for the third mode, almost no nonlinear behavior is observed, and the corresponding value of  $K$  would be very small. This mode dependence of  $K$  is probably due to the dependence of the minor losses on the particle displacement amplitude at  $x = x_2$ , that decreases with frequency, at a fixed drive ratio. If the value of  $K$  depends on the displacement amplitude, then the value of  $K$  could depend on  $V_e$ , at fixed frequency, although it is not suggested by the present measurements. The results presented here are based on a single measurement of the pressure at one point of the resonator, and on a global fitting of the  $D_r$  vs.  $V_e$  curve, using only one  $K$  coefficient. Further measurements should include the local measurement of the pressure drop at the geometrical discontinuity (using a pair of microphones and a velocity sensor), to estimate the value of  $K$  for every single voltage, that is every single particle displacement.

In the previous section, the linearity of  $D_{\text{memb}}$  vs.  $V_e$  was used to reject a possible nonlinearity in the loudspeaker behavior. This linearity was expected from a linear analysis (Eq. (41)) but one may question whether the minor losses would affect it. The velocity at the membrane calculated from DELTAE in the case where minor losses are added is shown in Fig. 7 for the first mode. It appears that the inclusion of minor losses does not change the linearity. Furthermore the error between the experimental data and the DELTAE results is almost constant and about 10% on the whole voltage range. These 10% correspond to the 10% error on the drive ratio at low voltages.

From the above discussion, it may appear that the coefficient of resistance in oscillating flow is comparable to what is expected directly from steady flow correlations,

at least when the particle displacement has a large enough value. However such a conclusion would have to be drawn with extreme caution due to the many approximations involved.

## 5. Conclusion

The results of analytical linear model for describing the coupling between a loudspeaker and a resonator including a convergent section has been derived and its results have been compared to measurements on a large range of amplitude. Comparison with measurements is good for low values of the excitation voltage, corresponding to low acoustic pressure amplitudes, especially for the first, one quarter-wavelength resonance mode. When the voltage is increased, measured drive ratios are lower than predicted. The disagreement grows as the square of the pressure amplitude, which indicates the presence of nonlinear phenomena. Nonlinearities associated with harmonics generation, turbulence, and loudspeaker behavior are low, and the only remaining plausible cause, the minor losses, give a satisfying explanation of the observed difference. Their effect could be estimated using steady flow correlations. The estimation for the coefficient of fluid resistance  $K$  was correct for the large-displacement first mode, but was over-estimated for the second and third modes, meaning that the coefficient  $K$  depends on the particle displacement. More extensive minor losses coefficients in oscillating flows are highly required to predict accurately the drive ratio in acoustic resonators driven at high amplitudes and including geometric discontinuities.

## References

- [1] Swift GW. Thermoacoustic engines. *J Acoust Soc Am* 1988;84:1145–80.
- [2] Bailliet HA, Lotton P, Bruneau M, Gusev V. Coupling between electrodynamic loudspeakers and thermoacoustic cavities. *Acustica* 2000;86:363–73.
- [3] Tijani MEH, Zeegers JCH, de Waele ATAM. A gas-spring system for optimizing loudspeakers in thermoacoustic refrigerators. *J Appl Phys* 2002;92:2159–65.
- [4] Arnott WP, Bass HE, Raspet R. General formulation of thermoacoustics for stacks having arbitrarily shaped pore cross section. *J Acoust Soc Am* 1991;90:3228–37.
- [5] Beranek L. *Acoustics*. New York: McGraw-Hill; 1954.
- [6] Scott J, Kelly J, Leembruggen G. New method of characterizing driver linearity. *J Audio Eng Soc* 1996;44(4):258–65.
- [7] Klippel W, Seidel U. Fast and accurate measurement of linear transducer parameter, Audio Engineering Society – AES Preprint 5308. In: 110th AES convention, 12–15 May 2001, Amsterdam, The Netherlands, 2001.
- [8] Paek I, Mongeau L, Braun JE. A method for estimating the parameters of electrodynamic drivers in thermoacoustic coolers. *J Acoust Soc Am* 2005;117:185–93.
- [9] Lawrenson CC, Lipkens B, Lucas TS, Perkins DK, Van Doren TW. Measurements of macrosonic standing waves in oscillating closed cavities. *J Acoust Soc Am* 1998;104:623–36.
- [10] Merkli P, Thomann H. Transition to turbulence in oscillating pipe flow. *J Fluid Mech* 1975;68:567–76.

- [11] Ward WC, Swift GW. Design environment for low amplitude thermoacoustic engines (DELTAE). *J Acoust Soc Am* 1994;95:3671–2. Program available from the Los Alamos National Laboratory (<http://www.lanl.gov/thermoacoustics/>).
- [12] Backhaus S, Swift GW. A thermoacoustic-Stirling heat engine: detailed study. *J Acoust Soc Am* 2000;107:3148–66.
- [13] Idelchik IE. Handbook of hydraulic resistance. 3rd ed. New York: Begell House; 1996.
- [14] Morris PJ, Boluriaan S, Shieh CM. Numerical simulation of minor losses due to a sudden contraction and expansion in high amplitude acoustic resonators. *Acta Acust United with Acust* 2004;90:393–409.
- [15] Wakeland RS, Keolian RM. Influence of velocity profile nonuniformity on minor losses for flow exiting thermoacoustic heat exchangers. *J Acoust Soc Am* 2002;112:1249–52.
- [16] Smith BL, Swift GW. Power dissipation and time-averaged pressure in oscillating flow through a sudden area change. *J Acoust Soc Am* 2003;113:2455–63.
- [17] Petculescu G, Wilen LA. Oscillatory flow in jet pumps: nonlinear effects and minor losses. *J Acoust Soc Am* 2003;113:1282–92.
- [18] Doller A. Acoustic minor losses in high amplitude resonators with single-sided junction. Ph.D. Dissertation, PennState University; 2004.
- [19] Swift GW. Thermoacoustics: a unifying perspective for some engines and refrigerators. Melville: Acoustical Society of America; 2002.

## Chapter 5

# **PIV studies of coherent structures generated at the end of a stack of parallel plates in a standing wave acoustic field**

by **X. Mao**, Z. Yu, A. J. Jaworski and D. Marx

Published in *Experiments in Fluids*

# PIV studies of coherent structures generated at the end of a stack of parallel plates in a standing wave acoustic field

Xiaoan Mao · Zhibin Yu ·  
Artur J. Jaworski · David Marx

Received: 15 March 2006 / Revised: 27 January 2008 / Accepted: 2 April 2008 / Published online: 25 April 2008  
© Springer-Verlag 2008

**Abstract** Oscillating flow near the end of a stack of parallel plates placed in a standing wave resonator is investigated using particle image velocimetry (PIV). The Reynolds number,  $Re_d$ , based on the plate thickness and the velocity amplitude at the entrance to the stack, is controlled by varying the acoustic excitation (so-called drive ratio) and by using two configurations of the stacks. As the Reynolds number changes, a range of distinct flow patterns is reported for the fluid being ejected from the stack. Symmetrical and asymmetrical vortex shedding phenomena are shown and two distinct modes of generating “vortex streets” are identified.

## 1 Introduction

Flow structures generated by steady flows past bluff bodies have been a subject of many theoretical and experimental studies, the classic example being formation of the von Karman “vortex street” behind circular cylinders (Kovasznay 1949). This class of phenomena is important in many industrial problems including: aerospace flows, civil and marine engineering, design of heat exchangers or the behaviour of overhead power cables. Somewhat more complex situation arises when steady flows are replaced by oscillatory flows (with or without the steady component),

the fundamental difference being that vortices shed in one half of the cycle impinge on the bluff body when the flow reverses and may interact with vortices shed during the other half of the cycle. This may lead to interesting “lock-on” effects resulting in an interaction between the flow and the structural components within (Chung and Kang 2003; Barbi et al. 1986).

Within the class of purely oscillatory flows, by far the most studied geometrical configurations were flows past circular cylinders (Obasaju et al. 1988; Iliadis and Anagnostopoulos 1998) although other geometries have been considered including a square cross-section (inclined at various angles to the flow) or a flat plate perpendicular to the flow (Bearman et al. 1985; Okajima et al. 1997) and triangular and T-shaped geometries (Al-Asmi and Castro 1992). Other studies investigated the effects of the proximity of the external boundaries on the flow (Sumer et al. 1991). “External” flows as well as “internal” oscillatory flows have been investigated. These include oscillatory flows in pipes with “wavy” walls (Ralph 1986), internally placed orifices (De Bernardinis et al. 1981) or internally baffled channels (Roberts and Mackley 1996).

It is widely accepted that the morphology of the flow structures present within oscillatory flows is governed by three similarity numbers: the Reynolds number ( $Re$ ), the Keulegan-Carpenter number ( $KC$ ) and the Stokes number ( $\beta$ ), although only two out of these are really independent, as Stokes number can be expressed as the ratio of Reynolds number to  $KC$  number. Tatsuno and Bearman (1990) studied the morphology of the flows generated from the oscillatory cylinder as a function of  $KC$  and  $\beta$  while similar studies were performed by Okajima et al. (1997) for square cylinders. These have shown a range of flow regimes ranging from fully attached symmetrical pair of vortices through to symmetrical and alternating vortex shedding.

X. Mao · Z. Yu · A. J. Jaworski (✉) · D. Marx  
School of Mechanical, Aerospace and Civil Engineering,  
The University of Manchester, Sackville Street, PO Box 88,  
Manchester M60 1QD, UK  
e-mail: a.jaworski@manchester.ac.uk

In all of the experimental studies mentioned above, the typical setup includes either the bluff body being oscillated through the stationary fluid, using some form of mechanical drive, or an oscillating incompressible fluid within U-tube type of water tunnel, with the bluff body being held stationary. However, it should be noted that similar flow problems including vortex shedding phenomena also arise in acoustic systems when the level of acoustic excitation is relatively high. These include systems such as pulse tube refrigerators, standing or travelling wave thermoacoustic devices or their components such as jet pumps, Stirling engines and refrigerators and others, where high intensity acoustic wave (or oscillatory flows in general) encounter sudden discontinuities in the cross-section of an acoustic duct.

The initial motivation for the current paper came from the need to understand the behaviour of the flow in a standing wave thermoacoustic device in the vicinity of the so called “thermoacoustic core”. This typically comprises of a stack of parallel plates (thermoacoustic stack) sandwiched between two heat exchangers (often also constructed as a set of shorter but thicker parallel plates with a somewhat larger pitch). The role of the thermoacoustic core is to either produce acoustic power due to the temperature gradient imposed by the heat exchangers or to consume externally supplied acoustic power in order to facilitate heat pumping from cold to hot heat exchanger by virtue of the so-called thermoacoustic effect (Swift 2002).

In the high-intensity acoustic field, the flow structures at the end of the stack, or the heat exchanger (or in the region in between) are very complex due to the discontinuities of the cross section and the oscillatory nature of the flow. Clearly, the energy transfer taking place within the thermoacoustic core will be affected by “entrance effects”, vortex shedding and generation (or suppression) of turbulence over different parts of the acoustic cycle. The existing models to calculate the performance of the thermoacoustic systems are based on the linear acoustic models (for example DeltaE, as described by Ward and Swift 2001) with only some corrections being made to account for non-linear acoustics effects such as turbulence. The development of such codes is hindered by the lack of understanding of the fundamental thermal-fluid processes.

Despite being rooted in the area of thermoacoustics, the current investigation should be seen on a more general level, namely the fundamental fluid dynamical processes of interest to a wider audience. This is the reason why the current research covers somewhat larger parameter space than would be expected from the point of view of thermoacoustic stacks alone and covers the range characteristic for finned heat exchangers and possibly beyond.

The experimental studies of the above phenomena in the context of thermoacoustics are very limited. Gopinath and

Harder (2000) studied the heat transfer effects from a single circular cylinder placed in an acoustic resonator (with a possible application to thermoacoustic heat exchangers). They identified two flow regimes: the laminar attached flow regime and the less understood regime where the vortex shedding is prevalent with much higher heat transfer coefficients. Blanc-Benon et al. (2003) used PIV measurements to investigate the flow field around and vortex shedding from a stack of parallel plates for relatively low drive ratios 1.0–1.5% and compared the experimental results to CFD simulations. They have shown the presence of symmetrical vortices, which on their two experimental configurations (“thin” and “thick” plates) took an “elongated” and “concentrated” form, respectively, but never fully detached from the plates. Mao et al. (2005) conducted similar PIV studies using a somewhat larger geometrical arrangement and higher drive ratios (up to 3%) and showed that at higher drive ratios the symmetrical vortices are replaced by alternately shed vortices. The current paper is an extension of this early work by providing more complete experimental data and its more detailed discussion and analysis.

## 2 Experimental apparatus and procedure

The experimental apparatus used in the current study (Fig. 1) was discussed in some detail by Marx et al. (2006) and therefore only a brief description is given here. Its main part is a 7.4-m long transparent Perspex pipe, with the internal cross-section  $134 \times 134$  mm, and the wall thickness of 8 mm. One end of the pipe (to the left of Fig. 1) is closed by an “end-cap” with a flush mounted pressure transducer. The other end is connected to a relatively large “loudspeaker box” ( $600 \times 600 \times 600$  mm) through a 0.3 m long pyramidal section to match the change in cross-sectional dimensions. The resonator is filled with air at atmospheric pressure and room temperature. The first mode of operation (quarter-wavelength) has a fundamental frequency  $f = 13.1$  Hz.

The experiments were conducted for two stacks of plates (shown schematically in Fig. 2). The length,  $l$ , of both stacks was 200 mm, while their width was 132 mm (some clearance had to be left between the stack and the internal resonator wall). Stack I comprised of 21 Perspex plates of thickness  $d = 1.1$  mm with the plate-to-plate spacing  $D = 5$  mm. Stack II was made out of eight Perspex plates with  $d = 5$  mm and  $D = 10$  mm. Both stacks were placed in the resonator 4.1 m from the end as schematically shown in Fig. 1. The drive ratio in the experiments was varied by changing the excitation voltage of the loudspeaker and controlled by measuring the amplitude of pressure oscillations recorded by the dynamic pressure transducer

**Fig. 1** Sketch of the experimental apparatus

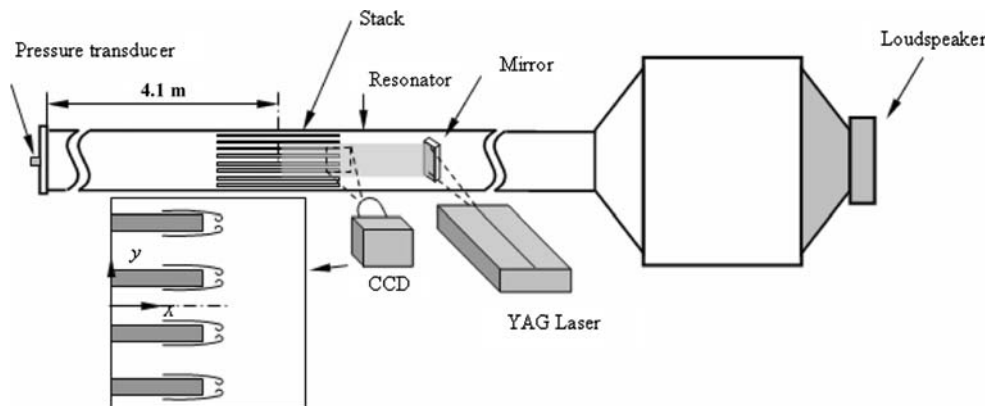
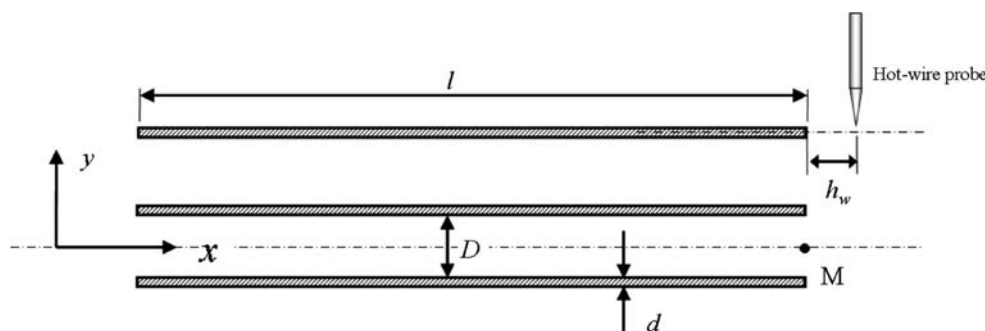


**Fig. 2** Geometry of the stack (only three plates shown)



mounted inside the end-cap of the resonator (Endevco Model 8510B-2).

Flow field measurements were performed using a PIV system by TSI. The light sheet from a dual Nd:YAG laser enters the resonator perpendicular to its axis, is reflected by a small mirror and becomes parallel to the resonator axis and normal to the surface of the stack plates. The flow is seeded by particles produced by a smoke generator using 50–50% mixture of glycerol and water, with typical droplet diameter in the range 1–10 microns. Images are taken by a 4 mega-pixel camera (TSI POWERVIEW) and post processed using commercial software (TSI INSIGHT). Cross correlation is used and the interrogation window is  $16 \times 16$  pixels.

The flow field measurements are performed at 20 phases within the acoustic cycle (i.e. every  $18^\circ$ ). Therefore an appropriate phase locking mechanism had to be developed. In this study the pressure oscillation measured by the pressure transducer mounted at the end cap was used as a reference. The output signal from the pressure transducer is connected to an “in-house” made pulse generator, which can generate a pulse sequence of the same frequency as the acoustic wave, but with variable time delay from the trigger point. The output of the pulse generator is connected to the synchroniser (TSI LASERPULSE) that controls the timing of the laser action and triggers the frame grabbing of camera. In this way, the captured images can be phase locked relative to the pressure oscillation (and by the same token to the

velocity oscillation, which could be verified independently both by PIV and hot wire measurements). Figure 3 illustrates the timing of 20 phases ( $\Phi_1, \Phi_2 \dots \Phi_{20}$ ) within the cycle, relative to both velocity and the pressure gradient oscillations. For each of the 20 phases, 100 pairs of images were taken to derive the phase-averaged velocity field. The field of view of the PIV images varied from  $25 \text{ mm} \times 25 \text{ mm}$  to  $60 \text{ mm} \times 60 \text{ mm}$ , depending on the flow features to be imaged. This corresponds to the resolution of the velocity vector field between 0.10 and 0.23 mm.

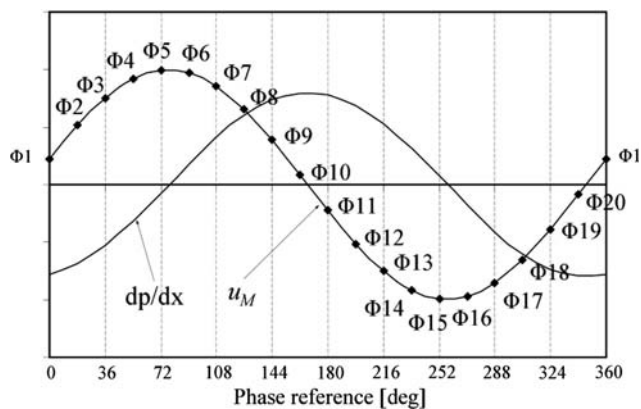


**Fig. 3** Phase-averaged velocity oscillation at point M and corresponding phases at which the PIV measurements are taken.  $dp/dx$  is the axial gradient of acoustic pressure in an oscillation period. (Simple-harmonic oscillation is assumed so that  $dp/dx$  is  $90^\circ$  out of phase of velocity oscillation)

Due to its nature, the PIV technique is not sufficiently “time-resolved” to permit measurements of the fluctuating components of velocity. Therefore the investigations of the vortex shedding frequencies, to be used in estimating typical Strouhal numbers, had to be conducted using standard hot wire methods. Velocity fluctuations were measured with SN type hot-wire probe (DANTEC) operated in the constant-temperature mode using a TSI IFA300 system. The probe is placed normal to the plate, while the sensor is normal to the axis of the resonator. The position of the probe is schematically shown in Fig. 2. For Stack I, the sensor is placed  $2d$  from the edge of the plate, while for Stack II this distance is  $4d$  because the large diameter of the probe support prevents the sensor to be closer to the plate end (the distance from the plate is denoted in Fig. 2 as  $h_w$ ). A high-pass filter set at 30 Hz is used to remove the signal component related to the fundamental frequency of 13.1 Hz. Both the filtered signal and the unfiltered signal are recorded with a sampling frequency of 5,000 Hz. 16,384 data points are acquired in a typical experimental condition.

### 3 Experimental results

#### 3.1 Overview of the experimental parameters and conditions

Table 1 summarises the stack dimensions and the basic acoustic excitation and flow conditions. In addition to stack geometry, the table contains porosity,  $\phi$ , defined as the ratio of the total cross-sectional area of the channels within the stack over the cross-sectional area of the resonator. For a stack of evenly spaced plates, this can be approximated by  $D/(D + d)$ , assuming that the gaps between the stack and the walls can be neglected. Drive ratio,  $D_r$ , is the ratio of the acoustic pressure amplitude at the closed end of the resonator,  $p_{1,c}$ , to the mean pressure in the resonator  $p_m$ . The values of the amplitude of the axial velocity,  $u_M$ , at point M (Fig. 2) were extracted from the phase-averaged velocity field for the 20 phases, by using the least square fitting method for a sinusoidal function.  $\xi$  is the displacement amplitude of the oscillating gas parcel. It can be calculated from  $u_M$  as  $\xi = u_M/\omega$ .

The Reynolds number used in the current analysis,  $Re_d$ , is based on the axial velocity amplitude,  $u_M$ , and the plate thickness,  $d$ , as

$$Re_d = \frac{u_M d}{\nu} \quad (1)$$

where  $\nu$  is the kinematic viscosity of air at ambient conditions. However, as will be shown later, for convenience of comparisons between different phases within the cycle it seems useful to introduce a Reynolds

**Table 1** Summary of stack dimensions and experimental conditions

	$d$ (mm)	$D$ (mm)	$l$ (mm)	$\phi$	$D_r$ (%)	$u_M$ (m/s)	$\xi$ (mm)	$Re_d$
Stack I	1.1	5.0	200	0.82	0.3	0.84	10.2	62
					0.6	1.68	20.4	123
					1.0	2.82	34.3	207
					1.5	4.32	52.5	317
					2.0	5.68	69.0	417
Stack II	5.0	10.0	200	0.67	0.3	0.95	11.5	317
					0.6	1.95	23.7	650
					1.0	3.24	39.4	1080
					1.5	5.04	61.2	1680
					2.0	6.90	83.8	2300

number based on the instantaneous value of velocity,  $u_M^*$ , at point M (later referred to as “phase Reynolds number”):

$$Re_d^* = \frac{u_M^* d}{\nu} \quad (2)$$

Of course,  $u_M^* = u_M \sin(\omega t + \theta)$ , but  $\theta$  could be zero, if one chooses to count the time from the moment when  $u_M^* = 0$ . Similarly, although strictly  $Re_d^*$  can be either positive or negative (depending on the direction of  $u_M^*$ ), it is easy to specify the flow as “out of the stack” and “into the stack” to avoid confusion. Of course, the relationship between the two Reynolds numbers is

$$Re_d^* = Re_d \sin(\omega t + \theta). \quad (3)$$

It is worth making two comments at this point: Firstly, introducing “phase Reynolds numbers” is not an entirely new idea. Yellin (1966) considered flow transition in pulsatile flows within blood vessels and used an analogue of  $Re_d^*$  defined here. Secondly, as will become clearer in later sections (especially 4.2 and 4.3) Reynolds number cannot be a unique similarity number defining the oscillatory flow behaviour in general. This should be remembered when looking at labelling of the experimental data which is made using Reynolds numbers defined by Eqs. (1) and (2).

#### 3.2 Oscillatory flow around the end of the stack

Figure 4 represents a typical example of the flow visualisation obtained in the oscillatory flow near the end of the stack, shown here to illustrate its main features. Here the flow past Stack I was investigated at the drive ratio of 1.0%, giving the Reynolds number  $Re_d = 207$  (other relevant parameters can be found in Table 1). The flow features are visualised by using the phase-averaged vorticity field. For brevity, only nine most characteristic phases are selected out of the 20 phases captured within the cycle. These are shown as a time sequence to illustrate the evolution of the flow structures. The phase Reynolds

number,  $Re_d^*$ , is included in the graphs; grey areas indicate the presence of the plates within the imaging domain.

As can be seen from Fig. 4, the flow can be divided into two main stages: the “ejection” stage, when the velocity at point M is toward  $x > 0$  (i.e. for phases  $\Phi 1$ – $\Phi 10$  as illustrated in Fig. 3) and the “suction” phase, when the velocity at point M is toward  $x < 0$  (i.e. for phases  $\Phi 11$ – $\Phi 20$  as illustrated in Fig. 3). As can be seen the generation of coherent structures takes place in the “ejection” stage discussed in Sect. 3.2.1.

### 3.2.1 Ejection stage

In general the ejection stage can be further subdivided into two different situations: acceleration stage (phases  $\Phi 1$ – $\Phi 5$ ) and deceleration stage (phases  $\Phi 6$ – $\Phi 10$ ). Several characteristic flow phenomena/patterns can be observed: (A) Formation of a pair of attached symmetric vortices; (B) Elongated vortex structures; (C) Break-up of elongated vortices into an asymmetric “vortex street”; (D) Alternate vortex shedding from the end of the plate. The details of

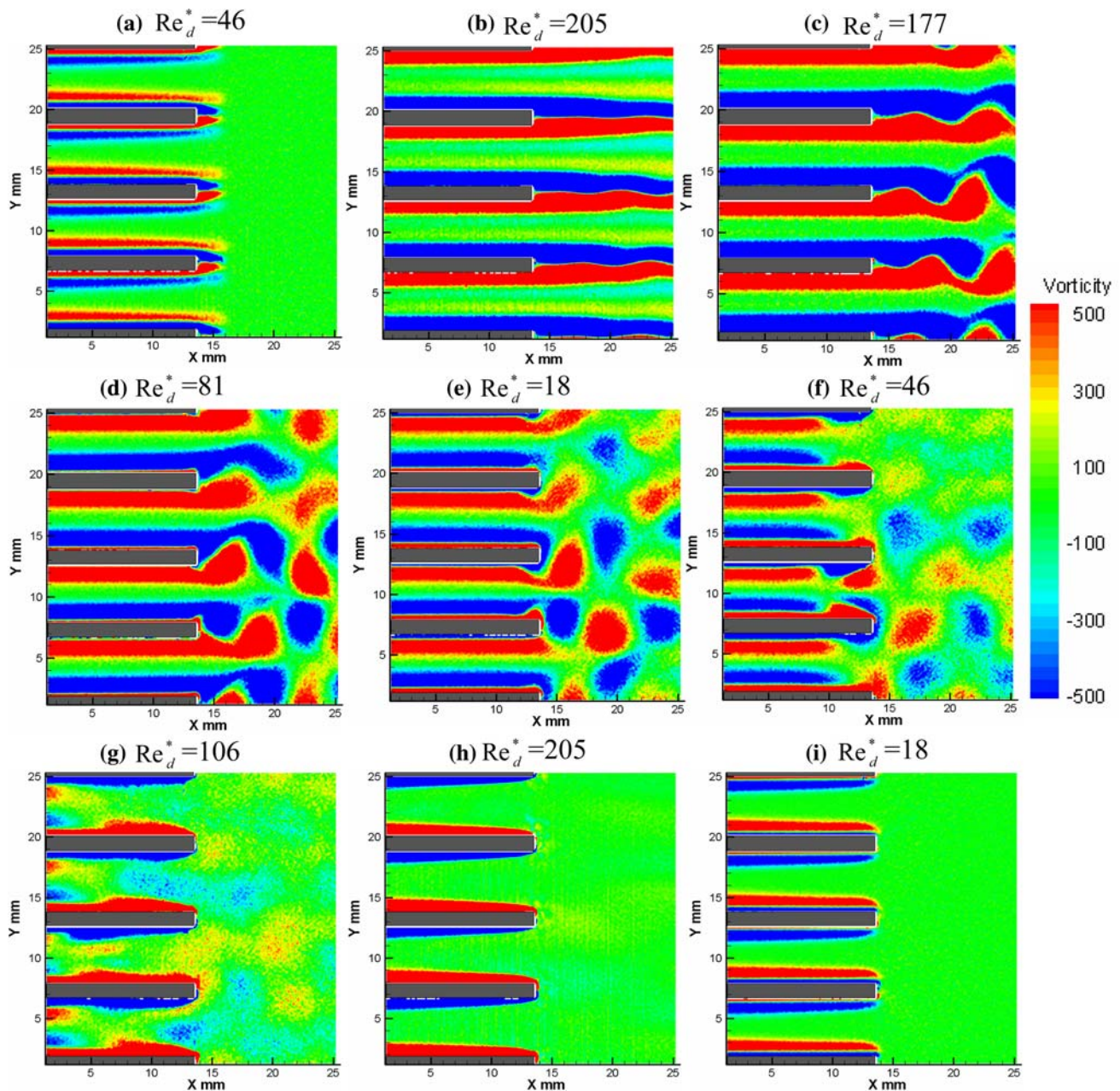


**Fig. 4** Vorticity contour map for the flow around the end of Stack I during one acoustic cycle. **a**  $\Phi 1$ , **b**  $\Phi 5$ , **c**  $\Phi 7$ , **d**  $\Phi 9$ , **e**  $\Phi 10$ , **f**  $\Phi 11$ , **g**  $\Phi 12$ , **h**  $\Phi 15$ , **i**  $\Phi 20$  ( $Re_d = 207$ ,  $D_r = 1.0\%$ ). The unit of vorticity legend is  $s^{-1}$

these characteristic flow patterns are described with reference to Fig. 4a–e.

**3.2.1.1 Formation of a pair of attached symmetric vortices** The flow in phase  $\Phi 1$  (Fig. 4a) has a positive velocity and starts to accelerate. Based on the instantaneous velocity at point M, the corresponding phase Reynolds number,  $Re_d^*$ , is about 47. A pair of vortex structures is formed at the end the plate. They are symmetrical relative to the centre-line of the plate in the  $x$ - $y$  plane. Similarly as in the classic case of the wake behind a plate with a square trailing edge (as found in Bachelor 2000), a recirculation region is formed at the end of the plate, where the pair of vortices remains attached. In the inner region of the channel formed by two neighbouring plates, there is a pair of shear layers with their vorticity in an opposite direction to the vorticity within the plate boundary layer.

Such a shear flow pattern exhibited in this phase is directly related to the typical velocity profile shown in Fig. 5a (taken at  $x = 5$  mm according to the coordinate system used in Fig. 4). The velocity oscillation of the flow in the central region is delayed in phase, compared with the flow in the boundary layer region. A peak value of velocity appears at some distance from the plate.

**3.2.1.2 Elongated vortex structures** As the velocity increases due to the flow acceleration the related phase Reynolds number increases and the flow pattern changes accordingly. At first (during phases  $\Phi 2$ – $\Phi 4$ ) the attached vortex structures remain symmetric but become elongated. However, as the velocity almost reaches its peak around phase  $\Phi 5$ , the very elongated vortex structures in the wake become “asymmetric” by exhibiting somewhat wavy pattern (as shown in Fig. 4b), which seems to be related to the loss of stability in the subsequent phases. The phase Reynolds number,  $Re_d^*$ , is about 206. Within the channel, the axial velocity profile changes significantly between phases  $\Phi 1$ – $\Phi 5$  by becoming flattened (Fig. 5b). The flow velocity

in the central region catches up with the velocity closer to the channel walls, which weakens the vorticity in this central region.

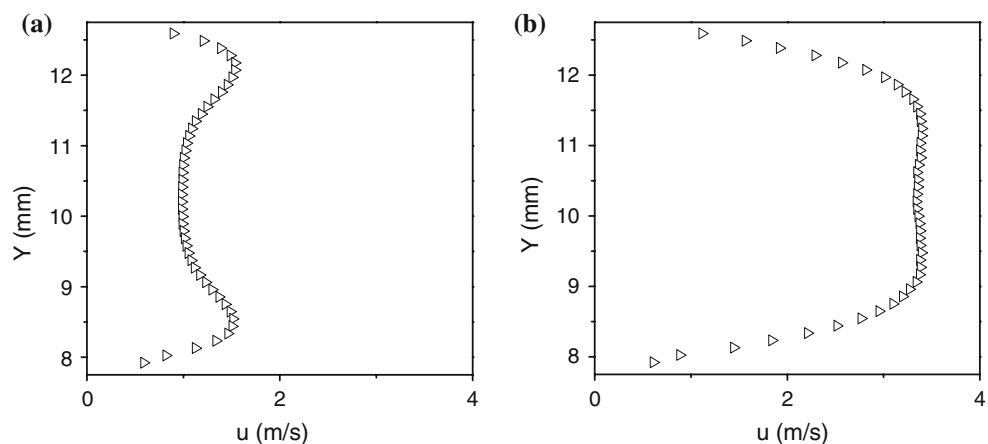
**3.2.1.3 Break-up of elongated vortices into an asymmetric “vortex street”** As illustrated in Fig. 3, velocity of the fluid leaving the channels of the stack reaches its maximum between  $\Phi 5$  and  $\Phi 6$  and so from then on the fluid enters the deceleration phase. Figure 4c ( $\Phi 7$ ) shows that the pair of elongated vortex structures has broken up into a “street” of individual vortices in the plate’s wake, very much resembling the classical von Karman street. At phase  $\Phi 7$ , the corresponding phase Reynolds number,  $Re_d^*$ , is about 177.

**3.2.1.4 Alternate vortex shedding from the end of the plate** Once the elongated vortex structures have broken up into the “street” of individual vortices, a different mechanism seems to take over, namely the vortices seem to be shed in an alternating fashion from the end of the plate in a manner resembling the classical bluff body vortex shedding. Figure 4d shows the resulting flow pattern for phase  $\Phi 9$  for the corresponding phase Reynolds number,  $Re_d^*$ , around 81. The flow slows down even further, and Fig. 4e shows an almost stationary “suspended” vortex pattern just before the flow reverses ( $\Phi 10$ ,  $Re_d^* = 18$ ).

### 3.2.2 Suction stage

As shown in Fig. 3, the direction of the flow reverses between phases  $\Phi 10$  and  $\Phi 11$ . The fluid and the vortex structures generated in the ejection stage are to be sucked back into the channels between the plates. Figure 4f (phase  $\Phi 11$ ) shows the beginning of such a process. The remains of the vortex street impinge on the end of the plate, the individual vortices becoming split into a series of vortices of much smaller size. The shear layers close to the channel walls are pushed away (displaced) further into the central region of the channel by the continually developing shear

**Fig. 5** Transverse profile of axial velocity taken at  $x = 5$  mm. Stack I, drive ratio 1%. **a**  $\Phi 1$ , **b**  $\Phi 5$ . ( $Y$  remains the same as the coordinate system used in Fig. 4)



layers in an opposite direction—see the channels in Fig. 4f. In addition, in the region near the end of the plate, the entry flow generates a strong shear region, which pushes back (eliminates) the shear layer formed in the ejection stage of the cycle.

In Fig. 4g ( $\Phi_{12}$ ), the displaced shear layer (which was originally formed in the ejection stage) and the scattered remains of the small vortices finally die out. The newly generated shear layer corresponding to the direction of the suction flow grows and develops.

In Fig. 4h ( $\Phi_{15}$ ), the negative flow velocity is at its peak value. The unsteadiness of the shear layer still visible in Fig. 4g and the scattered remains of the weak vortices close to the channel centre have disappeared. In general the shear layer next to the surface of the plates is quite similar with the developing boundary layer on a flat plate in the steady flow.

Following phase  $\Phi_{15}$  the suction flow starts to decelerate and the negative velocity approaches zero at about  $\Phi_{20}$  (see Fig. 4i). The flow direction is about to change, when the flow enters the ejection stage of the next cycle.

### 3.3 Comparisons between flows at various peak Reynolds numbers, $Re_d$

To gain further insight into the Reynolds number effects on the flow structure, the flow around the end of the stack was

studied at four more drive ratios (0.3, 0.6, 1.5 and 2.0%). In this section, the discussion will focus on the flow structures in the ejecting stages for varying drive ratios.

To save space, the PIV results are shown for a single plate, not an array of plates as previously shown in Fig. 4. Figure 6 shows the flow visualisations for five drive ratios studied (Fig. 6a–e), however instead of using drive ratios, the figures are labelled with the values of Reynolds number,  $Re_d$ , which is more meaningful from fluid mechanics point of view. In each of the figures, the images for five selected phases are shown:  $\Phi_2$ ,  $\Phi_4$ ,  $\Phi_6$ ,  $\Phi_7$  and  $\Phi_9$ , each image also being labelled with the value of the phase Reynolds number— $Re_d^*$ .

In the simplest approach, one can compare the evolution of the flow patterns during the ejecting stage for different drive ratios (different  $Re_d$ ) by looking at each column in Fig. 6 (i.e. columns a–e). However, one could also imagine a “flow pattern evolution” by looking at a selected phase in the cycle (for example  $\Phi_4$ ) and comparing the flow patterns for varying drive ratios (i.e.  $Re_d$ ). To do this one would have to inspect each row of Fig. 6 (rather than each column). In this way one could try to develop a relationship between the flow patterns and the phase Reynolds number,  $Re_d^*$ .

Figure 6a shows the results at drive ratio 0.3% ( $Re_d = 62$ ). It can be seen that a pair of vortex structures remains attached to the end of the plate in each phase and

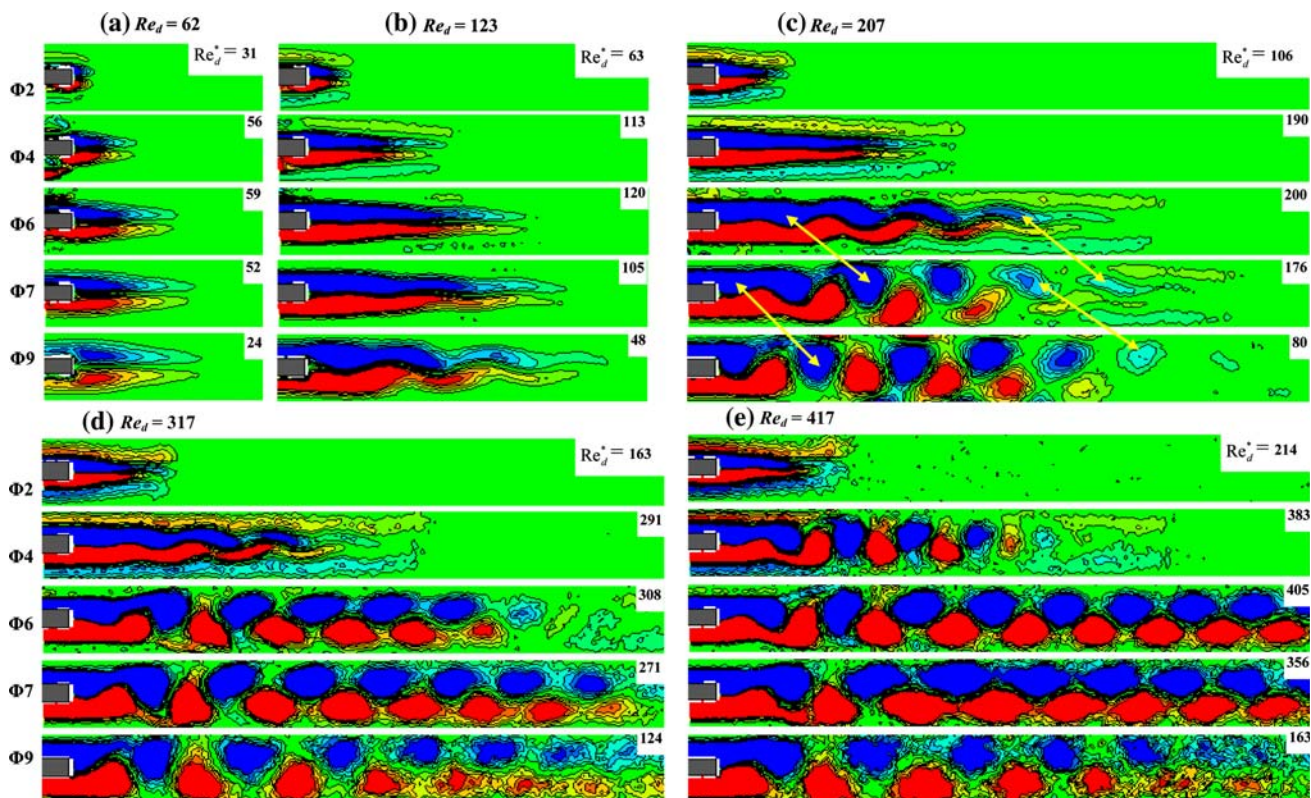


**Fig. 6** Vorticity field around the end of one plate in Stack I, shown for five drive ratios and five selected phases within the cycle; **a**  $D_r = 0.3\%$ ; **b**  $D_r = 0.6\%$ ; **c**  $D_r = 1.0\%$ ; **d**  $D_r = 1.5\%$ ; **e**  $D_r = 2.0\%$ ; colour scale is the same as for Fig. 4

remains symmetric relative to the centre line in all phases. The size and strength of the vortices clearly increases as the phase Reynolds number increases throughout the accelerating stage (see  $\Phi 2$  and  $\Phi 4$ ) and increases further in the decelerating flow up until phases  $\Phi 6$  or  $\Phi 7$ . As the vorticity fed from the plate boundary layer decreases, so does the strength of the vortices (see  $\Phi 9$ ).

Figure 6b shows the results at drive ratio 0.6% ( $Re_d = 123$ ). Compared with the vortex structures in Fig. 6a, the vortices become more and more elongated in the accelerating stage. Eventually (around phase  $\Phi 7$ ), the previously symmetrical structures become wavy and this “instability” amplifies in the deceleration phase (see the asymmetric wavy structure in phase  $\Phi 9$ ).

Figure 6c shows the results at drive ratio 1.0% ( $Re_d = 207$ ). They correspond to the results already shown in Fig. 4. From both figures, one can find that the vortex structure exhibits asymmetry in phases  $\Phi 5$  and  $\Phi 6$ , that is at an earlier phase than in Fig. 6b. The break-up of this wavy pattern into a vortex “street” and subsequent shedding from the plate occurs between phases  $\Phi 7$  and  $\Phi 9$ .

Quite similar results can be seen in Fig. 6d, for drive ratio 1.5% ( $Re_d = 317$ ). The vortex structures become unstable even earlier ( $\Phi 4$ ). Further increase of drive ratio, as illustrated in Fig. 6e (2.0%,  $Re_d = 417$ ), leads to even earlier break-up of the initial symmetrical structures—by phase  $\Phi 4$  a vortex “street” is already in place).

One could attempt a qualitative analysis by comparing images in Fig. 6 “row by row”; that is by looking at increasing drive ratios for a fixed phase. For example, the first row of figures shows phase  $\Phi 2$ . From Fig. 6a to Fig. 6e the phase Reynolds number increases from 31 to 214. One can find that, the attached pair of vortices elongates, but remains symmetric as the phase Reynolds number increases.

The second row of figures shows the “flow behaviour” for phase  $\Phi 4$ , as the phase Reynolds number increases from 56 to 383. One can clearly see an “evolution” of the flow patterns similar to phase-by-phase evolution: a pair of symmetric vortices (6a/ $\Phi 4$ ), elongated symmetric vortices (6b/ $\Phi 4$  and 6c/ $\Phi 4$ ) unstable/wavy elongated structure (6d/ $\Phi 4$ ) and alternate vortex shedding (6e/ $\Phi 4$ ).

The third, fourth and fifth rows show the flow pattern “evolution” for phases  $\Phi 6$ ,  $\Phi 7$  and  $\Phi 9$ , respectively. Similar trends in the “development” of the flow patterns can be observed. However, clearly, the vortex shedding pattern is present “earlier” when comparing drive ratios left to right.

### 3.4 Comparisons between flows around Stack I and Stack II

Similar experiments to those described with reference to Stack I were carried out for the second configuration: Stack

II (see Table 1 for details). The main reason for selecting this configuration was a further increase in the Reynolds number ( $Re_d$ ) and a change in the porosity of the stack. The same drive ratios were tested which, given a different porosity, resulted in somewhat modified velocities and displacements. The Reynolds numbers were increased roughly about five-fold.

Figure 7 shows the vorticity field around the end of one plate in Stack II (keeping the convention of Fig. 6, for Stack I). Results at five phases of the ejection stage are presented for the stack at the five drive ratios tested, corresponding to the Reynolds number  $Re_d$  of 317, 650, 1080, 1680 and 2300.

By comparing the flow around the end of plate in Figs. 6d and 7a, one can see that the value of  $Re_d$  in both cases is the same: 317. However, instead of an elongated vortex structure which breaks-up into a vortex “street” which was the main feature for Stack I, Stack II exhibits a different flow structure, namely a fully attached and symmetrical pair of vortices, somewhat similar to what was observed for drive ratio 0.3% on Stack I. However, for Stack II, the pair of vortices is much less elongated in the stream-wise direction (only about  $1d$  in terms of plate thickness).

Increasing  $Re_d$  to 650 leads to the vortex structures becoming asymmetric (see phase  $\Phi 9$  in Fig. 7b). This feature is more pronounced for  $Re_d = 1080$ —see phases  $\Phi 6$  to  $\Phi 9$  in Fig. 7c. Measurements at even higher drive ratios (Fig. 7d, e), show that the higher  $Re_d$ , the earlier in the cycle the asymmetric vortex shedding takes place. It is interesting to note that for Stack II, the two flow patterns at the ejection stage described under (B) and (C) in Sect. 3.2.1 (elongated vortex structures and their break-up) are absent.

Another interesting flow feature is the appearance of a pair of “counter-rotating” vortices, relative to the sense of rotation of the main vortices shed from the plate. The initial formation of these vortices is clearly seen for phase  $\Phi 2$  in Fig. 7a–e. These “counter-rotating” vortices seem to be convected far away from the plate, preceding the dominating von Karman-type of vortices subsequently shed over the ejection stage of the cycle. By phase  $\Phi 9$ , the vorticity of this pair of “counter rotating” vortices is practically dissipated. These small vortices seem to originate from the remains of the shear layer formed during the suction cycle. Similar feature is indeed present for Stack I, but has a much more elongated shape and is far less “concentrated” in terms of vorticity levels (see for example phase  $\Phi 4$  in Fig. 6d).

In summary, it seems that the main difference in the flow behaviour on two stacks investigated (I and II) is the mode of vortex shedding. While Stack I is dominated by elongated shear layers, which then suddenly break up into a “street” of individual vortices, Stack II exhibits alternate

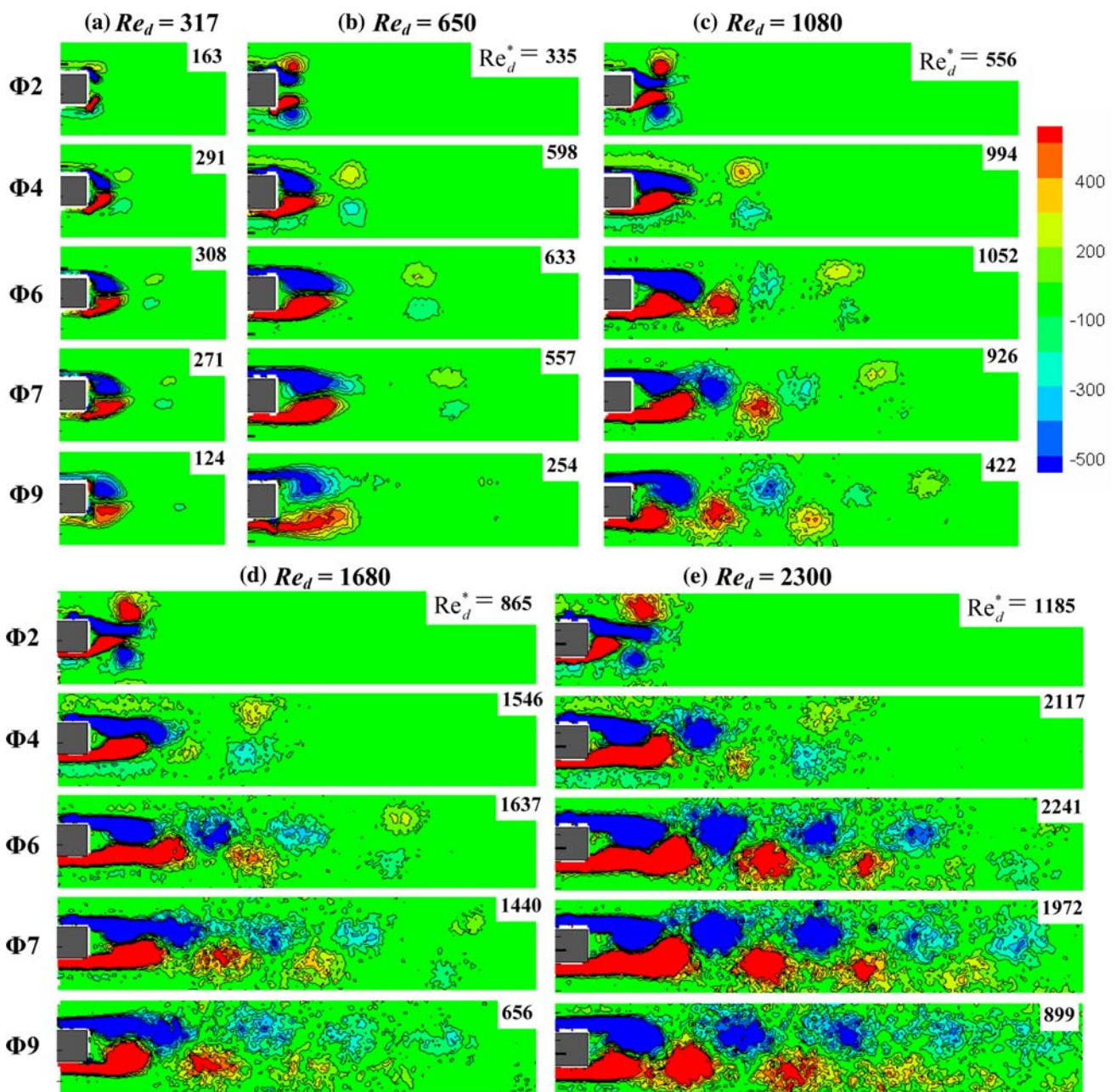


**Fig. 7** Vorticity field for the flow around the end of Stack II. **a**  $D_r = 0.3\%$ ; **b**  $D_r = 0.6\%$ ; **c**  $D_r = 1.0\%$ ; **d**  $D_r = 1.5\%$ ; **e**  $D_r = 2.0\%$

(bluff-body type) shedding very early on within the cycle (as long as the Reynolds number is large enough). This may well be responsible for the differences in Strouhal numbers discussed in Sect. 3.5.

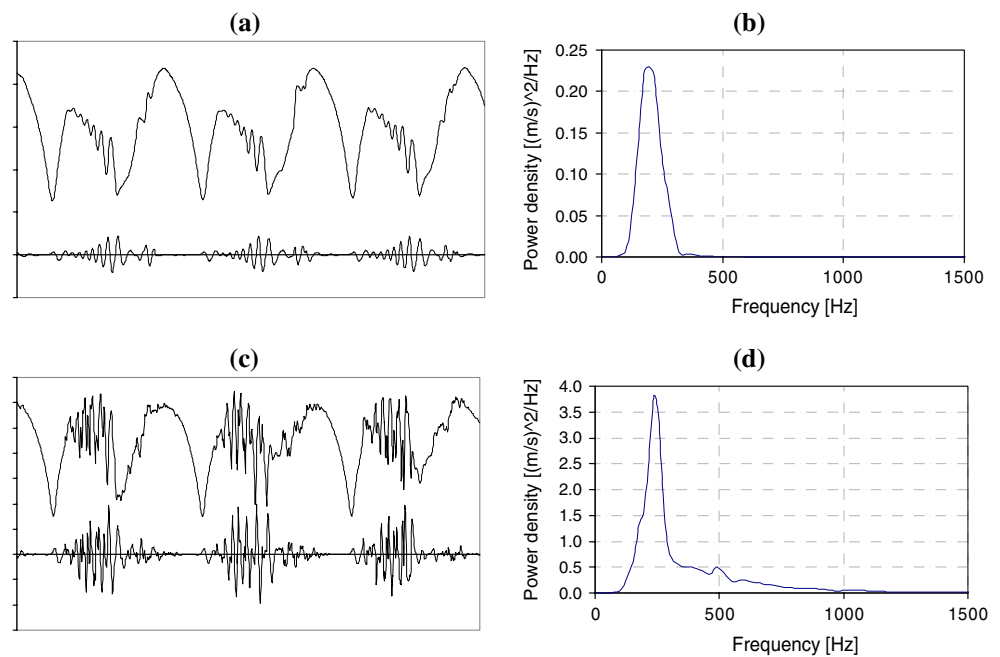
### 3.5 Frequency of vortex shedding

As illustrated in the previous sections, for both stacks, the vortices will start to shed in an alternate fashion for a sufficiently large Reynolds number,  $Re_d$ . This behaviour is similar to vortex shedding from bluff bodies in steady

flows. This part of the study looked at the dependence of vortex shedding frequency (and thus the Strouhal number) on the Reynolds number,  $Re_d$ , and the geometry of the stack. The measurements were performed using standard hot-wire anemometry methods (Sect. 2) in order to collect the fluctuating velocity signal behind the stack of plates.

Typical signal traces of the hot-wire anemometer output are shown in Fig. 8a and Fig. 8c for Stack I and Stack II, respectively. The top signal trace represents the unfiltered signal and the bottom one represents the filtered signal. Each “fluctuation burst” in the bottom signal trace

**Fig. 8** Signal trace of hot-wire sensor output close to the stack end, and the frequency spectrum of the signal trace; **a, b** Stack I ( $D_r = 1.0\%$ ;  $u_M = 2.7$  m/s;  $Re_d = 194$ ); **c, d** Stack II ( $D_r = 2.0\%$ ;  $u_M = 6.5$  m/s;  $Re_d = 2165$ )



represents an event of vortex shedding in the ejection stage of the acoustic cycle.

The frequency spectrum of the filtered signal trace is analyzed using Fast Fourier Transform (FFT). The signal trace is divided into data blocks, which contain 256 data points, starting at the same phase of an acoustic cycle, and including the whole “fluctuation burst” event. For each block of data, a frequency spectrum is obtained. Subsequently all such frequency spectra, obtained for a given experimental run, are ensemble-averaged and a mean frequency spectrum is obtained. This enables extracting a characteristic peak frequency. Figure 8b, d shows the mean frequency spectra of the corresponding signal traces in the left column of Fig. 8. As can be seen from the plots, the curve covers a narrow band of frequencies, as opposed to a sharp spike which would normally be obtained in steady flows past bluff bodies. This is most likely due to variations in the shedding frequency as the instantaneous velocity  $u_M$  changes over the ejection stage, but it may also reflect the fact that vortex shedding is “quasi-periodic” with the pattern changing slightly from cycle to cycle.

The peak frequency is subsequently used to calculate the values of Strouhal number,  $St$  defined here as  $f_{SH} d/u_M$ . Symbol  $f_{SH}$  is used to denote the “shedding frequency” (such as depicted in Fig. 8.) and to distinguish it from the rig’s operating frequency  $f = 13.1$  Hz.  $u_M$  is also used to calculate the corresponding values of  $Re_d$ . As shown in Fig. 9, for the cases investigated, the Strouhal number is between 0.18 and 0.20 for Stack II, and between 0.08 and 0.10 for Stack I. As already mentioned this difference between the values of the Strouhal number could be related to different phenomena that seem to govern the vortex

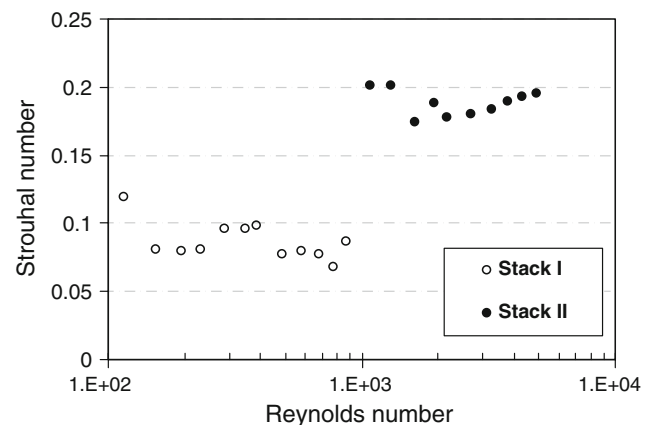


**Fig. 9** Strouhal number,  $St$ , versus Reynolds number,  $Re_d$ , based on the plate thickness

structure formation: a loss of stability of elongated shear layers for Stack I and bluff-body type of shedding for Stack II.

#### 4 Discussion of results and direction of further studies

This discussion section highlights some interesting problems in three areas that the current investigation touched upon: the issue of the interaction of the vortex structures originating from adjacent channels with each other, the somewhat paradoxical issue of the influence of the Reynolds number on the flow patterns for Stack I, and finally the effects of stack geometry. These are discussed in the three sub-sections below.

#### 4.1 “Mirror” versus “translational” symmetries between adjacent vortex streets

When inspecting the flow patterns generated by the stack of plates such as those shown in Fig. 4d, e, it is clear that the resulting vortex “streets” may exhibit either “mirror” or “translational” symmetries in relation to the channels’ centrelines. For example, looking at Fig. 4d, and counting the channels from the bottom of the graph, it is clear that for the first and second channels, the vortex streets have “mirror” symmetries, relative to the channel centre-line. However, for the third channel the symmetry is “translational” (or there is an “anti-symmetry”) in that the vortex pattern shed from the third plate could be overlapped with the vortex pattern shed from the fourth plate if the image was simply shifted upwards. It should be noted that similar problems are encountered in the steady flows past an array of plates (e.g. Guillaume and LaRue 2002). The future studies should investigate how the spacing between the plates within the stack influences this kind of symmetrical or anti-symmetrical alignment of vortices, and whether there is some kind of a “lock-on” effect when the plates are sufficiently close to one another. This relates to the question of porosity values addressed in Sect. 4.3.

#### 4.2 Reynolds number paradox

When Fig. 6 is studied “row-by-row”, that is for different drive ratios, but the same phase, one can see that as the phase Reynolds number increases the flow pattern “evolves” through the stages that are described as (A)–(D) in Sect. 3.2.1. The latter pattern (D) occurs at higher phase Reynolds number than patterns (A)–(C). However, when the flow patterns are studied “column-by-column”, that is for different phase Reynolds numbers within the same drive ratio, the relationship between the flow pattern and the phase Reynolds number is somewhat different. For example in Fig. 6c, the flow becomes unstable at  $\Phi 6$  ( $Re_d^* = 200$ ), and the vortex shedding is observed at  $\Phi 7$  ( $Re_d^* = 176$ ) and  $\Phi 9$  ( $Re_d^* = 80$ ). This indicates that the flow pattern that usually corresponds to a high Reynolds at an earlier phase can take place at a lower Reynolds number in the decelerating stage. One can find more examples of this phenomenon in Fig. 6. In Fig. 6e,  $Re_d^*$  is 214 at  $\Phi 2$ , and the flow has a pair of elongated symmetric vortex structure. On the other hand, in Fig. 6b,  $Re_d^*$  equals 48 at  $\Phi 9$ , and the flow shows a pair of elongated wavy vortices. This clearly illustrates that the transition between different flow patterns cannot be defined by Reynolds numbers alone.

There are at least two explanations for this flow behaviour (referred to here for brevity as “Reynolds number paradox”). The first factor could be the oscillating pressure gradient. It is well known that a favourable

pressure gradient (responsible for the flow acceleration) tends to suppress flow instabilities, while the adverse pressure gradient (responsible for the flow deceleration) tends to amplify them (e.g. Lee and Budwig 1991). This may explain why the vortex structures represented in Fig. 6c break up into a vortex street after phase  $\Phi 6$ . However, an alternative explanation could be found for the flows with higher Reynolds numbers (e.g. Fig. 6d, e, where the break-up occurs in the accelerating phase): namely that the vorticity generated on the surface of the plates is too strong to be convected downstream in the form of an elongated vortex structure and breaks-up so that the flow may assume a more efficient form (vortex street) to convect the vorticity downstream. It is likely that it is the combination of these two factors that decides on the exact nature of the transition between the flow patterns. These aspects of the flow could be studied by means of a rigorous flow stability analysis, which however is somewhat beyond the scope of the current experimental studies.

#### 4.3 Similarity issues—geometry and flow parameters

The geometry of a stack of parallel plates (in the 2D “cross-sectional” sense) can be described by three parameters: the plate thickness,  $d$ , the spacing between plates,  $D$  and the length of plates,  $l$ . In all tests presented here, the displacement amplitude of the oscillating gas parcel,  $\xi$ , is much smaller than the length of the plates  $l$ . Therefore, the effect of the stack length on the flow around the end of the stack can be neglected (Swift 1988). Furthermore, the stack porosity  $\phi$  can be defined as  $D/(D + d)$ , when the plates of the stack are placed evenly. In this case any two of the three parameters, i.e.  $d$ ,  $D$  and  $\phi$ , can uniquely define the stack geometry.

It is also obvious from the current experimental results that changing the Reynolds number,  $Re_d$ , can drastically change the observed flow patterns. However, a triad of two geometrical parameters and a velocity related parameter (Reynolds number or velocity itself) are not sufficient to define the problem entirely. Indeed a large body of literature related to the oscillatory flows past cylinders (Bearman et al. 1985; Badr et al. 1995; Lin et al. 1996; Iliadis and Anagnostopoulos 1998) suggests that frequency of the forcing flow must appear in the problem description in one form or another. A widely accepted parameter of this kind is Keulegan-Carpenter number (KC), usually defined as (velocity)/(frequency  $\times$  dimension). It is easy to show that this can be expressed here as the ratio of the displacement amplitude to the thickness of the plate,  $\xi/d$ . Of course  $\xi$  can be calculated from  $u_M$  as  $\xi = u_M/\omega$ , where  $\omega = 2\pi f$  is the angular frequency of the acoustic oscillation.

Unfortunately, the data available in the open literature, related to the geometry discussed in this paper (parallel

plates), is rather scarce and thus insufficient to perform meaningful similarity studies. The already mentioned paper by Blanc-Benon et al. (2003) allows extracting two experimental “cases” (which are only for relatively small drive ratios). The current work provides a few more “cases”, but there is no independent data to verify any similarities for larger drive ratios. It is therefore hoped that the current work will motivate other researchers to carry out similar studies in flow rigs of different designs.

Table 2 attempts to compare the experimental parameters between the current study and that of Blanc-Benon et al. (2003) for the situations where the flow visualisations in both studies are relatively similar.

The vorticity field for Stack I and Stack II at the conditions listed in the table is shown in Fig. 10 (with superimposed black arrows indicating the velocity vector). Blanc-Benon et al. (2003) used slightly different measurement protocol: only 16 phases were measured in an acoustic cycle and the phases were counted and labelled in a somewhat different way.

Figure 10a, b shows phases  $\Phi 7$  and  $\Phi 9$ , which seem to be closest to phases  $t_0 + 7T/16$  and  $t_0 + 9T/16$  in Fig. 3 of the paper by Blanc-Benon et al. (2003), related to the flow patterns for their Configuration B. In both situations one can see “elongated” symmetrical vortex structures.

Figure 10c, d shows phases  $\Phi 9$  and  $\Phi 11$ , which seem to be closest to phases  $t_0 + T/4$  and  $t_0 + 3T/8$  in Fig. 2 of the paper by Blanc-Benon et al. (2003), related to the flow patterns for their Configuration A. In both situations one can see more “concentrated” forms of vortices with the length comparable to the plate thickness.

As can be seen from Table 2, KC number has a value of 9.3 for Stack I when the drive ratio,  $D_r$  is 0.3% and 14 for Configuration B. For these two configurations, the vortex structures behind the plates are of a similar elongated form. When the vortex structures are concentrated at the end of plates, such as for Stack II and Configuration A, KC number has a relatively small value of 2.3 for Stack II and 1.4 for Configuration A. Therefore, in addition to the usual choice of the Reynolds number, porosity  $\phi$  and KC number seem to be a promising group of non-dimensional numbers that could be used to describe the effect of the stack geometry on the flow characteristics when an oscillating flow around the end of a stack of parallel plates is considered. Nevertheless further work would be required

(especially in experimenting with different frequencies and characteristic stack dimensions) to extend this kind of comparisons to other flow patterns, especially the alternating shedding that occurs for larger displacement amplitudes.

## 5 Conclusion

In this paper, the flow structures around the end of the stack of parallel plates in the oscillatory flow generated by an acoustic standing wave were investigated using PIV. The flow around two stack configurations was measured for a series of acoustic excitation levels (and thus displacement amplitudes). The resulting flow patterns have been documented and described in some detail. The main findings in this respect are as follows:

1. For the relatively small drive ratios the flow structures already identified by Blanc-Benon et al. (2003) are present within the flow. These include symmetrical and attached pairs of vortices which could be either “elongated” or “concentrated”. However when the drive ratios are increased, other flow patterns exist which lead to alternate type of vortex shedding (similar to von Karman “vortex streets” characteristic for flows past bluff bodies)
2. Two modes of the above mentioned “alternate shedding” were identified on the two stacks considered. The first mode seems to be related to an instability of the elongated shear layers, which leads to their break-up and “fragmentation” into a “vortex street” pattern. The second mode seems to be related to the classical Von Karman “vortex street” typically found in bluff body vortex shedding in steady flows. Interestingly, the two different modes seem to lead to two different values of Strouhal number.

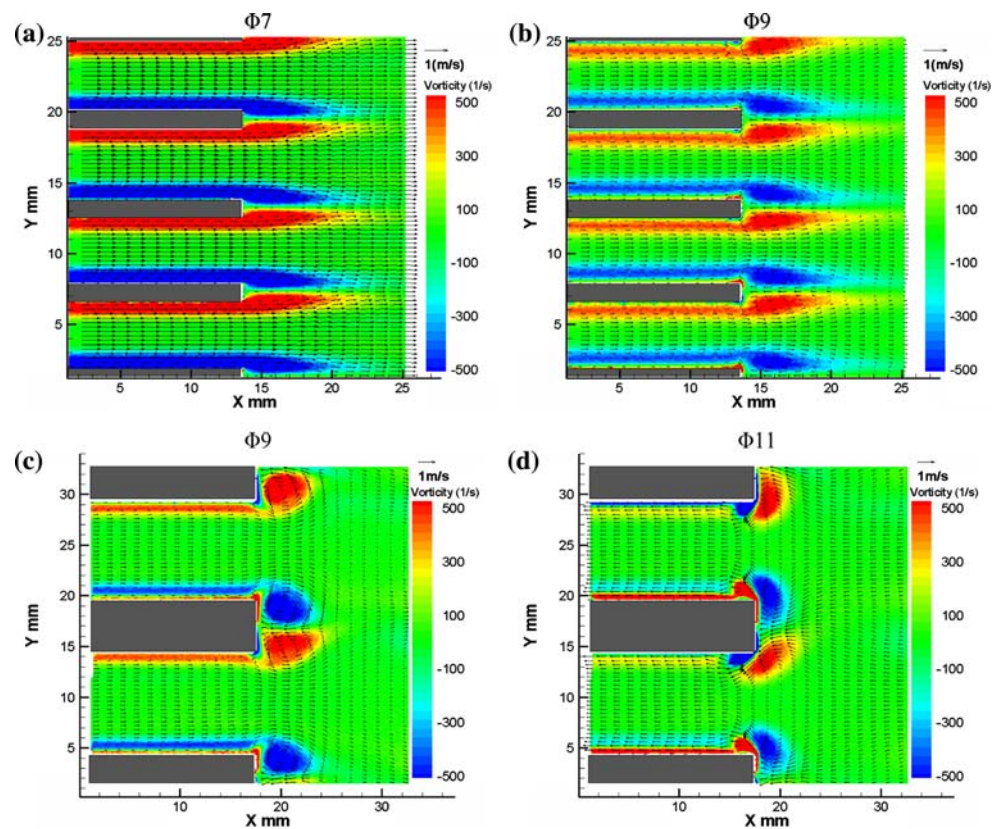
Furthermore, the problem of flow “similarities” was addressed, which was discussed in some detail in the context of the “mirror” and “translational” symmetries and the “Reynolds number paradox”, the latter related to the appearance of seemingly similar flow patterns at different phases of the cycle for different drive ratios on Stack I. It is thought that a rigorous stability analysis would be required to explain this flow behaviour.

**Table 2** Parameters of stack geometry and oscillating flow

	$d$ (mm)	$D$ (mm)	$l$ (mm)	$\phi$	$D_r$ (%)	$u_M$ (m/s)	$\xi$ (mm)	$Re_d$	KC
Stack I	1.1	5.0	200.0	0.82	0.3	0.84	10.2	62	9.3
Stack II	5.0	10.0	200.0	0.67	0.3	0.95	11.5	317	2.3
Configuration A <sup>a</sup>	1.0	2.0	25.8	0.67	1.0	1.71	1.4	119	1.4
Configuration B <sup>a</sup>	0.15	1.0	24.0	0.87	1.5	2.57	2.1	18	14.0

<sup>a</sup> Data adopted from Blanc-Benon et al. (2003)

**Fig. 10** Vorticity field (contour) and velocity field (vector) of the flow at the stack end. **a, b** Stack I ( $D_r = 0.3\%$ ); **c, d** Stack II ( $D_r = 0.3\%$ )



Finally, the results available in the open literature were compared to some of the results of the current work. The comparison showed that, in order to describe the kind of oscillations investigated here, other non-dimensional parameters should be considered, besides the Reynolds number. In particular, KC number has been pointed out as one possible similarity number. The conclusion that a pair of similarity numbers: Re and KC would be required for characterising oscillatory flows is not surprising given that it is known to appear for oscillatory flows past bluff bodies (e.g. the already mentioned works led by Bearman and Graham). However, the current work essentially deals with periodic structures present in the oscillatory flows. Unfortunately, investigations of such cases are few and far between. Research into the flows past multiple (periodic) bluff bodies are nevertheless available for steady (one-directional) cases (e.g. Auger and Coutanceau 1978; Hayashi et al. 1986; Moretti 1993; Le Gal et al. 1996). An additional parameter, to just using a Reynolds number, used in such studies is the ratio of pitch-to-diameter. In the present work a similar approach is adopted by introducing porosity,  $\phi$ , as an independent similarity number (notation  $D/(D + d)$  is in effect an inverse of pitch-to-diameter). Therefore, it seems reasonable to suggest that the triad of similarity numbers: Re, KC and  $\phi$  could be used as a starting point for characterisation of oscillatory flows past periodic structures. Further work to answer some of these important questions is planned.

An interesting point raised by one of the reviewers was related to finding the right scaling parameter for the Strouhal number analysed in Sect. 3.5. In the current work it is based on the plate thickness ( $d$ ), by analogy to bluff body shedding, where typically St is based on the transverse dimension of the body. The reviewer pointed out that there could be an analogy to jet flows made (the “jet diameter” being the spacing between the plates,  $D$ ). Simple experiments consisting of measuring shedding frequencies for stacks which had every other plate removed did not support the reviewer’s suggestion. Shedding frequency did not scale with  $D$  in the configurations studied. Nevertheless, it is possible to imagine that for certain configurations (e.g. very thick plates separated by narrow gaps) plate spacing may be more appropriate for calculating Strouhal numbers, because there would be very little interaction between adjacent “jets”. Selection of the scaling length is somewhat arbitrary (see for example comments by Moretti 1993 regarding flows past “arrays of tubes”), and often counterintuitive. For example Bunderson and Smith (2005) investigate two planar parallel jets, but derive their Strouhal numbers based on the width of the “centre-body” separating the two jets, not on the width of the jets. Clearly, in the case of oscillatory flows past the series of plates such as described in the current paper, a much larger body of data would be required before one could make a more informed choice regarding the best length scales for non-dimensional studies.

**Acknowledgments** The authors would like to acknowledge the support received from the Engineering and Physical Sciences Research Council (EPSRC), UK and Universities, UK.

## References

- Al-Asmi K, Castro IP (1992) Vortex shedding in oscillatory flow: geometrical effects. *Flow Meas Instrum* 3:187–202
- Auger JL, Coutanceau J (1978) On the complex structure of the downstream flow of cylindrical tube rows at various spacings. *Mech Res Commun* 5:297–302
- Bachelor GK (2000) An introduction to fluid dynamics. Cambridge University Press, Cambridge
- Badr HM, Dennis SCR, Kocabiyik S, Nguyen P (1995) Viscous oscillatory flow about a circular cylinder at small to moderate Strouhal number. *J Fluid Mech* 303:215–232
- Barbi C, Favier DP, Maresca CA, Telionis DP (1986) Vortex shedding and lock-on of a circular cylinder in oscillatory flow. *J Fluid Mech* 170:527–544
- Bearman PW, Downie MJ, Graham JMR, Obasaju ED (1985) Forces on cylinders in viscous oscillatory flow at low Keulegan-Carpenter numbers. *J Fluid Mech* 154:337–356
- Blanc-Benon Ph, Besnoin E, Knio O (2003) Experimental and computational visualization of the flow field in a thermoacoustic stack. *C.R. Mecanique* 331:17–24
- Bunderson NE, Smith BL (2005) Passive mixing control of plane parallel jets. *Exp Fluid* 39:66–74
- Chung YJ, Kang SH (2003) A study on the vortex shedding and lock-on behind a square cylinder in an oscillatory incoming flow. *JSME Int J Ser B* 46:250–261
- De Bernardinis B, Graham JMR, Parker KH (1981) Oscillatory flow around disks and through orifices. *J Fluid Mech* 102:279–299
- Gopinath A, Harder DR (2000) An experimental study of heat transfer from a cylinder in low-amplitude zero-mean oscillatory flows. *Int J Heat Mass Transf* 43:505–520
- Guillaume DW, LaRue JC (2002) Comparison of the numerical and experimental flowfield downstream of a plate array. *Trans ASME J Fluid Eng* 124:284–286
- Hayashi M, Sakurai A, Ohya J (1986) Wake interference of a row of normal flat plates arranged side by side in a uniform flow. *J Fluid Mech* 164:1–25
- Iliadis G, Anagnostopoulos P (1998) Viscous oscillatory flow around a circular cylinder at low Keulegan-Carpenter numbers and frequency parameters. *Int J Numer Method Fluid* 26:403–442
- Kovaszny LSG (1949) Hot-Wire Investigation of the Wake behind Cylinders at Low Reynolds Numbers, Proceedings of the Royal Society of London. Ser A Math Phys Sci 198(1053):174–190
- Lee T, Budwig R (1991) The onset and development of circular-cylinder vortex wakes in uniformly accelerating flows. *J Fluid Mech* 232:611–627
- Le Gal P, Peschard I, Chauve MP, Takeda Y (1996) Collective behaviour of wakes downstream a row of cylinders. *Phys Fluid* 8:2097–2106
- Lin XW, Bearman PW, Graham JMR (1996) A numerical study of oscillatory flow about a circular cylinder for low values of beta parameter. *J Fluid Struct* 10:501–526
- Mao X, Marx D, Jaworski AJ (2005) PIV measurement of coherent structures and turbulence created by an oscillating flow at the end of a thermoacoustic stack. In: Proceedings of the iTi conference in turbulence, Bad-Zwischenahn, Germany, 25–28 September
- Marx D, Mao X, Jaworski AJ (2006) Acoustic coupling between the loudspeaker and the resonator in a standing-wave thermoacoustic device. *Appl Acoust* 67:402–419
- Moretti PM (1993) Flow induced vibrations in arrays of cylinders. *Annu Rev Fluid Mech* 25:99–114
- Obasaju ED, Bearman PW, Graham JMR (1988) A study of forces, circulation and vortex patterns around a circular cylinder in oscillating flow. *J Fluid Mech* 196:467–494
- Okajima A, Matsumoto T, Kimura S (1997) Force measurements and flow visualization of bluff bodies in oscillatory flow. *J Wind Eng Ind Aerodynamics* 69–71:213–228
- Ralph ME (1986) Oscillatory flows in wavy-walled tubes. *J Fluid Mech* 168:518–540
- Roberts EPL, Mackley MR (1996) The development of asymmetry and period doubling for oscillatory flow in baffled channels. *J Fluid Mech* 328:19–48
- Sumer BM, Jensen BL, Fredsbe J (1991) Effect of a plane boundary on oscillatory flow around a circular cylinder. *J Fluid Mech* 225:271–300
- Swift GW (1988) Thermoacoustic engines. *J Acoust Soc Am* 84:1145–1180
- Swift GW (2002) Thermoacoustics: a unifying perspective for some engines and refrigerators. Acoustical Society of America, New York
- Tatsuno M, Bearman PW (1990) A visual study of the flow around an oscillating circular cylinder at low Keulegan-Carpenter numbers and low Stokes numbers. *J Fluid Mech* 211:157–182
- Ward B, Swift GW (2001) Design environment for low-amplitude thermoacoustic engines (DeltaE). Tutorial and User's Guide, Los Alamos National Laboratory
- Yellin EL (1966) Laminar-turbulent transition process in pulsatile flow. *Circ Res* 19:791–804

## Chapter 6

# **Application of PIV measurement techniques to study turbulence characteristics of oscillatory flows around parallel-plate structures in thermoacoustic devices**

by X. Mao and A. J. Jaworski

Published in: *Measurement Science and Technology*

# Application of particle image velocimetry measurement techniques to study turbulence characteristics of oscillatory flows around parallel-plate structures in thermoacoustic devices

Xiaoan Mao and Artur J Jaworski<sup>1</sup>

School of Mechanical, Aerospace and Civil Engineering, University of Manchester, Sackville Street, PO Box 88, Manchester M60 1QD, UK

E-mail: [a.jaworski@manchester.ac.uk](mailto:a.jaworski@manchester.ac.uk)

Received 28 June 2009, in final form 14 January 2010

Published 9 February 2010

Online at [stacks.iop.org/MST/21/035403](http://stacks.iop.org/MST/21/035403)

## Abstract

This paper describes the development of the experimental setup and measurement methodologies to study the physics of oscillatory flows in the vicinity of parallel-plate stacks by using the particle image velocimetry (PIV) techniques. Parallel-plate configurations often appear as internal structures in thermoacoustic devices and are responsible for the hydrodynamic energy transfer processes. The flow around selected stack configurations is induced by a standing acoustic wave, whose amplitude can be varied. Depending on the direction of the flow within the acoustic cycle, relative to the stack, it can be treated as an entrance flow or a wake flow. The insight into the flow behaviour, its kinematics, dynamics and scales of turbulence, is obtained using the classical Reynolds decomposition to separate the instantaneous velocity fields into ensemble-averaged mean velocity fields and fluctuations in a set of predetermined phases within an oscillation cycle. The mean velocity field and the fluctuation intensity distributions are investigated over the acoustic oscillation cycle. The velocity fluctuation is further divided into large- and small-scale fluctuations by using fast Fourier transform (FFT) spatial filtering techniques.

**Keywords:** oscillatory flow, parallel-plate structure, thermoacoustics, turbulence and coherence, spatial filtering

(Some figures in this article are in colour only in the electronic version)

## 1. Introduction

In thermoacoustic devices, an acoustic wave interacts with a stack of tightly spaced plates either to produce acoustic power, induced by a temperature gradient on the stack, or to obtain a temperature gradient along the stack, induced by an imposed acoustic wave. This is based on the thermoacoustic effect whereby appropriately phased pressure and velocity oscillations enable the compressible fluid to undergo a

thermodynamic cycle in the vicinity of a solid body. These processes have been utilized in thermoacoustic engines and coolers [1], whose main advantages are their lack of moving parts and construction simplicity; the conversion between thermal and acoustic energies is realized by an oscillating gas, without the need for piston–cylinder arrangements, sliding seals or harmful working fluids.

Figure 1 shows a schematic of a quarter-wavelength, standing wave device working as a refrigerator thanks to the acoustic power input,  $W_{ac}$ . Central to the device's operation

<sup>1</sup> Author to whom any correspondence should be addressed.

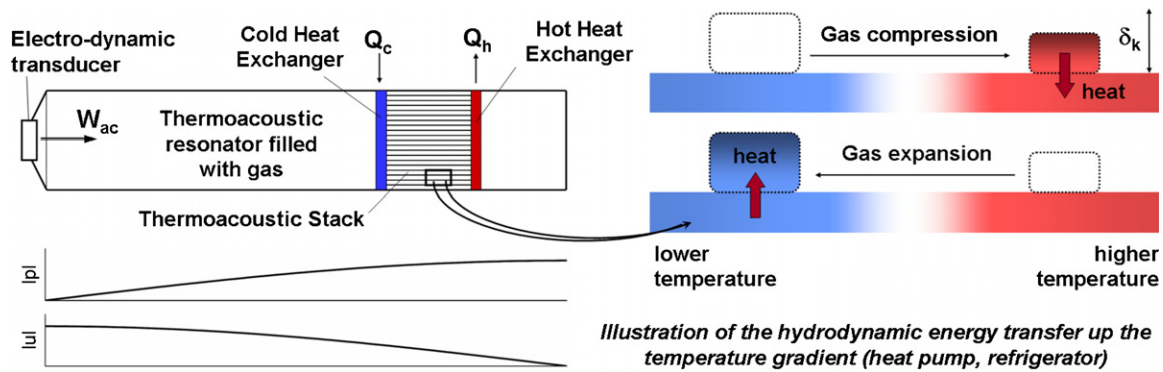


**Figure 1.** Schematic of a simple thermoacoustic cooler arrangement. The acoustically induced compression and expansion of fluid elements causes heat pumping effects along the stack.

is a thermoacoustic stack. This can be imagined as a series of plates forming a set of parallel channels. The gas pressure in the resonator oscillates acoustically at a frequency set by the resonance between the gas in the duct and the moving mass of the transducer. The distributions of pressure amplitude,  $|p|$ , and velocity amplitude,  $|u|$ , illustrate the standing wave present in the resonator. The oscillating gas, within a short distance of thermal penetration depth,  $\delta_v$ , from the adjacent solid boundaries, communicates heat with the stack (as shown on the right) and heat exchangers, and the acoustics of the system ensure that the timing between the pressure and gas displacement is such that heat (the cooling load,  $Q_c$ ) is pumped out of the cold heat exchanger towards the hot heat exchanger (and removed to the surroundings as denoted by  $Q_h$ ), using a hydrodynamic energy transfer ‘cascade’ enabled by compressing and expanding gas parcels. It is also possible to reverse the operation of such systems to form an engine; a high temperature gradient along the stack leads to a spontaneous generation of acoustic power which can be converted to electricity by a linear alternator. More complex systems can be built utilizing the concept of ‘travelling wave’ devices [2], which are not discussed here for simplicity.

The intensity of acoustic waves used in thermoacoustic applications is usually described by their ‘drive ratio’: the ratio of the maximum pressure amplitude of the acoustic wave to the mean pressure in the resonator ( $Dr$ ). It is thought that up to drive ratios of about 2–3% the fluid flow and heat transfer processes can be reliably described by the linear acoustic theory developed by Rott [3]. However, practical applications often require drive ratios as high as 10%, in which range the interaction between the acoustic field and the solid boundary is governed by complex thermal-fluid processes, which are still not fully understood. Large drive ratios correspond to large fluid displacements and velocity amplitudes, which in turn lead to significant nonlinear effects such as local pressure losses caused by the abrupt change of the cross section, acoustic streaming, vortex shedding and transition to turbulence. These factors can have a significant influence on the overall efficiency of thermoacoustic systems, yet they are still not quantified sufficiently for practical thermoacoustic applications. The current paper addresses these issues through developing appropriate measurement methodologies which could be applied to ‘model’ thermoacoustic devices in order

to study the fundamental fluid flow behaviour. As a first step, and an illustration of the measurement capabilities, it focuses on the flow at the extremity of the stack of parallel plates. It is thought that the flow behaviour in this region plays an important role in heat transfer processes between the stack and the heat exchangers, and so the proposed measurement techniques and experimental results are of both fundamental and practical importance.

## 2. Literature review

Particle image velocimetry (PIV) has been successfully applied in a great many areas of fluid mechanics; it is rather impractical to provide a detailed discussion here. Comprehensive reviews are available [4, 5], while *Measurement Science and Technology* devoted a series of special issues and ‘features’ to the subject [6–11] with over 70 research papers. Nowadays, PIV is considered a mature measurement technique, with many turn-key systems available in the market. The research challenge is therefore a continuous improvement of the accuracy and data interpretation methods as well as application of the PIV techniques to complex (often nonlinear) systems. In the context of thermoacoustic engines and refrigerators, the two technical challenges are to devise appropriate triggering/data sampling techniques that would enable defining reliably the measurement points within the acoustic cycle and data processing methods that would allow extracting average features of the resulting flow field and the statistical analysis which would characterize the unsteady characteristics of the flow.

The above-mentioned challenges are in some way similar to those of PIV imaging in internal combustion engines [12–14], where the flow must be sampled at selected phase angles of the engine cycle, while unsteady flow behaviour must be analysed through ensemble averaging over many cycles, rather than by the analysis of temporal signals, as is usually the case in steady flows—see the discussion provided by Towers and Towers in [5], pp 354–5, and in [12]. However, while measurement phase-locking is relatively straightforward for IC engines (e.g. crank angle), in thermoacoustics one needs to rely on the timing of the acoustic excitation to trigger the PIV imaging, which can be achieved by several different methods.

This adds additional complexity to the measurement as well as potentially some measurement uncertainty.

Applications of PIV for flow visualization or velocity measurement in acoustic systems were reported by Hann and Greated [15, 16] who used a double exposure on a single frame and an auto-correlation method. Campbell *et al* [17] carried out a review of PIV (as well as LDA) methods in sound measurement applications, and focused in particular on measurements illustrating streaming effects in acoustic systems using PIV. More recent work by Nabavi *et al* [18] focused on simultaneous measurement of acoustic and streaming velocities at selected phases of the acoustic cycle, the former obtained by cross-correlating two consecutive PIV images, while the latter was obtained by cross-correlating the alternative PIV images at the same phase. A good agreement between experiments and theoretical predictions was reported. A somewhat similar approach was adopted by Debesse *et al* [19] who measured acoustic and streaming velocities in a high-pressure (7–15 bar) standing wave resonator working with nitrogen at a frequency of 22 Hz. Here the acoustic excitation was induced by a thermoacoustic engine located at one end of the resonator, while the velocity fields were measured at the other end, through a short cylindrical section made out of glass.

The flow field around internal structures of thermoacoustic systems was perhaps first investigated by Blanc-Benon *et al* [20]. They used a quarter-wavelength thermoacoustic refrigerator configuration, driven by a loudspeaker at a frequency of 200 Hz. The experiments were conducted for two stacks: one with a plate thickness of 0.15 mm and plate spacing of 1.0 mm, the other with a plate thickness of 1.0 mm and plate spacing of 2.0 mm. The drive ratios were relatively low: 1.5% and 1.0%, respectively. The measurements were locked onto the loudspeaker signal. Vortex structures around the edges of stack plates were obtained by averaging of 100 PIV images taken at selected phases of the acoustic cycle (altogether 16 phases in an acoustic cycle were investigated). The results showed both concentrated and elongated eddies, which nevertheless remained attached to the plates. Further investigations of velocity fields generated by the oscillatory flow past the parallel-plate stacks were carried out by Castrejón-Pita *et al* [21], Berson and Blanc-Benon [22], Berson *et al* [23], Mao *et al* [24], Aben *et al* [25] and Jaworski *et al* [26]. Generally speaking all these works focused on velocity and vorticity fields in order to classify the flow morphology as a function of stack geometries and acoustic excitation levels. Some similarity criteria have also been suggested to find the controlling parameters for this type of flow.

Unfortunately, so far only the mean velocity and vorticity fields obtained by ensemble-averaging were investigated. Current work is driven by the interest in the fluid-mechanical aspects of the thermoacoustic systems, in particular the turbulence characteristics in the vicinity of the parallel-plate thermoacoustic stack, which may have a strong impact on the actual heat transfer intensity. The mean flow field features investigated experimentally [20–26] have been successfully replicated by various numerical works

(see for example [20, 27–30]). Unfortunately, there is a fundamental problem here since CFD typically uses time-dependent solutions of Navier–Stokes equations, which after a few cycles converge to numerically stable (i.e. highly repeatable) flow patterns. Unfortunately, the data presented in this paper show that the real flow field is highly unsteady in the sense that the cycle-to-cycle variations are significant. The similarity between actual measurements and CFD only arises when ensemble-averaged data are compared to time-dependent but ‘numerically stable’ results of CFD. In this sense CFD can reproduce well the mean flow field. Neither statistical velocity fluctuations nor small-scale eddies contained in the flow field and possibly generated by dissipating the large-scale vortices were reported. Another difficulty is that the flow conditions investigated by CFD have relatively small Reynolds and/or Mach numbers, which rarely promotes the occurrence of turbulence. As a result very little is known about the nature of turbulence in oscillatory flows as investigated in the present work, which is hoped to provide an important first step for further experimental work and some more advanced numerical studies.

### 3. Experimental apparatus and measurement techniques

The detailed description of the rig and its linear acoustic model is given in [31], while the PIV measurement technique is briefly introduced in [24]. Therefore, only essential information is provided to maintain the paper clarity. On the other hand, some new information is included in areas such as the analysis of seeding particles or triggering of the measurement system due to the specific nature of the journal.

#### 3.1. Resonator and stacks

Figure 2(a) shows a schematic diagram of the experimental rig with the main components and their dimensions. The working gas is air at atmospheric pressure and room temperature. The oscillatory flow is induced by a standing acoustic wave generated by a loudspeaker. The coupling of the square duct and the loudspeaker enables the rig to work as a quarter-wavelength resonator with the fundamental frequency of 13.1 Hz. Current experiments were carried out at drive ratios up to 3%. Construction of the rig described above allows testing arbitrary stack arrangements, at arbitrary locations along the resonator. In the current work, two stacks were tested, both of which had the length,  $l = 200$  mm and the width to fit the internal resonator width. The first stack (denoted as stack I) had  $d = 1.1$  mm thick plates, with the spacing between plates  $D = 5.0$  mm. The second stack (denoted as stack II) had  $d = 5.0$  mm thick plates, with the spacing between plates  $D = 10$  mm (see figure 2(b) for a stack schematic). The fluid particle displacement amplitude is normally less than half of the plate length; therefore, the flow disturbance from one end of the stack plates is considered too far to disturb the flow at the other end of the stack (in other words the plates can be assumed ‘semi-infinite’ in length). For both stacks, the distance separating the centre of the stack and the end plate of the resonator was 4.11 m.

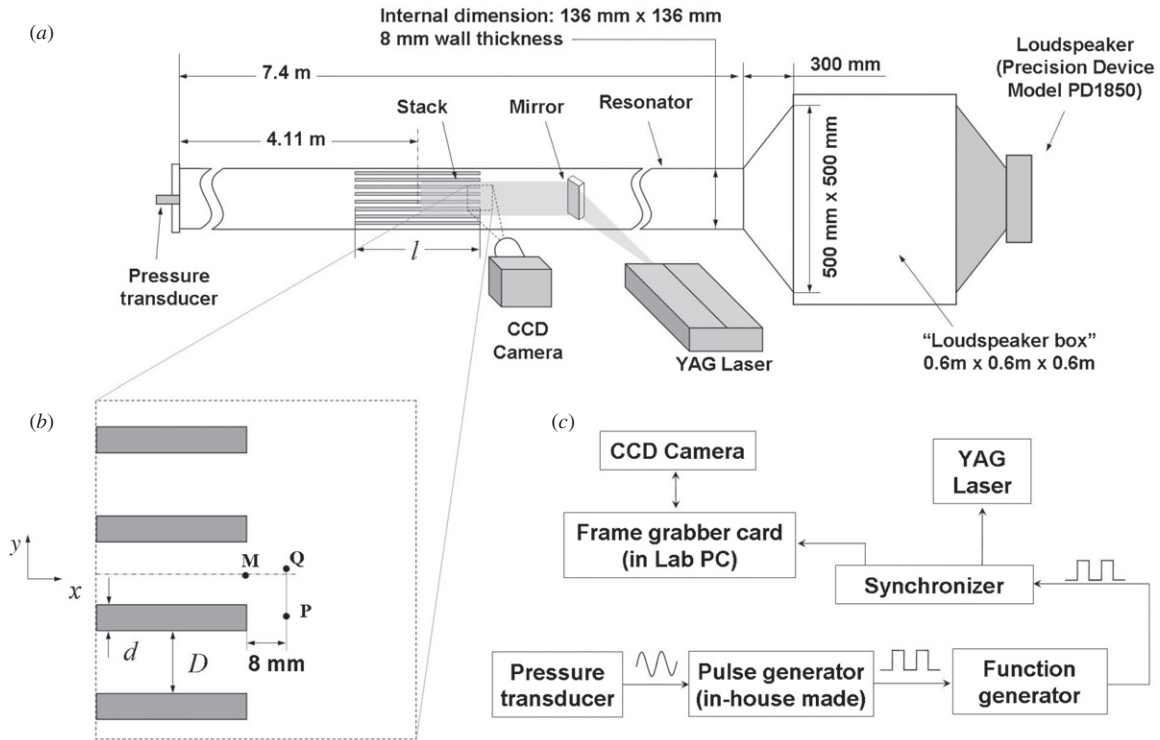


**Figure 2.** Schematic of experimental apparatus (a); details of the stack and imaging area (b) and block diagram of the triggering mechanism used for phase-locking in PIV measurements (c).

### 3.2. Flow seeding and laser illumination

Air in the resonator is seeded with olive oil droplets of sizes typically around  $1\ \mu\text{m}$ . The particle suspension was injected through an opening in the resonator wall, close to the location of the stack, while another opening far from the measurement zone allowed maintaining the atmospheric pressure inside the resonator. After the seeding was in place, the openings were blocked and a high-intensity acoustic wave was used to distribute the particles evenly within the measurement zone, after which the actual imaging was undertaken. After the tracer injection, a high tracer particle density of more than 15 particles in each interrogation spot in average can be obtained, which enables a relatively high detection probability of a valid velocity vector [32]. This quality particle suspension lasts typically for a period of a few minutes, during which the PIV measurements are undertaken. After a few minutes, the particles tended to settle, adhere to the internal surfaces or drifted away most likely due to streaming processes. Subsequently, the rig had to be cleaned inside and the seeding had to be re-applied before the next set of experiments.

In the PIV measurement of the velocity field, it is the velocity of the particles suspended in the fluid that is actually measured. Therefore, it is necessary for the particles to follow the flow faithfully. The unsteady motion of dispersed particles suspended in a continuous medium was modelled by Melling [33] (cf equation (2) in [33]). According to King [34] there are also additional forces induced by the acoustic radiation pressure (cf equation (76) in [34]) in a standing wave. However, in the experimental conditions considered, the acoustic radiation pressure on the tracer particle is about

seven orders of magnitude smaller than the acceleration force according to Stokes' law and it may be easily neglected here. Using the analysis by Melling [33], and considering that, in this case the particle density  $\rho_p$  and the fluid density  $\rho$  differ by three orders of magnitude, one can simplify Melling's equation to

$$\frac{\pi d_p^3}{6} \rho_p \frac{du_p}{dt} = -3\pi\mu d_p (u_p - u), \quad (1)$$

where  $d_p$  is the particle diameter,  $\mu$  (about  $1.81 \times 10^{-5}\ \text{kg m}^{-1}\ \text{s}^{-1}$  for air at 1 atm and  $20\ ^\circ\text{C}$ ) is the dynamic viscosity of the fluid,  $u_p$  and  $u$  are the instantaneous velocity of the particle and fluid respectively. Of course  $u$  is a nonlinear function of time in the unsteady flow around the stack plates and the equations of motion become difficult to solve. Relaxation time,  $\tau_s$ , could be used to measure the tendency of the particles to follow the fluid velocity, on the assumption that the particle velocity approaches the flow velocity exponentially, as described by equation (2.3) in [35]. The relaxation time  $\tau_s$  is defined as

$$\tau_s = \frac{d_p^2 \rho_p}{18\mu}. \quad (2)$$

Assuming that the particles follow the flow if  $u_p/u > 0.99$ , with no more than  $1^\circ$  phase lag, it can be shown that the maximum diameter of the particles should be about  $4.0\ \mu\text{m}$  for the acoustically driven oscillatory flow of interest ( $f = 13.1\ \text{Hz}$ ). Therefore, the choice of the smoke generator and the resulting particles used for PIV measurements seem reasonable.

A laser beam from a Nd:YAG pulsed laser (BigSky Laser) was expanded to form a divergent laser sheet in the

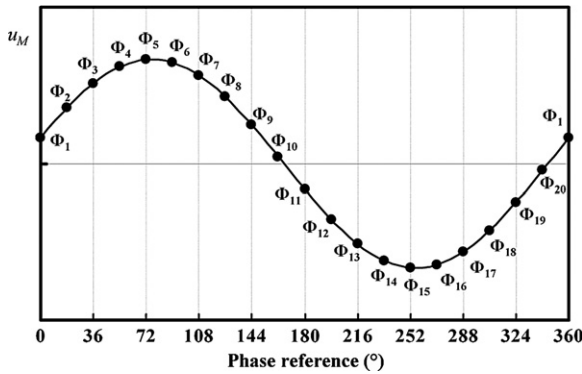


**Figure 3.** Phase-averaged velocity oscillation at a point M and corresponding phases at which the PIV measurements are taken.

vertical plane (figure 2(a)). It penetrated into the resonator perpendicularly to the resonator axis and was reflected by a small rectangular mirror (30 mm  $\times$  10 mm) to illuminate the flow into and out of the stack. The mirror was installed 0.7 m away from the end of the stack, while the laser aperture was about 0.3 m away from the mirror; the imaging area was approximately in the beam waist, where the laser sheet is about 1 mm thick, measured by using the ‘paper burn’ technique. It was confirmed by a preliminary PIV measurement (not shown here) that the presence of the mirror had no discernible effect on the oscillatory flow at the stack.

### 3.3. Details of PIV measurement

Figure 2(c) shows a block diagram of the PIV triggering mechanism used in the current study. The output signal of the pressure transducer shown in figure 2(a) is used as a phase reference to generate a TTL pulse sequence by an in-house-made circuitry, at the same frequency as the acoustic excitation provided to the loudspeaker. The TTL signal was used to synchronize the laser pulses and the image capturing by a 4 MP camera, so that the pictures were phase-locked to the pressure oscillation, thus the velocity oscillation in the resonator. The phase of the TTL signal can be shifted so that the flow in different phases of the acoustic oscillation can be observed. As schematically shown in figure 3, 20 phases (every 18°) were investigated in each acoustic cycle. Here the times when these 20 phases ( $\Phi_1, \Phi_2, \dots, \Phi_{20}$ ) appear are shown relative to the mean ensemble-averaged velocity at point M (cf figure 2(b)). In general, the flow corresponding to phases  $\Phi_1$ – $\Phi_{10}$ , when the fluid flows out of the stack with a positive velocity, is referred to as the ejection stage, while the flow corresponding to phases  $\Phi_{11}$ – $\Phi_{20}$ , when the fluid flows into the stack with a negative velocity, is referred to as the suction stage—both explained in more detail in section 4.3.

To determine the flow velocity in each phase, pairs of singly exposed images were captured. The time difference of images in each pair was determined by the laser pulse separation, which was chosen so that the particle displacements during the interval were generally not more than 1/4 of the interrogation area used to analyse the captured images [36]. Thus, the time separations between laser pulses were varied according to the velocity magnitude at the investigated phase, and the size of the investigated fields. A

flow field of smaller size was imaged to reveal the velocity gradient in the viscous boundary layer, while a larger size was applied to view the general pattern of the wake flow. The measured field size ranged from 25 mm  $\times$  25 mm to 60 mm  $\times$  60 mm for the investigated two-stack configurations.

The image processing was performed using commercial software (TSI INSIGHT<sup>TM</sup>). A standard fast Fourier transform (FFT) cross-correlation algorithm was used and the Gaussian peak detection algorithm was applied to identify the velocity vectors. The interrogation spots had a size of 32  $\times$  32 pixels, and were recursively reduced to 16  $\times$  16 pixels with a 50% overlap [37]. A validation was applied to the obtained velocity vector fields to remove spurious vectors. The spurious vectors were detected by using a ‘neighbourhood mean’ filter, which removes vectors that are out of the range of the mean value  $\pm$  three times standard deviation in a window of 3  $\times$  3 vectors. A median value was used rather than the mean to exclude any contribution from a spurious vector that may be present in the third row or column in the 3  $\times$  3 window, in the row-by-row scanning process.

## 4. Results and discussion

### 4.1. Validation of velocity measurement

PIV is an absolute method of velocity measurement, which relies on the displacement of tracer particles as captured by two consecutive images with known time separation. Nevertheless it seemed useful to validate the velocity measurement in two ways. Firstly, an acoustic wave was established in an empty resonator. Given that the pressure amplitude at the end of the resonator is known, it is easy to predict analytically the oscillatory velocity field in the centre of the resonator (at any axial location, for example, in the location where the stack would normally reside). These measurements simply confirmed that the measurement and data acquisition setup were working correctly. The absolute values of discrepancy between the predicted and measured velocity values at different phases were typically less than 3.6% of the velocity amplitude.

Secondly, ensemble-averaged velocity measurements were carried out within a selected channel between two stack plates and compared to theoretical predictions. It is known that the flow velocity in the stack channel at a relatively low drive ratio can be predicted accurately by the linear thermoacoustics theory [1]. Figure 4 shows the velocity distribution of the  $U$  component of the velocity for ten selected phases, obtained by PIV measurements of the flow around the end of stack II, along with the profiles predicted by linear thermoacoustics. The measured velocity profiles were obtained at a distance of  $2.4D$  into the channel. The  $y$  coordinate is normalized by the channel width  $D$  shown in figure 2. The selected case was measured at  $Dr = 0.3\%$ , which corresponds to the velocity amplitude of about  $1.05 \text{ m s}^{-1}$ . It can be seen that the measured mean velocity profiles reproduce very well the double boundary layers typically found in the oscillatory flows and the velocity magnitudes, except for  $\Phi_{11}$  and  $\Phi_{13}$  (see arrows in figure 4). The differences between measured and predicted velocities in

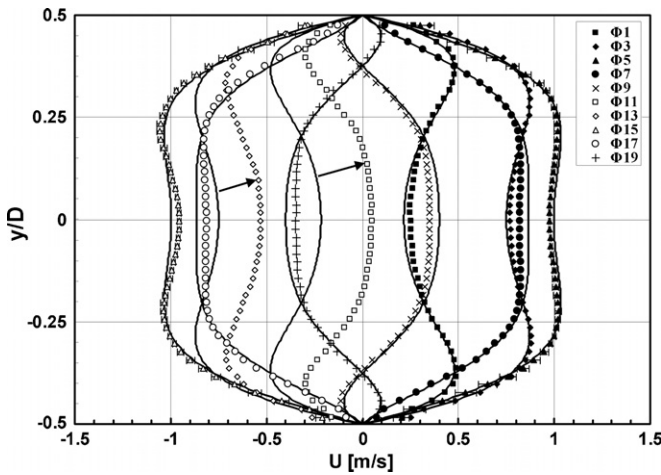


**Figure 4.** Velocity profiles for ten phases in the cycle: solid lines—theoretical predictions; symbols—ensemble-averaged measurements. Data shown for stack II at  $2.4D$  from the channel entry and  $Dr$  of 0.3%; arrows indicate the discrepancy between measured and theoretical profiles for  $\Phi_{11}$  and  $\Phi_{13}$ ; error bars for  $\Phi_5$  and  $\Phi_{15}$  show the standard deviation based on averaging of 100 PIV measurements.

these phases are caused by the entrance effects, which occur during the suction phase of the oscillatory flow [26]. Velocity profiles for  $\Phi_5$  and  $\Phi_{15}$  also have ‘error bars’ corresponding to the standard deviation of velocity values obtained on the basis of averaging 100 measurements. Generally, the standard deviation is less than 2% of the mean velocity amplitude in the central region of the channel. A higher fluctuation level in the boundary layer is probably caused by the wall-drag effect on the seeding particles in the vicinity of the solid boundary, which is well known to be highly nonlinear [38, 39]. Since the distance to the wall of any seeding particle position is a random variable, the strong nonlinearity leads to high fluctuations in velocity as inferred by the FFT/cross-correlation algorithm.

The velocity profiles of the oscillatory flow in a channel between two parallel plates are conceptually similar to those for the oscillatory flow in a circular pore, which is also often referred to as the Womersley profiles due to his pioneering work [40]. Nevertheless, the analytical expressions for the velocity profiles in the oscillatory flow in pores of a range of different geometries, such as square, circular and triangular shapes, as well as a channel between two parallel planes are available from Arnott [41].

#### 4.2. Ensemble averaging of the velocity field

For a typical experimental run, an arbitrary number,  $N$ , of instantaneous flow fields can be obtained for each of the 20 phases. Therefore, the data set obtained for each case consists of  $20 \times N$  instantaneous flow fields. Each instantaneous flow field provides two velocity components  $u(x, y, \Phi, i)$  and  $v(x, y, \Phi, i)$  at a spatial point  $(x, y)$ , at phase  $\Phi$  of each acoustic oscillation cycle  $i$ .

The classical Reynolds decomposition is used to separate the instantaneous flow fields into mean (ensemble-averaged) flow fields and their fluctuations, based on the assumption that

the mean velocity fields are the same at any time corresponding to the same phase in the acoustic cycle [42]. Therefore, from a group of instantaneous flow fields of the same phase, the corresponding mean velocities  $U(x, y, \Phi)$  and  $V(x, y, \Phi)$ , and the RMS values (standard deviation) of the velocity fluctuations,  $u'(x, y, \Phi)$  and  $v'(x, y, \Phi)$ , for each phase  $\Phi$  can be calculated as follows:

$$U(x, y, \Phi) = \frac{1}{N} \sum_{i=1}^N u(x, y, \Phi, i) \quad (3)$$

$$V(x, y, \Phi) = \frac{1}{N} \sum_{i=1}^N v(x, y, \Phi, i) \quad (4)$$

$$u'(x, y, \Phi) = \sqrt{\frac{1}{N} \sum_{i=1}^N (u(x, y, \Phi, i) - U(x, y, \Phi))^2} \quad (5)$$

$$v'(x, y, \Phi) = \sqrt{\frac{1}{N} \sum_{i=1}^N (v(x, y, \Phi, i) - V(x, y, \Phi))^2} \quad (6)$$

where the summation is over  $i = 1, \dots, N$  images taken at phase  $\Phi$ , and the prime indicates the fluctuation of a variable. Of course the RMS values of velocity fluctuations will contain both the uncertainty introduced by the measurement and the effects of the flow behaviour. Judging from the results shown in section 4.1 (and the results shown in later sections 4.3 and 4.4), the measurement uncertainty is relatively low compared to the component corresponding to true flow unsteadiness (1–2% versus tens of %—cf figures 9–12). Therefore, by using the traditional Reynolds decomposition one could separate the mean and fluctuating components of the instantaneous flow velocity, the latter containing all the unsteady features of the velocity field behaviour.

Of course it should be noted that turbulence is a three-dimensional phenomenon. However, due to the limitations of the measurement (2D system) as well as the practicalities of the physical setup and access, the current study only focused on the plane parallel to the resonator axis. Nevertheless, for reference purposes, some measurements were performed to estimate the fluctuations of the third ‘out-of-plane’ velocity component (typically denoted by  $w'$ ). Here, the laser sheet was aligned perpendicular to the resonator axis (5 mm from the end of stack II where the fluctuations were found to be the highest), while the camera recorded the image reflected in the mirror shown in figure 2. The maximum measured values of  $w'/U_a$  were about 12%, compared to 40% in  $(u'^2 + v'^2)^{0.5}/U_a$ , 29% in  $u'/U_a$  and 28% in  $v'/U_a$ ,  $U_a$  being the amplitude of the mean velocity in the  $x$  direction. This occurred when the fluid is moving out of the channel with the velocity magnitude near to its amplitude. Although the ‘out-of-plane’ fluctuations are clearly much lower than those in  $u$  and  $v$ , the results emphasize that in order to model the flow behaviour correctly, any future CFD modelling aiming to capture the turbulence physics correctly may have to be fully three dimensional—this point being an addition to the discussion at the end of section 2.

An important step in developing the measurement methodologies for characterizing oscillatory flows is to

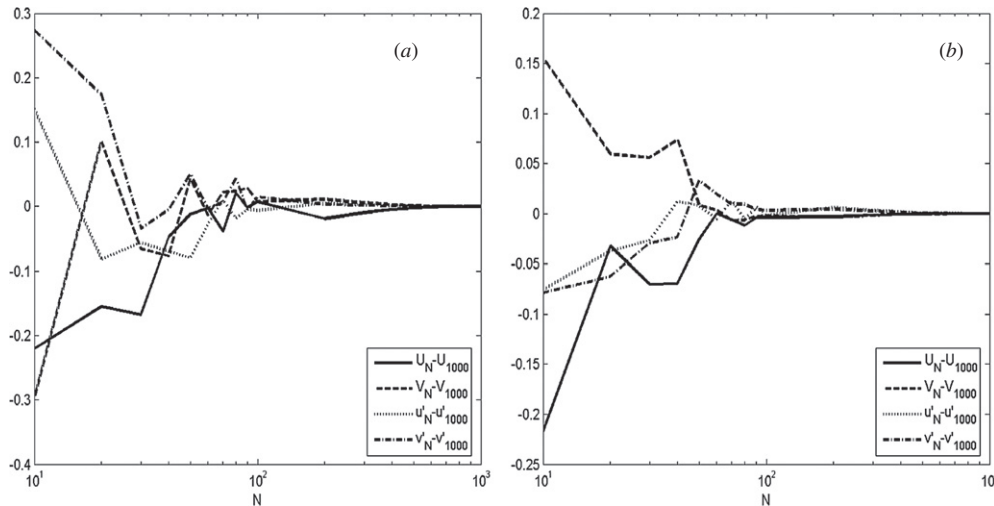


**Figure 5.** Effect of the number of instantaneous measurements,  $N$ , on the computation of the flow statistics at point P (a) and point Q (b). Note: units of vertical axes are in  $\text{m s}^{-1}$  for all variables. Index  $N$  indicates the number of PIV images taken to calculate a given statistic: either mean velocity or velocity fluctuation.

establish the number of instantaneous images for a reliable determination of mean flow features. Some studies [43] indicate that to reliably measure turbulence characteristics, 1000 frames had to be used, while others rely on a substantially smaller number of frames: Cenedese *et al* [44] used only 40 frames for extracting the steady mean flow features. In somewhat conceptually similar studies of average helicity and energy dissipation in a turbulent swirling jet, Regunath *et al* [45] argued that 500 frames was sufficient for their analysis. The effect of the number of instantaneous measurements pictures,  $N$ , on the flow statistics in the present measurement has been assessed by computing the statistics using up to 1000 frames. One thousand frames were taken for stack II, at phase  $\Phi_4$ . The result is shown in figure 5, corresponding respectively to point P which is along the centreline of the plate, and point Q in figure 2(b) (Q is located 9 mm above P). It is observed that a very good convergence is obtained for 1000 frames. For only 100 frames, the convergence is not rigorously reached, yet is judged sufficient to obtain a good representation of the flow over the whole flow field, and a reasonable representative of the convergent statistics. This was the reason for using  $N = 100$  frames in the current study, and this choice seemed also a reasonable trade-off between the accuracy and the storage capacity and data processing power available.

#### 4.3. Comparison between the instantaneous and averaged flow features

The detailed flow physics of the oscillatory flow in the experimental setup discussed in this paper has already been given in [24], based on the averaged flow field analysis. It will not be repeated here. It is perhaps important to note that there are two main stages in the oscillatory flow around a stack of plates: the first is the ‘ejection’ stage, where the flow is in the positive direction (cf figure 2) and the fluid emerges from the channels (phases  $\Phi_1 - \Phi_{10}$ ). Here typically the flow separates at the edges of the plates, and various types of vortical structures are rolled up. These may be shed into the flow if

the drive ratio is large enough, or may remain in the plate vicinity for small drive ratios. Figures 6(d) and 7(d) discussed later give a general idea about the type of vortex shedding occurring in the experiments. The patterns may resemble the classical von Karman vortex street, although there are clear differences in that the flow is not steady and is accelerated and decelerated in the half cycle discussed here. The exact features of the vortex shedding depend on the flow forcing and the geometry of the stack, although various similarity numbers have been suggested in [24]. The second stage of the flow is the ‘suction’ stage, where the flow is in the negative direction (phases  $\Phi_{11} - \Phi_{20}$ , also cf figure 2). During this period all the vortex structures generated in the ‘ejection’ stage (or their remains if they had time to dissipate) impinge back on the stack plates. Figure 8(d) discussed later illustrates the impingement of vortex structures onto the stack.

It is thought that these alternate processes of vortex shedding, flow reversal and vortex ‘re-impingement’ are critical to the understanding of the heat transfer modes between the stack and the heat exchangers (not studied in the current work). Previous work devoted to analysing flow patterns in the oscillatory flow past a stack of plates [20–26] has focused on the mean flow features and tacitly assumed that by taking a sufficient amount of instantaneous images for ensemble averaging, any variability of the flow between cycles would be smoothed out. However, this approach may be questionable especially if the instantaneous flow features are very different from the averaged ones, which may in turn have implications on the heat transfer predictions. So far no attempt has been made to quantify the cycle-to-cycle flow variability or to estimate to what extent are the instantaneous flow features different from the averaged ones. For the ease of the following discussion, the flow field data will be presented in terms of vorticity maps, rather than the velocity field.

Figure 6 shows an example of comparisons between the instantaneous vorticity field (three images have been selected at random from a string of 100 and shown as figures 6(a)–(c)) and the averaged vorticity field (figure 6(d)) for stack

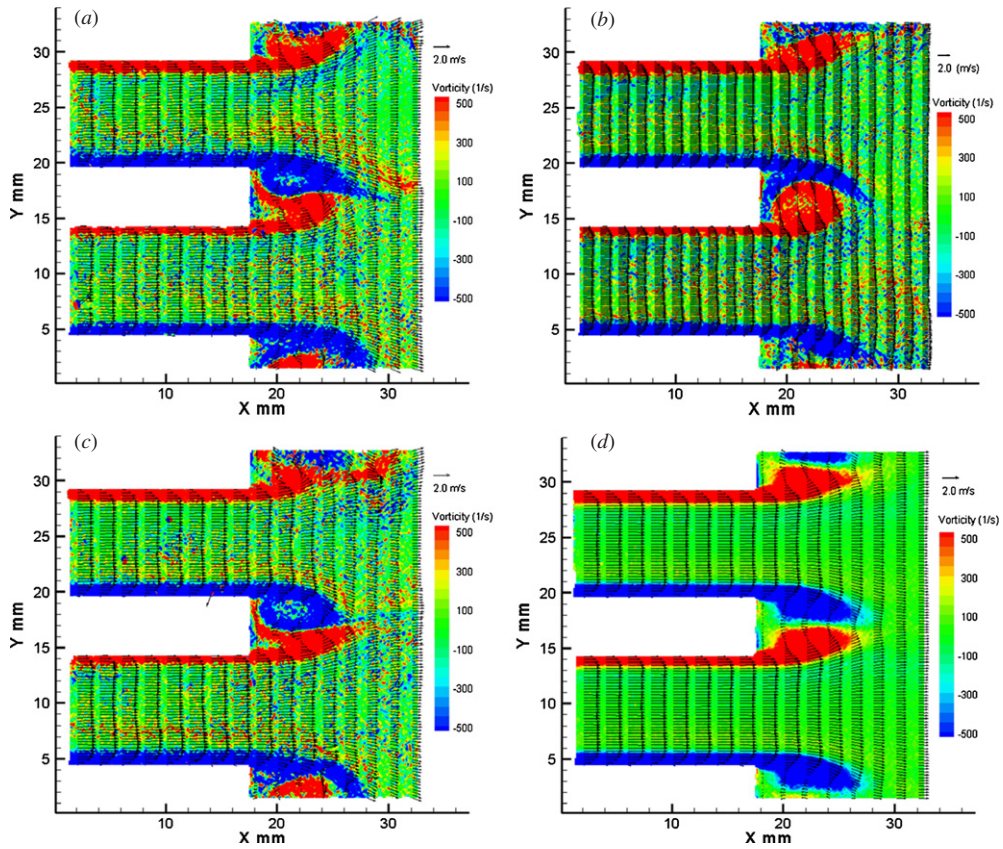


**Figure 6.** Illustration of the variability between vortex structures in three instantaneous images of the vorticity field (a)–(c). The average vorticity field resulting from ensemble averaging of 100 instantaneous images (d). Stack II,  $Dr = 0.6\%$ , phase  $\Phi_6$ .

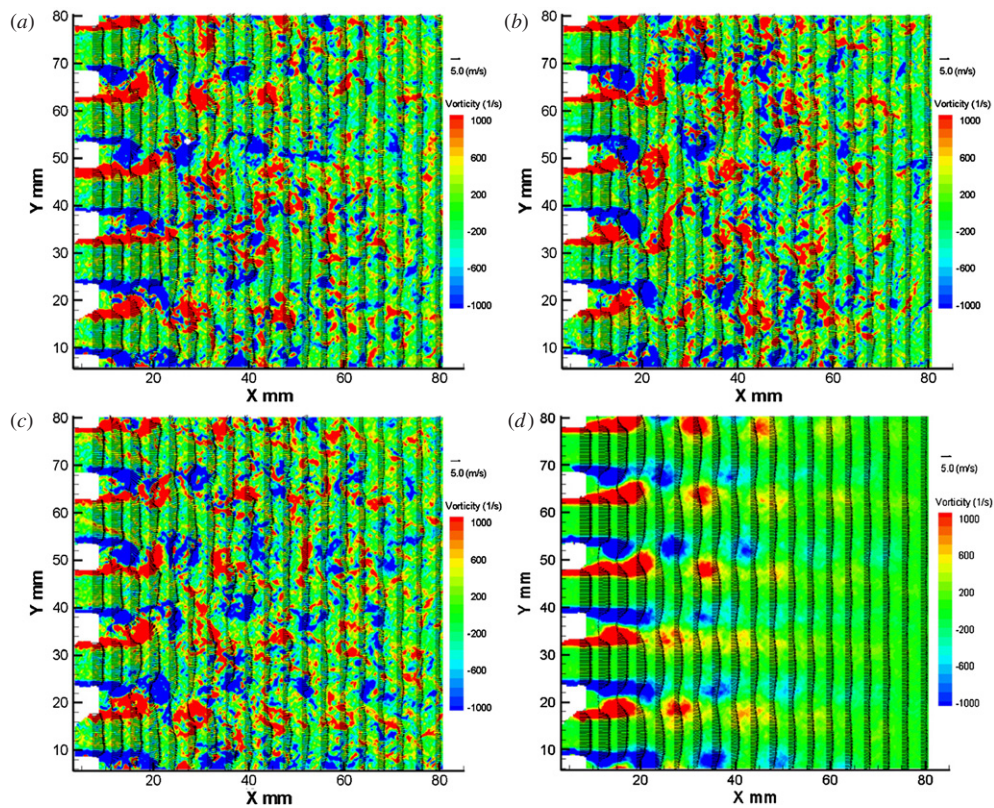


**Figure 7.** Illustration of the variability between vortex structures in three instantaneous images of the vorticity field (a)–(c). The average vorticity field resulting from ensemble averaging of 100 instantaneous images (d). Stack II,  $Dr = 2.0\%$ , phase  $\Phi_8$ .

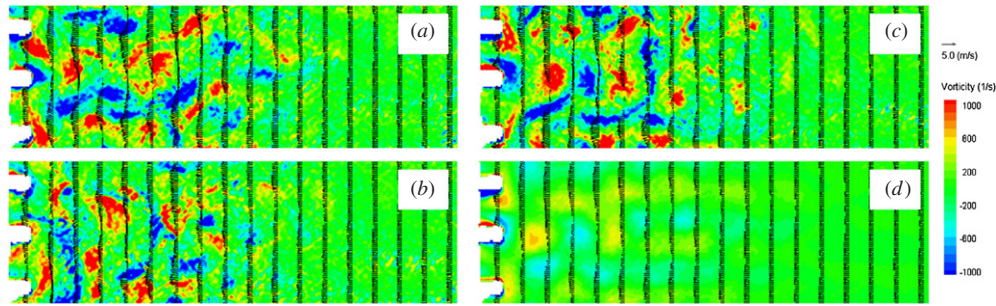


**Figure 8.** Illustration of the variability between vortex structures in three instantaneous images of the vorticity field (a)–(c). The average vorticity field resulting from ensemble averaging of 100 instantaneous images (d). Stack I,  $Dr = 1.0\%$ , phase  $\Phi_{12}$ .

II. Here the drive ratio is relatively low:  $0.6\%$ ; the selected phase is  $\Phi_6$ . In the references mentioned above, this type of flow pattern is referred to as symmetrical attached vortices on the basis of the averaged vorticity field. However, it is clear from the instantaneous images that the main vortices shed from the plate behave in a somewhat unsteady manner: they assume different shapes, strengths and spatial locations. In the ensemble-averaged vorticity field these features are simply filtered out as are some of the small-scale vortex structures, present in the flow field.

Figure 7 shows a similar comparison between the instantaneous and averaged vorticity fields for stack II at a significantly higher drive ratio of  $2.0\%$ , for a selected phase angle  $\Phi_8$  (note that this is a ‘zoomed-out’ view compared to figure 6). It can be seen that while the instantaneous images show a degree of chaotic behaviour and a multitude of vortex scales, the ensemble-averaged image in figure 7(d) still brings out an orderly von Karman-like vortex pattern, albeit with somewhat smaller vorticity magnitudes and spatially ‘smoothed out’. Figure 8 shows similar comparisons between instantaneous and ensemble-averaged flow fields for stack I and  $Dr = 1.0\%$ , except that phase  $\Phi_{12}$  has been chosen, in order to illustrate the impingement of vortex structures back onto the stack, taking place in the suction phase of the cycle.

The vorticity maps shown in this section clearly show that vortex shedding processes are stochastic in the sense that vortex strength, size and location are random and could be classed as quasi-periodic in nature (unlike the well-known von Karman vortex shedding). The latter is particularly clear when analysing the Fourier transforms of point-wise hot-wire measurements in the wake of the plate as already shown in [24]. Unfortunately, this feature could not be brought out in the current PIV study because the system repetition rate is too low to look at a single cycle at a high temporal resolution.

#### 4.4. Turbulence versus ‘total fluctuation’ intensity—spatial distribution

As already mentioned in section 4.2, for the cyclic flows as discussed in our paper, calculation of the time-series statistics (even if high-speed PIV was available) makes little sense due to the time dependence of the underlying mean flow. Therefore, it is usually assumed that the processes are ergodic and the data are collected at a fixed instant (phase) for a set of different

cycles in order to calculate the flow statistics at that selected phase. In the classical description of turbulent flows, the rms values of velocity fluctuations as defined by equations (5) and (6) lead to the concept of ‘turbulence intensity’ using an appropriately selected reference velocity from the mean flow. However, as discussed below, such calculations tend to take into account the unsteadiness introduced by the large-scale coherent structures together with the contributions from small-scale vortex structures usually understood as ‘turbulence’. This distinction may be important from the point of view of heat transfer modelling that may be the ultimate objective in the thermoacoustic context.

Therefore, for the purpose of this paper, it is proposed to use somewhat different terminology: the velocity fluctuations described by equations (5) and (6) would give rise to a ‘fluctuation intensity’. This is denoted as  $T$  (with appropriate indices as necessary) and calculated using the classical concepts of ‘turbulence intensity’. On the other hand, appropriately spatially filtered velocity fields (as described later in section 4.5) would give rise to ‘small-scale turbulence intensity’ (denoted as  $\theta$ ), understood as the contribution from vortex structures smaller than a certain cut-off length scale.

In view of the instantaneous and averaged PIV images discussed in the previous section, this section attempts to present a statistical description of the unsteady processes of vortex shedding occurring in the oscillatory flows, using the concept of the above-mentioned ‘fluctuation intensity’. Using the approach proposed by Pai [46] (for the classical turbulence intensity), the ‘fluctuation intensity’ could be similarly defined as

$$T_x = \sqrt{\overline{u^2}}/U^*; \quad T_y = \sqrt{\overline{v^2}}/U^*; \quad T_z = \sqrt{\overline{w^2}}/U^*, \quad (7)$$

where the overbar indicates a temporal mean function and  $U^*$  is a suitably chosen reference velocity. However, an alternative definition (also given by Pai [46]) suggests that the ‘fluctuation intensity’ could also be defined as a sum of components in all directions according to the following formula:

$$T = \sqrt{\frac{1}{3}(\overline{u^2} + \overline{v^2} + \overline{w^2})}/U^*. \quad (8)$$

Discussion in this section is limited to only a two-dimensional velocity field ( $u$  and  $v$ ) acquired from the 2D PIV measurements. To enable the comparison of the level of velocity fluctuations for different velocity amplitudes and

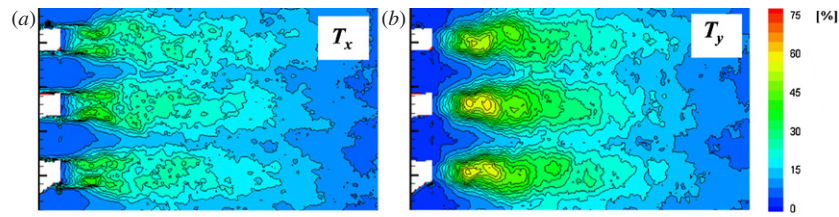


Figure 9. Distribution of  $x$  and  $y$  components of fluctuation intensity:  $T_x$  and  $T_y$ ; stack II,  $Dr = 2.0\%$ , phase  $\Phi_8$ .

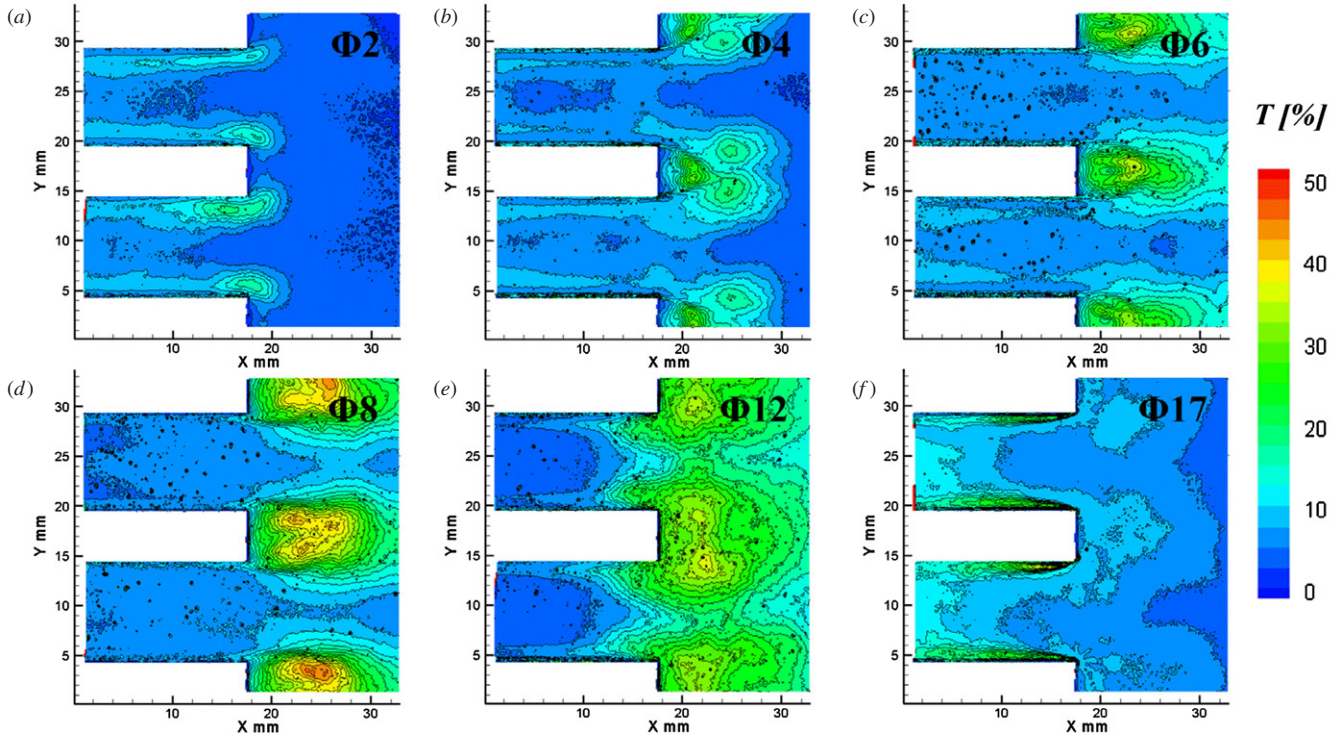


Figure 10. Distribution of the total fluctuation intensity,  $T$ ; stack II,  $Dr = 0.6\%$ .

various stacks, the ‘fluctuation intensities’ in the  $x$  and  $y$  directions,  $T_x$  and  $T_y$ , can be used (equation (7)), where the reference velocity is simply the amplitude of the mean velocity in the  $x$  direction,  $U_a$  (i.e. the acoustic velocity amplitude). However, it is perhaps somewhat easier to look at the combined quantity (total fluctuation intensity), by analogy to equation (8), which takes into account the velocity fluctuations in both the  $x$  and  $y$  directions, namely

$$T = \sqrt{u^2(x, y, \Phi) + v^2(x, y, \Phi)}/U_a. \quad (9)$$

Figure 9 shows the results of calculating the spatial distribution of  $x$  and  $y$  components of the fluctuation intensity within the PIV field of view for a selected case of stack II, drive ratio  $Dr = 2.0\%$  and phase  $\Phi_8$  (i.e. the case presented in figure 7). In the example presented, it can be clearly seen that the level of velocity fluctuations in the  $y$  direction (figure 9(b)) reaches around 50% level, which is relatively high and comparable to total fluctuation intensities that may occur in strong vortex wakes and highly reversed flows. However, as indicated at the beginning of this section, the interpretation of plots such as in figures 9(b) (or (a)) is not straightforward. It needs to be remembered that this particular type of flow contains

a mixture of large-scale coherent structures (discrete eddies) and smaller scale structures (which one would normally refer to as ‘turbulence’). It seems reasonable to assume that the large variation of velocity from one instantaneous image to the next may well be caused by the variation in the position of the large vortices, not the intensity of small-scale velocity fluctuations. Furthermore, it can be hypothesized that a high level of the fluctuation intensity in figure 9(b) corresponds to relatively high lateral displacements of vortex structures from cycle-to-cycle, while somewhat smaller turbulence intensities appearing in figure 9(a) may indicate a relatively lower level of longitudinal (stream-wise) variation in the position of discrete eddies from one cycle to another. However, the spatial distribution of  $x$  and  $y$  fluctuation intensities is relatively similar—therefore to simplify the results’ presentation in what is to follow, the total fluctuation intensity levels (equation (9)) will be presented. For example graphs 9(a) and 9(b) become ‘combined’ within the total fluctuation level  $T$  shown in graph 11(d).

Figure 10 shows the total fluctuation intensity distribution for six representative phases in the acoustic cycle for the case of stack II and drive ratio  $Dr = 0.6\%$  (cf figure 6), while

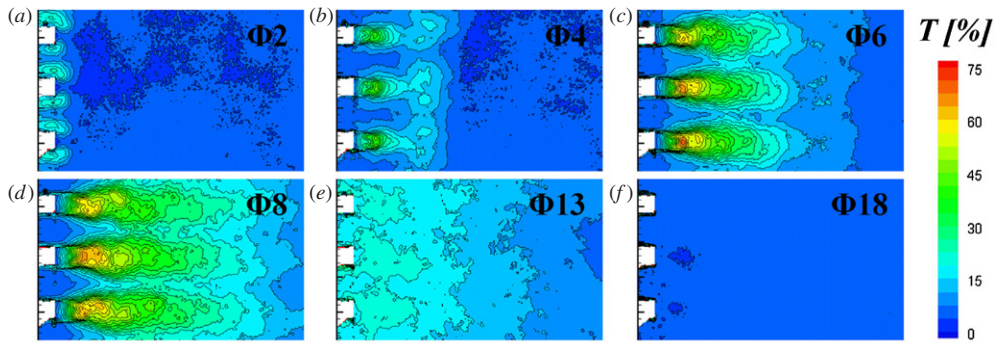


Figure 11. Distribution of the total fluctuation intensity,  $T$ ; stack II,  $Dr = 2.0\%$ .

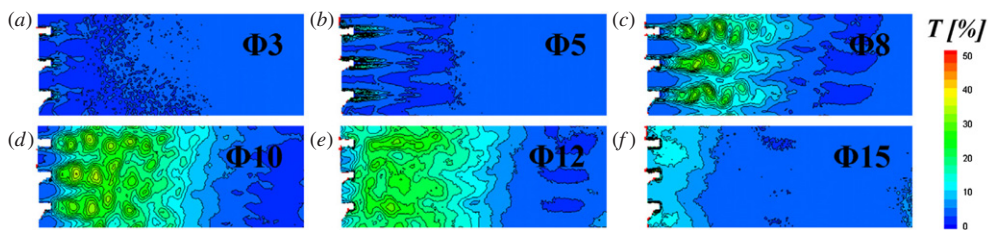


Figure 12. Distribution of the total fluctuation intensity,  $T$ ; stack I,  $Dr = 1.0\%$ .

figure 11 shows the total fluctuation intensity for six representative phases for the case of stack II and drive ratio  $Dr = 2.0\%$  (cf figure 7). Finally, figure 12 shows the total fluctuation intensity for six representative phases for the case of stack I and drive ratio  $Dr = 1.0\%$ .

It is clear that the statistics of the velocity fluctuations in the oscillatory flow around the end of the parallel-plate stack is closely related to the main flow features discussed in section 4.3 and in particular mirrors the behaviour (and unsteadiness) of the coherent structures that are present in the mean flow. The high velocity fluctuations occur during the ejection stage and are located outside of the stack; the peak values generated usually between phases  $\Phi_6$  and  $\Phi_{10}$ , i.e. in the deceleration phases of the ejection cycle. It can also be easily seen by inspecting figures similar to figures 10–12 obtained for all experimental cases where the level of fluctuations grows with the drive ratio; however, there must be differences between absolute values of  $T$  and its spatial distribution for the two stacks tested here.

To have some overall measure of flow unsteadiness, the turbulence kinetic energy, defined as

$$k = \frac{1}{2}(\overline{u^2} + \overline{v^2} + \overline{w^2}), \quad (10)$$

can be analysed ( $w$  component is simply taken as zero in two-dimensional analysis). Strictly speaking, this may have to be re-defined as ‘fluctuation kinetic energy’ to follow the logic of ‘fluctuation intensities’ described earlier. However, it is not thought to be necessary for the purpose of this paper. An integral of  $k$  was calculated over an area corresponding to one plate segment, and extending from the plate’s end 48.6 mm out of the stack (this was the maximum field of view that was obtained in the experiments for stack I), and then normalized by the area. Such an approach is often used in meteorological studies such as [47] and [48]. Figure 13(a)

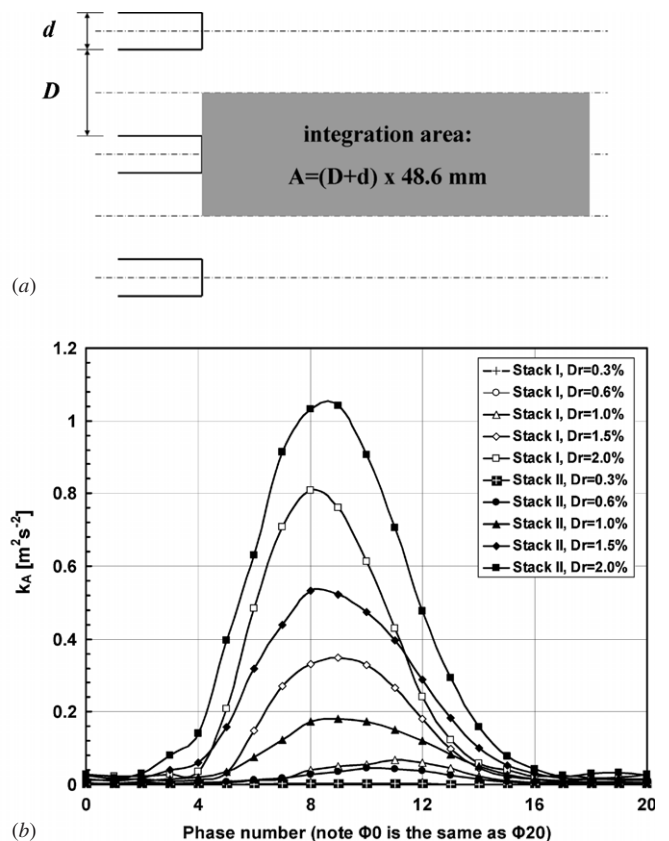
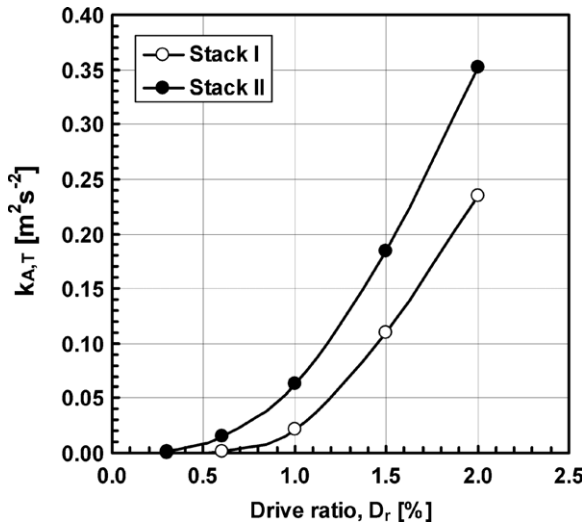


Figure 13. Illustration of the integration area for calculating averaged turbulent kinetic energy  $k_A$  over a sample area  $A$  (a); plot of  $k_A$  as a function of phase in the cycle for all experimental configurations (b).

illustrates schematically the integration area. For stack I it is 6.1 mm wide and for stack II it is 15 mm wide. The



**Figure 14.** Area- and cycle-averaged turbulent kinetic energy  $k_{A,T}$  as a function of drive ratio.

spatially averaged turbulence kinetic energy can be written as follows:

$$k_A = \frac{1}{A} \iint_A k(x, y, \Phi) dA. \quad (11)$$

Figure 13(b) shows the plots of  $k_A$  for all experimental cases as a function of phase in the cycle. As expected, the energy is low for cases when the oscillation is weak (drive ratios 0.3% and 0.6% for both stacks), but becomes appreciable for higher drive ratios. It is also clear that its magnitude is higher for stack II than for stack I. This is again not surprising due to the fact that the separations on relatively thicker plates generally produce stronger concentrated vortices that contribute more strongly to fluctuation intensities. Finally it is possible to integrate the curves such as those shown in figure 13(b) over the oscillation cycle to obtain an area- and cycle-averaged turbulent kinetic energy (denoted  $k_{A,T}$ ), which is illustrated in figure 14. It is possible to interpret this graph as an indication of the total energy contained in the flow related to velocity fluctuations due to coherent structures and small-scale turbulence.

#### 4.5. Separation of fluctuation intensity with regard to length scales: small-scale turbulence intensity

In the existing literature there have been many studies undertaken to investigate the effects of the turbulence intensity on heat transfer from solid bodies, such as circular cylinder [49, 50], elliptical cylinder [50], sphere [51] etc. For example, Kondjoyan and Daudin [50] studied the effect of the free stream turbulence intensity on the heat transfer coefficient on a circular cylinder and an elliptical cylinder when the Reynolds number was between 5000 and 30 000. The heat transfer coefficient,  $Nu$ , when the turbulence intensity is 40%, has a value of about two times its value when the turbulence intensity is 1.5%, which suggests that it is the small-scale turbulence (as opposed to large coherent structures) that is a major contributor to the heat transfer mechanisms. In [52, 53] the effects that the integral length scale, which characterizes

the dimension of eddies in the flow, may have on the heat transfer have also been investigated. Sak *et al* [53] observed a decrease in the heat transfer coefficient,  $Nu$ , with the increase of the relative turbulence length scale from 0.5 to 1.47, when the relative turbulence intensity of the flow towards a circular cylinder is kept constant at about 6.7%. Since the turbulence scale may be an important contributor to the intensity of the heat transfer and the current study is intended as a precursor to turbulence characterization in oscillatory flows, it seems appropriate to develop tools that could distinguish between the turbulence intensities contributed by various turbulence length scales present within the flow.

The instantaneous velocities  $u$  and  $v$ , following Reynolds decomposition and the definition in equations (3)–(6), are divided into the ensemble-averaged velocity and the fluctuation from the ensemble-averaged velocity:

$$\begin{aligned} u(x, y, \Phi, i) &= U(x, y, \Phi) + u'(x, y, \Phi, i); \\ v(x, y, \Phi, i) &= V(x, y, \Phi) + v'(x, y, \Phi, i). \end{aligned} \quad (12)$$

The idea behind the data processing described below is that it should be possible to further divide the fluctuation component into large- and small-scale fluctuations according to a specified cut-off length  $\lambda$  related to the size of the eddies present in the flow:

$$\begin{aligned} u(x, y, \Phi, i) &= U(x, y, \Phi) + u'_l(x, y, \Phi, i, \lambda) \\ &\quad + u'_s(x, y, \Phi, i, \lambda) \\ v(x, y, \Phi, i) &= V(x, y, \Phi) + v'_l(x, y, \Phi, i, \lambda) \\ &\quad + v'_s(x, y, \Phi, i, \lambda), \end{aligned} \quad (13)$$

where  $u'_l$ ,  $v'_l$ ,  $u'_s$  and  $v'_s$  indicate the large-scale fluctuations and small-scale fluctuations of velocity components  $u$  and  $v$ , respectively.

The rms value of the large-scale fluctuation ( $u'_l$  and  $v'_l$ ) and small-scale fluctuation ( $u'_s$  and  $v'_s$ ) would quantify the amount of the variation of each component at each phase at a position  $(x, y)$  with a cut-off length  $\lambda$ :

$$\begin{aligned} u'_{l,rms}(x, y, \Phi, \lambda) &= \sqrt{\frac{1}{N} \sum_{i=1}^N u_l'^2(x, y, \Phi, i, \lambda);} \\ v'_{l,rms}(x, y, \Phi, \lambda) &= \sqrt{\frac{1}{N} \sum_{i=1}^N v_l'^2(x, y, \Phi, i, \lambda)} \\ u'_{s,rms}(x, y, \Phi, \lambda) &= \sqrt{\frac{1}{N} \sum_{i=1}^N u_s'^2(x, y, \Phi, i, \lambda);} \\ v'_{s,rms}(x, y, \Phi, \lambda) &= \sqrt{\frac{1}{N} \sum_{i=1}^N v_s'^2(x, y, \Phi, i, \lambda).} \end{aligned} \quad (14)$$

Thus, a combined quantity to denote the amount of variation of velocity fluctuation at a large scale and small scale can be respectively described by  $\sqrt{u_{l,rms}^2 + v_{l,rms}^2}/U_a$  and  $\sqrt{u_{s,rms}^2 + v_{s,rms}^2}/U_a$  (the latter according to the nomenclature introduced in section 4.4 could be denoted as  $\theta$ ). Their values are normalized by the amplitude of the mean velocity to indicate the relative strength.

In order to separate the small-scale and large-scale fluctuations of the flow, a two-dimensional spatial fast Fourier

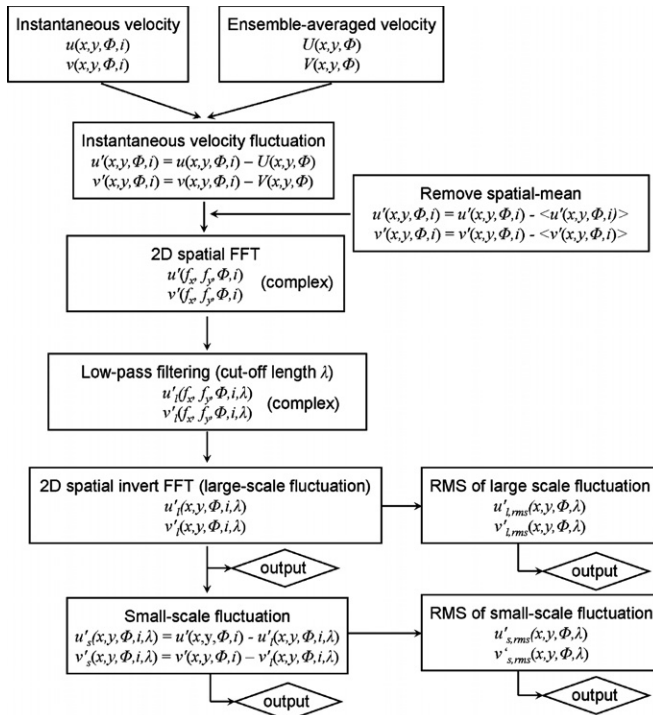


**Figure 15.** Schematic of the spatial filtering algorithm based on 2D FFT, for separating instantaneous velocity fields according to the length scales of eddies present in the flow.

transform (FFT) technique has been designed, and the essence of the calculation algorithm is illustrated in figure 15. The ensemble-averaged velocity field was first subtracted from the instantaneous two-dimensional velocity field to obtain the fluctuating velocity fields containing components  $u'(x, y, \Phi, i)$  and  $v'(x, y, \Phi, i)$ . Such ‘instantaneous fluctuating velocity fields’ were then separated into  $u$  and  $v$  components and each was separately transformed using the FFT into the spatial-frequency domain. Figure 16 shows the 2D amplitude spectra computed from the instantaneous fluctuation ( $u'$ ,  $v'$ ) using 2D spatial FFT for the velocity field which is depicted in figure 7(c). Interestingly, the high intensity ‘peaks’ in the

centre form relatively regular patterns and it is thought that they correspond to large-scale (low ‘wave-number’) coherent structures. Similar behaviour of the FFT was also observed by Piirto *et al* [54] for vortex shedding in steady flows. The rather random distribution of much lower amplitudes around the centre is thought to originate from the smaller scale (higher ‘wave-number’) eddies responsible for what was defined in section 4.4 as ‘small-scale turbulence’.

Subsequently, low-pass filtering was carried out by setting to zero all the Fourier coefficients below the desired cut-off characteristic length  $\lambda$ . The instantaneous low-pass filtered fluctuation velocity fields in the space domain were obtained by an inverse Fourier transform of the velocity data in the spatial-frequency domain. The high-pass filtered fluctuation velocity field for each instant was obtained by subtracting the low-pass filtered fluctuation velocity field and the ensemble-averaged velocity field from the instantaneous velocity field. Of course, the cut-off spatial-frequency or cut-off length  $\lambda$  is a critical parameter in the process of spatial filtering in order to separate the contribution of small-scale fluctuations from large-scale fluctuations. However, the determination of its value is rather arbitrary in this case and is partly limited by the spatial resolution of the velocity field from 2D PIV results.

Figure 17 (again based on the results shown in figure 7(c)) shows the decomposition of an instantaneous velocity field into two parts: the large-scale velocity fluctuation field (top row) and the small-scale velocity fluctuation field (bottom row), based on the original ensemble-averaged field shown in figure 7(d) and the instantaneous field shown in (c). The vorticity fields shown in figure 17 are simply reconstructed using the fluctuation component of velocity to visualize the different vorticity scales. The cut-off length  $\lambda$  was set as 1.9 mm (left column) and 3.9 mm (right column) respectively. A substantial part of the flow structures formed at the plate ends is included in the large-scale fluctuations, and they are essentially different in strength, size and location from instant to instant; otherwise they would have been included in the ensemble-averaged flow field. The reconstructed vorticity field below the cut-off length scales reveals randomly distributed small-scale eddies that would

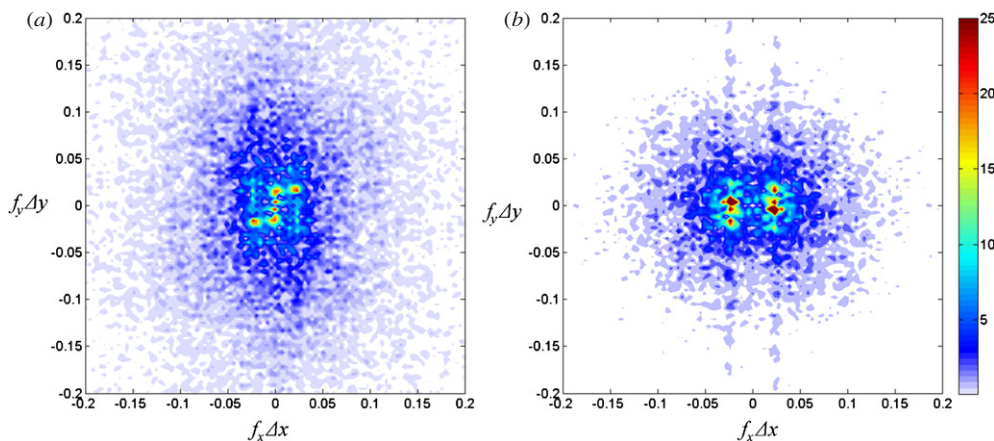


**Figure 16.** 2D amplitude spectrum maps computed from the instantaneous fluctuation  $u'$  (a) and  $v'$  (b) using 2D spatial FFT  $f_x \Delta x$  and  $f_y \Delta y$  being the spatial-frequency in the respective directions. An arbitrary scale is used for comparisons.

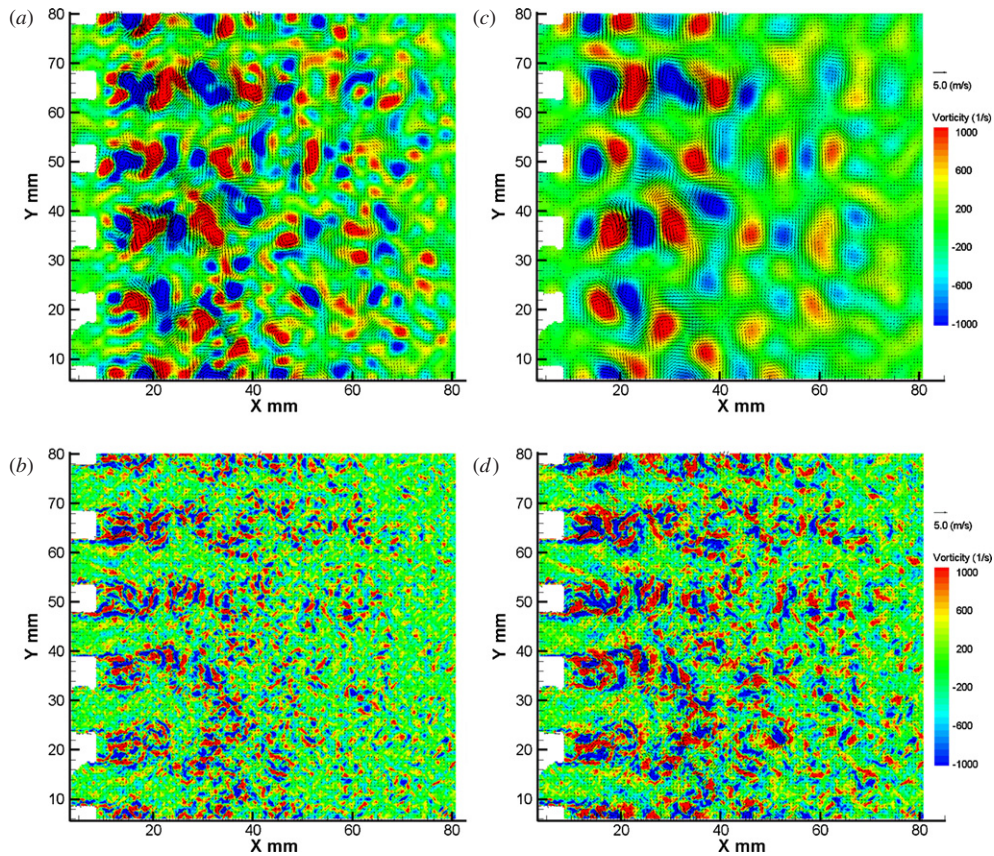


**Figure 17.** Velocity and vorticity fields obtained from spatial filtering of data shown in figure 7(c), using the cut-off length of 1.9 mm (a) and (b), and 3.9 mm (c) and (d). The top row shows large-scale vortex structures obtained from instantaneous velocity fluctuation after low-pass filtering, while the bottom row corresponds to high-pass filtering. Stack II,  $Dr = 2.0\%$ , phase  $\Phi_8$ .

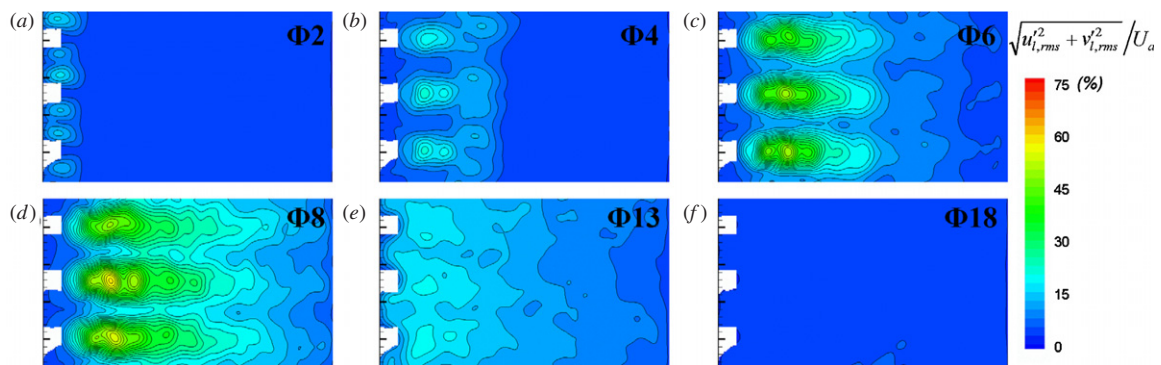


**Figure 18.** Distribution of the relative large-scale fluctuation; stack II,  $Dr = 2.0\%$ ,  $\lambda = 3.9$  mm.

be responsible for ‘small-scale turbulence’ as described in section 4.4.

The distributions of the combined rms value of large-scale fluctuation and small-scale fluctuation (turbulence intensity) are shown in figures 18 and 19 respectively, for the case of stack II at  $Dr = 2.0\%$ , and the cut-off length chosen as 3.9 mm. The regions in the flow field affected by the large- and small-scale fluctuation are somewhat similar at each individual phase, although small-scale fluctuation tends to be stronger in an area closer to the plate end. It is interesting to see that the combined rms value of large-scale fluctuation can reach about 50% of the mean velocity amplitude, while the combined rms value

of small-scale fluctuation is rarely more than 20% of the mean velocity amplitude. Compared with the distribution of the total fluctuation intensity shown in figure 11, the distribution of the combined rms value of large-scale fluctuation reveals that it contributes a large part to the evaluated total fluctuation intensity at least at this test condition.

## 5. Conclusion and future work

This paper addresses the need for understanding turbulence characteristics of oscillatory flows past a stack of parallel plates. This particular configuration is important in the

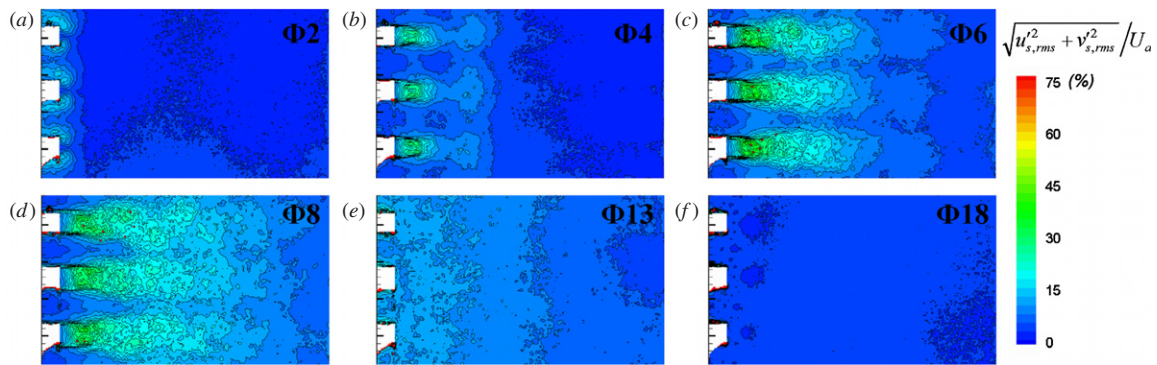


**Figure 19.** Distribution of the relative small-scale fluctuation; stack II,  $Dr = 2.0\%$ ,  $\lambda = 3.9$  mm.

context of thermoacoustic engines and refrigerators, where an oscillatory flow is responsible for hydrodynamic energy transport along the stack, but also facilitates heat transfer between the stack and adjacent heat exchangers. The focus of this work is on the development of PIV measurement techniques and methods of data processing and representation for characterization of turbulent flows at the end of the parallel-plate stack.

A typical focus of the previous work was on the flow pattern characterization of the fluid motion out of the stack (i.e. ejection stage) based on the ensemble averaging of a large number of phase-locked PIV images. However, the presented results indicate that such a description is relatively simplistic. The cycle-to-cycle variability of the flow field can be very significant, and to the authors' knowledge this aspect has not gained a sufficient recognition. The results presented in this paper show that it is possible to describe the unsteady/turbulent flow behaviour using classical Reynolds decomposition and subsequently analyse the fluctuation intensity 'maps'. Furthermore, it has been suggested that simplified parameters such as area-averaged or area-cycle-averaged turbulent kinetic energy can be used to compare the flow unsteadiness generated by different stack configurations and flow forcing. It is hoped that such data could help the modelling efforts on predicting the heat transfer rates between stacks and heat exchangers. However, in addition to the classical approach of calculating the fluctuation intensities a new methodology was proposed for spatial filtering of instantaneous fluctuation velocity fields in order to separate the contributions from large- and small-scale flow structures to the overall fluctuation intensity. It has been suggested that the term 'turbulence intensity' should only be associated with the small-scale vortex structures, which are more likely to control the heat transfer processes.

However, the work presented is only a first step in developing a deeper understanding of energy transfer processes in thermoacoustic systems. There are two clear shortcomings of current approach. Firstly, the configuration is simplified to enable the evaluation of measurement methodologies—in reality the stack will be coupled to a heat exchanger and so the flow field will be much more complicated, especially as the two structures would effectively be in each other's wakes. Secondly, the arrangement studied is isothermal, and so there is no opportunity to

study the actual heat transfer processes. Therefore, a further improvement would be to impose appropriate thermal boundary conditions on the structures studied and combine PIV with temperature field measurement, for example, by planar laser-induced fluorescence (PLIF). These will be the directions of future experimental work. Finally, based on such experimental results, significant research effort is needed on performing similarity analysis on a wide range of geometrical configurations to formulate criterial equations describing the energy transfer mechanisms.

## Acknowledgments

The authors wish to thank the Engineering and Physical Sciences Research Council UK for supporting this work under grants GR/S26842/01, GR/T04502/01 (EPSRC Advanced Research Fellowship), GR/T04519/01 and EP/E044379/1.

## References

- [1] Swift G W 1988 Thermoacoustic engines *J. Acoust. Soc. Am.* **84** 1145–80
- [2] Yazaki T, Iwata A, Maekawa T and Tominaga A 1998 Traveling wave thermoacoustic engine in a looped tube *Phys. Rev. Lett.* **81** 3128–31
- [3] Rott N 1980 Thermoacoustics *Adv. Appl. Mech.* **20** 135–75
- [4] Adrian R J 2005 Twenty years of particle image velocimetry *Exp. Fluids* **39** 159–69
- [5] Schroeder A and Willert C E 2008 *Particle Image Velocimetry—New Developments and Recent Applications* (Berlin: Springer)
- [6] Kompenhans J and Tropea C 1997 Editorial *Meas. Sci. Technol.* **8** (12) doi:10.1088/0957-0233/8/12/001
- [7] Trinité M and Lecordier B 2001 Editorial *Meas. Sci. Technol.* **12** (9) doi:10.1088/0957-0233/12/9/001
- [8] Tropea C 2002 Editorial *Meas. Sci. Technol.* **13** (7) doi:10.1088/0957-0233/13/7/001
- [9] Hinsch K D and Herrmann S F 2004 Holographic particle image velocimetry (Editorial) *Meas. Sci. Technol.* **15** (4) doi:10.1088/0957-0233/15/4/E01
- [10] Sung H J, Kim K C and Lee S J 2004 5th International Symposium on Particle Image Velocimetry, PIV '03 (Editorial) *Meas. Sci. Technol.* **15** (6) doi:10.1088/0957-0233/15/6/E01
- [11] Okamoto K 2006 6th International Symposium on Particle Image Velocimetry 2005 (Editorial) *Meas. Sci. Technol.* **17** (7) doi:10.1088/0957-0233/17/7/E01
- [12] Guibert P and Lemoyne L 2002 Dual particle image velocimetry for transient flow field measurements:

- autocorrelation estimation of in-cylinder flow of a spark ignition engine turbulence *Exp. Fluids* **33** 355–67
- [13] Bevan K E and Ghandhi J B 2008 Particle image velocimetry measurements of in-cylinder flow in a four-stroke utility engine and correlation with combustion measurements *J. Eng. Gas Turbines Power* **130** 032802-1–11
- [14] Reuss D L, Megerle M and Sick V 2002 Particle-image velocimetry measurement errors when imaging through a transparent engine cylinder *Meas. Sci. Technol.* **17** 1029–35
- [15] Hann D B and Greated C A 1997 Particle image velocimetry for the measurement of mean and acoustic particle velocities *Meas. Sci. Technol.* **8** 656–60
- [16] Hann D B and Greated C A 1997 The measurement of flow velocity and acoustic particle velocity using particle-image velocimetry *Meas. Sci. Technol.* **8** 1517–22
- [17] Campbell M, Cosgrove J A, Greated C A, Jack S and Rockliff D 2000 Review of LDA and PIV applied to the measurement of sound and acoustic streaming *Opt. Laser Technol.* **32** 629–39
- [18] Nabavi M, Siddiqui M H K and Dargahi J 2007 Simultaneous measurement of acoustic and streaming velocities using synchronized PIV technique *Meas. Sci. Technol.* **18** 1811–7
- [19] Debesse Ph, Baltean-Carlès D, Lusseyran F and François M-X 2008 Experimental analysis of nonlinear phenomena in a thermoacoustic system *AIP Conf. Proc.* **1022** 355–8
- [20] Blanc-Benon P, Besnoin E and Knio O M 2003 Experimental and computational visualization of the flow in a thermoacoustic stack *C R. Méc.* **331** 17–24
- [21] Castrejón-Pita J R, Castrejón-Pita A A, Huelsz G and Tovar R 2006 Experimental demonstration of the Rayleigh acoustic viscous boundary layer theory *Phys. Rev. E* **73** 036601
- [22] Berson A and Blanc-Benon Ph 2007 Nonperiodicity of the flow within the gap of a thermoacoustic couple at high amplitudes *J. Acoust. Soc. Am.* **122** EL122–7
- [23] Berson A, Michard M and Blanc-Benon Ph 2008 Measurement of acoustic velocity in the stack of a thermoacoustic refrigerator using particle image velocimetry *Heat Mass Transfer* **44** 1015–23
- [24] Mao X, Yu Z, Jaworski A J and Marx D 2008 PIV studies of coherent structures generated at the end of a stack of parallel plates in a standing wave acoustic field *Exp. Fluids* **45** 833–46
- [25] Aben P C H, Bloemen P R and Zeegers J C H 2009 2D PIV measurements of oscillatory flow around parallel plates *Exp. Fluids* **46** 631–41
- [26] Jaworski A J, Mao X, Mao X and Yu Z 2009 Entrance effects in the channels of the parallel plate stack in oscillatory flow conditions *Exp. Therm. Fluid Sci.* **33** 495–502
- [27] Worlikar A S and Knio O M 1996 Numerical simulation of a thermoacoustic refrigerator. Part I: unsteady adiabatic flow around the stack *J. Comput. Phys.* **127** 424–51
- [28] Worlikar A S, Knio O M and Klein R 1998 Numerical simulation of a thermoacoustic refrigerator. Part II: stratified flow around the stack *J. Comput. Phys.* **144** 299–324
- [29] Besnoin E and Knio O M 2004 Numerical study of thermoacoustic heat exchangers *Acta Acust. –Acust.* **90** 432–44
- [30] Marx D and Blanc-Benon Ph 2004 Computation of the mean velocity field above a stack plate in a thermoacoustic refrigerator *C. R. Mec.* **332** 867–74
- [31] Marx D, Mao X and Jaworski A J 2006 Acoustic coupling between the loudspeaker and the resonator in a standing-wave thermoacoustic device *Appl. Acoust.* **67** 402–19
- [32] Keane R D and Adrian R J 1990 Optimization of particle image velocimeters. Part I: double pulsed systems *Meas. Sci. Technol.* **1** 1202–15
- [33] Melling A 1997 Tracer particles and seeding for particle image velocimetry *Meas. Sci. Technol.* **8** 1406–16
- [34] King L V 1934 On the acoustic radiation pressure on spheres *Proc. R. Soc. Lond. A* **147** 212–40
- [35] Raffel M, Willert C E, Wereley S T and Kompenhans J 2007 *Particle Image Velocimetry, A Practical Guide* 2nd edn (Berlin: Springer)
- [36] Keane R D and Adrian R J 1991 Optimization of particle image velocimeters: II. Multiple pulsed systems *Meas. Sci. Technol.* **2** 963–74
- [37] Hart D P 1999 Super-resolution PIV by recursive local-correlation *J. Vis.* **3** 187–94
- [38] Zimmerman W B 2002 The drag on sedimenting discs in broadside motion in tubes *Int. J. Eng. Sci.* **40** 7–22
- [39] Zimmerman W B 2004 On the resistance of a spherical particle settling in a tube of viscous fluid *Int. J. Eng. Sci.* **42** 1753–78
- [40] Womersley J R 1955 Method for the calculation of velocity, rate of flow and viscous drag in arteries when the pressure gradient is known *J. Physiol.* **127** 553–63
- [41] Arnott W P 1991 General formulation of thermoacoustics for stack having arbitrarily shaped pore cross sections *J. Acoust. Soc. Am.* **90** 3228–37
- [42] Hino M, Kashiwayanagi M, Nakayama A and Hara T 1983 Experiments on the turbulence statistics and the structure of a reciprocating oscillatory flow *J. Fluid Mech.* **131** 363–400
- [43] Hyun B S, Balachandar R, Yu K and Patel V C 2003 Assessment of PIV to measure mean velocity and turbulence in open-channel flow *Exp. Fluids* **35** 262–7
- [44] Cenedese A, Doglia G, Romano G P, De Michele G and Tanzini G 1994 LDA and PIV velocity measurements in free jets *Exp. Therm. Fluid Sci.* **9** 125–34
- [45] Regunath G S, Zimmerman W B, Tesař V and Hewakandamby B N 2008 Experimental investigation of helicity in turbulent swirling jet using dual-plane dye laser PIV technique *Exp. Fluids* **45** 973–86
- [46] Pai S-I 1957 *Viscous Flow Theory: II. Turbulent Flow* (New York: Van Nostrand)
- [47] Nelson M A, Brown M J, Pardyjak E R and Klewicki J C 2004 Area-averaged profiles over the mock urban setting test array *Proc. 5th Symp. on the Urban Environment (23–26 August)* pp 577–81
- [48] Nelson M A, Pardyjak E R, Klewicki J C, Pol S U and Brown M J 2007 Properties of the wind field within the Oklahoma city park avenue street canyon. Part I: mean flow and turbulence statistics *J. Appl. Meteorol. Climatol.* **46** 2038–54
- [49] Lowery G W and Vachon R I 1975 The effect of turbulence on heat transfer from heated cylinders *Int. J. Heat Mass Transfer* **18** 1229–42
- [50] Kondjoyan A and Daudin J D 1995 Effects of free stream turbulence intensity on heat and mass transfers at the surface of a circular cylinder and an elliptical cylinder, axis ratio 4 *Int. J. Heat Mass Transfer* **38** 1735–49
- [51] Lavender W J and Pei D C T 1967 The effect of fluid turbulence on the rate of heat transfer from spheres *Int. J. Heat Mass Transfer* **10** 529–39
- [52] Peyrin F and Kondjoyan A 2002 Effect of turbulent integral length scale on heat transfer around a circular cylinder placed cross to an air flow *Exp. Therm. Fluid Sci.* **26** 455–60
- [53] Sak C, Liu R, Ting D S-K and Rankin G W 2007 The role of turbulence length scale and turbulence intensity on forced convection from a heated horizontal circular cylinder *Exp. Therm. Fluid Sci.* **31** 279–89
- [54] Piirto M, Ihalainen H, Eloranta H and Saarenrinne P 2001 2D spectral and turbulence length scale estimation with PIV *J. Vis.* **4** 39–49

## Chapter 7

# Oscillatory flow at the end of parallel plate stacks – phenomenological and similarity analysis

by X. Mao and A. J. Jaworski

Published in: *Fluids Dynamics Research*

# Oscillatory flow at the end of parallel-plate stacks: phenomenological and similarity analysis

Xiaoan Mao and Artur J Jaworski

School of Mechanical, Aerospace and Civil Engineering, The University of Manchester, George Begg Building, Sackville Street, Manchester M13 9PL, UK

E-mail: [a.jaworski@manchester.ac.uk](mailto:a.jaworski@manchester.ac.uk)

Received 6 September 2009, in final form 21 May 2010

Published 18 August 2010

Online at [stacks.iop.org/FDR/42/055504](http://stacks.iop.org/FDR/42/055504)

Communicated by M Asai

## Abstract

This paper addresses the physics of the oscillatory flow in the vicinity of a series of parallel plates forming geometrically identical channels. This type of flow is particularly relevant to thermoacoustic engines and refrigerators, where a reciprocating flow is responsible for the desirable energy transfer, but it is also of interest to general fluid mechanics of oscillatory flows past bluff bodies. In this paper, the physics of an acoustically induced flow past a series of plates in an isothermal condition is studied in detail using the data provided by PIV imaging. Particular attention is given to the analysis of the wake flow during the ejection part of the flow cycle, where either closed recirculating vortices or alternating vortex shedding can be observed. This is followed by a similarity analysis of the governing Navier–Stokes equations in order to derive the similarity criteria governing the wake flow behaviour. To this end, similarity numbers including two types of Reynolds number, the Keulegan–Carpenter number and a non-dimensional stack configuration parameter,  $d/h$ , are considered and their influence on the phenomena are discussed.

(Some figures in this article are in colour only in the electronic version)

## 1. Introduction and background

In thermoacoustic devices, an acoustic wave interacts with internal solid structures (referred to as thermoacoustic stacks or regenerators) either to produce acoustic power, induced by a temperature gradient on the stack (an engine), or to obtain a temperature gradient along the stack, induced by an imposed acoustic wave (a cooler). This is based on the well-known thermoacoustic effect (Rayleigh 1894), where appropriately phased pressure and velocity oscillations enable the compressible fluid to undergo a thermodynamic cycle in the vicinity of a solid body. Figure 1 shows schematically the physics behind generating useful acoustic energy in a standing wave thermoacoustic engine. Detailed analysis is provided by Swift (1988).

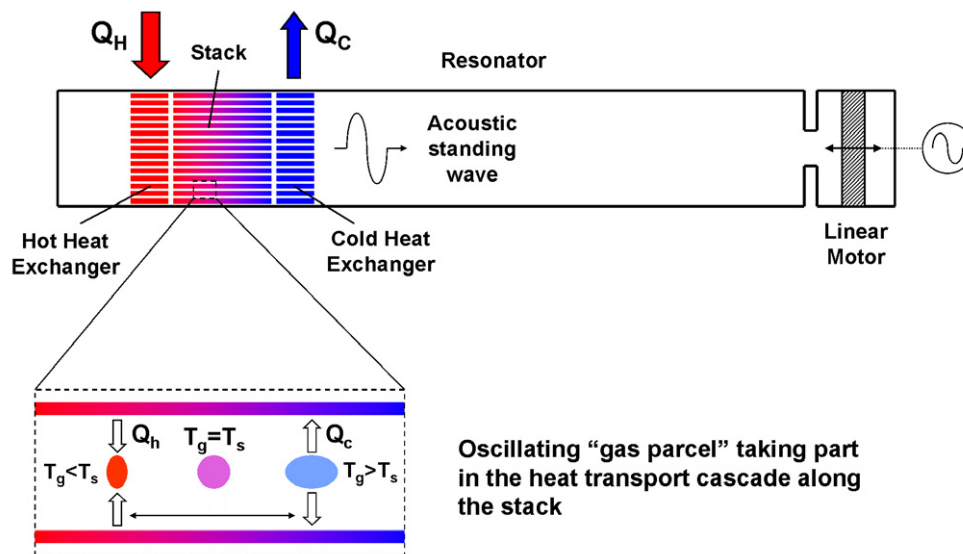


Figure 1. Illustration of the oscillatory gas motion coupled with heat transfer to/from the solid.

The main advantages of thermoacoustic devices are their simplicity of construction, high reliability, potentially low cost and environmental friendliness. The thermodynamic cycle takes place in an environmentally benign oscillating gas (air, helium, nitrogen, etc) without the need for any timing mechanisms involving moving parts. Thermoacoustic devices are an attractive alternative in certain niche applications including electricity generation for spacecraft, low-cost electricity generators for rural areas and gas liquefaction systems for remote oil rigs or for the utilization of industrial waste heat. However, the systems built so far suffer from poor thermodynamic efficiency compared to the efficiency that is theoretically achievable (Paek *et al* 2005). It is believed that a better understanding of the thermo-fluid processes within the internal components is important to aid the design of thermoacoustic systems of higher efficiency.

It is well known that the linear thermoacoustic theory can reliably predict the performance at low amplitudes of acoustic pressure (Rott 1980, Swift 1988). However, at high amplitudes, which are required for such systems to operate in practical industrial applications, nonlinear effects become significant; these include acoustic streaming as well as vortex shedding and turbulence generation, especially at abrupt changes of cross-sectional areas such as the end of thermoacoustic stacks. Therefore, there is a need for understanding the oscillatory flow processes in the vicinity of such internal structures, which potentially can adversely affect the achievable efficiencies of thermoacoustic systems.

In thermoacoustic devices, arrays of tightly spaced parallel plates are often used as stacks or regenerators because of the ease of manufacture and their theoretical performance (Backhaus and Swift 2001). Similarly, some of the popular thermoacoustic heat exchangers (fin-and-tube type) are essentially parallel-plate structures that facilitate heat input and removal to and from stack/regenerator assemblies. Clearly, the heat transfer efficiencies achieved by thermoacoustic heat exchangers are strongly affected by the state of the flow passing through them. In the general sense, flows past these types of internal structures can be seen as the problem of an oscillatory flow with zero mean past a series of bluff bodies (i.e. individual plates or fins), which is the background of the present paper.

Over the last century, numerous studies of the flow field behaviour due to steady flows past bluff bodies have been conducted, one of the earliest usually cited being the work of von Karman on vortex shedding behind a circular cylinder (Kovasznay 1949). However, a somewhat more relevant topic to the current work is the oscillatory flow past bluff bodies. The majority of such studies have been conducted for circular cylinders due to the practical applications of wind engineering, marine and coastal engineering, chemical engineering and heat exchangers—good examples are given by Berger and Wille (1972), Bearman *et al* (1980) and Bearman (1984).

The oscillatory flow around stacks of plates of finite thickness and square edges has received some attention both numerically (Worlikar and Knio 1996, Worlikar *et al* 1996) and experimentally, for example from Mao *et al* (2005, 2008), Aben *et al* (2009) and most recently Shi *et al* (2009). Some important flow features such as the symmetrical concentrated vortex pairs attached to the plate ends or the elongated vortex pairs that break up into ‘vortex-street’ type of structures were observed Mao *et al* (2008). In various experimental papers of this kind, the stack plates used have a relatively large range of thickness: from 0.15 mm to a few millimetres, and as a result, the flow behaviour at the stack end differs dramatically from one case to another. For example, as reported by Mao *et al* (2008), flow features at the end of 5.0 mm thick stack plates resemble von Karman vortex shedding, while in nearly the same conditions, flow features at the end of 1.1 mm thick plates include long shear layers that lose their stability and break up into discrete vortices. However, the purpose of the work by Mao *et al* (2008) was to study the development of the flow structures (patterns), formed around the stack end during the oscillation cycle, as a function of the flow oscillation amplitude (described by the drive ratio) varying within a certain range. Thus, the flow behaviour was essentially studied as a function of the ‘phase Reynolds number’, as well as the ‘peak Reynolds number’. In the statement of future work, it was noted that a more comprehensive similarity analysis should be carried out in future and it has been hypothesized that appropriate similarity numbers such as the Reynolds number, the Keulegan–Carpenter (KC) number and a geometrical parameter such as, for example, stack porosity could be used for the characterization of the oscillatory flow past parallel-plate stacks.

In practical thermoacoustic devices, the plate thickness is often of the order of 0.1 mm, whereas heat exchanger fins can be significantly thicker, e.g. in the range of 2.0 mm to ensure good heat removal properties—see e.g. Hoffer (1986) or Backhaus and Swift (2001). Therefore, it is practically important to understand the flow behaviour at the stack end for a wide range of stack geometries, the controlling parameters and their critical values to distinguish the different flow regimes. The current work explores further the ideas put forward in the previous work by Mao *et al* (2008) in order to study the similarity of the oscillating flows around parallel-plate stacks and attempt to map the flow conditions in a non-dimensional parameter space. In this paper, the common features of the oscillatory flows at the stack end are presented first, based on the PIV measurements of velocity and vorticity fields near parallel-plate stacks in an isothermal condition (i.e. neglecting heat transfer effects). Then a set of non-dimensional parameters is proposed by normalizing the governing Navier–Stokes equations to describe the oscillatory flow around an array of rectangular plates, followed by further analysis and discussion.

## 2. Experimental apparatus and method

The experimental apparatus used in the current study has been described in detail by Marx *et al* (2006), while the details of the Particle Image Velocimetry (PIV) measurement system implemented within the rig were given by Mao *et al* (2008). Therefore, only the essential

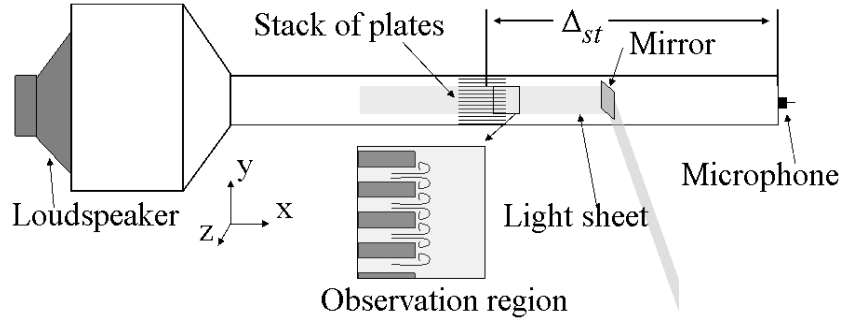


Figure 2. Schematic illustration of the experimental rig.

information will be repeated in this paper. As illustrated in figure 2, the rig is essentially a standing wave resonator made out of a transparent duct with  $136 \text{ mm} \times 136 \text{ mm}$  cross-section, operating at 13.1 Hz, and filled with air in atmospheric conditions. Within the resonator, two different stacks of plates (1.1 and 5.0 mm thick plates with a spacing between plates of 5.0 and 10.0 mm, respectively) were subjected to acoustic excitation, which in turn creates oscillatory flow conditions in the vicinity of the stack. Several levels of acoustic excitation, expressed in terms of the so-called drive ratio,  $D_r$ , the ratio of the maximum acoustic pressure amplitude (as indicated by the microphone shown in figure 2) to the mean pressure, were used for each stack configuration. In this way, the dependence of flow characteristics on the displacement and velocity amplitudes of the oscillatory flow could be studied.

The oscillatory flow at the stack end, in the plane perpendicular to the stack plates but along the resonator axis, was recorded using the phase-locked PIV measurement. Twenty phases in each acoustic cycle (every  $18^\circ$ ) were investigated. For each phase, 100 instantaneous velocity fields were obtained and the ensemble-averaged (mean) velocity fields were further used to obtain the vorticity fields,  $\Omega$ , used in subsequent figures.

### 3. Physics of the oscillatory flow: linear theory versus experimental observations

#### 3.1. Linear theory approximation

When the flow inside a channel formed by parallel plates is not affected by the ‘entrance effect’ caused by the discontinuity of the solid boundary condition at the plate end and the amplitude of the flow oscillation is sufficiently small for the flow to remain laminar, the profile of the longitudinal velocity component,  $u$ , across the channel can be well described by the following equation written in complex notation (Arnott 1991, Swift 2001):

$$u_1(x, y, t) = \frac{p_A \sin(kx)}{\phi \rho c} \left[ 1 - \frac{\cosh[(1+i)y/\delta_v]}{\cosh[(1+i)y_0/\delta_v]} \right] e^{i\omega t} \quad (1)$$

with the continuity of the volume flow rate considered in the stack. Subscript ‘1’ indicates that the velocity is an acoustic variable that has the frequency of the acoustic oscillation; the peak acoustic pressure amplitude,  $p_A$ , is measured at the nearest pressure antinode;  $x$  is the location of the stack in the resonator relative to the pressure antinode, and  $\phi$  is the porosity of the stack, defined as the ratio of the void cross-sectional area of the stack to its total area;  $y$  is the distance from the centreline of the channel of width  $2y_0$ , and  $\delta_v = (2\nu/\omega)^{1/2}$  is the viscous penetration depth,  $\nu = \mu/\rho$  being the kinematic viscosity; and  $c$  is the speed

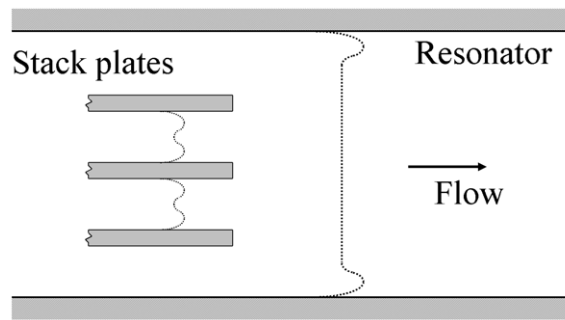


**Figure 3.** Schematic diagram of velocity profiles in the resonator and inside the stack channels, in the half-cycle when the flow direction is from left to right. Only parts of three plates are shown.

of sound. It can be seen that the time-dependent velocity is defined by the product of three terms. The first term,  $p_A \sin(kx) / \phi \rho c$ , which can also be denoted by  $\langle u_{1,x} \rangle$ , is defined as the amplitude of the cross-sectional average velocity (over  $y$ ) of the flow in the stack. It can be calculated from the linear acoustic field in a resonator, as if the stack was absent; however, the porosity in the denominator provides the correct scaling to account for the stack presence.  $e^{i\omega t} = \cos(\omega t) + i \sin(\omega t)$  indicates the time dependence of the velocity. The term in square brackets in (1) defines the spatial distribution of the velocity in the parallel channels formed by the plates, introduced by the viscous effects.

The viscous effects are normally limited to a thin boundary layer close to the plate surface. In the flow channels formed between parallel plates, this boundary layer limit is approached at about five times  $\delta_v$  from the solid body. Therefore, for a flow channel with  $2y_0 > 10\delta_v$ , the flow in the central region of the channel is practically unaffected by the boundary conditions, which means that the velocity profiles are relatively flat in the central region. In this case, the presence of neighbouring plates has negligible effects on the velocity profiles around the plate under consideration, except that it does change the average velocity amplitude in the stack of plates due to the reduction of the cross-sectional area (compared to an empty resonator).

It should also be noted that in the boundary layer, the velocity profiles often exhibit an ‘annular effect’; that is a common feature of oscillatory flows: with increasing distance from the wall, the velocity values often increase to reach a local maximum before decreasing further away from the wall. This name follows the terminology first introduced in studies of the oscillatory flow in pipes, where it was more appropriate. The ‘annular effect’ essentially promotes a double shear layer structure on each side of the plate. The ‘inner’ shear layer (closer to the plate surface), however, seems to be always dominant because of the larger strain, while the shear layer further away from the plate surface is weaker, although it is still discernible. The ‘inner’ shear layer is essentially limited to a region of about  $2\delta_v$  from the plate surface.

Figure 3 shows schematically the velocity profiles in two locations when the flow is generally from left to right: one inside the stack and the other outside the stack, both being sufficiently far away from the stack end not to be affected by one another. In the stack, channel the velocity profile affected by the viscous effects extends from the plate surface. Within the resonator the viscous effects are only limited to a relatively short distance from the resonator wall—the flow in most of the cross-sectional area of the resonator behaves as an inviscid plug flow with a flat velocity profile.

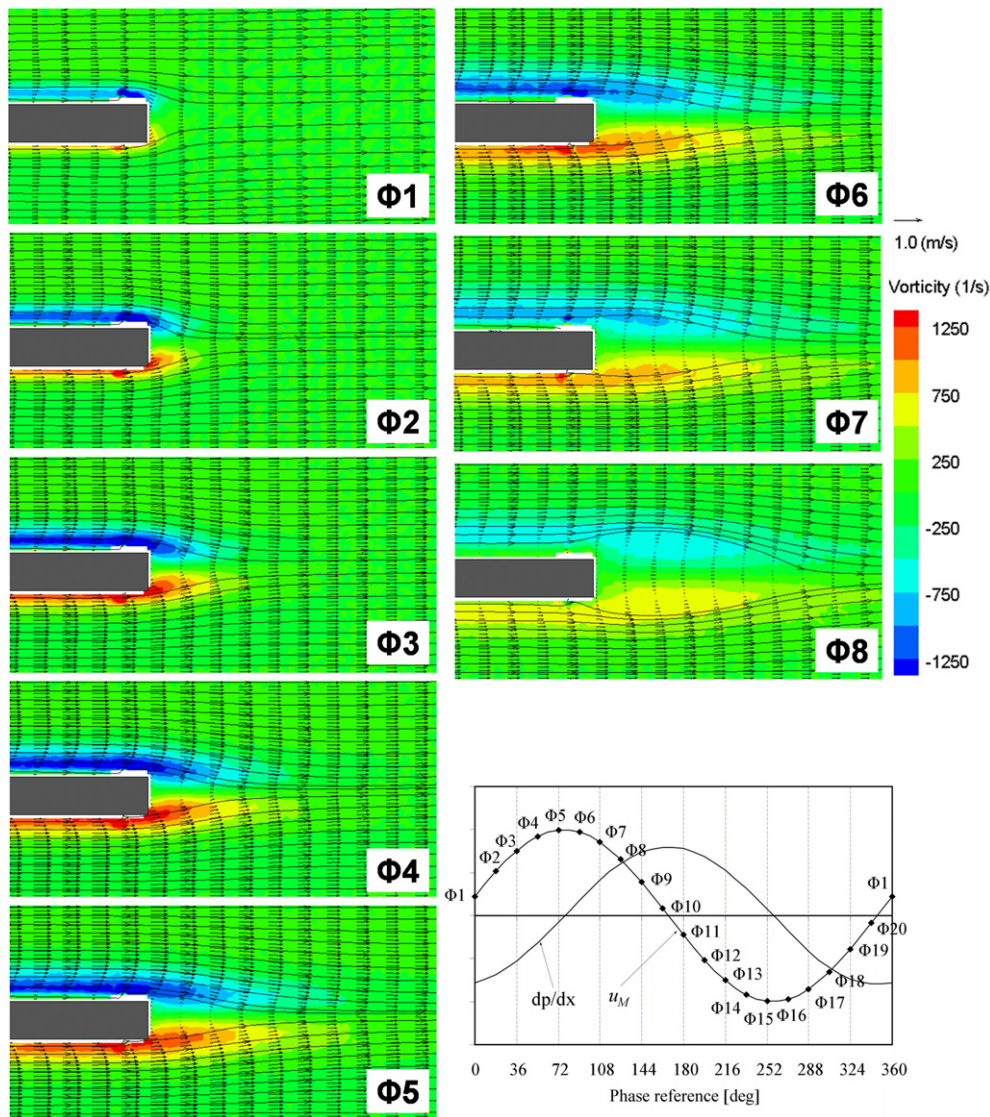


**Figure 4.** Mean velocity field (black arrows) superimposed on vorticity field (colour contour) in phases  $\Phi 1$ – $\Phi 8$ , for  $D_r = 0.3\%$ . The streamlines indicate that the flow is from left to right. Plate thickness is 1.1 mm and plate spacing is 5.0 mm. The positions of the phases corresponding to the acoustic cycle are shown in the bottom right corner.

### 3.2. Experimental observations at the end of the stack

Of course, in practical systems the description provided by the linear theory is invalid close to the abrupt changes in the resonator cross-section, where the velocity profiles need to ‘adjust’ themselves to the discontinuities. Figure 4 is a representative illustration of the velocity field (black arrows), superimposed on the vorticity field (colour contours) related to the flow induced at the end of 1.1 mm thick plates at  $D_r = 0.3\%$  for phases  $\Phi 1$ – $\Phi 8$ . The arrows on the streamlines indicate that the flow in this part of the acoustic cycle is from left to right.

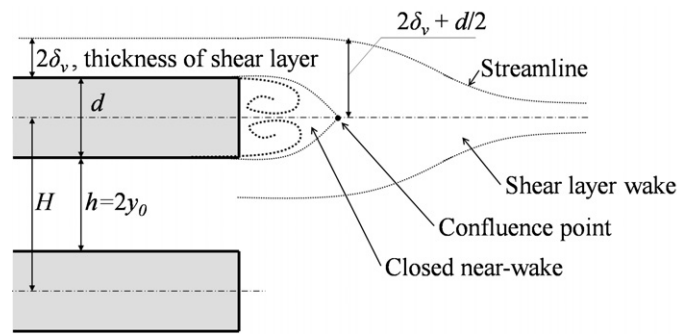


Figure 5. Structure of the flow at the end of a stack of sharp-edged plates of finite thickness.

The position of each phase in the acoustic cycle is represented in the plot of acoustic velocity versus time in the bottom right corner of figure 4.

Close to the end of the sharp-edged plate, the flow separation occurs at the trailing edges, during the phases when the flow is out of the stack into the open area of the resonator. When the amplitude of the flow velocity oscillation is small, a distinct symmetric closed near-wake (i.e. a recirculation region) is formed, as illustrated by the streamlines in figure 4. This flow field around the stack end could be divided into several characteristic regions as schematically shown in figure 5, based on the observation of the results of measurements. The shear layers originating from the stack channel extend downstream and join each other forming a shear layer wake. At a position nearest to the plate end, the shear layers meet at the end of the near-wake at a confluence point, where the longitudinal velocity component is zero.

The closed near-wake normally consists of two counter-rotating eddies, whose lateral distance is normally limited by the plate thickness. The longitudinal size of the closed near-wake, from the plate end to the confluence point, can be estimated from the velocity distribution along the centreline of the stack plate. The velocity profiles along the plate centreline are shown in figure 6(a) for phases between  $\Phi 1$  and  $\Phi 8$ . From phase  $\Phi 1$  to  $\Phi 5$ , the flow in the stack channel and the 'free-stream' outside of the stack is in an acceleration stage and the velocity of the flow increases monotonically with the distance from the plate end, except for the closed near-wake. In phase  $\Phi 1$ , the flow velocity at about 2.2 mm downstream from the plate end is about  $0.28 \text{ m s}^{-1}$  and it is constant further downstream for there is little effect from the flow separation at the plate end. At this phase, the closed near-wake around the plate end is not formed yet, because there is no reversing flow of a negative velocity. In phases from  $\Phi 2$  to  $\Phi 5$ , the velocity of the flow outside the stack increases. The closed near-wake gradually forms and extends further downstream; at the same time a reversing flow begins to appear.

From phase  $\Phi 6$ , the flow starts to decelerate (due to the decreasing mean flow velocity), while the direction of the flow remains from left to right. It is interesting to see that the closed near-wake continues to extend and this can also be clearly observed in  $\Phi 6$ – $\Phi 8$  in figure 4, judging from the size of the vortex structure. The maximum velocity of the recirculating flow is comparable to that of the 'free stream' in the deceleration phases  $\Phi 7$  and  $\Phi 8$ . The confluence point is located where the velocity is zero as illustrated by figure 6(b). It is about 0.55 mm away from the plate end in phase  $\Phi 3$ , i.e. about half of the plate thickness. The shear layer wake region extends from the confluence point to the location where the longitudinal velocity on the plate centreline is comparable to 'free stream': in the example shown in figure 6(b), it is about 4 times the plate thickness. By looking at phases from  $\Phi 1$  to  $\Phi 4$ , it

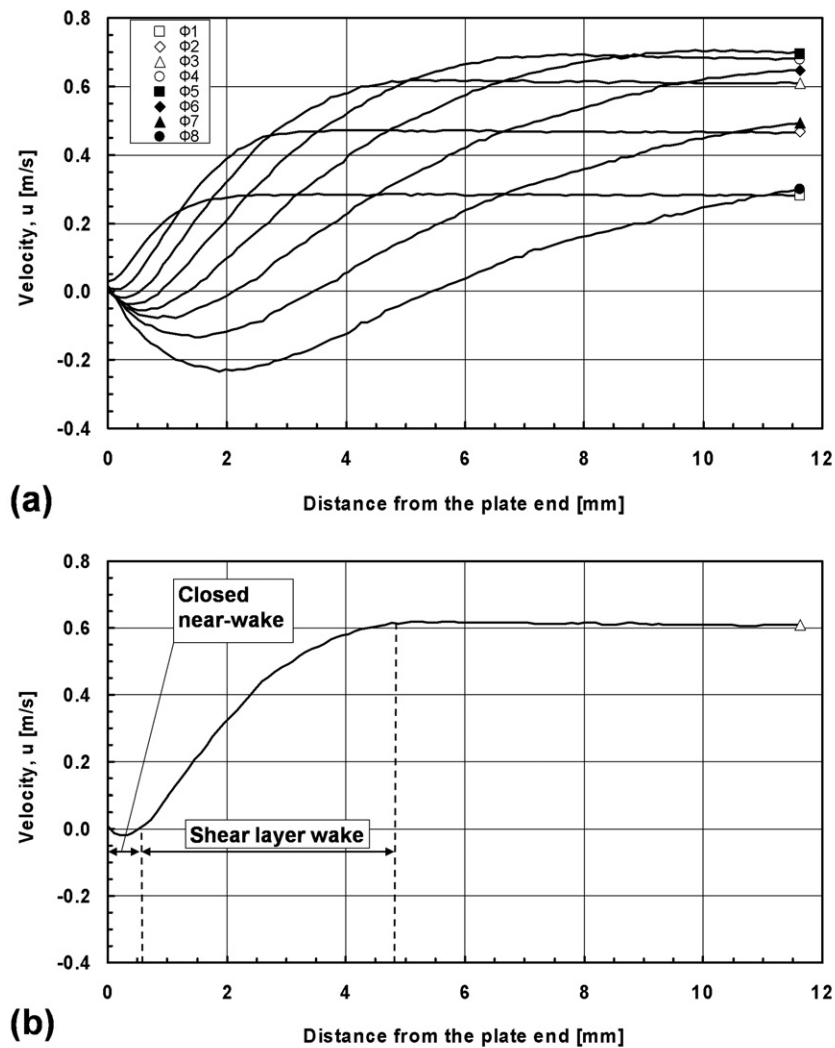


**Figure 6.** Distribution of the longitudinal velocity,  $u$ , along the plate centreline for eight phases (a); illustration of the regions in the wake (b); data for a stack with  $d = 1.1$  mm and  $h = 5.0$  mm, at  $D_r = 0.3\%$ .

is clear that the size of the shear layer wake also increases with time (see the vorticity contour in figure 4). It is uncertain from this plot, however, whether the development of the shear layer wake would continue in the decelerating stage.

The longitudinal size of the closed near-wake (the recirculation region) versus the phase in the acoustic cycle is plotted for  $D_r = 0.3\%$  in figure 7, together with analogous plots for  $D_r = 0.6\%$  when the shear layer wake remains symmetrical and  $D_r = 1.0\%$  when the shear layers eventually break up and form a sequence of vortices in the wake. For drive ratios 0.3 and 0.6%, the length of the recirculation region increases monotonically with time, the growth being faster for higher drive ratios. However, this behaviour changes for  $D_r = 1.0\%$  after phase  $\Phi 5$ . The increase of the recirculation region length is interrupted by the instability of the shear layer wake, as seen in figure 8. The wake made up of a pair of free shear layers is no

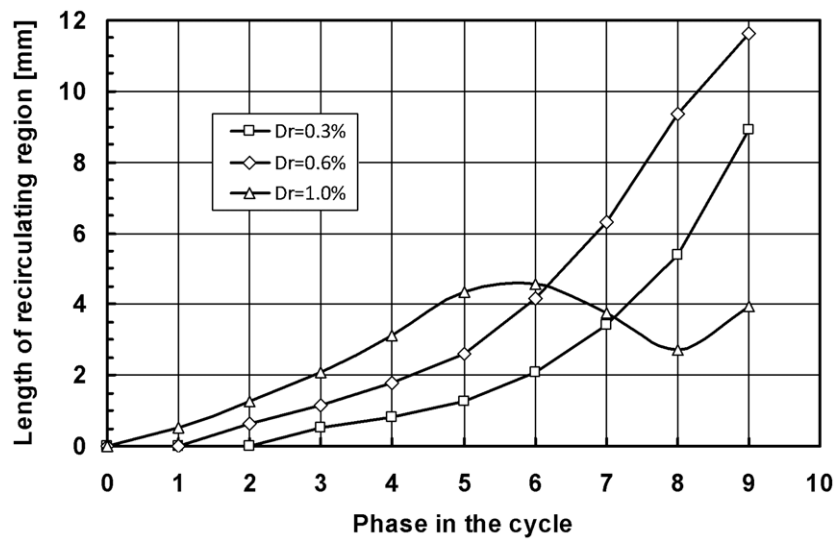


**Figure 7.** Variation of recirculation region length with consecutive phases in an acoustic cycle, for the stack of plates of 1.1 mm thickness.

longer symmetrical after phase  $\Phi_4$ , but becomes unstable and a lateral oscillation commences at the confluence point, as illustrated by the decrease of the recirculation region length in figure 7.

For the case of 5 mm thick plates, the evolution of coherent structures forming due to the separation processes is somewhat different in qualitative terms from the case of 1.1 mm thick plates. At relatively small acoustic excitation levels (e.g.  $D_r = 0.3\%$ , as shown in figure 9(a)), the vortex structures formed at the end of each plate are a pair of concentrated eddies that are symmetrical about the centreline of the plate. The length of these symmetrical vortex structures at the plate end is quite short compared to the plate thickness, unlike the very elongated vortex structures around the thin plates of 1.1 mm thickness. When the oscillation amplitude of the flow around the plate stack increases (e.g.  $D_r = 1.0\%$ , as shown in figure 9(b)), the shear layers start to roll up into discrete vortices in an alternate fashion, as soon as the symmetric wake is no longer maintained. The elongated vortex structures characteristic for the thin plates, and their further breaking up into a ‘vortex street’, is not observed here—see for example Mao *et al* (2008). These distinct flow features, occurring as a consequence of having thin versus thick plates or low versus high drive ratios, should be reflected in the non-dimensional parameter space, as long as the right similarity parameters can be found. The following section will focus on defining suitable similarity numbers to characterize the types of flow discussed here.

#### 4. Non-dimensional parameters controlling oscillatory flows at the stack end

For a typical oscillatory fluid flow induced by a one-dimensional plane acoustic wave around a stack of evenly spaced parallel plates discussed in this paper, there are three groups of parameters that determine the flow behaviour. The first one includes the properties of the fluid, such as density,  $\rho$ , and dynamic viscosity,  $\mu$ . The second one includes the geometry of the stack of parallel plates: the plate length,  $l$ , the plate thickness,  $d$ , and the channel

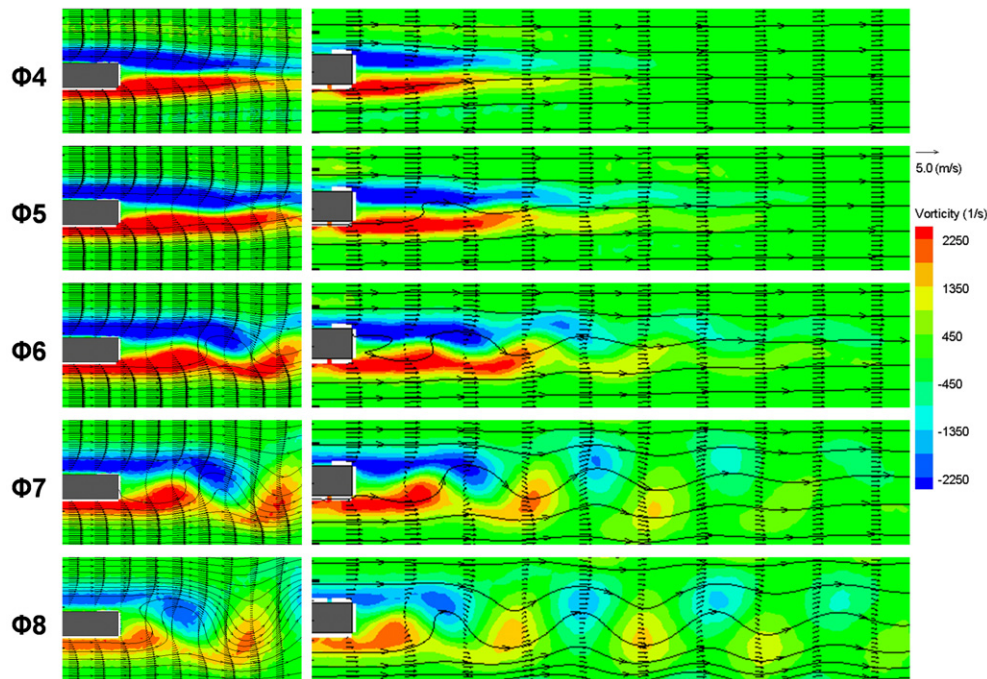


**Figure 8.** Mean velocity field (black arrows) superimposed on the vorticity field (colour contours) for phases from  $\Phi 4$  to  $\Phi 8$  at  $D_r = 1.0\%$ . The streamlines indicate that the flow is from left to right. The stack plates are 1.1 mm thick with 5.0 mm gap between the plates. The results in the left column are obtained with a higher spatial resolution, while the right column has a lower spatial resolution but a larger investigated area.

height between plates,  $h$ . The span-wise dimension of the stack of plates is not considered if the flow around it is treated as a two-dimensional problem. The third group should include the operating conditions of the acoustic wave such as its angular frequency,  $\omega (= 2\pi f)$ , and the local longitudinal velocity amplitude of the flow,  $u_a$ . However, there are only three independent fundamental physical quantities that describe the seven parameters listed above; these are 'length', 'time' and 'mass'. Therefore, according to the Buckingham-Pi theorem, four independent non-dimensional parameter groups could determine the characteristics of the oscillatory flow around the plates. However, the stack length,  $l$ , is eliminated in the discussions to follow in order to simplify the analysis, on the basis of the fact that the fluid displacement is usually much smaller than the stack length and thus the number of non-dimensional parameter groups drops to three. Of course, it is well known that the selection of non-dimensional parameters is non-unique and the analysis presented below will show two alternative 'sets of three'. A more general analysis, including for example the stack length, as well as other alternative sets of three non-dimensional parameters are possible based on analogous procedures to those described.

#### 4.1. Normalization

It is assumed that the fluid is incompressible (which is valid only when the amplitude of the acoustic pressure oscillation is small) and that it has a constant viscosity,  $\mu$ . The viscous force

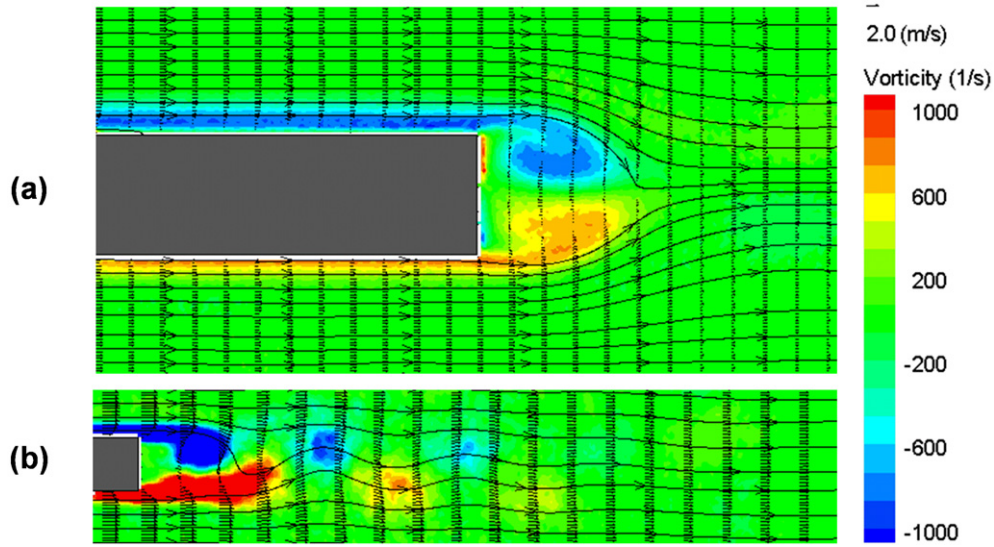


**Figure 9.** Mean velocity field (black arrows) superimposed on the vorticity field (colour contours) for phase  $\Phi_7$  at (a)  $D_r = 0.3\%$  (a close view) and (b)  $D_r = 1.5\%$  (a zoom-out view). The stack plates are 5.0 mm thick with 10.0 mm gap between plates.

due to the fluid expansion can be ignored. The motion of a Newtonian fluid can be described by the Navier–Stokes equations, which in a simplified differential form can be written as

$$\begin{aligned} \frac{\partial u}{\partial t} + u \frac{\partial u}{\partial x} + v \frac{\partial u}{\partial y} + \frac{1}{\rho} \frac{\partial p}{\partial x} &= \frac{\mu}{\rho} \left( \frac{\partial^2 u}{\partial x^2} + \frac{\partial^2 u}{\partial y^2} \right), \\ \frac{\partial v}{\partial t} + u \frac{\partial v}{\partial x} + v \frac{\partial v}{\partial y} + \frac{1}{\rho} \frac{\partial p}{\partial y} &= \frac{\mu}{\rho} \left( \frac{\partial^2 v}{\partial x^2} + \frac{\partial^2 v}{\partial y^2} \right), \end{aligned} \quad (2)$$

when the body forces (e.g. gravity) on unit mass of fluid can be neglected.

As mentioned above, the plate length,  $l$ , is assumed large enough for the flow disturbance caused by one end of the plate not to have an effect on the flow at the other end of the plate. The amplitude of the velocity oscillation at the stack position in an empty resonator,  $u_a$ , the plate thickness,  $d$ , and the inverse of the angular frequency of the acoustic oscillation,  $1/\omega$ , are chosen as the characteristic scales of velocity, length and time, respectively.  $\rho c u_a$  is chosen as the characteristic scale of pressure,  $\rho c$  being the characteristic impedance of the fluid and  $c$  the speed of sound. The non-dimensional variables can then be written accordingly as

$$u^* = \frac{u}{u_a}, \quad v^* = \frac{v}{u_a d/h}, \quad x^* = \frac{x}{d}, \quad y^* = \frac{y}{d}, \quad t^* = \omega t, \quad p^* = \frac{p}{\rho c u_a}. \quad (3)$$

The superscript  $*$  denotes a non-dimensional variable. Of course, these are arbitrary choices of characteristic scales; other alternative approaches are possible.

The ‘thermodynamic’ pressure  $p$  in equation (2) can be considered as a sum of three parts: the static pressure (or the mean pressure), the acoustic pressure originating from the propagation of the acoustic oscillation, and the dynamic pressure. The mean pressure in a thermoacoustic system is not dependent on either  $x$  or  $y$  in the resonator, so its spatial gradient

is zero. The acoustic pressure is much larger than the dynamic pressure in a typical acoustic field where the particle velocity is much smaller than the sound speed ( $u_a \ll c$ ). Therefore,  $\rho c u_a$  is chosen as the pressure reference scale in this case.

Substituting equation (3) into (2), the normalized momentum equation can be written as follows:

$$\begin{aligned} Re_\omega \frac{\partial u^*}{\partial t^*} + Re_d \left( u^* \frac{\partial u^*}{\partial x^*} + \frac{d}{h} v^* \frac{\partial u^*}{\partial y^*} \right) + \frac{Re_d}{Ma} \frac{\partial p^*}{\partial x^*} &= \frac{\partial^2 u^*}{\partial x^{*2}} + \frac{\partial^2 u^*}{\partial y^{*2}}, \\ Re_\omega \frac{\partial v^*}{\partial t^*} + Re_d \left( u^* \frac{\partial v^*}{\partial x^*} + \frac{d}{h} v^* \frac{\partial v^*}{\partial y^*} \right) + \frac{Re_d h}{Ma d} \frac{\partial p^*}{\partial y^*} &= \frac{\partial^2 v^*}{\partial x^{*2}} + \frac{\partial^2 v^*}{\partial y^{*2}}. \end{aligned} \quad (4)$$

In the above equations, four non-dimensional parameter groups are defined.  $Re_\omega = \omega d^2/\nu$  is defined as the kinematic Reynolds number, following Worlikar and Knio (1996). It is also sometimes referred to as the Valensi number (Richardson 1963, Choi *et al* 2004) or the non-dimensional frequency parameter (Berger and Wille 1972). In thermoacoustics, the viscous penetration depth,  $\delta_v$ , is often used as an alternative indication of the acoustic oscillation frequency. Therefore, the kinematic Reynolds number can be rewritten as  $Re_\omega = 2(d/\delta_v)^2$ : the ratio of the plate thickness to the viscous penetration depth. The conventional Reynolds number,  $Re_d = u_a d/\nu$ , is simply defined based on the amplitude of velocity oscillation,  $u_a$ , and the plate thickness,  $d$ .

The third non-dimensional parameter,  $d/h$ , the ratio of the plate thickness to the channel height, takes into account the effect of the existence of neighbouring plates in the stack. The channel height has an effect on the flow in two respects. Firstly, the blockage effect of the plates on the flow in the resonator has to be considered when the plate thickness is comparable with the channel height. The velocity amplitudes inside the stack differ significantly from the velocity in the empty resonator,  $u_a$  due to the blockage effect.  $d/h$  is equivalent to  $1/\phi - 1$ ,  $\phi$  being the porosity of the stack that is defined as  $\phi = h/(h + d)$  when the plates are arranged evenly. Secondly, the flow behaviour inside each channel has to be considered when the channel height,  $h$ , is comparable to the thickness of the viscous boundary layer. It is clearly demonstrated that the oscillatory flow in a circular pipe remains laminar if the internal diameter of the pipe is less than approximately ten times the viscous penetration depth until the Reynolds number based on the internal diameter is over 1000 (Ohmi and Iguchi 1982).

Although it may appear from equation (4) that the acoustic Mach number ( $Ma = u_a/c$ ) defined as the ratio of the local acoustic velocity amplitude to the sound speed is a fourth non-dimensional parameter, in reality  $c$  being constant and the flow being assumed incompressible, it has merely the meaning of velocity amplitude. It is often much smaller than unity in an acoustic field encountered in thermoacoustic applications. With the assumption of an incompressible flow, the ratio  $Re_d/Ma$  is in effect a constant.

The amplitude of the acoustic oscillation may be indicated also by the displacement amplitude,  $\xi_a = u_a/\omega$ . The Keulegan–Carpenter number,  $KC (= \xi_a/d)$ , defined as the ratio of the acoustic displacement amplitude to the plate thickness, can be introduced to indicate the flow oscillation amplitude. It is often used to describe the flow characteristics, drag/lift force or pressure distribution in the problems of bluff bodies at rest in an oscillatory flow or oscillating bluff bodies in a quiescent fluid (Bearman and Graham 1980, Guilmineau and Queutey 2002), where  $KC$  is defined as  $u_a/fd$ , the ratio of the flow orbit to the body characteristic length, with  $f$  being the frequency of flow oscillation. For a circular cylinder in an oscillating flow, the oscillating flow can be classified into different flow regimes, such as the flow that remains attached and symmetrical, the separating flow that remains symmetrical,

asymmetric shedding of vortices and so forth, depending mainly on KC and weakly on the Reynolds number  $Re_d$  (Guilmineau and Queutey 2002).

It is worth noting that another non-dimensional number, the Strouhal number ( $St = fd/u_a$ ), could be used, in place of KC, to describe the oscillating flow characteristics (this is effectively the inverse of KC). It should be noted that  $f$  is the frequency of the acoustic oscillation (i.e. oscillatory flow forcing), not the frequency of vortex shedding often investigated in steady flows past bluff bodies. This ‘forcing’ Strouhal number has already been used e.g. in the study of oscillatory flow around a circular cylinder (Badr *et al* 1995).

The Reynolds number,  $Re_d$ , can then be expressed as the product of KC and the kinematic Reynolds number,  $Re_d = KCRe_\omega$ . Accordingly, equation (4) can be rewritten as

$$\begin{aligned} \frac{\partial u^*}{\partial t^*} + KC \left( u^* \frac{\partial u^*}{\partial x^*} + \frac{d}{h} v^* \frac{\partial u^*}{\partial y^*} \right) + \frac{KC}{Ma} \frac{\partial p^*}{\partial x^*} &= \frac{1}{Re_\omega} \left( \frac{\partial^2 u^*}{\partial x^{*2}} + \frac{\partial^2 u^*}{\partial y^{*2}} \right), \\ \frac{\partial v^*}{\partial t^*} + KC \left( u^* \frac{\partial v^*}{\partial x^*} + \frac{d}{h} v^* \frac{\partial v^*}{\partial y^*} \right) + \frac{KC}{Ma} \frac{h}{d} \frac{\partial p^*}{\partial y^*} &= \frac{1}{Re_\omega} \left( \frac{\partial^2 v^*}{\partial x^{*2}} + \frac{\partial^2 v^*}{\partial y^{*2}} \right). \end{aligned} \quad (5)$$

It is clear that out of the three non-dimensional numbers,  $Re_d$ ,  $Re_\omega$  and KC, only two are independent, one of which could include the frequency,  $\omega$ , and the other the amplitude of the acoustic oscillation, either  $u_a$  or  $\xi_a$ . Equations (4) and (5) reveal that for a given non-dimensional oscillation amplitude of the flow ( $Re_d$  or KC), the relative importance of the unsteady acceleration term and the viscous term in an oscillatory flow could be loosely described by the kinematic Reynolds number,  $Re_\omega$ . Similarly, for a given kinematic Reynolds number,  $Re_\omega$ , the Reynolds number,  $Re_d$ , describes the relative importance of the contributions from the convective acceleration term and the viscous term, and KC describes the relative importance of the contributions from the unsteady acceleration term and the convective acceleration term. The four force terms in equation (4) or (5) clearly indicate that an individual non-dimensional number could not fully describe the equilibrium of the forces. In general, if  $Re_\omega \gg 1$ , meaning the unsteady acceleration term is much larger than the viscous term, the effect of viscosity on oscillatory flow will be limited to a thinner viscous boundary layer around the solid. This is also indicated by the definition of  $Re_\omega$  as  $2(d/\delta_v)^2$ —for a given plate thickness  $d$ , a larger  $Re_\omega$  gives smaller  $\delta_v$ , the viscous penetration depth. For a flow having a large  $Re_d (\gg 1)$ , the convective acceleration term become larger than the viscous term, which could indicate that the flow being unsteady may undergo a transition to turbulence. KC, considered as the ratio of the flow displacement amplitude to the characteristic length scale (e.g. the plate thickness), could also be considered as  $u_a/\omega d$ . For  $KC \gg 1$  the flow displacement amplitude is much greater than the plate thickness. In other words, the flow velocity amplitude is much greater or the frequency of the flow oscillation is much smaller for a given plate thickness. The effect of having  $KC \gg 1$  is to make the unsteady acceleration term much smaller than the convective acceleration term, and the behaviour of the oscillatory flow around the bluff bodies becomes less affected by the unsteady acceleration and in any instant of the oscillation the oscillatory flow acts more like a unidirectional steady flow (as if the unsteady acceleration term was dropped).

In summary, for the oscillatory flow induced by a one-dimensional plane acoustic wave around a stack of parallel plates, it involves density,  $\rho$ , and dynamic viscosity,  $\mu$ , of the fluid, the geometry of the stack described by  $l$ ,  $d$  and  $h$  and the operating condition,  $u_a$ , and the frequency. When the fluid is considered incompressible, isothermal and having a constant viscosity, the similarity of the fluid mechanics around a series of parallel plates in an acoustic field could be evaluated by the non-dimensional parameters groups ( $Re_\omega$ ,  $Re_d$  and  $d/h$ ) or ( $Re_\omega$ , KC and  $d/h$ ), if the plate length is considered to be large enough.

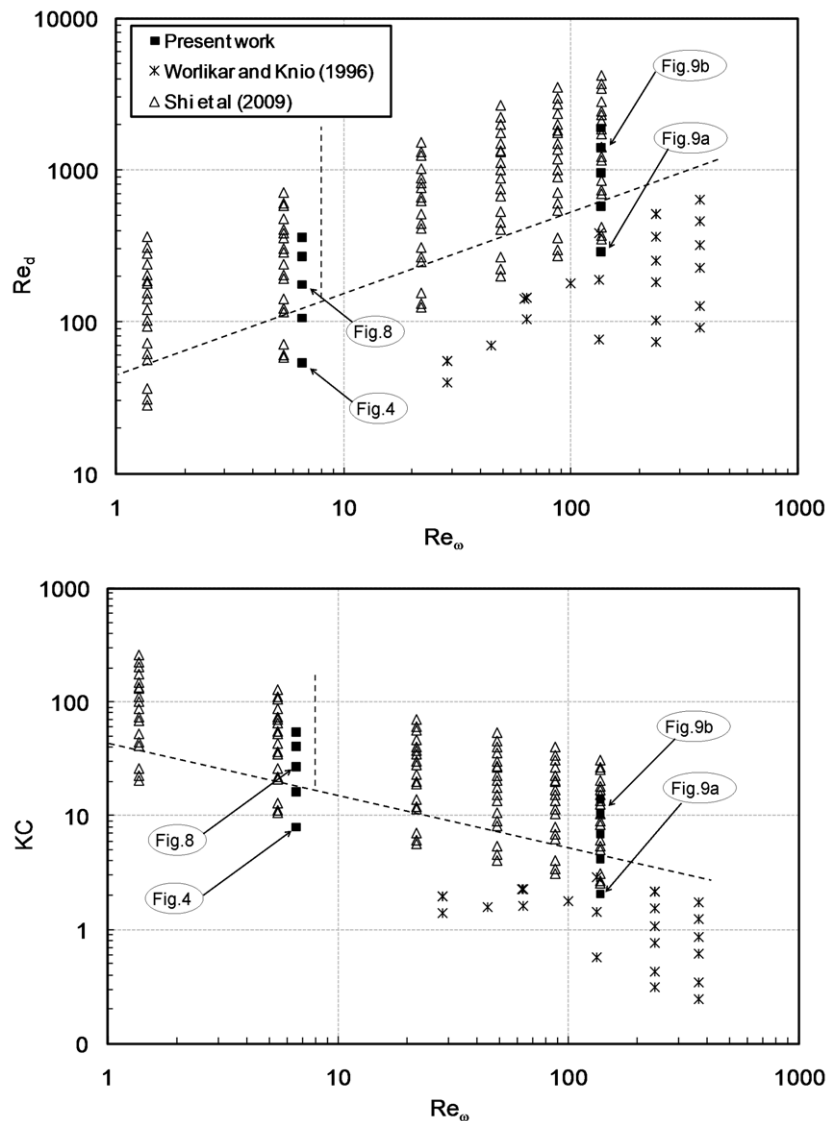


**Figure 10.** Operating conditions of oscillatory flow around a stack of plates in the non-dimensional parameter groups ( $Re_\omega$  versus  $Re_d$ ) and ( $Re_\omega$  versus  $KC$ ).

#### 4.2. Illustration of the non-dimensional parameters concept through experimental results

Following the choice of the non-dimensional parameters to describe the behaviour of the oscillatory flow around the end of the stack of plates, the operating conditions of the oscillatory flow in the present study are shown using ( $Re_\omega$  versus  $Re_d$ ) and ( $Re_\omega$  versus  $KC$ ) planes, as illustrated in figure 10. Also shown are the data points collected from the work conducted numerically by Worlikar and Knio (1996) and experimentally by Shi *et al* (2009). The porosity,  $\phi$ , of the stacks studied is between 0.5 and 0.8 and  $d/h$  is between 0.25 and 0.5.

By visually inspecting the available data related to the development of the wake flow around the end of the stack, in particular with regard to the flow features presented and discussed in previous sections, it is possible to divide either of the two spaces,  $(Re_\omega$  and  $Re_d)$  or  $(Re_\omega$  and KC), into several characteristic regions. This is illustrated by the dashed lines drawn in figure 10. These separate regions are characterized by different behaviours of the wake flow as discussed later in this section. Both the oblique and vertical dashed lines are simple straight lines in the log–log  $(Re_\omega$  versus  $Re_d)$  and  $(Re_\omega$  versus KC) planes. The oblique line can be expressed as  $Re_d = 44.0Re_\omega^{0.538}$  in the  $(Re_\omega$  versus  $Re_d)$  plane and  $KC = 44.0Re_\omega^{0.438}$  in the  $(Re_\omega$  versus KC) plane. The vertical line corresponds to  $Re_\omega = 8$  when the plate thickness is equivalent to  $2\delta_v$ . However, clearly the dashed lines indicating the ‘transitions’ of the flow patterns between these regions can only be sketched approximately (similar procedures are well known in defining ‘transitions’ in multiphase flows).

In general, the state of the flow below the dashed oblique line is often symmetric about the plate centreline, even though the symmetric vortex structure may have a larger longitudinal length compared with the plate thickness when  $Re_\omega$  is smaller than 8, while the vortex structure often takes the form of much concentrated eddies when  $Re_\omega$  is larger than 8. On the other hand, the flow behind the end of the plates in the region above this line is often asymmetric. Complicated flow patterns, such as the shear layers in the wake breaking up into ‘vortex street’-type structures or the shear layers rolling up into vortices and shedding in an alternate fashion, may start to appear.

The region above the dashed oblique line can be further separated into two sub-regions by the vertical dashed line. The flow in the conditions that fall into the left region can often develop into an elongated shear layer structures at the end of the plate. Then this elongated shear layer becomes asymmetric possibly due to the instability of the shear layers and eventually breaks up into discrete vortices. On the right-hand side of the vertical dashed line, the flow at the end of the plate often exhibits vortex shedding before the elongated shear layer structure can be formed and leads to a pattern similar to the von Karman vortex street. However, admittedly, the flow in both regions could develop into much more complicated flow patterns when  $Re_d$  or KC increases further, as shown by Shi *et al* (2009).

The flow conditions of the four cases discussed in section 3 are indicated by arrows in figure 10. The flow pattern of each of these two cases below the oblique line (i.e. figures 4 and 9(a)) clearly represents the state of flow behind the plate stack. It is interesting to see that the flow conditions that all fall into the same region as that for figure 9(a) are collected from the numerical work by Worlikar and Knio (1996), who adopted similar geometrical configurations of plate stacks to that used by Atchley *et al* (1990) in an experimental study of the acoustically generated temperature gradient due to the thermoacoustic effect. The behaviour of the flow in each sub-region above the oblique line can be illustrated by figure 8 and 9(b) when the values of  $Re_d$  and KC are not very far from the line.

The presence of neighbouring plates around the plate studied could have an effect on the gradient of the velocity profile in the shear layer wake and thus on the ability of the wake flow to remain symmetric. However, it is still rather difficult at this stage to identify the effect of channel width on flow on the basis of the available experimental and numerical data. Therefore, the effect of the non-dimensional number,  $d/h$ , or the porosity,  $\phi$ , on flow behaviour is not distinguishable in these graphs.

## 5. Discussion and conclusion

This paper investigates the behaviour of the oscillatory flow past a stack of parallel plates when the fluid moves out of the stack (the so-called ‘ejection stage’ of the cycle). It can be

seen that during this part of the acoustic cycle, the flow exhibits some similarities to the wake flow of a unidirectional steady flow past a bluff body, such as a circular cylinder (Zdravkovich 1997). Essentially, the wake flow is made up of two shear layers with vorticity of opposite signs that are fed from the stack channel. There may be a recirculation region formed next to the plate end and surrounded by the shear layers. The size of the recirculation region increases while the flow speeds up in the initial stage of the ‘ejection’; it then continues to grow even in the deceleration phases of the ‘ejecting’ flow. The flow in the recirculation region finally joins with the flow that reverses its direction and starts to move into the stack.

The oscillating flow at the end of the plate also shows interesting behaviour when the velocity amplitude varies. At small amplitudes the shear layers in the wake may remain symmetric and produce attached symmetrical vortex structures. However, for larger velocity amplitudes the flow may lose its symmetry and stability, resulting in such flow patterns as ‘break-up’ of the shear layers and alternate vortex shedding. It is shown that the break-up of the shear layers may undergo a transition to the alternate shedding; however, the alternate shedding may also start in the first place without such a transition taking place. It seems plausible that both the lateral and longitudinal dimensions of the shear layers in the wake define the flow patterns and their development.

From the normalization of the governing equations of the oscillatory flow motion around a parallel plate, groups of non-dimensional parameters are proposed. Each set of non-dimensional parameters essentially consists of: (i) one kinematic parameter, i.e. the kinematic Reynolds number  $Re_\omega$ , (ii) one dynamic parameter, i.e. the Reynolds number  $Re_d$  or KC, or more indirectly the drive ratio,  $D_r$ , and (iii) a stack configuration parameter,  $d/h$ , or the porosity  $\phi$ . Alternatively, the Womersley number (Womersley 1955),  $Wo = h/\delta_v$ , could be used as the stack configuration parameter, for it is simply equivalent to  $h/d(Re_d/2KC)^{1/2}$ . As indicated in equation (1), the  $Wo$  number could be used to describe the interaction of the viscous boundary layers on the neighbouring plates. Therefore, the non-dimensional parameter groups ( $Re_\omega$ ,  $Re_d$  and  $Wo$ ) or ( $Re_\omega$ , KC and  $Wo$ ) could be used in place of the non-dimensional parameter groups ( $Re_\omega$ ,  $Re_d$  and  $d/h$ ) or ( $Re_\omega$ , KC and  $d/h$ ).

An additional parameter, the non-dimensional stack length, i.e. the aspect ratio  $l/d$ , may need to be considered when the displacement amplitude of the fluid oscillation is comparable to the stack length so that the assumption that the flow disturbance at one end of the stack has no effect on the flow at the other end of the stack is no longer valid. Figure 10 demonstrates how the data collected from the current study and the data from other studies that can be found in the existing literature can be gathered in a single plot and divided into regions of distinct flow behaviour—in a similar way to known flow regime maps in other areas of fluid mechanics.

In order to further understand the relationship between non-dimensional governing parameters and flow behaviour, experimental data from much more diverse experimental conditions than those obtained as part of the current study will be required. In particular, the critical values of the non-dimensional parameters, which correspond to the transition from symmetric to asymmetric wake flows, need to be studied. Similarly, the effects of the channel width on the flow pattern should be investigated.

## References

- Aben P C H, Bloemen P R and Zeegers J C H 2009 2-D PIV measurements of oscillatory flow around parallel plates *Exp. Fluids* **46** 631–41
- Arnott W P, Bass H E and Raspet R 1991 General formulation of thermoacoustics for stacks having arbitrarily shaped pore cross sections *J. Acoust. Soc. Am.* **90** 3228–37

- Atchley A A, Hofer T J, Muzzerall M L, Kite M D and Ao C 1990 Acoustically generated temperature gradients in short plates *J. Acoust. Soc. Am.* **88** 251–63
- Backhaus S and Swift G W 2001 Fabrication and use of parallel plate regenerators in thermoacoustic engines *Proc. 36th Intersociety Energy Conversion Engineering Conf. (IECEC)* vol 1, ed S Somasundaram *et al* (New York: ASME) pp 453–8
- Badr H M, Dennis S C R, Kocabiyik S and Nguyen P 1995 Viscous oscillatory flow about a circular cylinder at small to moderate Strouhal number *J. Fluid Mech.* **303** 215–32
- Bearman P W 1984 Vortex shedding from oscillating bluff bodies *Annu. Rev. Fluid Mech.* **16** 195–222
- Bearman P W and Graham J M R 1980 Vortex shedding from bluff bodies in oscillatory flow: a report on Euromech 119 *J. Fluid Mech.* **99** 225–45
- Berger E and Wille R 1972 Periodic flow phenomena *Annu. Rev. Fluid Mech.* **4** 313–40
- Choi S, Nam K and Jeong S 2004 Investigation on the pressure drop characteristics of cryocooler regenerators under oscillating flow and pulsating pressure conditions *Cryogenics* **44** 203–10
- Guilmineau E and Queutey P 2002 A numerical simulation of vortex shedding from an oscillating circular cylinder *J. Fluids Struct.* **16** 773–94
- Hofer T J 1986 Thermoacoustic refrigerator design and performance *PhD Thesis* Physics Department, University of California, San Diego, CA
- Kovaszny L S G 1949 Hot-wire investigation of the wake behind cylinders at low Reynolds numbers *Proc. R. Soc. A* **198** 174–90
- Mao X, Marx D and Jaworski A J 2005 PIV measurement of coherent structures and turbulence created by an oscillating flow at the end of a thermoacoustic stack *Progress in Turbulence II, Proc. iTi Conf. in Turbulence 2005 (Springer Proceedings in Physics* vol 109, 2007) ed M Oberlack *et al* (Berlin: Springer) pp 99–102
- Mao X, Yu Z, Jaworski A J and Marx D 2008 PIV studies of coherent structures generated at the end of a stack of parallel plates in a standing wave acoustic field *Exp. Fluids* **45** 833–46
- Marx D, Mao X and Jaworski A J 2006 Acoustic coupling between the loudspeaker and the resonator in a standing-wave thermoacoustic device *Appl. Acoust.* **67** 402–19
- Ohmi M and Iguchi M 1982 Critical Reynolds number in an oscillating pipe flow *Bull. JSME* **25** 165–72
- Paek I, Braun J E and Mongeau L 2005 Second law performance of thermoacoustic systems *J. Acoust. Soc. Am.* **118** 1892
- Rayleigh J W 1945 *The Theory of Sound, 1894* (New York: Dover)
- Richardson P D 1963 Note: Comments on viscous damping in oscillating liquid columns *Int. J. Mech. Sci.* **5** 415–8
- Rott N 1980 Thermoacoustics *Adv. Appl. Mech.* **20** 135–75
- Shi L, Yu Z and Jaworski A J 2009 Vortex formation at the end of the parallel-plate stack in the standing-wave thermoacoustic device *Proc. 16th Int. Congress on Sound and Vibration (Kraków, Poland, 5–9 July 2009)*
- Swift G W 1988 Thermoacoustic engines *J. Acoust. Soc. Am.* **84** 1145–80
- Swift G W 2001 *Thermoacoustics: A Unifying Perspective for Some Engines and Refrigerators* (Sewickley, PA: Acoustical Society of America)
- Womersley J R 1955 Method for the calculation of velocity, rate of flow and viscous drag in arteries when the pressure gradient is known *J. Physiol.* **127** 553–63
- Worlikar A S and Knio O M 1996 Numerical simulation of a thermoacoustic refrigerator I: unsteady adiabatic flow around the stack *J. Comput. Phys.* **127** 424–51
- Worlikar A S, Knio O M and Klein R 1996 Numerical simulation of a thermoacoustic refrigerator *Proc. ESAIM* vol 1 pp 363–75
- Zdravkovich M M 1997 *Flow Around Circular Cylinders, Volume 1: Fundamentals* (Oxford: Oxford University Press)

# Chapter 8 Conclusions and suggestions for future work

This presented work focused on studies of the fluid flow occurring around parallel-plate stacks in a standing-wave thermoacoustic device at a low operating frequency. The following main conclusions can be drawn (accompanied by the relevant discussion) based on the presented work.

1. A standing wave thermoacoustic system has been designed and constructed. An analytical linear model has been developed for describing the coupling between the loudspeaker and the resonator including a convergent section. Comparisons between the results of the analytical model and the measurement show a good agreement when the acoustic oscillation amplitude is small. The increasing discrepancy between the analytical results and measurement at larger acoustic oscillation amplitude is found to be mainly caused by the minor loss. It is understood that the coefficient of fluid resistance obtained for steady flow condition can also be used for oscillatory flows if the resonator is operated at the first mode resonance and when the particle displacement amplitude is large. However, a further and more extensive study of the minor losses in oscillatory flow is necessary if one needs to establish a reliable model to work for high oscillation amplitude.
2. Velocity and vorticity fields of the acoustically excited oscillatory flow around parallel-plate stacks are measured by using PIV techniques. The flow structures around the end of the stacks are investigated for a series of acoustic excitation levels (and thus displacement amplitudes). Flow patterns such as symmetrical and attached pairs of vortices which could be either “elongated” or “concentrated” are observed. When the drive ratios are increased, the flow in the tested range of conditions could evolve into patterns resembling alternate vortex shedding, similar to von Karman “vortex streets” characteristic for flows past bluff bodies. Two modes of such an “alternate shedding” are identified, which are likely caused by different flow physics. The first mode seems to be related to the instability of the elongated shear layers, while the second mode seems to be related to the classical von Karman “vortex street”.

3. The temporal variation of the flow velocity at the end of the parallel plate stack is recorded by employing the hot wire anemometry technique. The frequency of velocity fluctuation related to the various types of flow pattern is investigated. Interestingly, two different values of Strouhal number (around 0.1 and 0.2) are related to the two different modes. These values are confirmed by a later study (Shi et al, 2010) carried out for similar conditions at Reynolds number from 200 to 5000, in which a general trend is discovered for the Strouhal number to increase with Reynolds number up to a limiting value of about 0.2.
4. The turbulence characteristics of oscillatory flows past stacks of parallel plates have been studied. It has been shown that the unsteady/turbulent flow behaviour can be described by using classical Reynolds decomposition with the resulting fluctuation intensity ‘maps’. Further simplified parameters such as area-averaged or area-cycle-averaged turbulent kinetic energy are suggested to be used in the description of the flow unsteadiness.
5. A new methodology was also proposed for spatial filtering of instantaneous fluctuation velocity fields in order to separate the contributions from large- and small-scale flow structures to the overall fluctuation intensity. It is suggested that the term ‘turbulence intensity’ should only be associated with the small scale vortex structures, which are more likely to control the heat transfer processes.
6. The oscillatory flow past a stack of parallel plates when the fluid moves out of the stack (so-called “ejection stage” of the cycle) exhibits some similarities to the wake flow of a unidirectional steady flow past a bluff body. The wake flow is thought to be essentially made up of two shear layers with vorticity of opposite signs that are fed from the stack channel. It seems plausible that the behaviour of and the interaction between the shear layers determine the different flow structure to form and develop at the plate ends.
7. A similarity analysis of the governing equations of the oscillatory flow motion around a parallel plate is carried out. Groups of non-dimensional parameters are identified. Each set of non-dimensional parameters essentially consists of: (i) one kinematic parameter, i.e. the kinematic Reynolds number  $Re_\omega$ , (ii) one dynamic parameter, i.e. the Reynolds number  $Re_d$  or  $KC$ , or more indirectly the drive ratio,  $Dr$ , and (iii) a stack configuration parameter,  $d/h$ , or the porosity  $\phi$ , or the Womersley number,  $Wo = h/\delta_v$ .

Based on this, the non-dimensional parameters groups ( $Re_\omega$ ,  $Re_d$  and  $Wo$ ) or ( $Re_\omega$ ,  $KC$  and  $Wo$ ) or ( $Re_\omega$ ,  $Re_d$  and  $d/h$ ) or ( $Re_\omega$ ,  $KC$  and  $d/h$ ) are suggested as appropriate “triads” to be used with oscillatory flows past parallel plate stacks. It is demonstrated that the discovered flow patterns can be categorized into groups in the non-dimensional parameter space.

Some further works could be done towards a better understanding of the fluid flow and (in a longer term) the heat transfer process in a more practical arrangement of thermoacoustic stack and heat exchangers. It would be particularly interesting to look at the following issues:

1. Effect of an adjacent parallel-plate structure on the flow. The configuration used in this study is simplified to enable the evaluation of measurement methodologies. In reality the stack will be coupled to a heat exchanger and so the flow field will be much more complicated, especially as the two structures would effectively be in each other's wakes.
2. The thermal effect on the flow field. The arrangement studied in this work is isothermal, and so there is no opportunity to study the actual heat transfer processes. Therefore a further improvement would be to impose appropriate thermal boundary conditions on the structures studied and combine PIV with temperature field measurement, for example by Planar Laser Induced Fluorescence (PLIF).
3. The effect of finite length on the flow. For the stack, the acoustic displacement amplitude is generally much smaller than the plate length. Therefore the non-dimensional stack length or the aspect ratio  $l/d$  is neglected. However, it may need to be considered when the displacement amplitude of the fluid oscillation is comparable to the plate length, such as that of a heat exchanger. The flow disturbance at one end of the plate may have significant effect on the flow at the other end of the plate.
4. In order to further understand the relationship between the non-dimensional governing parameters and the flow behaviour, experimental data from much more diverse experimental conditions than these obtained as part of the current study will be required. In particular, the critical value at which the transition of the wake flow around the plate end from being symmetric to asymmetric and the effect of the channel width on the flow pattern need to be studied.

# Appendix A

## Additional information about the measurement techniques used during the course of the experimental programme

In the “alternative format” thesis, the information related to the experimental setup, procedures and details of the instrumentation used is typically distributed between individual “papers-chapters”. Some information judged as “trivial”, “obvious” or “standard practice” to the scientific community may be neglected altogether. The guidance on the alternative format indicates that in order to guarantee the coherence of the thesis it may be advisable to construct a stand-alone appendix which contains the experimental details, otherwise scattered throughout the thesis, and which could serve as a starting point for any researchers attempting to follow up the research described in the thesis. Current Appendix A is included to fulfil the above stated needs.

### A.1 Hot-wire anemometry and experimental measurements

#### A.1.1 Introduction

Hot-wire anemometry, sometimes also called constant temperature anemometry (CTA) is an indirect measurement technique of flow velocity. It is a point-wise measurement technique appropriate for the measurement of time series of velocity in one, two or three dimensional gas and liquid flows. The velocity of the flow in which a sensing element is immersed is related to the heat transfer rate between the sensing element and the flow. This relationship can be found from the calibration procedure for each particular piece of sensing element and a transfer function can then be derived. The transfer function is then used to convert the acquired data from the measurements to velocity. The sensing element is usually made of a short piece of very fine Tungsten or Platinum wire. The constant temperature anemometry has been used to measure the flow velocity probably for over a century (Comte-Bellot, 1976). Nowadays, the constant temperature anemometry is still broadly used in the studies of fluid flow phenomena, particularly, in the study of the turbulence characteristics of the flow because of its high temporal resolution and

continuous signal output – see, for example, Tutu and Chevray (1975), Antonia, Orlandi and Romano (1998) and Siebert and Lehmann (2007).

Measurement of the oscillatory flow velocity by using CTA technique has been carried out by Ingard and Ising (1967) and Dubbelday (1986) in an acoustic field, and Ohmi et al (1982) in an oscillatory pipe flow, among many others. Ingard and Ising (1967) measured the oscillatory flow velocity at the centre of an orifice using a hot-wire probe. Not much detail about the application of the hot-wire anemometer, however, is available from this publication. Dubbelday (1986) studied the possible application of a hot film sensor to the measurement of the particle velocity in an oscillating medium of liquid. The response of the hot film was found more sensitive for an acoustic oscillation of a lower frequency. The effect of the natural convection on the output signal was also studied. In a short communication by Lebedeva and Dragan (1991), very brief information on the amplitude calibration in intensive sound fields with oscillating velocity amplitude from 0.15m/s to 10m/s and frequency from 16 Hz to 2 kHz was summarized. Multiple techniques, such as, standing wave resonator, travelling wave field together with two-microphone method and the known flow in the neck of Helmholtz resonator were applied in the calibration process. The dependence of the sensitivity of the sensor response on the oscillation frequency was also found. However, detailed information on the calibration and phase relationship between the oscillating pressure and velocity were missing. Measurements of acoustic velocity using the hot-wire anemometry were also reported by Grushin and Lebedeva (2001), and Grushi, Dragan and Lebedeva (2001).

The calibration of the hot-wire sensor in a standing wave acoustic field was studied and the detailed information was presented by Huelsz and López-Alquicira (2001). Both the amplitude and phase of the response of the hot-wire sensor was carefully calibrated in less intensive sound field in air with an oscillating velocity range of 0.03m/s to 0.8m/s. It was based on the principle that for standing waves, the velocity oscillation amplitude can be calculated from the local pressure oscillation amplitude if the adiabatic condition can be assumed. The profile of amplitude of the oscillating velocity and the phase difference between the oscillating velocity and pressure measured using a calibrated hot-wire sensor compared well with the predicted data by the linear acoustic theory of a standing wave resonator (Huelsz, Lopez-Alquicira and Ramos, 2002).

As a summary, a few points need to be further emphasised in relation to the application of the constant temperature anemometry in a purely oscillating flow, such as that in an acoustic field. Typically, the time variation of the CTA output signal has a frequency of two times that of the fluid motion (Dubbelday, 1986). This is because the hot-wire sensor is sensitive to the flow velocity normal to its axis but cannot discriminate the direction of the flow – the directional ambiguity feature of the constant temperature anemometry technique. Secondly, due to the fact that the velocity of the oscillating flow to be measured is oscillating about a zero value, the effect of natural convection is not negligible, in particular when the flow reverses its direction. But if the hot-wire probe is so placed that the flow, which is oscillating in the horizontal direction, is actually moving in the bi-normal direction of the sensor, the natural convection effect will be the same for both directions and will be intrinsically included in the *in-situ* calibration procedure. Thirdly, due to the thermal inertia of the sensor, the response of the hot-wire sensor does not reach the base voltage value obtained in still air, and it usually becomes more obvious for an oscillating flow of higher frequency. A further concern of the velocity measurement in the oscillating flow field is that the flow at the half cycle flowing back may be contaminated by the presence of the probe. Experiments showed that such a possibility does not exist because disturbances produced by the probe disappear when the flow reverses its direction (Ohmi et al, 1982).

### **A.1.2 Principles and the hot-wire anemometry system**

A constant temperature anemometer normally consists of a Wheatstone bridge, of which one arm is replaced with the sensor, a fine filament made of Tungsten or Platinum (Fig. A.1). The sensing element is maintained at a constant temperature higher than that of the fluid by applying a constant voltage to the sensor. When the probe is placed in a flow field, the heated sensor is cooled by the flow and the change of its resistance breaks the balance of the bridge. The Wheatstone bridge is kept balanced by automatic adjustment of the heating current, the magnitude of which determines the mean velocity. The heat transferred from the element to the flow passing it can be measured by the amount of the input electrical power. The accuracy of this method is usually very much dependent on the understanding of the relationship between the flow velocity and the heat transfer between the flow and the sensing element.

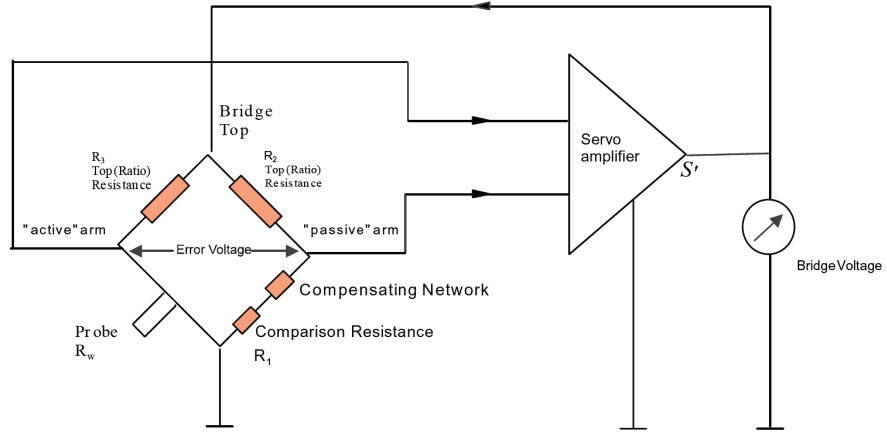


**Figure A.1 Schematic of a hot-wire anemometer (Jensen 2004)**

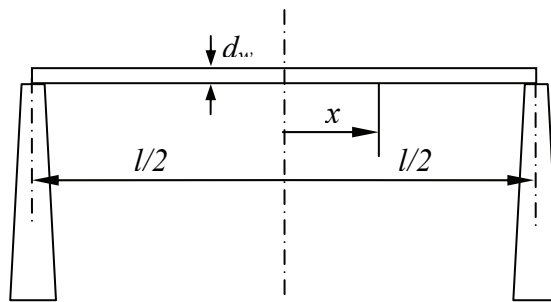


**Figure A.2 Geometry of hot-wire sensor**

The geometry of the sensor of the hot-wire probe and the coordinate applied are shown in Fig. A.2. The full heat balance of the wire of a unit length can be described by the equation (Bruun 1995):

$$\frac{I^2 \chi_w}{A_w} = \pi d_w h (T_w - T_a) - k_w A_w \frac{\partial^2 T_w}{\partial x^2} + \pi d_w \sigma \varepsilon (T_w^4 - T_s^4) + c_w \rho_w A_w \frac{\partial T_w}{\partial t} \quad (\text{A.1})$$

based on the assumption of an infinitely long wire. On the left hand side of the Equation is the heat generation rate on the wire element by an electrical current,  $I$ .  $\chi_w$  is the electrical resistivity of the wire material at the local wire temperature,  $T_w$ , and  $A_w$  is the cross-sectional area of the wire. The first term on the right hand side of the equation is the forced-convection heat transfer rate on the wire element to the fluid passing through it.  $d_w$  is the diameter of the wire,  $h$  is the heat transfer coefficient, and  $T_a$  is the temperature of the fluid around it. The second term is the total conduction heat transfer rate out of the wire element.  $k_w$  is the thermal conductivity of the wire material at temperature  $T_w$ . The negative sign shows the direction of the heat transferred, out of the wire element. The third term is

the radiation heat transfer rate.  $\sigma$  is the Stefan-Boltzmann constant,  $5.67 \times 10^{-8} \text{ W}/(\text{m}^2 \cdot \text{K}^4)$ ,  $\varepsilon$  is the emissivity of the wire, and  $T_s$  is the temperature of the surroundings. The fourth term is the heat storage rate.  $\rho_w$  is the density of the wire material and  $c_w$  is the specific heat of the wire material per unit mass. The characteristics of Tungsten wire used in the study are listed in Table A.1.

**Table A.1 Characteristics of Tungsten wire**

Diameter	$d_w$	5.0	$\mu\text{m}$
Cross-sectional area	$A_w$	$0.196 \times 10^{-10}$	$\text{m}^2$
Density	$\rho_{w,20}$	19.3	$\text{g}/\text{cm}^3$
Electrical resistivity	$\chi_{w,20}$	5.4	$\mu\Omega \cdot \text{cm}$
Temperature coefficient of resistivity	$\alpha_{20}$	0.0036	1/K
Thermal conductivity	$k_{w,0-100}$	1.73	$\text{W}/(\text{cm} \cdot \text{K})$
Specific heat	$c_{w,25}$	133	$\text{J}/(\text{kg} \cdot \text{K})$
Coefficient of thermal expansion	$\beta_{w,0-100}$	$4.5 \times 10^{-6}$	1/K

In most CTA applications, the term for the radiation heat transfer rate is very small and neglected. The emissivity,  $\varepsilon$ , of Tungsten is 0.24 ~ 0.27 at normal operating temperature between 100 and 250 °C. Thus the radiation heat transfer rate

$$E = \pi d_w \sigma \varepsilon (T_w^4 - T_s^4) \approx \pi d_w \sigma \varepsilon (T_{w,m}^4 - T_a^4) \quad (\text{A.2})$$

is about  $1.5 \times 10^{-2} \text{ W}/\text{m}$ , according to Eq. (A.1). If the overall heat transfer rate of  $100 \text{ W}/(\text{m}^2 \cdot \text{K})$  is assumed, the forced-convection heat transfer rate,  $\pi dh(T_w - T_a)$ , is about  $0.35 \text{ W}/\text{m}$ . Compared with this, the radiation heat transfer rate,  $E$ , is small and can be neglected. However, it may introduce error when the forced-convection heat transfer rate is small, which could be true at instants when the oscillating flow reverses.

Although the temperature of the wire is virtually controlled to be constant in the constant temperature mode, the temperature of the wire is non-uniform along its length. In this case Eq (A.1) becomes

$$\frac{I^2 \chi_w(x)}{A_w} = \pi d_w h(x) [T_w(x) - T_a] - k_w A_w \frac{\partial^2 T_w(x)}{\partial x^2} \quad (\text{A.3})$$

The wire resistance  $R_w$  at temperature  $T_w(x)$  can be obtained by integrating  $\chi_w/A_w$  along the wire once the temperature dependence of the resistivity for hot-wire material is known.

More generally, by using a mean wire temperature,  $T_{w,m}$ , the wire resistance  $R_w$  can be obtained from

$$R_w = R_{20} [1 + \alpha_{20} (T_{w,m} - T_{20})] \quad (\text{A.4})$$

Therefore, in the case of an infinitely long wire, whose temperature dependence of  $x$  can be neglected, for a wire segment of length  $l$ , Eq. (A.3) becomes,

$$I^2 R_w = \frac{\pi l k}{\alpha_0 R_0} (R_w - R_a) \text{Nu} \quad (\text{A.5})$$

The dimensionless Nusselt number is defined as  $\text{Nu} = hd_w/k$ . Consider that the convective heat transfer from a wire in a cross-flow often has a correlation between the Nusselt number,  $\text{Nu}$ , and the Reynolds number,  $\text{Re} = ud_w/\nu$ , based on the flow velocity,  $u$ , of the form

$$\text{Nu} = A + B\text{Re}^n \quad (\text{A.6})$$

Equation (A.5) becomes

$$E_w^2 = A + Bu^n \quad (\text{A.7})$$

Here,  $E_w = I_w R_w$  denotes the wire voltage, and the constants  $A$  and  $B$  include all other relevant constants. The same correlation is used in practice when a finite-length wire element has to be used. The values of  $A$ ,  $B$  and  $n$  can be determined by a suitable calibration procedure. For convenience of use, Eq. (A.7) is sometimes replaced by a polynomial correlation found in the calibration process, such as

$$u = A + BE_w + CE_w^2 + DE_w^3 + FE_w^4 \dots \quad (\text{A.7})$$

A four degree polynomial is often found sufficient in practical use.

In the research described in this thesis, the velocity oscillation at the measured points was sensed by a Dantec 55P11 probe with  $5\mu\text{m}$  diameter tungsten wire. The probe was connected to the constant temperature anemometer (TSI IFA300) via a standard 5 meter

BNC cable. In all measurements, a 1.8 overheat was used. With the effective implementation of SmartTune™ bridge optimization circuitry, IFA300 can achieve a frequency response of up to 250 kHz without tuning. The signal output was digitized and recorded by the DAQ device (Omega DaqTemp 14A). The hot-wire probe was placed normal to the plate and the axis of the resonator, at set distance from the edge of the plate. In the transverse direction normal to the plate, the hot-wire probe was traversed using a micrometric traverse.

### A.1.3 Calibration of a hot wire probe

The calibration of the hot-wire sensor was carried out in the same resonator, in which the characteristics of the flow around parallel plate stacks are to be studied. When the calibration of the hot wire sensor was carried out in the resonator, the stack was removed from the resonator. The transverse size of the cross section of the resonator is far smaller than the length of the resonator so that a plain wave can be assumed in the resonator and linear acoustics is assumed to be valid. This was used as a known velocity source to calibrate the hot-wire probe. The pressure oscillation at the cross section where the hot-wire probe was calibrated was measured with a condenser microphone (Brüel & Kjør, Model 4136). A piezo-resistive pressure transducer (Endevco, Model 8510B-2) was mounted on the end plate of the resonator to measure the acoustic pressure amplitude in the resonator.

At a position far away from the wall of the resonator, the fluid experiences an adiabatic process. The oscillating velocity amplitude and its temporal variation are defined as

$$u_a(x) = \frac{p_A \sin(kx)}{\rho_m a}, \quad u_a(x, t) = \frac{p_A \sin(kx)}{i \rho_m a} e^{i \omega t} \quad (\text{A.8})$$

where  $p_A$  is the pressure amplitude at the closed end of the resonator,  $\rho_m$  is the density of the fluid at the mean temperature  $T_m$  and the mean pressure  $p_m$ .  $a$  is the sound speed,  $k$ , the wave number, is  $2\pi/\lambda$ , and  $x$  is the distance between the location of the hot wire probe and the closed end of the resonator.

Note that the velocity oscillation in the resonator is always coupled with a pressure oscillation, thus a temperature oscillation. The hot wire sensor is sensitive to the change of both the flow velocity and the temperature. To minimize the effect of the temperature oscillation, a position at the velocity antinode (pressure node) is preferred for calibration,

particularly when high amplitude standing wave is used to excite velocity oscillation of large amplitude.

Because of the velocity direction ambiguity of the hot-wire anemometry, only positive output signal can be obtained from the anemometer, as shown in Fig. A.3. Also shown in the figure is the time variation of the acoustic velocity with its absolute value in the middle graph. It is seen that the temporal variation of the CTA output signal very much resembles the rectified acoustic velocity. The minimum value of output signal in one cycle, corresponding to a zero acoustic velocity, is the base voltage  $E_b$ . The thermal inertia of the hot-wire sensor elevates the base voltage compared to the value measured in stagnant air. This problem causes unreliable velocity value from the constant temperature anemometer when the acoustic velocity is small, or during the flow reversal.

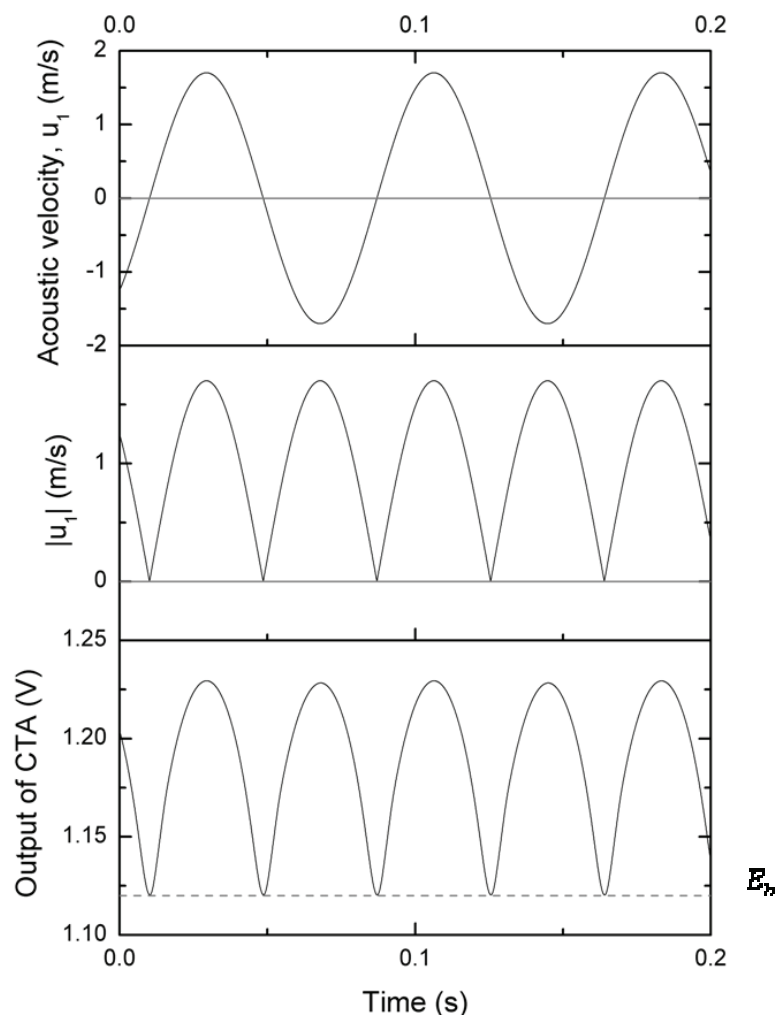


**Figure A.3 Time variation of the acoustic velocity, its absolute value and output of the constant temperature anemometer**

To obtain the correlation of the voltage signal of the constant temperature anemometer and the acoustic velocity, one can plot the amplitude of the output voltage against the amplitude of the reference velocity at different drive ratios. This is the approach used by Huelsz and López-Alquicira (2001). Alternatively, one can plot the waveform of the anemometer output against the acoustic velocity oscillation for one cycle, at a relatively large drive ratio to cover a larger range of velocity. The second method leads to the difficulty of finding the reference velocity in a corresponding phase in the oscillation cycle. In addition, this method is based on the assumption that the time response of the sensor is constant when the acoustic velocity varies. This may not always be true, particularly when the anemometer is applied to an acoustic wave of high frequency. Therefore the first approach is more convenient and reliable for practical application and it was also used in this study. An example result of the calibration is reproduced in Fig. A.4.

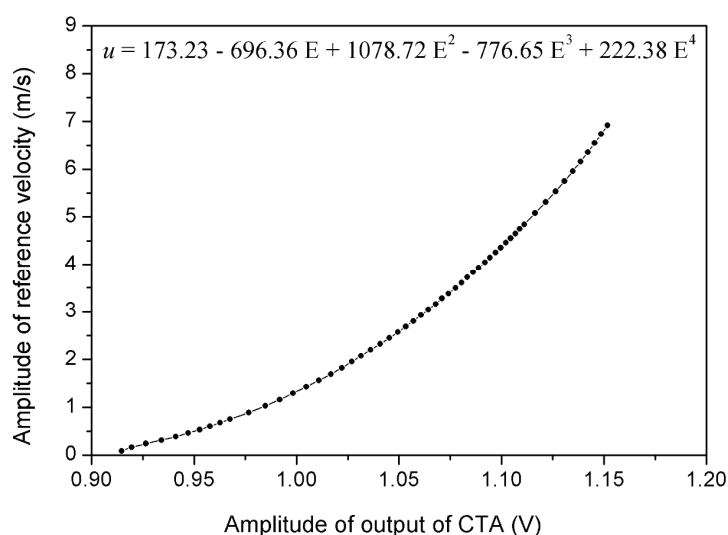


**Figure A.4 Amplitude of CTA output vs amplitude of reference velocity at different drive ratios, and the fitted polynomial correlation**

#### **A.1.4 Data acquisition and processing**

After the calibration, the hot wire sensor is used to measure the acoustic velocity of the flow in the wake of the stack plate. The frequency of velocity fluctuation in the wake was estimated to be no more than 2.0 kHz within the range of velocity studied from a preliminary test. According to Nyquist theory, the sampling frequency is therefore set to 2.5 times the maximum signal frequency of interest. Therefore, in the measurement, the hot-wire signal was recorded with a sampling frequency of 5 kHz by the data acquisition card (Omega DAQTemp14A). 16,384 data points were acquired for each experimental run.

The acquired voltage data were converted to velocity values by using the correlation equation from the calibration. The signals were then analyzed using the Fast Fourier Transform (FFT) method in order to extract the peak frequencies in the frequency spectra.

## **A.2 Particle image velocimetry and experimental measurements**

### **A.2.1 Introduction**

Particle image velocimetry (PIV) is a quantitative flow measurement technique by which two or three components of the velocity of the flow in a plane or even a volume can be measured at a time instant. In a typical 2D PIV measurement, the movement of small tracer particles in a plane illuminated by a light sheet, usually generated by a laser, is recorded on a digital camera. Analysis of successive images then enables the vector velocity field of the fluid flow to be determined. Since, typically, the particulate velocity vectors are measured simultaneously at many thousands of points in the flow, this is a whole field measurement technique, and is much faster and less laborious than point-wise measurement techniques such as LDA and CTA. Statistical methods are used to determine average velocity vectors for clusters of particles in small regions of the flow plane known as “interrogation spots”. The ability to capture the vector velocity distribution across a whole flow field instantaneously makes the PIV technique a very useful tool in studying fluid flows.

The historical development of PIV has been reported in a number of review articles, including Adrian (1991, 2005) and Grant (1997). PIV has been developed up to a point where it is now widely available from commercial suppliers. Its capability has extended to the measurement of the three velocity components in a plane (stereoscopic and holographic PIV) and even a three-dimensional volume (tomographic PIV); see, for example, Arroyo and Greated (1991), Royer (1997), Hinsch (2002), Ciofalo, Signorino and Simiano (2003), Elsinga, van Oudheusden and Scarano (2006) and Elsinga et al (2006, 2008). Another important achievement is its application in the measurement of micro-scale flow in micro-fluidic devices ( $\mu$ PIV); see, for example, Santiago et al (1998) and Shinohara et al (2004). All these make PIV a useful and popular experimental tool in fluid mechanics; and it has been used with considerable success in a variety of applications, such as aerodynamics.

Experience shows that the PIV technique can be applied to the measurement of acoustic velocity fields, and particularly acoustic streaming, for example by Hann and Greated (1997a, 1997b), Campbell et al (2000) and Nabavi, Siddiqui and Dargahi (2007). The measured velocity field in a standing wave resonator is the superposition of the streaming

velocity and the acoustic velocity. The magnitude of the acoustic velocity is typically several times larger than that of the streaming velocity. As a result, in a given velocity measurement, the streaming velocity component is suppressed by the acoustic velocity component. The streaming velocity can be obtained by either removing the acoustic velocity component or performing the velocity measurement in a location where the acoustic velocity is also small or negligible, such as in the vicinity of a velocity node. The latter strategy was used by Arroyo and Greated (1991), and Hann and Greated (1997b). Limited by the time resolution of the hardware and the availability of the digital CCD camera, the motions of the tracer particles in several acoustic cycles were imaged on a single film. To derive the acoustic velocity field, a special algorithm was developed for this purpose. Nabavi et al (2007) used a synchronized PIV technique to measure acoustic streaming, ideally anywhere in the resonator, whether a large amplitude acoustic velocity was present or not. In this technique, PIV images precisely in phase but separated by a time difference of one or more acoustic cycles were cross-correlated to obtain the streaming velocity field, while the acoustic velocity field was obtained by cross-correlating two consecutive PIV images.

### **A.2.2 Principle of the particle image velocimetry**

A very brief description of the principle of the PIV technique is given here. More detailed and comprehensive information can be found in the work of Raffle et al (2007) and the 490 references given there. PIV is a non-intrusive measurement technique which infers the local velocity of the fluid from the velocity of tracer particles (or seeding particles). These particles of optimal size must be distributed evenly in the flow region to be investigated and at a certain density for high quality PIV images. The flow under investigation is illuminated twice in succession using a light sheet generated by a pulsed laser. The duration of the particle illumination must be short so that the particles do not move significantly and cause streaking. The images of the illuminated particle in the chosen flow field are captured by a CCD camera.

The recorded images are then evaluated to obtain the average particle displacements between the first and second images for the clusters of seeding particles in the interrogation spot. The average particle displacement is converted to the physical displacement of the particle in the fluid, taking into account the magnification factor of the camera lenses. A local velocity vector can be calculated from the particle displacement and the time difference between the two laser pulses. These calculations assume that the tracer particles

faithfully follow the flow patterns and therefore move with the local flow velocity between the two laser pulses.

In order to determine the instantaneous velocity vectors in a flow field, the PIV technique requires a fluid flow with appropriate tracer particles mixed into it, a pulsed laser sheet to illuminate the tracer particles, a CCD camera to record the planar images of the seeded flow, and a computer for post-processing the recorded images.

To obtain accurate results, the tracer particles should be small enough to follow the fluid motion accurately and, at the same time, be large enough to be clearly visible when illuminated by the laser light. Ideally, the particle density should be of the same order as that of the flowing fluid, so that they are neutrally suspended in the fluid and the gravitationally induced velocity is zero. Tracking of the fluid motion also requires that the diameter of the tracer particles is small in order not to disturb the flow and to minimise their inertia. However, for the tracer particles to be seen clearly on the image, they should have good light-scattering capabilities, implying that they should have a different refractive index from that of the fluid into which they are mixed and be relatively large. Otherwise, laser pulses of high energy should be employed so that there is enough light scattered from the particles to be captured by the camera. It can be seen that these apparent contradictions call for a careful choice of tracer particles and a compromise between the requirement for small size to improve their ability to track the flow fluctuations and the need to increase the size of the particles to improve light scattering (Melling, 1997).

When seeding the flow, careful consideration should be given to the variations in velocity of the tracer particles across the flow measurement area. A homogeneous medium particle distribution density has been found to be most desirable, since this leads to high quality images which, in turn, yield the best results when statistical PIV evaluation techniques are applied (Raffel, 1998). Currently, there is no definitive method of calculating how much seeding should be added to a flow to achieve this medium particle distribution density, so that a tedious trial and error method must generally be resorted to. Generally, acceptable PIV results are likely to be obtained when the distribution of seeding particles is such that there are three or more particle pairs per interrogation spot. However, no significant increase in accuracy has been reported in research for cases with more than five particle pairs per interrogation spot. Whenever possible, the fluid and the seeding particles should be thoroughly mixed before entering the section illuminated by laser sheet, so as to

disperse the particles evenly and ensure that their distribution is approximately uniform across the entire fluid flow measurement plane.

There is a wide variety of tracer particles for PIV applications but, in general, smoke or fog particles with diameter near or below  $1.0\ \mu\text{m}$  are used for PIV experiments involving gaseous flows. This smoke is mostly produced by vaporization or atomization of oil (Melling, 1997).

Lasers are the most convenient and widely used light sources for PIV applications, mainly because of their ability to emit a monochromatic light beam of very high power which, by the use of the appropriate optics, is very easily converted to a thin light sheet. A light sheet is usually desirable with this technique, since only the tracer particles in the specified plane in the flow field need to be illuminated and recorded on the image. Thus, the light sheet should be thin enough to ensure that the recorded images constitute a true representation of what is happening in that plane of the flow. If the light sheet is too thick, the camera will capture out-of-plane particles, resulting in the flow analysis being based upon a volume rather than a plane.

In order to capture two consecutive planar images, the laser beam is pulsed twice in succession within a short time interval, known as the “pulse separation”, which is equal to the time delay between the two illumination pulses. The pulse separation should be long enough to enable the accurate determination of particle displacements between the first and second images, but short enough to avoid particles with an appreciable out-of-plane velocity component leaving the light sheet between subsequent illuminations (Raffel, 1998). In order to avoid blurring of the images, the pulse duration should be short enough to “freeze” the particles during the pulse exposure time. The pulsed laser beam is usually conditioned by a combination of cylindrical and spherical lenses, which control the width and thickness of the sheet respectively.

A camera with high sensitivity and high spatial resolution is preferred to capture and record the pairs of particle images which show the instantaneous velocity distribution in the illuminated flow area. The camera should be positioned so as to view the imaging area defined by the light sheet as near as possible to the perpendicular direction, meaning that optical access in two orthogonal planes must always be provided for. The images of the illuminated particles are recorded either on a single camera frame by double exposure, or

on two separate camera frames in the more advanced technique using a double pulsed laser. In the latter case, the recording of separate images is made possible by the use of a specialised CCD camera with frame straddling capability.

The principle behind the frame straddling technique, which allows the operation of the PIV system to be adjusted to optimise its performance according to the flow conditions, is illustrated in Fig. A.5. The principle is that the first laser pulse is set to occur towards the end of the exposure of the first frame and the second laser pulse at the beginning of the exposure of the second frame. In the PIV software used (TSI INSIGHT 3G™), positioning of the first laser pulse at the end of the first frame was achieved by setting a pulse delay time. The process of image acquisition involves a CCD camera capturing the first image and transferring this to a buffer memory, before capturing the second image and repeating this process. This whole sequence is repeated for successive pairs of images, and the pairs of particle images produced are transferred and stored in the computer memory.

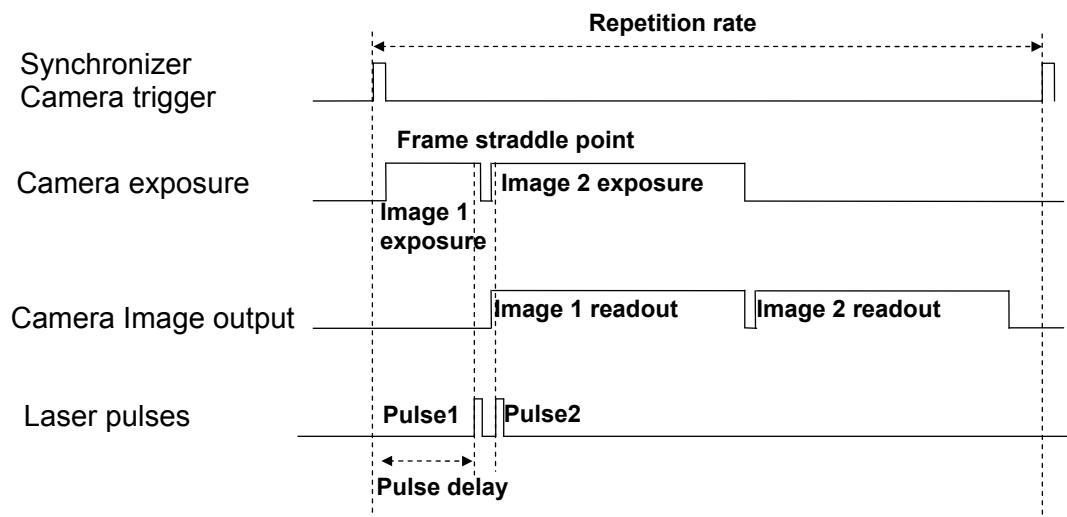


**Figure A.5 Timing diagram for PIV imaging in frame straddling mode**

In order to calculate the instantaneous velocity vector distributions and determine other properties of the flow field from a particular pair of field images, the PIV software incorporates image processing algorithms which employ statistical methods to evaluate the average velocity from all individual particle displacements in a small region. This is accomplished by dividing the flow field of each image into small sub-areas known as interrogation spots. Through application of the PIV processing algorithms, a local displacement vector is determined for each interrogation spot for the particle images shown by the first and second illumination pulses. Two methods are available here. Either double

exposed, single frame images are processed using an auto-correlation algorithm, or images captured on separate frames through the frame straddling technique are processed using the cross-correlation algorithm. The latter method was used in the work presented. The successive image pairs captured using the frame straddling technique, processed by means of the cross-correlation algorithm, yields the direction of the particle movements, which is otherwise a problem of directional ambiguity for the double exposed, single frame method. In this case, cross-correlation of the image pairs, within the same interrogation spot, yields the particle displacements and the direction of the displacement corresponds to the movement of the particles from the first to the second frame. This process is repeated for all the interrogation spots needed to cover the whole flow field in order to determine the instantaneous velocity vector distribution across the flow field.

For each interrogation spot, application of a “peak finder” algorithm allows determination of the location of the displacement peak, which then yields a single velocity vector for each interrogation spot. A search of the literature reveals that there are a number of peak finder algorithms in use. Among these, the development of the Gaussian peak finder has led to the determination of these displacement peaks with improved accuracy, enabling smaller interrogation spots to be utilised, thereby leading to an increase in the spatial resolution of the PIV technique (Raffel, 1998). This is the algorithm used in the present study.

### **A.2.3 PIV system and experimental arrangement**

The PIV technique explained above was applied to study the oscillating flow in the resonator when complex flow channels were introduced by the presence of the parallel-plate stack. The PIV laser system (Big Sky Laser, CFR PIV system) consisted of two separate, fully functional standard laser systems (CFR200), each composed of a frequency doubled Nd:YAG laser, a power supply unit and a self-contained cooling unit (Big Sky Laser, Ultra ICE). The two laser systems could be run simultaneously, or either could be run independently of the other. When running both lasers simultaneously, the flash lamps of the two laser systems would be triggered externally to maintain the time difference required between laser pulses from each laser head, for example, by a synchronizer unit as in the application for this study. Each laser head of this PIV laser system is able to deliver a maximal energy of 200 mJ per pulse at 532 nm. The pulse duration is typically less than 8 ns. For the PIV application, the two laser heads were placed side by side on a common base, behind a beam combiner module, so that the two successive laser pulses illuminated the same flow field.

The laser beam from the laser system had a diameter of about 6 mm. Optical lenses had to be used to expand the laser beam into a sheet to illuminate the seeded flow in a plane. A combination of a spherical lens with a focal length of 1000 mm and a cylindrical lens with a focal length of -25 mm was mounted onto the exit of the beam combiner module. In order to ensure that the waist of the laser sheet, where its thickness was smallest, was located at the stack end, the 1000 mm spherical lens had to be placed one metre from the stack end.

In order to illuminate the flow in the stack channel to be studied, the laser sheet entered the resonator perpendicular to the resonator axis through one of its walls and was reflected by the mirror placed in the resonator at 45° towards the laser beam. The distance between the mirror and the stack end was made as large as possible, so that introducing the mirror and its support had a minimal effect on the flow around the stack. In preliminary experiments, the laser sheet was projected directly onto the stack, perpendicular to the plate surface. But to reach the plates located in the middle of the stack where the measurements were performed, the light had to go through a number of plates, which reduced its intensity to such an extent that the PIV system could not be deployed.

The camera used to capture PIV images was a progressive scan CCD camera (TSI Powerview™ Plus 4MP), having 2048 × 2048 light-sensitive pixels. It operated at a maximum repetition rate of 16 frames per second and provided a 12-bit grey scale output. The minimum frame straddling time offered for PIV capture was about 200 ns, making possible the measurement of very high speed flow. A 105 mm f/2.8D AF Micro Nikkor lens was attached to the camera via an F-mount.

In all the PIV experiments performed in this study, the camera was always operated in one of two modes. The “free-run mode”, where images are viewed from the camera with no synchronisation between the laser and camera, was used during the setup of any new experiment and while checking and adjusting the distribution density of seeding particles, while the “frame straddling mode” was used to acquire the actual PIV images of the flow field. The images were taken only when a triggering signal was received, and the timing of the camera to capture images was synchronised with the laser.

A synchroniser (TSI, LASERPULSE™, Model 610034) was used to control the timing of the laser and the CCD camera during the process of acquiring PIV images. The timing

pulse sequence for the operation of the camera in the frame straddling mode was triggered to start by the signal from the phase locking pulse generator. To adjust the phase of the triggering pulse corresponding to the acoustic oscillation, a function generator (TTi, Model TG1010A) was added between the phase locking pulse generator and the synchronizer. It was set to “trigger mode” and the signal from the phase locking pulse generator was used as the trigger signal here. The phase of its auxiliary output was adjusted as needed and the signal from the auxiliary output was fed into the synchroniser. The function generator shared a time base with the function generator used to generate the driving signal to the loudspeaker. The pulse delay introduced in the laser system was typically less than 300  $\mu\text{s}$ , and its consistency during the measurement had no effect on the time difference of the trigger signal.

A fog machine (ProSound) was used to generate the seeding particles. A mixture of 50% glycerol and 50% water was used as the fog fuel and typical droplet diameter was in the range 1–10 micrometres. The glycerol was diluted in this way to make the fog generated less dense. The mist (fog) produced was injected into the resonator through a hole, which was otherwise sealed during the measurement. During the injection of the mist of tracer particles, the acoustic wave was turned off. Unlike the steady flow, the oscillating flow in the standing wave resonator had zero mean velocity and the acoustic displacement amplitude was usually small. The injected tracer particles usually took a long time to be distributed evenly in the chamber when the acoustic wave was turned off. This is an advantage from the point of view that a relatively small volume of tracer particles would last a quite long period in the measurement. It was found that an acoustic wave of relatively high amplitude would help the particles to diffuse more rapidly before the actual measurement was conducted.

The accuracy of determining the flow velocity field strongly depends on the ability of the particles suspended in the flow medium to follow the flow. A model was given by Melling (1997) to describe the motion and tracking characteristics of suspended particles in a continuous medium. In an acoustic field, another force affecting the motion of particles, caused by acoustic radiation pressure may be taken into account (King, 1934). However, in the experimental conditions considered, the acoustic radiation pressure on the trace particle is much smaller than the acceleration force and it may be neglected here. Considering that the olive oil particle density  $\rho_p$  ( $= 915 \text{ kg/m}^3$ ) is much larger than the fluid density  $\rho$  (e.g. the density of air is  $1.2 \text{ kg/m}^3$ ), one can simplify Melling’s equation as follows:

$$\frac{\pi d_p^3}{6} \rho_p \frac{du_p}{dt} = -3\pi\mu d_p (u_p - u) \quad (\text{A.9})$$

where  $d_p$ ,  $u_p$ ,  $u$  and  $\mu$  are the particle diameter, the instantaneous velocity of the particle and fluid and the dynamic viscosity of the fluid, respectively. The instantaneous velocity of the fluid,  $u$ , is a nonlinear function of time in the oscillatory flow and the equation of motion is difficult to solve. Raffel (2002) made an assumption that the particle velocity approaches the fluid velocity exponentially if the particle density is much greater than the fluid density:

$$u_p = u \left( 1 - e^{-\frac{t}{\tau_s}} \right). \quad (\text{A.10})$$

The relaxation time  $\tau_s$  is given by

$$\tau_s = \frac{d_p^2 \rho_p}{18\mu} \quad (\text{A.11})$$

The relaxation time remains a convenient measure for the tendency of particles to reach velocity equilibrium with the fluid. Assuming the particles follow the flow for  $u_p/u > 0.99$ , the maximum acceptable diameter for a particle of olive oil is  $4.04 \mu\text{m}$  for the oscillatory flow driven by the acoustic wave with 13.1 Hz frequency. Hence, the choice of oil droplet generator and resulting particles are considered to be appropriate for the present PIV measurements.

#### A.2.4 Image acquisition and post-processing

INSIGHT 3G<sup>TM</sup> (TSI) was used for image capturing and processing. This allowed the user to set the operating parameters for the hardware components and the timing parameters for the laser and the camera. An acoustic oscillation cycle was divided into 20 phases and the oscillating flow around the stack was studied phase by phase, with the help of the phase locking mechanism. 100 pairs of PIV images were taken for each of the 20 phases in a typical run. Therefore, in each experimental run corresponding to a typical flow condition, 2000 pairs of images were captured and stored for post-processing.

The size of the field of view in the region around the stack varied between 25 mm × 25 mm and 60 mm × 60 mm. Therefore the maximum spatial resolution achieved was about 0.1 mm, which corresponds to six data points within the laminar viscous boundary layer in this study. In addition, the time separation between the laser pulse pairs needs to be varied according to the velocity magnitude at the selected phase and the size of the viewing area, in order to meet the recommended criterion that the displacement of the seeding particles between two images should be as large as possible but should not exceed one-quarter of the interrogation window (Adrian, 1997).

Processing of raw PIV images in order to convert them into velocity vector files was also accomplished using INSIGHT 3G™ software, while determination and display of other flow field properties used Tecplot® 10 and MATLAB® 6.5 programs. Since the area of the raw image covered both the channel section and part of the stack plates forming the channels, a region of interest (ROI) was defined and applied to each of the images in order to restrict the vector calculations to this area, and the area taken by the stack plates in the images was excluded in the processing procedure.

To process the images, velocity vector fields were calculated using the cross-correlation algorithm based on the recursive (multi-pass) grid engine, progressively decreasing the size of the interrogation spot from 32 × 32 pixels with a 50% overlap to 16 × 16 pixels. This algorithm was chosen because it offers improved spatial resolution compared to the use of a constant interrogation spot size in the calculations (Raffel, 1998). The Gaussian peak finder algorithm was used, since research has shown that this algorithm has lower bias and precision errors than most peak finder algorithms (Forliti, 2000).

Even with a carefully configured experiment, there is still the probability that about 5% of the velocity vectors will be false. These errors arise because of the loss of some particle pairs, resulting from low seeding density or out-of-plane motion: these effects lead to spurious vectors and cause a reduction in the quality of the results (Nogueira, 1997). Vector validation algorithms are designed to detect these spurious vectors, filter them and then fill the holes left by the vectors removed, through an interpolation process. The validation algorithm which was applied here was the “mean filter”, based on a 3 × 3 “neighbourhood size”. The velocity vector to be validated was rejected if the absolute difference between its magnitude and the average over its neighbours was above a certain tolerance. In practice, this tolerance was varied for different runs depending on the velocity

vector values. This was accomplished through interactive validation, working only on the area of the images defined as the region of interest. Once the vectors had been calculated and validated, the vector files were saved. They could then be opened using the Tecplot® 10 program so that other properties of the flow field could be calculated, displayed and visualised.

### A.2.5 Phase locking mechanism

To study the fluid flow in the thermoacoustic stack, the velocity fields were statistically evaluated on the basis of ensemble averaging. This required the acquisition of data corresponding to a single phase of an acoustic cycle. In particular, in PIV measurement of the flow velocity, the phase when the images of the tracer particles in the flow are taken needs to be fixed in relation to the acoustic oscillation, so that the results at the same phase but at different instants are comparable.

For this purpose, a circuit, referred to as “phase locking pulse generator” was developed in house. The circuit diagram is shown in Fig. A.6. A sinusoidal signal, for example the signal from a pressure transducer, is used as phase reference. When a positive slope is detected by operational amplifier OP1 and comparator 1, and when the value of the pressure signal is detected to be larger than a preset voltage on the potentiometer by operational amplifier OP2 and comparator 2, a positive TTL pulse is generated. This pulse signal is used as the triggering source in subsequent measurements. Generally, a phase delay would be introduced between the generated TTL pulse sequence and the input pressure signal, and is dependent on the frequency of the input pressure signal. For this application, the frequency of the acoustic wave, thus the frequency of the pressure signal, was fixed. The phase delay between the generated TTL pulse and the input pressure signal was therefore fixed. This phase delay can be measured when phase information is required.

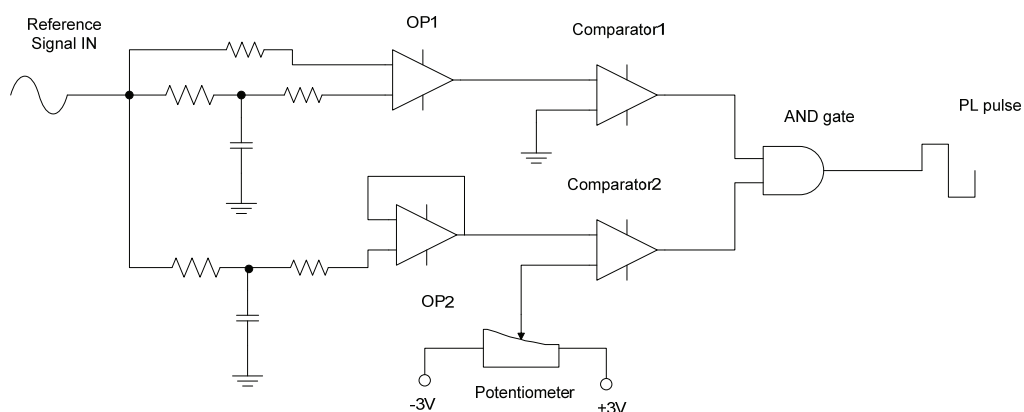


**Figure A.6 Schematic diagram of the phase locking pulse generator**

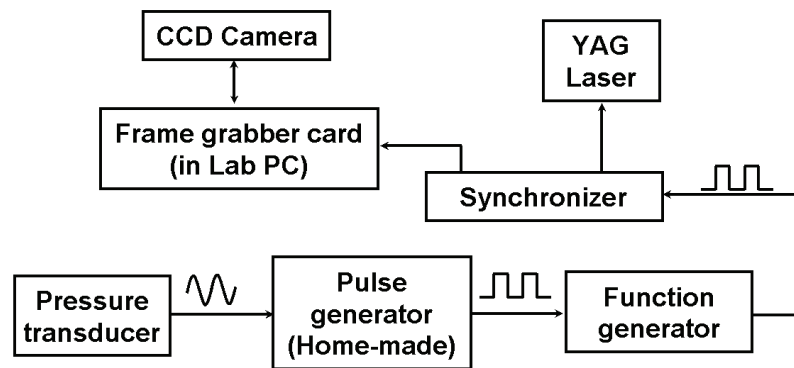


**Figure A.7 Block diagram of phase-locking mechanism in PIV measurements**

The phase locking pulse generator was then combined with a TTL signal generator to trigger the laser action and record the image by the camera. Figure A.7 shows a diagram of the phase-locking mechanism used in the PIV measurements for the current study. The sinusoidal output from the pressure transducer mounted at the end of the acoustic resonator was used as a phase reference signal. A TTL pulse sequence was generated from the phase locking pulse generator at the same frequency as the acoustic excitation provided to the loudspeaker. The TTL signal was then input to the synchronizer of the PIV system, which coordinates the operation of the frame grabber, the CCD camera and the laser. Therefore, the acquired images were in certain phase of the pressure oscillation, and thus the velocity oscillation in the resonator. The TTL signal output from the function generator can be delayed relative to the TTL signal from the phase locking pulse generator with a resolution of one degree. Thus, the flow in different phases of the acoustic oscillation can be investigated.

### **A.2.6 Determination of vorticity**

Vorticity is one of the most important quantities in fluid dynamics. It is very useful in gaining insight into the flow phenomena and flow patterns in many fluid mechanics problems. In this study, the vorticity fields are often used together with, and sometimes superimposed onto, the velocity fields to help the identification of the flow patterns in the oscillatory flow around the end of the stack plates.

The vorticity fields are not obtained directly from PIV measurements. Instead, the vorticity is obtained from the calculation of derivatives of the velocity from first principles:

$$\omega_z = \frac{\partial v}{\partial x} - \frac{\partial u}{\partial y} \quad (\text{A.12})$$

when a two-dimensional velocity field,  $u(x, y)$ ,  $v(x, y)$  is considered as in this study. The accuracy of vorticity field used for identifying vortex patterns is directly related to the accuracy of the velocity vector obtained from PIV measurements. Assume that the measured velocity components are  $u^* = u + \varepsilon$  and  $v^* = v + \varepsilon$ , where  $\varepsilon$  represents the absolute errors of velocity components. The vorticity field ( $\omega_z$ ) can be evaluated using a suitable finite difference scheme, such as a second order central difference scheme. This can be written:

$$\omega_z = \frac{\partial v}{\partial x} - \frac{\partial u}{\partial y} = \left( \frac{v_{i+1}^* - v_{i-1}^*}{2\Delta x} + \Delta x^2 \mathfrak{R} + \frac{\varepsilon}{\Delta x} \right) - \left( \frac{u_{j+1}^* - u_{j-1}^*}{2\Delta y} + \Delta y^2 \mathfrak{R} + \frac{\varepsilon}{\Delta y} \right) \quad (\text{A.13})$$

where  $\mathfrak{R}$  stands for higher order terms (Lourenco and Krothapalli, 1995).  $u_{j-1}^*$ ,  $u_{j+1}^*$ ,  $v_{i-1}^*$  and  $v_{i+1}^*$  are the values of velocity components ( $u$  and  $v$ ) on the grid next to point  $(i, j)$  in the corresponding  $y$  ( $j$ ) and  $x$  ( $i$ ) direction, respectively. The accuracy of the calculated vorticity depends on two components. The first is the truncation error associated with the finite difference scheme used, of order  $(\Delta x^2, \Delta y^2)$ . The second is due to the uncertainty,  $\varepsilon$ , in the velocity measurement and of order  $(1/\Delta x, 1/\Delta y)$ . A grid of smaller size is preferred to have high spatial resolution of the flow field. This is favourable to minimize the truncation error. On the contrary, it would increase the error due to velocity uncertainty. It is suggested that there exists an optimum grid size for which the total error is minimized, for a given velocity measurement error,  $\varepsilon$ . It can also be seen that a meaningful vorticity can be obtained if the error in the velocity measurement,  $\varepsilon$ , is kept to a small level (Lourenco and Krothapalli, 1995). It has been shown by the validation of PIV measurement results against theoretical predication that the velocity measurements in the current study have very small uncertainty. This suggests that the errors in the vorticity measurements should be relatively small and the acquired vorticity fields are reliable.

# Appendix B

## Input file for analysis with DeltaEC

```

TITLE Basic input for coupling of loudspeaker & resonator
!->D:\coupling.out
!Created with DeltaEC version 6.0b2 under win32,
using Win 5.1.2600 (Service Pack 2) under Python DeltaEC.
!----- 0 -----
BEGIN          Initialize things
  1.0133E+05 a Mean P Pa
    13.100   b Freq Hz
    296.15   c TBeg K
  2421.9     d |p| Pa G
  -129.54    e Ph(p) deg G
    0.0000   f |U| m^3/s
    0.0000   g Ph(U) deg
air          Gas type
!----- 1 -----
VSPEAKER      LOUDSPEAKER
  0.1000 a Area m^2          2421.9 A |p| Pa
  5.5000 b R ohms           -129.54 B Ph(p) deg
  0.0000 c L H              0.13928 C |U| m^3/s
  31.570 d BLProd T-m       174.78 D Ph(U) deg
  0.1930 e M kg            166.77 E Htot W
  1.0970E+04 f K N/m        95.100 F Edot W
  8.0000 g Rm N-s/m        166.77 G WorkIn W
  14.100 h |V| V           70.000 H Volts V
                               4.8199 I Amps A
                               -8.6623 J Ph(Ze) deg
                               0.13929 K |Ux| m^3/s
ideal          Solid type
!----- 2 -----
DUCT          SHORT DUCT
  0.3410 a Area m^2          2377.2 A |p| Pa
  2.3360 b Perim m          -129.86 B Ph(p) deg
  0.6000 c Length m         0.40806 C |U| m^3/s
  5.0000E-04 d Srough       151.40 D Ph(U) deg
                               166.77 E Htot W
ideal          Solid type
!----- 3 -----
CONE          CONICAL SECTION
  0.2600 a AreaI m^2        2241.0 A |p| Pa
  2.0400 b PerimI m        -130.48 B Ph(p) deg
  0.2200 c Length m         0.44223 C |U| m^3/s
  1.8000E-02 d AreaF m^2    150.51 D Ph(U) deg
  0.5360 e PerimF m        166.77 E Htot W
  5.0000E-04 f Srough       94.456 F Edot W
ideal          Solid type
!----- 4 -----
MINOR
sameas 3d a Area m^2        2210.2 A |p| Pa
  0.7000 b K+              -125.03 B Ph(p) deg
  0.7000 c K-              0.44223 C |U| m^3/s
                               150.51 D Ph(U) deg
                               166.77 E Htot W
                               47.194 F Edot W

```

```

!----- 5 -----
DUCT          LONG SMALL DUCT
sameas  3d a Area  m^2          1.0331E+04 A |p| Pa
sameas  3e b Perim m           60.062 B Ph(p) deg
       7.4600 c Length m       1.5655E-05 C |U| m^3/s
       5.0000E-04 d Srough      60.062 D Ph(U) deg
                                166.77 E Htot W
ideal          Solid type      8.0863E-02 F Edot W
!----- 6 -----
SURFACE       CLOSED END
sameas  5a a Area  m^2          1.0331E+04 A |p| Pa
                                60.062 B Ph(p) deg
                                1.8083E-14 C |U| m^3/s
                                -152.16 D Ph(U) deg
                                166.77 E Htot W
ideal          Solid type      -7.9023E-11 F Edot W
!----- 7 -----
HARDEND       HARDEND
       0.0000 a R(1/z)          =7G  1.0331E+04 A |p| Pa
       0.0000 b I(1/z)          =7H  60.062 B Ph(p) deg
       0.0000 c Htot W          1.8083E-14 C |U| m^3/s
                                -152.16 D Ph(U) deg
                                166.77 E Htot W
                                -7.9023E-11 F Edot W
                                -3.3831E-14 G R(1/z)
                                2.1320E-14 H I(1/z)

! The restart information below was generated by a previous run
! and will be used by DeltaEC the next time it opens this file.
guessz  0d  0e
xprecn -4.2780E-02  7.7032E-04
targs   7a  7b
! Plot start, end, and step values.  May be edited if you wish.
! Outer Loop:                               | Inner Loop .

```

# Appendix C

## MATLab script for analysis of the coupling of acoustic driver and resonator

```
%%%%%%%%%%%%%%%%%%%%%%%%%%%%%%%%%%%%%%%%%%%%%%%%%%%%%%%%%%%%%%%%%%%%%%%%%
%
%                               COUPLING OF ACOUSTIC DRIVER AND RESONATOR
%
%%%%%%%%%%%%%%%%%%%%%%%%%%%%%%%%%%%%%%%%%%%%%%%%%%%%%%%%%%%%%%%%%%%%%%%%%

clear all;
close all;
precision = 'double';

%%%%%%%%%%%%%%%%%%%%%%%%%%%%%%%%%%%%%%%%%%%%%%%%%%%%%%%%%%%%%%%%%%%%%%%%% General constants %%%%%%%%%%%%%%%%%%%%%%%%%%%%%%%%%%%%%%%%%%%%%%%%%%%%%%%%%%%%%%%%%%%%%%%%%%

p0 = 101325;           % (pa) ambient pressure
T0 = 273.15 + 23;     % (K) ambient temperature
R = 287.096;          % (J/kg.K) gas constant
cp = 1004.836;        % (J/kg.K) Isobaric specific heat
gamma = 1.4;          % specific heat ratio
rho0 = p0/(R*T0);     % (kg/m3) density of air at p0 & T0
c0 = sqrt(gamma*R*T0); % (m/s) sound speed
nu = 1.85*10^(-5)/rho0; % (m2/s) kinematic viscosity of air
kappa = 0.026/(rho0*cp); % (m2/s) thermal diffusivity of air

%%%Characteristics of the loudspeaker(Measured values) %%%%%%%%%%%%%%%%%%%%%%%%%%%%%%%%%%%%%%%%%%%%%%%%%%%%%%%%%%%%%%%%%%%%%%%%%%

S = 0.10;             % (m2) Cross-sectional area of loudspeaker
Re = 5.5;             % (Ohm) Electrical resistance of the coil
Le = 0;               % Electrical inductance of the coil
Bl = 31.57;          % (T.m)Bl product
m = 0.193;           % (kg) Moving mass
s = 10970;           % (N/m) Suspension stiffness
h = 8;               % (Ns/m) Suspension damping

%%%%%%%%%%%%%%%%%%%%%%%%%%%%%%%%%%%%%%%%%%%%%%%%%%%%%%%%%%%%%%%%%%%%%%%%%Characteristics of the resonator %%%%%%%%%%%%%%%%%%%%%%%%%%%%%%%%%%%%%%%%%%%%%%%%%%%%%%%%%%%%%%%%%%%%%%%%%%

%===== Positions of sections =====

x0 = 0;               % speaker membrane position
x1 = 0.6;             % large end of the cone section
x2 = 0.82;           % small end of the section
xa = 0.90;           % abscissa of the cone apex
x3 = 8.28;           % tube end

%===== Geometry of each section =====

rA = 0.292;           % half the height of part A
rB = 0.255;           % half the height of part B(x=x1)
rC = 0.067;           % half the height of part C
SA = 0.341;           % cross-sectional area of part A
SBx1 = 0.260;         % cross-sectional area of part B(x=x1)
```

```

SBx2 = 0.018; % cross-sectional area of part B(x=x2)
SC = SBx2; % cross-sectional area of part C

%%%%%%%%%%%%%%%%%%%%%%%%%%%%%%%%%%%%%%%%%%%%%%%%%%%%%%%%%%%%%%%%%%%%%%%% Variables %%%%%%%%%%%%%%%%%%%%%%%%%%%%%%%%%%%%%%%%%%%%%%%%%%%%%%%%%%%%%%%%%%%%%%%%%

f = 0.01:0.01:100; % frequency of signal to loudspeaker
omega = 2*pi.*f;
Ve = 14.1; % (V) input voltage to the loudspeaker
[Ves,errmsg] = sprintf('%0.3g',Ve);

%%%%%%%%%%%%%%%%%%%%%%%%%%%%%%%%%%%%%%%%%%%%%%%%%%%%%%%%%%%%%%%%%%%%%%%% Calculations of the Wave Amplitude and Reflection Factor%%%%%%%%%%%%%%%%%%%%%%%%%%%%%%%%%%%%%%%%%%%%%%%%%%%%%%%%%%%%%%%%%%%%%%%%

deltanu = sqrt(2*nu./omega); % viscous penetration depth
deltakappa = sqrt(2*kappa./omega); % thermal penetration depth

fnuA = (1-i).*deltanu/rA; %
fkappaA = (1-i).*deltakappa/rA; %
kA = omega./c0.*sqrt((1+(gamma-1).*fkappaA)./(1-fnuA)); %
kB = omega./c0; %
fnuC = (1-i).*deltanu/rC; %
fkappaC = (1-i).*deltakappa/rC; %
kC = omega./c0.*sqrt((1+(gamma-1).*fkappaC)./(1-fnuC)); %
RC = exp(-2*i.*kC*x3); %
x2p = x2-xa;
ZSB2 = rho0*c0/SBx2; %
ZSC = omega.*rho0./(SC.*kC.*(1-fnuC)); %
Z2 = ZSC.*(exp(-i.*kC*x2)+RC.*exp(i.*kC*x2));
Z2 = Z2./(exp(-i.*kC*x2)-RC.*exp(i.*kC*x2)); %
RB = (Z2.*(1-i./(kB*x2p))-ZSB2);
RB = RB./(Z2.*(1+i./(kB*x2p))+ZSB2).*exp(-2*i.*kB*x2p); %

x1p = x1-xa;
ZSA = omega.*rho0./(SA.*kA.*(1-fnuA)); %
ZSB1 = rho0*c0/SBx1; %
Z1 = ZSB1.*(exp(-i.*kB*x1p)+RB.*exp(i.*kB*x1p));
Z1e = (1-i./(kB*x1p)).*exp(-i.*kB*x1p);
Z1e = Z1e-RB.*(1+i./(kB*x1p)).*exp(i.*kB*x1p);
Z1 = Z1./Z1e; %
RA = (Z1-ZSA)./(Z1+ZSA).*exp(-2*i.*kA*x1); %

Zac = ZSA.*(exp(-i.*kA*x0)+RA.*exp(i.*kA*x0));
Zac = Zac./(exp(-i.*kA*x0)-RA.*exp(i.*kA*x0)); % <
Ze = Re+i.*omega*Le; %
Zmec = h+i.*(m.*omega-s./omega); %
U0 = S*B1*Ve./(Ze.*(Zmec+S*S.*Zac)+B1*B1); % <
A = ZSA.*U0./(exp(-i.*kA*x0)-RA.*exp(i.*kA*x0)); %
B = A*x1p.*(exp(-i.*kA*x1)+RA.*exp(i.*kA*x1));
B = B./(exp(-i.*kB*x1p)+RB.*exp(i.*kB*x1p)); %
C = B/x2p.*(exp(-i.*kB*x2p)+RB.*exp(i.*kB*x2p));
C = C./(exp(-i.*kC*x2)+RC.*exp(i.*kC*x2)); %

%%%%%%%%%%%%%%%%%%%%%%%%%%%%%%%%%%%%%%%%%%%%%%%%%%%%%%%%%%%%%%%%%%%%%%%% Calculations required %%%%%%%%%%%%%%%%%%%%%%%%%%%%%%%%%%%%%%%%%%%%%%%%%%%%%%%%%%%%%%%%%%%%%%%%%

===== Frequency response of the resonator =====

===== Frequency range (0 ~ 100 Hz) =====

pCx3 = C.*(exp(-i.*kC*x3)+RC.*exp(i.*kC*x3)); %
Dr = abs(pCx3)/p0; % Drive ratio = pC(x3)/p0

===== Print on screen the resonance frequencies =====
[Drmax,DrI] = max(Dr(1201:1400)); fres1 = f(1200+DrI);

```

```

% f= 12.01 ~ 14.00
[Drmax,DrI] = max(Dr(3301:3700)); fres2 = f(3300+DrI);
% f= 33.01 ~ 37.00
[Drmax,DrI] = max(Dr(5501:6100)); fres3 = f(5500+DrI);
% f= 55.01 ~ 61.00
[Drmax,DrI] = max(Dr(7701:8500)); fres4 = f(7700+DrI);
% f= 77.01 ~ 85.00
fprintf('f1 is %5.2f;\nf2 is %5.2f;\n', fres1, fres2);
fprintf('f3 is %5.2f;\nf4 is %5.2f;\n', fres3, fres4);
fprintf('\n\n');

fig1 = Figure(1);
set(fig1, 'units','centimeters');
set(fig1, 'position', [1. 3. 17. 12.]); %[left, bottom, width, height]
set(gca, 'fontsize', 18);
plot(f, Dr*100, 'k');
xlabel('Frequency f [Hz]'); ylabel('|p_A|/p_m [%]');
eval(['text(50,3.0,'V_e=',Ves,' Volts','','fontsize',18 );'])

%===Pressure and velocity vs. the position in the resonator =====
%===== At chosen frequency (first resonance frequency) =====
%
Fig2 = Figure(2);
set(fig2, 'units','centimeters');
set(fig2, 'position', [1. 3. 17. 12.]); %[left, bottom, width, height]
set(gca, 'fontsize', 18);
%
x = x0:0.001:x3; % x axis in the resonator
[nn,xs] = size(x); clear nn; % total count of x
for xi = 1:xs
    if x(xi)<=x1
        p(xi)=A*(exp(-i*kA*x(xi))+RA*exp(i*kA*x(xi)));
        u(xi)=kA*(1-fnuA)/(omega*rho0)*A;
        u(xi)= u(xi)*(exp(-i*kA*x(xi))-RA*exp(i*kA*x(xi)))
    elseif (x(xi)>x1)&(x(xi)<x2)
        xp = x(xi)-xa;
        p(xi)=B/xp*(exp(-i*kB*xp)+RB*exp(i*kB*xp));
        u(xi)=B/(rho0*c0*xp)*((1-i/(kB*xp))*exp(-i*kB*xp)-
RB*(1+i/(kB*xp))*exp(i*kB*xp));
    elseif x(xi)>=x2
        p(xi)=C*(exp(-i*kC*x(xi))+RC*exp(i*kC*x(xi)));
        u(xi)=kC*(1-fnuC)/(omega*rho0)*C*(exp(-i*kC*x(xi))-
RC*exp(i*kC*x(xi)));
    end
end
plot(x,abs(p)/p0,'k'); hold on
plot(x,abs(u)/c0,'k');
xlabel('Position x [m]'); ylabel('|p(x)|/p_0 and |u(x)|/c_0');
text(3,0.025,'V_e=14.1 Volts','fontSize',18 );
%
%=====
clear all
%%%%%%%%%% END %%%%%%%%%%

```

# Bibliography

- Aben P.C.H. and Zeegers J.C.H., 2006, High amplitude oscillatory gas flow in interaction with solid boundaries, Proceedings of the 7th Congress of the French Acoustics Society.
- Aben P.C.H., Bloemen P.R. and Zeegers J.C.H., 2009, 2-D PIV measurements of oscillatory flow around parallel plates, Experiments in Fluids, 46, 631-641.
- Adrian R.J., 1991, Particle imaging techniques for experimental fluid mechanics, Annual Review Fluid Mechanics, 23, 261-304.
- Adrian R.J., 2005, Twenty years of particle image velocimetry, Experiments in Fluids, 39, 159-169.
- Al-Asmi K. and Castro I.P., 1992, Vortex shedding in oscillatory flow: geometrical effects, Flow Measurement and Instrumentation, 3(3), 187-202.
- Anagnostopoulos P. and Minear R., 2004, Blockage effect of oscillatory flow past a fixed cylinder, Applied Ocean Research, 26(3-4), 147-153.
- Antonia R.A., Orlandi P. and Romanno G.P., 1998, Scaling of longitudinal velocity increments in a fully developed turbulent channel flow, Physics of Fluids, 10(12), 3239-3241.
- Arnott W.P., Bass H.E. and Raspet R., 1991, General formulation of thermoacoustics for stacks having arbitrarily shaped pore cross sections, Journal of the Acoustical Society of America, 90(6), 3228-3237.
- Arroyo M.P. and Greated C.A., 1991, Stereoscopic particle image velocimetry, Measurement Science and Technology, 2, 1181-1186.
- Atchley A.A., Hofler T.J., Muzzerall M.L., Kite M.D. and Ao C., 1990, Acoustically generated temperature gradients in short plates, Journal of the Acoustical Society of America, 88, 251-263.
- Auger J. L. and Coutanceau J., 1978, On the complex structure of the downstream flow of cylindrical tube rows at various spacings, Mechanical Research Communication, 5, 297-302.
- Bachelor G.K., 2000, An introduction to fluid dynamics, Cambridge University Press, Cambridge.
- Backhaus S. and Swift G.W., 2000, A thermoacoustic-Stirling heat engine: detailed study, Journal of Acoustical Society of America, 107, 3148-3166.
- Backhaus S. and Swift G.W., 2001, Fabrication and use of parallel plate regenerators in thermoacoustic engines, Proceedings of 36th Intersociety Energy Conversion Engineering Conference (IECEC), July 29 - August 2, Savannah, Georgia, U.S.
- Badr H.M., Dennis S.C.R., Kocabiyik S. and Nguyen P., 1995, Viscous oscillatory flow about a circular cylinder at small to moderate Strouhal number, Journal of Fluid Mechanics, 303, 215-232
- Bailliet H., Lotton P., Bruneau M., and Gusev V., 2000, Coupling between electrodynamic loudspeakers and thermoacoustic acoustic cavities, Acustica united with Acta Acustica, 86, 363-373.
- Bailliet H., Lotton P., Bruneau M., Gusev V., Valière J.C. and Gazengel, B., 2000, Acoustic power flow measurement in a thermoacoustic resonator by means of laser

- Doppler anemometry (LDA) and microphonic measurement, *Applied Acoustics*, 60(1), 1-11.
- Barbi C., Favier D.P., Maresca C.A. and Telionis D.P., 1986, Vortex shedding and lock-on of a circular cylinder in oscillatory flow, *Journal of Fluid Mechanics*, 170, 527-544.
- Bearman P.W. and Graham J.M.R., 1980, Vortex shedding from bluff bodies in oscillatory flow: A report on Euromech 119, *Journal of Fluid Mechanics*, 99, 225-245.
- Bearman P.W., 1984, Vortex shedding from oscillating bluff bodies, *Annual Review of Fluid Mechanics*, 16, 195-222.
- Bearman P.W., Downie M.J., Graham J.M.R. and Obasaju E.D., 1985, Forces on cylinders in viscous oscillatory flow at low Keulegan-Carpenter numbers, *Journal of Fluid Mechanics*, 154, 337-356.
- Beranek L., 1954, *Acoustics*, McGraw-Hill.
- Berger E. and Wille R., 1972, Periodic flow phenomena, *Annual Review of Fluid Mechanics*, 4, 313-340.
- Berson A. and Blanc-Benon Ph., 2007, Nonperiodicity of the flow within the gap of a thermoacoustic couple at high amplitudes, *Journal of Acoustical Society of America*, 122(4), EL122-EL127.
- Berson A., Michard M. and Blanc-Benon Ph., 2008, Measurement of acoustic velocity in the stack of a thermoacoustic refrigerator using particle image velocimetry, *Heat Mass Transfer*, 44, 1015-1023.
- Besnoin E. and Knio O.M., 2004, Numerical study of thermoacoustic heat exchangers, *Acta Acustica United with Acustica*, 90, 432-444.
- Bevan K.E. and Ghandhi J.B., 2008, Particle image velocimetry measurements of in-cylinder flow in a four-stroke utility engine and correlation with combustion measurements, *Journal of Engineering for Gas Turbines and Power*, 130, 032802-1-11.
- Blanc-Benon P., Besnoin E. and Knio O.M., 2003, Experimental and computational visualization of the flow in a thermoacoustic stack, *Comptes Rendus Mécanique*, 331, 17-24.
- Browne L.W.B., Antonia R.A., 1987, The effect of wire length on temperature statistics in a turbulent wake, *Experiments in Fluids* 5, 426-428.
- Bruun H.H., 1995, *Hot-wire anemometry, principles and signal analysis*, Oxford University Press.
- Bunderson N.E. and Smith B.L., 2005, Passive mixing control of plane parallel jets *Experiments in Fluids*, 39, 66-74.
- Campbell M., Cosgrove J.A., Greated C.A., Jack S. and Rockliff D., 2000, Review of LDA and PIV applied to the measurement of sound and acoustic streaming, *Optics and Laser Technology*, 32, 629-639.
- Cao N., Olson J.R., Swift G.W. and Chen S., 1996, Energy flux density in a thermoacoustic couple, *Journal of the Acoustical Society of America*, 99(6), 3456-3464.
- Castrejón-Pita J.R., Castrejón-Pita A.A., Huelsz G. and Tovar R., 2006, Experimental demonstration of the Rayleigh acoustic viscous boundary layer theory, *Physical Review E*, 73(3), 036601.
- Cenedese A., Doglia G., Romano G.P., Michele G.De and Tanzini G., 1994, LDA and PIV velocity measurements in free jets, *Experimental Thermal and Fluid Science*, 9, 125-134.
- Ceperley, P.H. (1979), A pistonless Stirling engine – The travelling wave heat engine, *Journal of the Acoustical Society of America*, 66(5), 1508-1513.

- Choi S., Nam K. and Jeong S., 2004, Investigation on the pressure drop characteristics of cryocooler regenerators under oscillating flow and pulsating pressure conditions, *Cryogenics*, 44, 203-210.
- Chung Y.J. and Kang S.H., 2003, A study on the vortex shedding and lock-on behind a square cylinder in an oscillatory incoming flow, *JSME International Journal, Series B*, 46(2), 250-261.
- Ciofalo M., Signorino M., and Simiano M., 2003, Tomographic particle image velocimetry and thermography in Rayleigh-Bénard convection using suspended thermochromic liquid crystals and digital image processing, *Experiments in Fluids*, 34, 156-172.
- Collis D.C. and Williams M.J., 1959, Two dimensional convection from heated wires at low Reynolds numbers, *Journal of Fluid Mechanics*, 6, 357-384.
- Comte-Bellot G., 1976, Hot-wire anemometry, *Annual Review of Fluid Mechanics*, 8, 209-231.
- Cooper W.L., Yang K.T. and Nee V.W., 1993, Fluid mechanics of oscillatory and modulated flows and associated applications in heat and mass transfer - A review, *Journal of Energy, Heat and Mass Transfer*, 15, 1-19.
- Debesse Ph., Baltean-Carlès D., Lusseyran F. and François M.-X., 2008, Experimental analysis of nonlinear phenomena in a thermoacoustic system, *AIP Conference Proceedings*, 1022, 355-358.
- De Bernardinis B., Graham J.M.R. and Parker K.H., 1981, Oscillatory flow around disks and through orifices, *Journal of Fluid Mechanics*, 102, 279-299.
- Doller A., 2004, Acoustic minor losses in high amplitude resonators with single-sided junction, Ph.D. Dissertation, Pennsylvania State University, United States.
- Drake D.G., 1965, On the flow in a channel due to a periodic pressure gradient, *The Quarterly Journal of Mechanics and Applied Mathematics*, 18(1), 1-10.
- Dubbelday, P.S., 1986, Hot-film anemometry measurement of hydroacoustic particle motion, *Journal of the Acoustical Society of America*, 79(6), 2060-2066.
- Duffourd S., 2001, Thermoacoustic refrigerator: experimental and analytical studies for miniaturization, Ph.D Thesis, L'École Centrale De Lyon, France. (in French)
- Elsinga G.E., van Oudheusden B.W. and Scarano F., 2006, Experimental assessment of Tomographic PIV accuracy, 13th International Symposia on Application of Laser Techniques to Fluid Mechanics, Lisbon, Portugal, 26-29 June, 2006.
- Elsinga G.E., Scarano F., Wieneke B., and van Oudheusden B.W., 2006, Tomographic particle image velocimetry, *Experiments in Fluids*, 41, 933-947.
- Elsinga G.E., Wieneke B., Scarano F., and Schröder A., 2008, Tomographic 3D-PIV and applications, *Particle Image Velocimetry, New Developments and Recent Applications*, Schroeder, A. and Willert, C.E. (Eds.), *Topics in Applied Physics*, Vol.112, Springer.
- Feldman K.T., Jr., 1968a, Review of the literature on Rijke thermoacoustic phenomena, *Journal of Sound and Vibration*, 7(1), 83-89.
- Feldman K.T., Jr., 1968b, Review of the literature on Sondhauss thermoacoustic phenomena, *Journal of Sound and Vibration*, 7(1), 71-82.
- Ferreira R.L. and Vieira E.D.R., 2004, Flow around modified circular cylinders, *Engenharia Termica (Thermal Engineering)*, 5, 62-67.
- Forliti D.J., Strykowski P.J. and Debatin K., 2000, Bias and precision errors of digital particle image velocimetry, *Experiments in Fluids*, 28, 436-447.

- Gedeon D., 1986, Mean-parameter modelling of oscillating flow, *Journal of heat transfer*, 108(3), 513-518.
- Gerrard J.H. and Hughes M.D., 1971, The flow due to an oscillating piston in a cylindrical tube: a comparison between experiment and a simple entrance flow theory, *Journal of Fluid Mechanics*, 50(1), 97-106.
- Gopinath A. and Harder D.R., 2000, An experimental study of heat transfer from a cylinder in low-amplitude zero-mean oscillatory flows, *International Journal of Heat and Mass Transfer*, 43, 505-520.
- Grant I., 1997, Particle Image Velocimetry: a review, *Proceedings of the Institution of Mechanical Engineers, Part C, Journal of Mechanical Engineering Science*, 211, 55-76.
- Grushin A.E., Lebedeva I.V., 2001, Determining the amplitude of a sound wave oscillatory velocity with a thermo-anemometer in a flowing medium, *Measurement Techniques*, 44(5), 541-543.
- Grushin A.E., Dragan S.P. and Lebedeva I.V., 2001, Dependence of acoustic stream velocity on the intensity of sound in the waveguide, *Proceedings of XI Session of the Russian Acoustical Society, Moscow, November 19-23*, 286-288.
- Guibert P. and Lemoyne L., 2002, Dual particle image velocimetry for transient flow field measurements: Autocorrelation estimation of in-cylinder flow of a spark ignition engine turbulence, *Experiments in Fluids*, 33, 355-367.
- Guillaume D.W. and LaRue J.C., 2001, Comparison of the vortex shedding behaviour of a single plate and a plate array, *Experiments in Fluids*, 30(1), 22-26.
- Guillaume D.W. and LaRue J.C., 2002, Comparison of the numerical and experimental flow field downstream of a plate array, *Transaction of ASME - Journal of Fluid Engineering*, 124, 284-286.
- Guilmineau E. and Queutey P., 2002, A numerical simulation of vortex shedding from an oscillating circular cylinder, *Journal of Fluids and Structures*, 16(6), 773-794.
- Hann D.B. and Greated C.A., 1994, Acoustic measurements in flows using photon correlation spectroscopy, *Measurement Science and Technology*, 5(2), 157-164.
- Hann, D.B. and Greated, C.A., 1997a, Particle image velocimetry for the measurement of mean and acoustic particle velocities, *Measurement Science and Technology*, 8(6), 656-660.
- Hann D.B. and Greated C.A., 1997b, The measurement of flow velocity and acoustic particle velocity using particle image velocimetry, *Measurement Science and Technology*, 8(12), 1517-1522.
- Hart D.P., 1999, Super-resolution PIV by recursive local-correlation, *Journal of Visualization*, 3(2), 187-194.
- Hayashi M., Sakurai A. and Ohya J., 1986, Wake interference of a row of normal flat plates arranged side by side in a uniform flow, *Journal of Fluid Mechanics*, 164, 1-25.
- Hinsch, K.D., 2002, Holographic particle image velocimetry, *Measurement Science and Technology*, 13, R61-R72.
- Hinsch K.D. and Herrmann S.F., 2004, Holographic particle image velocimetry (Editorial), *Measurement Science and Technology*, 15, doi: 10.1088/0957-0233/15/4/E01.
- Hino M., Kashiwayanagi M., Nakayama A. and Hara T., 1983, Experiments on the turbulence statistics and the structure of a reciprocating oscillatory flow, *Journal of Fluid Mechanics*, 131, 363-400.

- Hino, M., Sawamoto, M. and Takasu, S., 1976, Experiments on transition to turbulence in an oscillatory pipe flow, *Journal of Fluid Mechanics*, 75(2), 193-207.
- Højstrup J., Rasmussen K. and Larsen, S.E., 1976, Dynamic calibration of temperature wires in still air, *DISA Information*, 20, 22-30.
- Hofler T.J., 1986, Thermoacoustic refrigerator design and performance, Ph.D. Thesis, University of California, San Diego, United States.
- Huelsz G. and López-Alquicira F., 2001, Hot-wire anemometry in acoustic waves, *Experiments in Fluids*, 30(3), 283-285.
- Huelsz G., Lopez-Alquicira F. and Ramos E., 1998, Measurements of temperature and velocity oscillations in acoustic waves, *The Journal of the Acoustical Society of America*, 103, 2765-2767.
- Huelsz G., López-Alquicira F., and Ramos E., 2002, Velocity measurements in the oscillatory boundary layer produced by acoustic waves, *Experiments in Fluids*, 32, 612-615.
- Huelsz G. and Ramos E., 1998, Temperature measurements inside the oscillatory boundary layer produced by acoustic waves, *The Journal of the Acoustical Society of America*, 103(3), 1532-1537.
- Huelsz G. and Ramos E., 1999, An experimental verification of Rayleigh's interpretation of the Sondhauss tube, *The Journal of the Acoustical Society of America*, 106(4), 1789-1793.
- Hyun B.S., Balachandar R., Yu K. and Patel V.C., 2003, Assessment of PIV to measure mean velocity and turbulence in open-channel flow, *Experiments in Fluids*, 35, 262-267.
- Idelchik I.E., 1996, *Handbook of Hydraulic Resistance*, 3rd Edition, New York, Begell House.
- Iliadis G. and Anagnostopoulos P., 1998, Viscous oscillatory flow around a circular cylinder at low Keulegan-Carpenter numbers and frequency parameters, *International Journal for Numerical Methods in Fluids*, 26(4), 403-442.
- Ingard U. and Ising H., 1967, Acoustic nonlinearity of an orifice, *Journal of the Acoustical Society of America*, 42(1), 6-17.
- Iwai H., Mambo T., Yamamoto N. and Suzuki K., 2004, Laminar convective heat transfer from a circular cylinder exposed to a low frequency zero-mean velocity oscillating flow, *International Journal of Heat and Mass Transfer*, 47, 4659-4672.
- Jaworski A.J., Mao X.A., Mao X.R. and Yu Z., 2009, Entrance effects in the channels of the parallel plate stack in oscillatory flow conditions, *Experimental Thermal and Fluid Science*, 33(3), 495-502.
- Jensen K.D., 2004, Flow measurements, *Journal of the Brazilian Society of Mechanical Sciences and Engineering*, XXVI(4), 400-419.
- Kang S., Patil B., Zarate J.A. and Roy R.P., 2001, Isothermal and heated turbulent upflow in a vertical annular channel – Part I. Experimental measurements, *International Journal of Heat and Mass Transfer*, 44, 1171-1184.
- Keane R.D. and Adrian R.J., 1990, Optimization of particle image velocimeters, Part I: Double pulsed systems, *Measurement Science and Technology*, 1, 1202-1215.
- Keane R.D. and Adrian R.J., 1991, Optimization of particle image velocimeters, Part II: Multiple pulsed systems, *Measurement Science and Technology*, 2, 963-974.
- King L.V., 1934, On the acoustic radiation pressure on spheres, *Proceedings of the Royal Society of London, Series A, Mathematical and Physical Sciences*, 147, 212-240.

- Kinsler L.E. and Frey A.R., 1962, *Fundamentals of Acoustics*, 2nd Edition, John Wiley & Sons, London.
- Klippel W. and Seidel U., 2001, Fast and accurate measurement of linear transducer parameter, Audio Engineering Society - AES Preprint 5308, in: 110th AES convention, 12-15 May 2001, Amsterdam, The Netherlands.
- Kompenhans J. and Tropea C., 1997, Editorial, *Measurement Science and Technology*, 8, doi: 10.1088/0957-0233/8/12/001.
- Kondjoyan A. and Daudin J. D., 1995, Effects of free stream turbulence intensity on heat and mass transfers at the surface of a circular cylinder and an elliptical cylinder, axis ratio 4, *International Journal of Heat and Mass Transfer*, 38(10), 1735-1749.
- Kovaszny L.S.G., 1949, Hot-Wire Investigation of the Wake behind Cylinders at Low Reynolds Numbers, *Proceedings of the Royal Society of London, Series A, Mathematical and Physical Sciences*, 198(1053), 174-190.
- Kramers H.A., 1949, Vibrations of a gas column, *Physica*, 15, 971-984.
- Krijger J.K.B., Hillen B. and Hoogstraten H. W., 1991, Pulsating entry-flow in a plane channel, *Zeitschrift für Angewandte Mathematik und Physik (ZAMP)*, 42(1), 139-153.
- Kurzweg U.H., 1985, Enhanced heat conduction in oscillating viscous flows within parallel-plate channels, *Journal of Fluid Mechanics*, 156, 291-300.
- Kurzweg U.H., 1986a, Heat transfer device for the transport of large conduction flux without net mass transfer, US Patent 4,590,993.
- Kurzweg U.H., 1986b, Temporal and spatial distribution of heat flux in oscillating flow subjected to an axial temperature gradient, *International journal of heat and mass transfer*, 29(12), 1969-1977.
- Kurzweg U.H. and Zhao L.D., 1984, Heat transfer by high frequency oscillations: A new hydrodynamic technique for achieving large effective thermal conductivities, *Physics of Fluids*, 27, 2624-2627.
- Kurzweg U.H., Lindgren E.R. and Lothrop. B., 1989, Onset of turbulence in oscillating flow at low Womersley number, *Physics of Fluids, A, Fluid Dynamics*, 1, 1972-1975.
- LaRue J.C., Deaton T. and Gibson C.H., 1975, Measurement of high-frequency turbulent temperature, *Review of Scientific Instruments*, 46 (6), 757-764.
- Lavender W.J. and Pei D.C.T., 1967, The effect of fluid turbulence on the rate of heat transfer from spheres, *International Journal of Heat and Mass Transfer*, 10, 529-539.
- Lawrenson C.C., Lipkens B., Lucas T.S., Perkins D.K. and van Doren T.W., 1998, Measurements of macrosonic standing waves in oscillating closed cavities, *Journal of the Acoustical Society of America*, 104, 623-636.
- Le Gal P., Peschard I., Chauve M.P. and Takeda Y., 1996, Collective behaviour of wakes downstream a row of cylinders, *Physics of Fluids*, 8, 2097-2106.
- Lebedeva I.V. and Dragan S.P., 1991, Calibration of hot-wire anemometer in sound fields, *Dantec Information*, 10, 12-13.
- Lee T. and Budwig R., 1991, The onset and development of circular cylinder vortex wakes in uniformly accelerating flows, *Journal of Fluid Mechanics*, 232, 611-627.
- Lin X.W., Bearman P.W. and Graham J.M.R., 1996, A numerical study of oscillatory flow about a circular cylinder for low values of beta parameter, *Journal of Fluids and Structures*, 10, 501-526.
- Ling S.C. and Atabek H.B., 1972, A nonlinear analysis of pulsatile flow in arteries, *Journal of Fluid Mechanics*, 55, 493-511.

- Lourenco L.M. and Korthapalli A., 1995, On the accuracy of velocity and vorticity measurements with PIV, *Experiments in Fluids*, 18, 421-428.
- Lowery G.W. and Vachon R.I., 1975, The effect of turbulence on heat transfer from heated cylinders, *International Journal of Heat and Mass Transfer*, 18, 1229-1242.
- Mao X., Marx D. and Jaworski A.J., 2007, PIV measurement of coherent structures and turbulence created by an oscillating flow at the end of a thermoacoustic stack, *Progress in Turbulence II*, in: *Proceedings of the iTi (interdisciplinary turbulence initiative) Conference in Turbulence*, Bad-Zwischenahn, Germany, 25–28 September, 2005, Springer *Proceedings in Physics*, 109, 99-102.
- Marx D. and Blanc-Benon Ph., 2004, Computation of the mean velocity field above a stack plate in a thermoacoustic refrigerator, *Comptes Rendus Mécanique*, 332, 867-874.
- Meinhart C., Wereley S. and Santiago J., 1999, PIV measurements of a micro channel flow, *Experiments in Fluids*, 27, 414-419.
- Melling, A. (1997), Tracer particles and seeding for particle image velocimetry, *Measurement Science and Technology* 8, 1406-1416
- Merkli P. and Thomann H., 1975a, Thermoacoustic effects in a resonance tube, *Journal of Fluid Mechanics*, 70(1), 161-177.
- Merkli P. and Thomann H., 1975b, Transition to turbulence in oscillating pipe flow, *Journal of Fluid Mechanics*, 68(3), 567-576.
- Molezzi M.J. and Dutton J.C., 1993, Application of particle image velocimetry in high speed separated flows, *AIAA Journal*, 33, 438-446.
- Moretti P.M., 1993, Flow induced vibrations in arrays of cylinders, *Annual Review of Fluid Mechanics*, 25, 99-114.
- Morris P.J., Boluriaan S. and Shieh C.M., 2004, Numerical simulation of minor losses due to a sudden contraction and expansion in high amplitude acoustic resonators, *Acta Acustica United with Acustica*, 90, 393-409.
- Nabavi M., Siddiqui M.H.K. and Dargahi, J., 2007, Simultaneous measurement of acoustic and streaming velocities using synchronized PIV technique, *Measurement Science and Technology*, 18(7), 1811-1817.
- Nagano Y. and Tsuji T., 1994, Recent developments in hot- and cold-wire techniques for measurements in turbulent shear flows near walls, *Experimental Thermal and Fluid Science*, 9, 94-110.
- Nam K. and Jeong S., 2003, Measurement of cryogenic regenerator characteristics under oscillating flow and pulsating pressure, *Cryogenics*, 43, 575-581.
- Nehari D., Armenio V. and Ballio F., 2004, Three-dimensional analysis of the unidirectional oscillatory flow around a circular cylinder at low Keulegan-Carpenter and beta numbers, *Journal of Fluid Mechanics*, 520, 157-186.
- Nelson M.A., Brown M.J., Pardyjak E.R. and Klewicki J.C., 2004, Area-averaged profiles over the mock urban setting test array, *Proceedings of the 5th Symposium on the Urban Environment*, August 23-26, 2004, 577-581.
- Nelson M.A., Pardyjak E.R., Klewicki J.C., Pol S.U. and Brown M. J., 2007, Properties of the wind field within the Oklahoma city park avenue street canyon, Part I, mean flow and turbulence statistics, *Journal of Applied Meteorology and Climatology*, 46, 2038-2054.
- Nogueira J., Lecuona A. and Rodriguez P.A., 1997, Data validation, false vectors correction and derived magnitudes calculation on PIV data, *Measurement Science and Technology*, 8, 1493-1501.

- Obasaju E.D., Bearman P.W. and Graham J.M.R., 1988, A study of forces, circulation and vortex patterns around a circular cylinder in oscillating flow, *Journal of Fluid Mechanics*, 196, 467-494.
- Ohmi M. and Iguchi M., 1982, Critical Reynolds number in an oscillating pipe flow, *Bulletin of JSME*, 25(200), 165-172.
- Ohmi M., Iguchi M., Kakehashi K. and Masuda T., 1982, Transition to turbulence and velocity distribution in an oscillating pipe flow, *Bulletin of JSME*, 25(201), 365-371.
- Ohmi M., Iguchi M. and Urahata I., 1982, Flow patterns and frictional losses in an oscillating pipe flow, *Bulletin of JSME*, 25(202), 536-543.
- Okajima A., 1982, Strouhal numbers of rectangular cylinders, *Journal of Fluid Mechanics*, 123, 379-398.
- Okajima A., Matsumoto T. and Kimura S., 1997, Force measurements and flow visualization of bluff bodies in oscillatory flow, *Journal of Wind Engineering & Industrial Aerodynamics*, 69-71, 213-228.
- Okamoto K., 2006, 6th International Symposium on Particle Image Velocimetry 2005 (Editorial), *Measurement Science and Technology*, 17, doi: 10.1088/0957-0233/17/7/E01.
- Paek I., Braun J.E. and Mongeau L., 2005, Second law performance of thermoacoustic systems, *Journal of the Acoustical Society of America*, 118, 1892.
- Paek I., Mongeau L. and Braun J. E., 2005, A method for estimating the parameters of electrodynamic drivers in thermoacoustic coolers, *Journal of Acoustical Society of America*, 117, 185-193.
- Pai S-I, 1957, *Viscous flow theory, II – Turbulent flow*, D. van Nostrand Company, Inc.
- Paranthoen P., Petit C. and Lecordier J.C., 1982, The effect of the thermal prong-wire interaction on the response of a cold wire in gaseous flows, *Journal of Fluid Mechanics*, 124, 457-473.
- Peacock J.A. and Stairmand J.W., 1983, Film gauge calibration in oscillatory pipe flow, *Journal of Physics, E, Scientific Instruments*, 16(6), 571-576.
- Petculescu G. and Wilen L. A., 2003, Oscillatory flow in jet pumps: nonlinear effects and minor losses, *Journal of Acoustical Society of America*, 113, 1282-1292.
- Peyrin F. and Kondjoyan A., 2002, Effect of turbulent integral length scale on heat transfer around a circular cylinder placed cross to an air flow, *Experimental Thermal and Fluid Science*, 26, 455-460.
- Piirto M., Ihalainen H., Eloranta H. and Saarenrinne P., 2001, 2D Spectral and Turbulence Length Scale Estimation with PIV, *Journal of Visualisation*, 4, 39-49.
- Ponta F.L. and Aref H., 2005, Vortex synchronization regions in shedding from an oscillating cylinder, *Physics of Fluids*, 17, 011703.
- Ponta F.L. and Aref H., 2006, Numerical experiments on vortex shedding from an oscillating cylinder, *Journal of Fluids and Structures*, 22(3), 327-344.
- Prasad A.K., 2000, Stereoscopic particle image velocimetry, *Experiments in Fluids*, 29, 103-116.
- Prasad A.K. and Adrian R.J., 1993, Stereoscopic particle image velocimetry applied to liquid flows, *Experiments in Fluids*, 15, 49-60.
- Putnam, A.A., Dennis, W.R. (1956), Survey of organ-pipe oscillations in combustion systems, *Journal of the Acoustical Society of America* 28(2), 246-259.

- Raffel M., Willert C.E., Wereley S.T. and Kompenhans J., 2007, Particle Image Velocimetry - A Practical Guide, 2nd Edition, Springer.
- Ralph M.E., 1986, Oscillatory flows in wavy-walled tubes, *Journal of Fluid Mechanics*, 168, 518-540.
- Ramaprian B.R. and Tu S.W., 1980, An experimental study of oscillatory pipe flow at transitional Reynolds numbers, *Journal of Fluid Mechanics*, 100, 513-544.
- Rawlins W., Redebaugh R. and Timmerhaus K.D., 1993, Thermal anemometry for mass flow measurement in oscillating cryogenic gas flows, *Review of Scientific Instruments*, 64 (11), 3229-3235.
- Rayleigh Lord, J.W., 1945, the Theory of Sound, 2nd Edition revised and enlarged, New York, Dover Publications, Vol. 2, Sections 322g-j.
- Regunath G.S., Zimmerman W.B., Tesař V. and Hewakandamby B.N., 2008, Experimental investigation of helicity in turbulent swirling jet using dual-plane dye laser PIV technique, *Experiments in Fluids*, 45, 973-986.
- Reuss D.L., Megerle M. and Sick V., 2002, Particle-image velocimetry measurement errors when imaging through a transparent engine cylinder, *Measurement Science and Technology*, 17, 1029-1035
- Richardson E.G., 1922, The theory of the singing flame, *Proceedings of the Physical Society of London*, 35, 47-54.
- Richardson E.G. and Tyler E., 1929, The transverse velocity gradient near the mouths of pipes in which an alternating or continuous flow of air is established, *Proceedings of the Physical Society*, 42(1), 1-15.
- Richardson P.D., 1963, Note: Comments on viscous damping in oscillating liquid columns, *International Journal of Mechanical Sciences*, 5(5), 415-418.
- Roach P.D. and Bell K.J., 1989, Analysis of pressure drop and heat transfer data from the reversing flow test facility, NASA STI/Recon Technical Report, N 89, 27984.
- Roberts E.P.L. and Mackley M.R., 1996, The development of asymmetry and period doubling for oscillatory flow in baffled channels, *Journal of Fluid Mechanics*, 328, 19-48.
- Roshko A., 1954, On the Development of Turbulent Wakes from Vortex Streets, National Advisory Committee for Aeronautics, NACA Tech Report, 1191.
- Rott N., 1969, Damped and thermally driven acoustic oscillations in wide and narrow tubes, *Journal of Applied Mathematics and Physics (ZAMP)*, 20, 230-243.
- Rott N., 1973, Thermally driven acoustic oscillations, Part II, stability limit for Helium, *Journal of Applied Mathematics and Physics (ZAMP)*, 24, 54-72.
- Rott N., 1974a, The influence of heat conduction on acoustic streaming, *Journal of Applied Mathematics and Physics (ZAMP)*, 25, 417-421.
- Rott N., 1974b, The heating effect connected with non-linear oscillations in a resonance, *Journal of Applied Mathematics and Physics (ZAMP)*, 25, 619-634.
- Rott N., 1975, Thermally driven acoustic oscillations, Part III, second-order heat flux, *Journal of Applied Mathematics and Physics (ZAMP)*, 26, 43-49.
- Rott N., 1976a, Thermally driven acoustic oscillations, Part IV, tubes with variable cross-section, *Journal of Applied Mathematics and Physics (ZAMP)*, 27, 197-224.
- Rott N., 1976b, Thermally driven acoustic oscillations, Part V, gas-liquid oscillations, *Journal of Applied Mathematics and Physics (ZAMP)*, 27, 325-334.

- Rott N., 1976c, Acoustical streaming and thermal effects in pipe flow with high viscosity, *Journal of Applied Mathematics and Physics (ZAMP)*, 27, 709-715.
- Rott N., 1980, Thermoacoustics, *Advances in Applied Mechanics*, 20, 135-175.
- Royer H., 1997, Holography and particle image velocimetry, *Measurement Science and Technology*, 8, 1562-1572.
- Sak C., Liu R., Ting D.S.-K. and Rankin G.W., 2007, The role of turbulence length scale and turbulence intensity on forced convection from a heated horizontal circular cylinder, *Experimental Thermal and Fluid Science*, 31, 279-289.
- Santiago J.G., Wereley S.T., Meinhart C.D., Beebe D.J. and Adrian R.J., 1998, A particle image velocimetry system for microfluidics, *Experiments in Fluids*, 25, 316-319.
- Schroeder A. and Willert C.E. (eds.), 2008, *Particle Image Velocimetry - New Developments and Recent Applications*, Springer-Verlag, Berlin, Heidelberg.
- Scott J., Kelly J. and Leembruggen G., 1996, New method of characterizing driver linearity, *Journal of the Audio Engineering Society*, 44(4), 258-265.
- Sergeev S.I., 1966, Fluid oscillations in pipes at moderate Reynolds numbers, *Fluid Dynamics*, 1(1), 121-122.
- Seume J.R., 1988, An experimental investigation of transition in oscillating pipe flow, Ph. D. Thesis, Minnesota University, Minneapolis, United States.
- Shemer L., Wygnanski I. and Kit E., 1985, Pulsating flow in a pipe, *Journal of Fluid Mechanics*, 153, 313-337.
- Shi L., Yu Z. and Jaworski A.J., 2009, Vortex formation at the end of the parallel-plate stack in the standing-wave thermoacoustic device, *Proceedings of The Sixteenth International Congress on Sound and Vibration, Kraków, Poland, 5-9 July 2009*.
- Shi L., Yu Z. and Jaworski A.J., 2010, Vortex shedding flow patterns and their transitions in oscillatory flows past parallel-plate thermoacoustic stacks, *Experimental Thermal and Fluid Science*, 34(7), 954-965.
- Shi L., Yu Z. and Jaworski A.J., 2011, Investigation into the Strouhal numbers associated with vortex shedding from parallel-plate thermoacoustic stacks in oscillatory flow conditions, *European Journal of Mechanics - B: Fluids*, 30(2), 206-217.
- Shinohara K., Sugii Y., Aota A., Hibara A., Tokeshi M., Kitamori T. and Okamoto K., 2004, High speed micro-PIV measurements on transient flow in microfluidic devices, *Measurement Science and Technology*, 15, 1965-1970.
- Siebert H. and Lehmann K., 2007, On the use of hot-wire anemometers for turbulence measurements in clouds, *Journal of Atmospheric and Oceanic Technology*, 24(6), 980-993.
- Siegel R., 1987, Influence of oscillation-induced diffusion on heat transfer in a uniformly heated channel, *Journal of Heat Transfer*, 109, 244-247.
- Smith B.L. and Swift G.W., 2003, Power dissipation and time-averaged pressure in oscillating flow through a sudden area change, *Journal of the Acoustical Society of America*, 113, 2455-2463.
- Sumer B.M., Jensen B.L. and Fredsbe J., 1991, Effect of a plane boundary on oscillatory flow around a circular cylinder, *Journal of Fluid Mechanics*, 225, 271-300.
- Sung H.J., Kim K.C. and Lee S.J., 2004, 5th International Symposium on Particle Image Velocimetry, PIV'03 (Editorial), *Measurement Science and Technology*, 15, doi: 10.1088/0957-0233/15/6/E01.

- Swift G.W., Migliori A., Wheatley J.C. and Garrett S.L., 1982, Calibration of a dynamic pressure transducers using reciprocity in a plane wave resonator, *Journal of the Acoustical Society of America*, 72 (S1), S81.
- Swift G.W., 1988, Thermoacoustic engines, *Journal of the Acoustical Society of America*, 84(4), 1145-1180.
- Swift G.W., 2002, *Thermoacoustics: A unifying perspective for some engines and refrigerators*, Acoustical Society of America. Melville, New York.
- Taconis K.W., Beenakker J.J.M., Nier A.O.C. and Aldrich, L.T., 1949, Measurements concerning the vapour-liquid equilibrium of solutions of He<sup>3</sup> in He<sup>4</sup> below 2.19°K, *Physica*, 15, 733-739.
- Tatsuno M. and Bearman P.W., 1990, A visual study of the flow around an oscillating circular cylinder at low Keulegan-Carpenter numbers and low Stokes numbers, *Journal of Fluid Mechanics*, 211, 157-182.
- Thompson M.W. and Atchley A.A., 2005, Simultaneous measurement of acoustic and streaming velocities in a standing wave using laser Doppler anemometry, *Acoustical Society of America Journal*, 117(4), 1828-1838.
- Thompson M.W., Atchley A.A. and Maccarone M.J., 2005, Influences of a temperature gradient and fluid inertia on acoustic streaming in a standing wave, *The Journal of the Acoustical Society of America*, 117(4), 1839-1849.
- Tijani M.E.H., Zeegers J.C.H. and de Waele A.T.A.M., 2002, A gas-spring system for optimizing loudspeakers in thermoacoustic refrigerators, *Journal of Applied Physics*, 92(4), 2159-2165.
- Trinité M. and Lecordier B., 2001, Editorial, *Measurement Science and Technology*, 12, doi: 10.1088/0957-0233/12/9/001.
- Tropea C., 2002, Editorial, *Measurement Science and Technology*, 13, doi: 10.1088/0957-0233/13/7/001.
- Tutu N.K., Chevray R., 1975, Cross-wire anemometry in high intensity turbulence, *Journal of Fluid Mechanics*, 71(4), 785-800.
- Uchida S., 1956, The pulsating viscous flow superposed on the steady laminar motion of incompressible fluid in a circular pipe, *Zeitschrift für Angewandte Mathematik und Physik (ZAMP)*, 7(5), 403-422.
- Vignola J.F., Berthelot Y.H. and Jarzynski J., 1991, Laser detection of sound, *The Journal of the Acoustical Society of America*, 90(3), 1275-1286.
- Wakeland R.S. and Keolian R.M., 2002, Influence of velocity profile nonuniformity on minor losses for flow existing thermoacoustic heat exchangers, *Journal of the Acoustical Society of America*, 112, 1249-1252.
- Ward W.C. and Swift G.W., 1994, Design environment for low amplitude thermoacoustic engines (DELTAEC). *Journal of Acoustical Society of America*, 95, 3671-3672. Also, Ward W.C., Clark J. and Swift G.W., 2008, Design environment for low-amplitude thermoacoustic energy conversion (DeltaEC), Users Guide, Los Alamos National Laboratory. Program available from the Los Alamos National Laboratory (<http://www.lanl.gov/thermoacoustics/>).
- Wetzel M. and Herman C., 1999, Experimental study of thermoacoustic effects on a single plate, Part II: heat transfer, *Heat and Mass Transfer*, 35, 433-441.
- Wetzel M. and Herman C., 2000, Experimental study of thermoacoustic effects on a single plate, Part I: temperature fields, *Heat and Mass Transfer*, 36, 7-20.

- West G.S. and Apelt C.J., 1982, The effects of tunnel blockage and aspect ratio on the mean flow past a circular cylinder with Reynolds numbers between 104 and 105, *Journal of Fluid Mechanics*, 114, 361-377.
- Wheatley J., Hofler T., Swift G.W. and Migliori A., 1983a, Experiments with an intrinsically irreversible acoustic heat engine, *Physical Review Letters*, 50(7), 499-502.
- Wheatley J., Hofler T., Swift G.W. and Migliori A., 1983b, An intrinsically irreversible thermoacoustic heat engine, *Journal of the Acoustical Society of America*, 74(1), 153-170.
- Williamson C.H.K., 1988, The existence of two stages in the transition to three dimensionality of a cylinder wake, *Physics of Fluids*, 31, 3165-3168.
- Williamson C.H.K. and Roshko A., 1988, Vortex formation in the wake of an oscillating cylinder, *Journal of fluids and structures*, 2(4), 355-381.
- Womersley J.R., 1955a, Method for the calculation of velocity, rate of flow and viscous drag in arteries when the pressure gradient is known, *Journal of Physiology*, 127, 553-563.
- Womersley J.R., 1955b, Oscillatory motion of a viscous liquid in a thin-walled elastic tube, I: The linear approximation for long waves, *Philosophical Magazine (Series 7)*, 46(373), 199-221.
- Worlikar A.S., Knio O.M. and Klein R., 1996, Numerical simulation of a thermoacoustic refrigerator, *Proceedings of ESAIM (European Series in Applied and Industrial Mathematics)*, 1, 363-375.
- Worlikar A.S. and Knio O.M., 1996, Numerical simulation of a thermoacoustic refrigerator, Part I: Unsteady adiabatic flow around the stack, *Journal of Computational Physics*, 127, 424-451.
- Worlikar A.S., Knio O.M. and Klein R., 1998, Numerical simulation of a thermoacoustic refrigerator, Part II: Stratified flow around the stack, *Journal of Computational Physics*, 144, 299-324.
- Wu P., Lin B., Zhu S., He Y., Ren C. and Wang F., 1990, Investigation of oscillating flow resistance and heat transfer in the gap used for cryocoolers, *Proceedings of the 13th Intersociety Energy Conversion Engineering*.
- Wyngaard J.C., 1971, The effect of velocity sensitivity on temperature derivative statistics in isotropic turbulence, *Journal of Fluid Mechanics*, 48, 763-769.
- Yamanaka G., Kikura H., Takeda Y. and Aritomi M., 2002, Flow measurement on an oscillating pipe flow near the entrance using the UVP method, *Experiments in Fluids*, 32(2), 212-220.
- Yazaki T., Iwata A., Maekawa T. and Tominaga A., 1998, Traveling wave thermoacoustic engine in a looped tube, *Physics Review Letter*, 81(15), 3128-3131.
- Yazaki T., Tominaga A. and Narahara Y., 1979, Stability limit for thermally driven acoustic oscillation, *Cryogenics*, 19(7), 393-396.
- Yazaki T., Tominaga A. and Narahara Y., 1980, Experiments on thermally driven acoustic oscillations of gaseous Helium, *Journal of Low Temperature Physics*, 41, 45-60.
- Yellin E.L., 1966, Laminar-turbulent transition process in pulsatile flow, *Circulation Research*, 19, 791-804.
- Zdravkovich, M.M., 1996, Different modes of vortex shedding: an overview, *Journal of Fluids and Structures*, 10(5), 427-437.
- Zdravkovich M.M., 1997, *Flow around circular cylinders, Volume 1: Fundamentals*, Oxford University Press.

- Zhao T. and Cheng P., 1995, A numerical solution of laminar forced convection in a heated pipe subjected to a reciprocating flow, *International Journal of Heat and Mass Transfer*, 38(16), 3011-3022.
- Zhao T. and Cheng P., 1996a, Experimental studies on the onset of turbulence and frictional losses in an oscillatory turbulent pipe flow, *International Journal of Heat and Fluid Flow*, 17(4), 356-362.
- Zhao T. and Cheng P., 1996b, The friction coefficient of a fully developed laminar reciprocating flow in a circular pipe, *International Journal of Heat and Fluid Flow*, 17(2), 167-172.
- Zhao T. and Cheng P., 1996c, Oscillatory heat transfer in a pipe subjected to a laminar reciprocating flow, *Journal of Heat Transfer*, 118, 592-598.
- Zhao T. and Cheng P., 1998, Heat transfer in oscillatory flows, *Annual Review of Heat Transfer*, 9, 1-64.
- Zimmerman W.B., 2002, The drag on sedimenting discs in broadside motion in tubes, *International Journal of Engineering Science*, 40, 7-22.
- Zimmerman W.B., 2004, On the resistance of a spherical particle settling in a tube of viscous fluid, *International Journal of Engineering Science*, 42, 1753-1778.